

Hydrogen interactions with silicon-on-insulator materials

The research described in this thesis was performed at the Department of Defects in Materials of the Interfaculty Reactor Institute (IRI) and at the Delft Institute of Microelectronics and Submicron technology (DIMES), Delft University of Technology, Delft, The Netherlands. The project was supported by the Dutch Technology Foundation (STW), project DEL-4038.

Hydrogen interactions with silicon-on-insulator materials

PROEFSCHRIFT

ter verkrijging van de graad van doctor
aan de technische Universiteit Delft,
op gezag van de Rector Magnificus prof. dr. ir. J. T. Fokkema
voorzitter van het College voor Promoties,
in het openbaar te verdedigen op maandag 13 januari 2003 om 13:30 uur

door

Antonio Juan Rivera de Mena

Licenciado en Ciencias Físicas, Universidad Complutense, Madrid
geboren te Madrid, Spanje

Dit proefschrift is goedgekeurd door de promotor:
Prof. dr. A. van Veen

Samenstelling promotiecommissie:

Rector Magnificus, Prof. dr. A. van Veen	voorzitter Rijksuniversiteit Groningen, Technische Universiteit Delft, promotor
Dr. J.M.M. de Nijs	KPN Telecom
Prof. dr. A. Stesmans	Katholieke Universiteit, Leuven
Prof. dr. F.H.P.M. Habraken	Universiteit Utrecht
Prof. dr. L.K. Nanver	Technische Universiteit Delft
Prof. dr. ir.C.W.E. van Eijk	Technische Universiteit Delft
Prof. Dr. Ir. J.W. Slotboom	Technische Universiteit Delft

Dr. ir. J.M.M. de Nijs en Dr. H. Schut hebben als begeleiders in belangrijke mate aan de totstandkoming van dit proefschrift bijgedragen

Published and distributed by: DUP Science

DUP Science is an imprint of
Delft University Press
P.O. Box 98
2600 MG Delft
The Netherlands
Telephone: +31 15 2785678
Fax: +31 15 2785706
E-mail Info@library.TUdelft.nl

ISBN 90-407-2374-5

Keywords: Silicon-on-insulator / hydrogen / carrier injection / positron annihilation / thermal desorption / MOS capacitors

Copyright © 2002 by A. Rivera

All rights reserved. No part of the material protected by this copyright notice may be reproduced or utilised in any form or by any means, electronic or mechanical, including photocopying, recording or by any information storage and retrieval system, without permission from the publisher: Delft University Press.

Printed in the Netherlands

Contents

CHAPTER 1. INTRODUCTION	1
1.1. SOI MATERIALS	2
1.2. ROLE OF HYDROGEN	3
1.3. SCOPE OF THIS THESIS	4
CHAPTER 2. DEFECT REACTIONS AND MODELLING	7
2.1. CHARGE BUILD UP, DANGLING BOND GENERATION AND HYDROGEN RELEASE IN MOS STRUCTURES SUBJECTED TO HOLE INJECTION	8
2.2. THERMAL RELEASE OF DEUTERIUM FROM SiO ₂	9
2.3. POSITRON TRANSPORT ALONG SiO ₂ LAYERS OF MOS STRUCTURES	10
2.3.1. <i>General problem</i>	10
2.3.2. <i>The Ps formation</i>	11
2.3.3. <i>Initial concentrations</i>	12
2.3.4. <i>The transport equations</i>	15
2.3.5. <i>Observables</i>	16
CHAPTER 3. EXPERIMENTAL	19
3.1. SAMPLE TREATMENT	20
3.1.1. <i>Cleaning, metallisation and etching</i>	20
3.1.2. <i>Ion implantation</i>	20
3.1.3. <i>Sample annealing</i>	22
3.2. DESORPTION SPECTROMETRY	23
3.2.1. <i>Thermal desorption spectrometry</i>	23
3.2.2. <i>Radiation-induced desorption spectrometry</i>	35
3.3. POSITRON BEAM ANALYSIS	36
3.3.1. <i>Doppler broadening of annihilation radiation</i>	38
3.3.2. <i>Two-dimensional correlation of annihilation radiation</i>	41
CHAPTER 4. HYDROGEN-RELATED HOLE CAPTURE AND POSITIVE CHARGE BUILD UP IN BURIED OXIDES	43
4.1. INTRODUCTION	44
4.2. EXPERIMENTAL	44
4.2.1. <i>Sample preparation</i>	44
4.2.2. <i>Comments on the large area capacitors</i>	45
4.3. RESULTS	45
4.4. DISCUSSION	53
4.4.1. <i>Evidence of hole-induced hydrogen release</i>	53
4.4.2. <i>Relation between hole capture and charge build up</i>	53
4.4.3. <i>Relation between hole capture and generation of Si• defects</i>	54
4.5. CONCLUSIONS	55

CHAPTER 5. HYDROGEN UPTAKE AND RELEASE IN BURIED OXIDES	57
5.1. INTRODUCTION	58
5.2. EXPERIMENTAL	58
5.3. TDS RESULTS ON SAMPLES WITH TOP SI LAYER REMOVED	59
5.3.1. <i>Annealing in deuterium gas</i>	59
5.3.2. <i>Ion implantation</i>	60
5.3.3. <i>Discussion</i>	61
5.4. THE EFFECT OF THE TOP SI LAYER	64
5.5. CONCLUSIONS	65
CHAPTER 6. DEFECT GENERATION AND ANNEALING	67
6.1. THE TOP SILICON LAYER OF SOI STRUCTURES	68
6.1.1. <i>Sample description</i>	68
6.1.2. <i>Results and discussion</i>	69
6.1.3. <i>Conclusions</i>	74
6.2. DEFECT GENERATION AND ANNEALING IN SiO ₂	75
6.2.1. <i>Sample description</i>	75
6.2.2. <i>Positron analysis SiO₂: the role of positronium</i>	76
6.2.3. <i>Hole and electron injection in SiO₂</i>	81
6.2.4. <i>Deuterium and helium implantation in SiO₂ structures</i>	85
6.2.5. <i>Annealing of defects</i>	93
6.2.6. <i>Conclusions</i>	98
CHAPTER 7. POSITRON TRANSPORT IN MOS SYSTEMS: APPLICATION TO INTERFACE STUDIES	99
7.1. POSITRON TRANSPORT IN SiO ₂	100
7.1.1. <i>Experimental</i>	100
7.1.2. <i>Observation of positron transport in SiO₂</i>	101
7.1.3. <i>Determination of the Al/SiO₂ cluster point</i>	105
7.1.4. <i>Positronium reduction under the application of electric fields</i>	106
7.1.5. <i>Modelling the combined effect of positron transport and Ps reduction</i>	109
7.1.6. <i>Positron implantation in the depletion layer of the Si substrate</i>	114
7.1.7. <i>Modelling the positronium reduction in the presence of an electric field</i>	116
7.1.8. <i>Suppression of positron transport</i>	118
7.2. SiO ₂ /Si INTERFACE STUDIES	119
7.2.1. <i>Samples and sample treatments</i>	119
7.2.2. <i>Identification of the SiO₂/Si interface</i>	120
7.2.3. <i>Positronium formation at the interfaces</i>	123
7.2.4. <i>Potential barrier at the SiO₂/Si interface</i>	123
7.2.5. <i>SiO₂/Si interface for different oxides and treatments</i>	125
7.2.6. <i>SiO₂/Si interface under very high positive fields; electron injection from the Si substrate</i>	128
7.3. CONCLUSIONS	128
CHAPTER 8. AMORPHOUS AND HETEROGENEOUS HYDROGENATED SILICON DEPOSITED ON SILICON DIOXIDE	131
8.1. INTRODUCTION	132
8.2. SUMMARY OF PREVIOUS WORK	133
8.3. SAMPLE PREPARATION	134
8.4. THE DEPOSITED LAYERS	135
8.5. THE INTERFACES BETWEEN THE DEPOSITED LAYERS AND SiO ₂	142
8.6. CONCLUSIONS	144

REFERENCES	147
SUMMARY	151
SAMENVATTING	155
ACKNOWLEDGEMENTS	159
CURRICULUM VITAE	161

Chapter 1

Introduction

Research on silicon-based materials for the semiconductor industry has been carried out for more than half a century. The success is evident. One only has to think of the marvellous computers that we use nowadays, which half a century ago were only present in the most imaginative minds and probably as a Science-Fiction product. Periodically, for already many years, news is spread claiming the end of the silicon era. However, silicon technology continues expanding even when its physical limit seem reached. This is a clear consequence of the intense research devoted to it.

It is interesting that despite so many years of such intense research, there remain many topics of new research. In many cases this “new” research is not new at all but an upgrade of work started a long time ago that needs revision or that was never totally brought to conclusion. This is a clear consequence of the high degree of understanding demanded in many cases and of the many subtle aspects that must be understood in order to get a clear picture of the phenomena involved. Finally, that will lead to successful predictions, which is the goal of this research.

Hydrogen studies in Si/SiO₂ systems are a clear example of the points mentioned above. The number of intricate processes in which hydrogen plays an important role is enormous and by no means irrelevant. Hydrogen is definitely omnipresent. It can be accumulated at any interface, in voids in Si, in metal contacts, in solution in both Si and SiO₂ or forming chemical bonds with both types of atoms or even with dopants. It is present in atomic, molecular or charged states and virtually during any treatment applied to the samples: in the form of water, forming part of chemicals and even in ultra high vacuum systems as the main component. Hydrogen is responsible for many unexpected situations, usually related to device malfunction.

In the case of Silicon-On-Insulator (SOI) materials, the role of hydrogen is even more important, because it is often present in large amounts. The understanding of all these aspects is an ever-improving process. The present thesis is intended to be a contribution to this process. A number of conclusive results are obtained, which hopefully will help others with their research, approaching the end of the silicon era or prolonging its supremacy.

1.1. SOI materials

Definitely, the dominant position of silicon is due to the unique properties of SiO_2 acting as the counterpart of silicon in planar technology. The interface Si/SiO_2 is the most appropriate one for the fabrication of integrated circuits. This is due to the excellent properties of SiO_2 . Water is not soluble in SiO_2 . It has good mechanical properties. It has good dielectric properties. Finally, it screens electrostatic effects allowing the induction of electric fields from a metal gate, which is the basis of the metal oxide semiconductor (MOS) technology.

The MOS system consists of a silicon dioxide layer between an electrode (generally, poly-Si or Al) and a silicon substrate. The bias applied to the top electrode (gate) determines the density of charge carriers in the silicon substrate. This is employed in MOS field effect transistors (MOSFET) to control the current flowing between two terminals called source and drain.

Silicon-On-Insulator (SOI) materials are composed of a SiO_2 layer sandwiched between two crystalline Si layers, see Fig. 1.1. The advantage of this type of materials is that they permit the fabrication of integrated circuits, in which neighbouring MOS field effect transistors (MOSFET) are electrically insulated from each other, see Fig. 1.2. This type of isolation reduces the parasitic capacitance and the cross-talk between devices, improves the current drive, sub-threshold characteristics and current gain.

SOI devices are especially suitable for low-voltage integrated circuits such as those employed in cellular phones. Due to the particular configuration of devices built with SOI materials, they are particularly appropriate for applications in hostile environments, i.e., on-board of satellites, or for high temperature applications. The advantages have been understood by the semiconductor industry and nowadays, major producers like Philips, IBM, Sharp or Motorola already employ SOI materials.

There are several techniques to fabricate SOI materials. This thesis is focused on the two most popular ones: SIMOX (Separation by implantation of oxygen) and Unibond.

SIMOX material is created by the implantation of oxygen ions into a crystalline silicon substrate at a sufficiently high temperature (550-600°C) to avoid amorphisation of the Si substrate. A post implantation annealing of several hours at 1300-1350°C in an Ar ambient containing 0.5% O_2 is necessary to achieve good quality. Typically the top Si layer is 200 nm-thick and the buried oxide (BOX) 400 nm-thick.

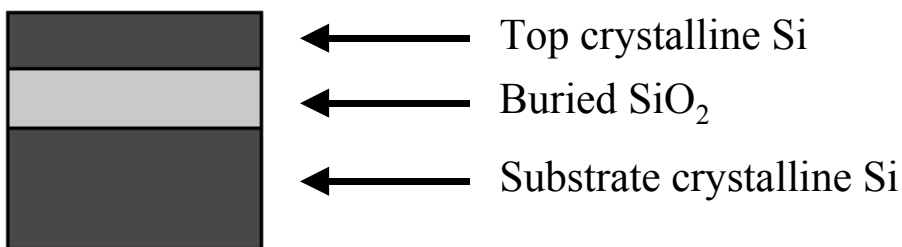


Fig. 1.1. Structure of SOI materials.

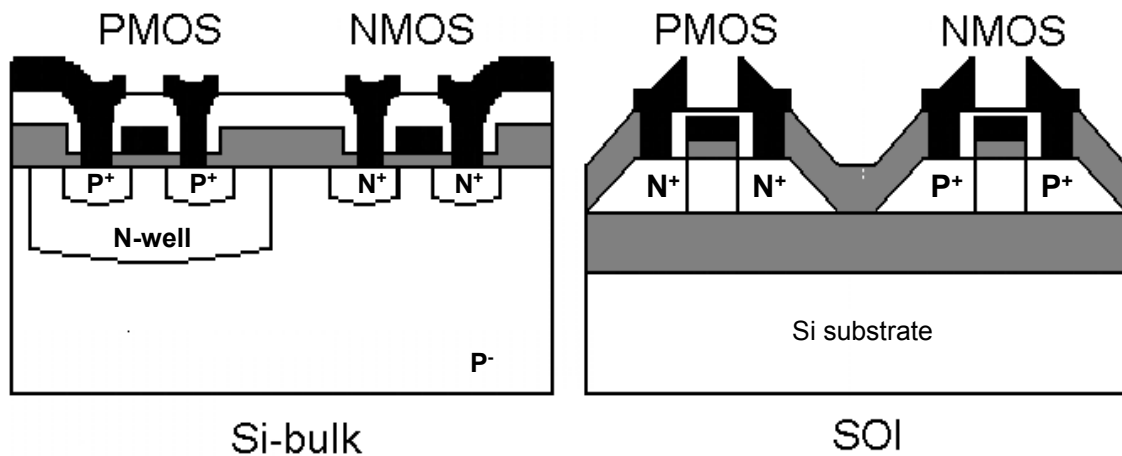


Fig. 1.2. MOSFET transistors fabricated with bulk Si (left) or with SOI material (right). The black areas represent metal connections, the grey ones SiO₂ and the white ones Si.

Unibond samples are fabricated by the Smart Cut method, which is based on the generation of blistering in a crystalline sample by high dose hydrogen implantation and subsequent annealing. The generation of blisters causes a thin film to be split off the substrate. The driving force behind this mechanism is the huge gas pressure in the cavities created by ion implantation and subsequent annealing. The films split by this method contain few defects. The fabrication mechanism consists of several steps:

- Oxidation of two silicon wafers.
- Ion implantation through the oxide layer of one of the wafers.
- Hydrophilic binding at room temperature of both wafers.
- Heat treatment at 400-600°C, in order to split the wafer implanted with hydrogen, giving rise to an SOI structure that must be annealed at 1100°C for 2 h to remove silanol groups from the binding interface. The remaining wafer can be re-used.
- Finally, the SOI structure must be polished to eliminate roughness at the surface.

Despite the advantages mentioned above for MOSFET transistors integrated in SOI material, the SOI materials themselves contain an important number of defects. This is due to the fabrication processes, which are much more complex than in conventional bulk-Si technology, [Afanas'ev et al. 1997, Krause et al. 1998, Revesz et al. 1996].

1.2. Role of hydrogen

Electrically active defects present in the different layers of MOS structure, i.e. Si, SiO₂ or the interface, will change the behaviour of the device, because the charge on the gate will not only be compensated by mobile charges in the silicon substrate, but also by charges at the

defects. The accumulation of charge during operation will degrade the device. In modern semiconductor technology defect densities exceeding 10^{10} cm^{-2} are unacceptable.

Despite the beneficial role of hydrogen as a passivating agent of interface defects, it has been observed that defect generation is often related to the hydrogen concentration in the sample, see e.g. [Winokur 1989]. Hydrogen plays a direct role in many degradation processes, e.g., trap creation [DiMaria et al. 1995, Afanas'ev et al. 1995], donor generation at the Si/SiO₂ interface [de Nijs et al. 1994] and depassivation of dangling bonds [Stesmans 2000b]. In addition, it may also cause leakage currents [Afanas'ev et al. 1999], induce electronic states in the Si band gap [Holm et al. 1991] and form complexes with shallow dopant impurities reducing their activity [Pankove et al. 1983].

Hydrogen is always present in Si-SiO₂ and in the ambients in which devices are operated or fabricated and can become active by regular treatments like annealing, e.g. to activate dopants, or by sample exposure to ionising radiation, e.g. during lithography. Annealing will lead to the incorporation of hydrogen in the samples, while exposure to radiation will result in charge generation, holes or electrons, which in turn can lead to hydrogen release from trapped configurations in very reactive states: atomic or ionic. In this sense, it has been shown that electrons interact with Si-OH groups (cross-section $\sim 10^{-17} \text{ cm}^2$) [Nicollan et al. 1971] releasing atomic hydrogen. On the other hand, holes interact with Si-H defects releasing H⁺ protons [Afanas'ev et al. 2000], which are very reactive and considered responsible for the build up of positive charge at the interface.

In SIMOX buried oxides the hydrogen uptake during annealing in hydrogen is surprisingly high [Myers et al. 1993, Zimmerman et al. 1998]. Such a high concentration can lead to fast degradation. Therefore, it is important to understand the role of hydrogen and its interactions in order to keep it under control.

1.3. Scope of this thesis

Two principal techniques were employed in this thesis: thermal desorption spectrometry (TDS) and positron beam analysis (PBA). These techniques are not standard in semiconductor research. The objective was to explore new possibilities and supply new data on the defect structure of SOI samples. By means of TDS, information on the configuration of hydrogen binding to defects in SiO₂ can be extracted, in addition to the total number of hydrogen atoms involved. By means of PBA, information on open volume and negatively charged defects can be obtained since positrons are easily trapped at these defects.

The application of these techniques to the study of SOI materials required a technical effort to adapt them to the special requirements of semiconductor studies, see Chapter 3. In order to apply TDS, a new system was designed and mounted which permits performing hydrogen studies by minimising the background contribution. Positron beam studies were applied to the oxides in which positronium is easily formed. This led to the development of appropriate models to describe the results taking into account the role of positronium. In

addition, *electric fields* were applied to MOS capacitors during PBA measurements. This results in an exotic but attractive way of getting information from the samples.

A demonstration of the capabilities of these techniques is given in Chapters 4 to 8. In Chapter 4, the combined use of PBA, TDS and electrical measurements results in an important contribution to the understanding of the basis of hole injection in MOS devices. A substantial amount of experimental data was obtained in this way.

TDS studies of hydrogen release from SiO₂ structures discussed in Chapter 5 provided information on the hydrogen bond configurations in these samples and on the release mechanisms active during thermal annealing.

In Chapter 6, PBA measurements are employed to study the top Si layer of SOI structures, providing information on oxygen-related defects present in the SIMOX top layer. In addition, the BOX layers of different SOI samples are studied after different treatments such as electron injection, hole injection, thermal annealing and ion implantation. These treatments are employed to simulate real processes. The defects generated by these treatments are identified by PBA.

Chapter 7 is focused on interface studies by PBA under the simultaneous application of electric fields. Prior to the interpretation of the results, a model was developed to account for positron transport in the oxide.

Finally, Chapter 8 is devoted to the study of other SOI systems, i.e., those that have an amorphous silicon layer on top and are employed for solar cell applications and thin film transistors. Large voids, undetected by other techniques were identified by PBA. In addition, interface studies were performed on different samples with the technique developed in Chapter 7.

In Chapter 2 the models employed in subsequent chapters to describe experimental results are introduced.

Chapter 2

Defect reactions and modelling

It is virtually impossible to prevent the presence of hydrogen in SiO₂. Hydrogen species are very reactive in SiO₂ leading to passivation of dangling bonds. Atomic species can interact with bound hydrogen resulting in hydrogen release. In addition, charge carriers, i.e. electrons and holes interact with hydrogen containing defects leading to the release of hydrogen species and the accumulation of charge in the oxide. The principal reactions involving hydrogen species in SiO₂ are introduced in this chapter and are used in subsequent chapters to explain experimental results. Chapter 4 discusses the relation among holes injected into SiO₂ layers, charge build up, molecular hydrogen release and dangling bond generation. Hydrogen release from SiO₂ is the subject of Chapter 5. Finally, Chapter 7 discusses the positron transport in MOS structures.

2.1. Charge build up, dangling bond generation and hydrogen release in MOS structures subjected to hole injection

The build up of positive charge in oxides upon irradiation has been classically associated with the trapping of holes by oxygen vacancies resulting in paramagnetic E' centres, which were thought to be positively charged [Lenahan et al. 1984, Witham et al. 1987, Kim et al. 1988]. This model has been questioned [Afanas'ev et al. 2000] in the light of evident contradictions with a large number of experiments, see e.g. Refs. in [Afanas'ev et al. 2000]. Alternatively, a model based on the interaction between hydrogen and oxides has been proposed [Afanas'ev et al. 2001]. In the frame of this model the $O_3\equiv Si-H$ centre has been identified as the bulk hole trap with a cross-section $\sigma = (3-4)\times 10^{-14} \text{ cm}^2$. Upon hole trapping, a proton (H^+) is liberated and the centre is converted into the paramagnetic E' centre ($O_3\equiv Si\cdot$), following the reaction



where h^+ represents a hole. The liberated proton can be trapped in the oxide or travel to the Si/SiO₂ interface where donor-like interface states can be formed. In addition, the proton can be neutralised (H^0) by capturing an electron (e^-) from the Si substrate following



Finally, the neutralised proton (H^0) can form stable H₂ molecules. Both species are mobile at room temperature and both can interact with the generated $O_3Si\cdot$ centres re-entering the hole trapping process. The H₂ molecules can also escape from the oxide. These processes are described by



In the case of MOS samples annealed in deuterium gas after metallisation (see Chapter 4), both hydrogen and deuterium atoms play a role in the model.

The hole trapping process can be described by means of a first order trapping model,

$$\frac{\partial c_t}{\partial t} = c_h \alpha_h (c_0 - c_f) = c_h v_h \sigma (c_0 - c_f), \quad (2.6)$$

where $c_t(t) = [O_3\equiv Si-H]$ is the number of non-filled hole traps, t denotes the injection time, c_h is the hole concentration, α_h the hole capture coefficient, $c_0 = [O_3\equiv Si-H]_0$ the initial number of hole traps, $c_f = [O_3\equiv Si\cdot]$ the concentration of already filled hole traps, v_h the hole drift velocity and $\sigma = v_h \alpha_h$ is the hole capture cross section. The most accessible parameter during hole

injection is the intensity (J) of the current density which flows through the structure. Since $J/q = v_h c_h$ where q denotes the unit charge,

$$\frac{\partial c_t}{\partial t} = \frac{J\sigma}{q}(c_0 - c_f). \quad (2.7)$$

Assuming that J is constant, we can write

$$\frac{\partial c_t}{\partial t} = \frac{J\sigma}{q} c_0 \exp\left(-\frac{J\sigma}{q} t\right). \quad (2.8)$$

Equation (2.8) describes the kinetics of the hole capture process. This expression is used in Chapter 4 to extract the hole capture cross section.

2.2. Thermal release of deuterium from SiO₂

As will be explained in Chapter 5, deuterium is supposed to be trapped forming Si-D and Si-OD groups, the latter being more stable. The reactions



do not represent the actual release mechanism. Experimental data presented in Chapter 5 will show that they are not plausible. Ab initio calculations [Vitiello et al. 2000] indicate that these reactions can only occur at very high temperatures. In addition, $\text{O}_3\equiv\text{Si}\cdot$ (E' centre) and $\text{O}_3\equiv\text{Si-O}\cdot$ non-bridging oxygen hole centres (NBOHC) defects are not observed after thermal annealing experiments of SiO₂ samples. Instead, we consider the interaction of dissolved molecular hydrogen (H₂, HD or D₂) with Si-D and Si-OD. In this way the release of deuterium from Si-D or Si-OD groups giving $\text{O}_3\equiv\text{Si}\cdot$ and $\text{O}_3\equiv\text{Si-O}\cdot$, respectively, will follow



where the energies of reaction $H_{\text{Si-D}}$ and $H_{\text{O-D}}$ are the experimental values obtained in TDS experiments under the assumption of first order kinetics. The validity of this assumption relies on the fact that the concentration of dissolved species (mainly H₂) is more or less constant, which implies that the kinetics is governed by the concentration of Si-D and Si-OD groups.

Fig. 2.1 shows a diagram of the total energy of D₂ in the SiO₂ system. It shows schematically the difference between the barriers for the release of atomic deuterium from Si-D or Si-OD groups (4.6 and 5.5 eV respectively) and the barriers for the release of molecular deuterium (2.5 and 3.4 eV). The release of the molecular species is much more favourable (for a further description see Chapter 5).

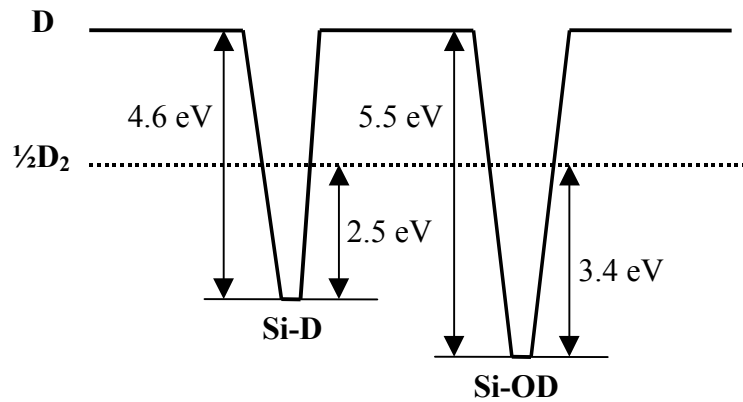


Fig. 2.1. Diagram of the total energy of a deuterium atom in interaction with SiO₂. Two trapping sites Si-D and Si-OD are shown. $\frac{1}{2} D_2$ denotes D bound to in the molecule D₂.

The molecular hydrogen (H₂, HD or D₂) obtained from reaction (2.12) can escape from the sample, and is then detected by TDS. It can also re-enter the release process by means of reactions like (2.12), or interact with the Si• and Si-O• defects generated leading to the experimentally observed passivation effect. The passivation reactions are



2.3. Positron transport along SiO₂ layers of MOS structures

2.3.1. General problem

The application of an electrical bias to a MOS device leads to the appearance of an electric field across the oxide. Positrons implanted in the oxide are drifted by this electric field owing to their electric charge. The slowing down of the implanted positrons leads to the generation of electron-hole pairs (on average 1 pair is created for every 17 eV of energy deposited in electron implantation experiments [Benedetto et al. 1986]). At low applied electric fields most of the generated electrons and holes recombine. However, higher electric fields produce charge separation. Thus, a significant fraction of electrons escapes recombination and is drifted across the oxide. Holes travel slowly and can interact with Si-H groups giving Si• defects, at which positrons can be trapped, as explained in Section 2.1, see also Chapter 4. Positronium (Ps) is formed by the interaction of the implanted positron with one of the quasi-free electrons generated during the positron slowing-down process, see Section 3.3. Since Ps is electrically neutral, the electric field does not have any influence on its motion. Due to the low diffusivity of Ps, it acts as a “trap” for positrons, suppressing positron response to the electric field. Finally, the fraction of Ps depends on the strength of the applied electric field.

2.3.2. The Ps formation

Due to the low intensity of the positron beam, the positive charge build up at the interface is considered negligible during VEP experiments. This is not true for experiments performed with a high intensity positron beam (see Chapter 3). This assumption was corroborated by in situ CV measurements. The number of Si• defects created by the interaction of holes and Si-H defects is considered to be small because the hole concentration is low at any time. In addition, these defects are in general easily passivated in the region across which positrons travel (see Chapter 4).

The electric field is supposed to be unaffected by the presence of the extra charge carriers introduced by the positron implantation because the average number of carriers in the sample is small and because positive and negative charges compensate each other. Therefore the electric field is assumed to be constant in the oxide layer and parallel to the axis Z, which represents the positron implantation direction.

Positrons implanted in the SiO₂ layer, once thermalised follow the drift diffusion equation

$$\frac{\partial n_p}{\partial t} = D_p \nabla^2 n_p - v_p \nabla n_p - (\lambda_b + \kappa_t + \alpha_{Ps} n_e) n_p, \quad (2.15)$$

where n_p is the positron concentration, D_p is the positron diffusion coefficient, v_p the positron drift velocity, λ_b the positron annihilation rate in bulk SiO₂, κ_t is the positron trapping rate at Si• defects which is assumed to be constant, α_{Ps} the positronium formation rate constant and n_e the electron concentration.

Similarly for the electrons generated by positron implantation

$$\frac{\partial n_e}{\partial t} = D_e \nabla^2 n_e + v_e \nabla n_e - (\alpha_R n_h + \alpha_{Ps} n_p) n_e, \quad (2.16)$$

where D_e is the electron diffusion coefficient, v_e the electron drift velocity, α_R the electron-hole recombination rate, α_{Ps} the Ps formation rate and n_h the hole concentration.

Since the mobility of holes is much smaller than that of electrons, we consider that holes are frozen during the time that positrons and electrons are mobile and interact. In addition, due to the repulsive Coulombic force between positrons and holes, we neglect mutual interaction. Therefore, we can write for holes

$$\frac{\partial n_h}{\partial t} = -\alpha_R n_h n_e. \quad (2.17)$$

Since the positron mobility μ_p is relatively small, we can assume that the following relation is valid for the electric fields employed in this thesis

$$v_p = \mu_p E_z, \quad (2.18)$$

where E_z is the electric field along the axis Z . Then we can write equation (2.15) as

$$\frac{\partial n_p}{\partial t} = D_p \nabla^2 n_p - \mu_p E_z \frac{\partial n_p}{\partial z} - (\lambda_b + \kappa_t + \alpha_{Ps} n_e) n_p. \quad (2.19)$$

We can not write an equation analogous to (2.18) for electrons because at high electric fields, the velocity is not linear with the electric field. Instead, it reaches a saturation value of about 2.0×10^7 cm/s [Hughes 1978]. On the other hand, we can neglect the Ps formation term in (2.16) because the electron concentration is much larger than the positron concentration. Therefore, we can write equation (2.16) as

$$\frac{\partial n_e}{\partial t} = D_e \nabla^2 n_e + v_e \frac{\partial n_e}{\partial z} - \alpha_R n_h n_e. \quad (2.20)$$

2.3.3. Initial concentrations

Positron studies are performed with beams of intensity 10^5 - 10^8 e^+ s^{-1} cm^{-2} . The annihilation process is much faster than the implantation rate. Therefore, we assume that there is no more than one positron at any given time in the sample. Due to the large spot size of the incident positrons (0.8 cm^2), it is very unlikely that one positron meets holes (still in transit) generated by another positron. Therefore the initial concentration of holes is considered to be equal to that of the electrons. The initial concentration of electrons and holes was obtained by Monte-Carlo simulations [Pimblot et al. 2000] of positron implantation at a certain energy followed by slowing down to 25 eV. Fig. 2.2 shows the projection of one electron track onto the plane XZ. Coordinate z is the implantation axis. \mathbf{r}_c indicates the position of the positron just after slowing-down. This position is taken as the centre of a sphere of radius 40 nm (see figure). The electron centroid is calculated with the electrons inside this sphere. This centroid is considered to be the centre of a spur (\mathbf{r}_s) containing the electrons generated during the slowing-down of the incoming positron. Once \mathbf{r}_s is known, it is assumed to be the origin of coordinates (0,0,0). Then, the distribution of electrons, positrons and holes around the spur centre is obtained. In order to obtain accurate results, 10,000 tracks were processed per every positron implantation energy under consideration. These distributions were found to possess spherical symmetry. In addition, they are independent of the position \mathbf{r}_c where the implanted positron ends up. Therefore, we can reduce the problem to one coordinate, r , the distance to the spur centre and obtain the distribution of electrons, holes and positrons around the spur centre as a function of the distance to \mathbf{r}_s , ($g_e(r)$, $g_h(r)$ and $g_p(r)$, respectively). Fig. 2.3 is an example showing the electron, hole and positron concentration as a function of the distance to the centre of the spur. The concentrations can be approximated by gaussian functions of the following form

$$g_e(r) = I_e \exp\left(-\frac{1}{2} \frac{r^2}{b_e^2}\right), \quad (2.21)$$

$$g_h(r) = I_h \exp\left(-\frac{1}{2} \frac{r^2}{b_h^2}\right), \quad (2.22)$$

$$g_p(r) = I_p \exp\left(-\frac{1}{2} \frac{r^2}{b_p^2}\right), \quad (2.23)$$

where b_e , b_h and b_p represent the standard deviation of the electron, hole or positron distribution, respectively, and I_e , I_h and I_p are constants. The Monte-Carlo simulations show that the electron, hole and positron distributions are independent of the positron implantation energy for the energies of 6, 10 and 14 keV employed in the simulations.

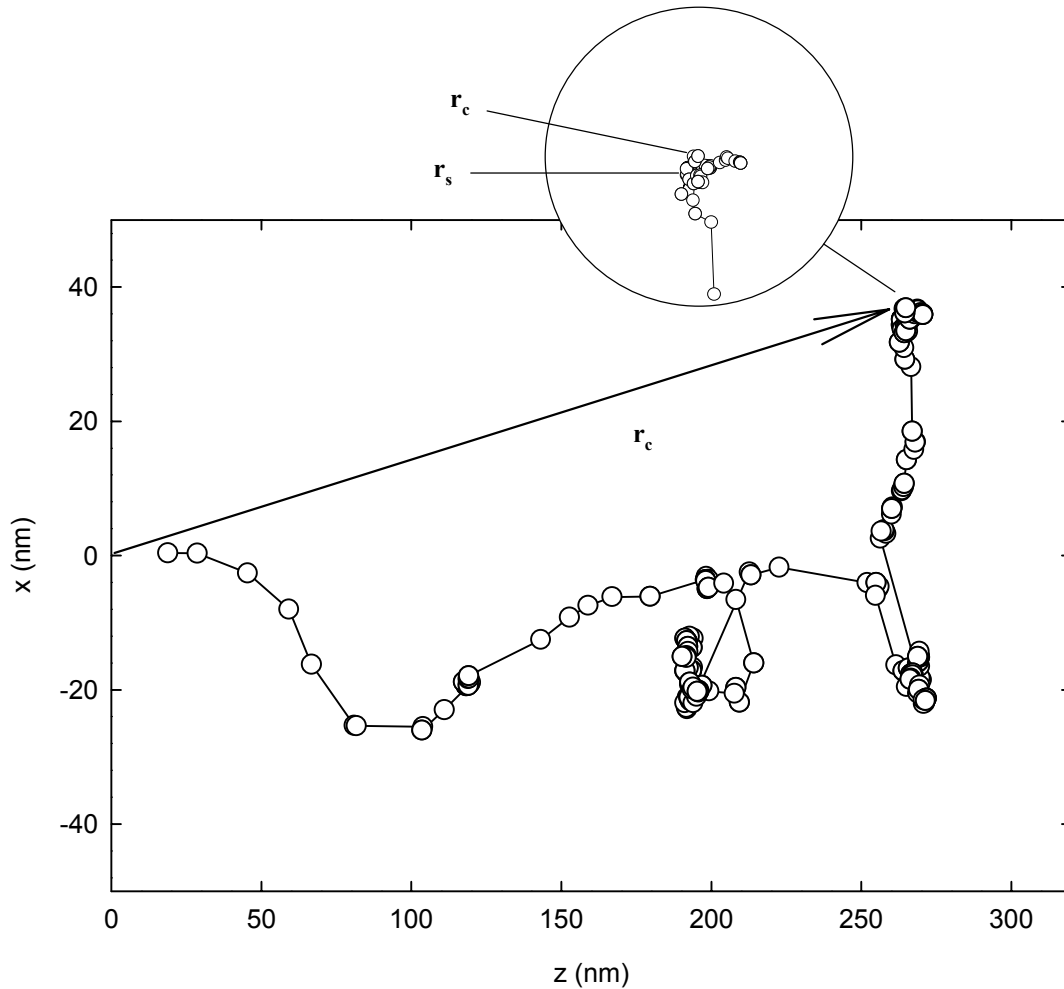


Fig. 2.2. Projection onto the XZ plane of the electron tracks generated by an incoming positron implanted at 6 keV. Coordinate z is the direction of the incoming positron. The vectors r_c and r_s represent the position of the positron just slowed-down and the position of the electron centroid around the positron, respectively. The circle contains a magnification of the final part of the track.

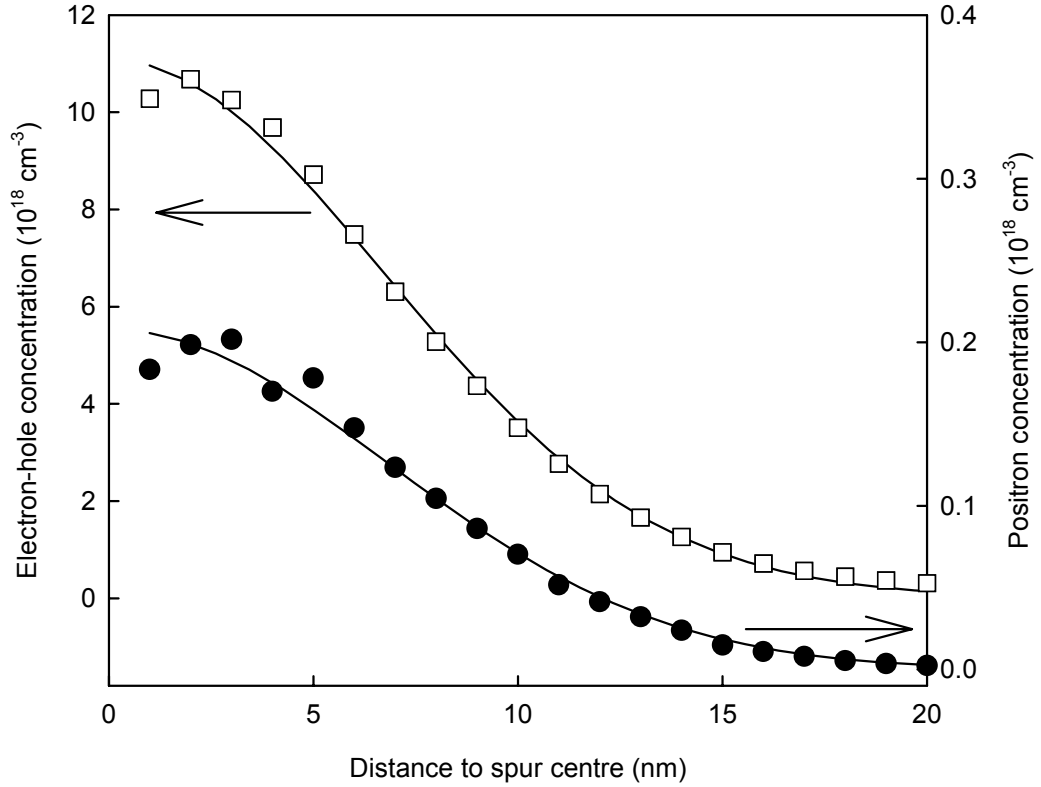


Fig. 2.3. Electron or hole concentration (open symbols) and positron concentration (solid symbols) as a function of the distance to the centre of the spur, which is taken as the origin of coordinates. The concentrations correspond to an incoming positron at 6 keV. The solid lines are gaussian fits.

The thermalisation of positrons and electrons to energies of the order of the thermal energy can be expressed by means of the normal distributions $g_{th,e}(r)$ and $g_{th,p}(r)$, respectively,

$$g_{th,e}(r) = I_{th,e} \exp\left(-\frac{1}{2} \frac{r^2}{l_{th,e}^2}\right), \quad (2.24)$$

$$g_{th,p}(r) = I_{th,p} \exp\left(-\frac{1}{2} \frac{r^2}{l_{th,p}^2}\right), \quad (2.25)$$

where $l_{th,e}$ and $l_{th,p}$ denote the electron and positron thermalisation length, respectively. These quantities represent the average distance travelled by the electron or positron during thermalisation. Then, the resulting thermalised distributions of electrons and positrons ($\chi_e(r)$ and $\chi_p(r)$, respectively) are obtained as

$$\chi_e(r) = g_e(r) \otimes g_{th,e}(r), \quad (2.26)$$

$$\chi_p(r) = g_p(r) \otimes g_{th,p}(r), \quad (2.27)$$

whereas the distribution of holes is expected not to change from (2.22).

The positron distribution $\chi_p(r)$ represents the probability of finding a positron at a certain distance from the spur centroid, while the electron and hole distributions, $\chi_e(r)$ and $g_h(r)$, represent the average concentrations of electrons and holes around an implanted positron. The hole distribution was found to have a standard deviation $b_h = 7$ nm and the concentration at the centre of the spur is $I_h = 1 \times 10^{19} \text{ cm}^{-3}$ (see Chapter 7). The electron concentration is slightly different due to the thermalisation process. These values are in agreement with those obtained indirectly for electron implantations with energies of a few keV [Ausman et al. 1975, Curtis et al. 1974, Srour et al. 1974]. They indicate that ionisation is very effective at the end of the track, in agreement with the value of the stopping power [Berger et al. 1964, Berger et al. 1966, Nelms 1956].

2.3.4. The transport equations

In general there is no need to solve the three-dimensional time-dependent diffusion equation because the system is *per se* time independent. This statement does not apply to the Ps formation process. The reason is that equations (2.15)-(2.17) have electron-hole recombination terms and Ps formation terms which are strongly time dependent. In addition, the one-dimensional approximation is only valid provided the Ps formation process is much slower than the drift process. For the range of electric fields of interest this condition is not fulfilled. However, it is interesting to note that when the Ps formation term tends to zero the problem becomes purely stationary. This occurs at moderate electric fields, when the electron and positron distributions drift in opposite directions, typically beyond a few ps. Therefore, we can solve the problem in two independent steps: (i) the time-dependent, three-dimensional system of diffusion equations (2.15)-(2.17), in order to estimate the Ps fraction; (ii) the one-dimensional stationary diffusion equation for positrons that did not form Ps, in order to estimate the fraction of positrons annihilated in every layer.

In positron beam analysis the problem is usually reduced to the solution of the one-dimensional stationary diffusion equation [van Veen 1990].

$$D_p \frac{\partial^2 n_p}{\partial z^2} - \mu_p E_z \frac{\partial n_p}{\partial z} - (\lambda_b + \kappa_t) n_p + I(z) = 0, \quad (2.28)$$

where n_p represents now the time averaged positron concentration. The other terms have been introduced above apart from $I(z)$ which corresponds to the energy dependent positron implantation rate, usually given by the so-called Makhovian distribution [Nieminen et al. 1980, Valkealahti et al. 1984].

The electron, hole and positron distributions around the spur centre were found not to depend on the positron implantation depth, as discussed above. This indicates that the first part of the problem, the Ps formation, is independent of the implantation depth of each particular positron, while the second part, the bulk annihilation and drift to the interfaces,

mainly depends on the distance between the point of positron implantation and the interface, considered in the Makhovian distribution. In order to fix the boundary conditions, we assume that the boundaries are perfect absorbers.

2.3.5. Observables

The positron fraction remaining in the oxide layer at the instant $t=t_1$ corresponding to one positron implanted with energy E_p , thermalised at z_0 and under an electric field E_z is given by

$$f_p(E_p, E_z, t_1) = A \int_{z=0}^{z=l} n_p(E_p, E_z, z, t_1) dz, \quad (2.29)$$

where A is the surface area of the sample and l the thickness of the oxide layer.

The total positronium fraction formed in the oxide at time $t=t_1$, corresponding to one positron implanted with energy E_p , thermalised at z_0 and under an electric field E_z is given by

$$f_{Ps}(E_p, E_z, t_1) = \int_0^{t_1} A \int_{z=0}^{z=l} \alpha_{Ps} n_e(E_p, E_z, z, t) n_p(E_p, E_z, z, t) dz dt. \quad (2.30)$$

Ps formation ceases above time t_{Ps} , because the concentration of electrons is strongly reduced by recombination with holes and in addition positrons and electrons are separated by the electric field. Once the Ps formation process ceases, we can make use of (2.28) to describe the transport of free positrons to the interface, as explained above. The solution of this equation gives the concentration of positrons in the sample under stationary conditions $n_p(E_p, E_z, z)$. This reduces the calculation time necessary to solve the problem by at least two orders of magnitude.

Assuming a positron implantation rate given by a Makhovian profile $I(z)$ normalised to unity, we can estimate the fraction of positrons trapped or annihilated in the bulk, f_b , as a function of the electric field and the implantation energy. Since a fraction of the positrons was previously considered to annihilate at Ps states, this fraction should be corrected accordingly in the following way

$$f_b(E_p, E_z) = (1 - f_{Ps}) \int_{z=0}^{z=l} (\lambda_b + \kappa_t) n_p(E_p, E_z, z) dz. \quad (2.31)$$

The total fraction of positrons reaching the interface can then be calculated as

$$f_{IF}(E_p, E_z) = 1 - f_{Ps} - f_b. \quad (2.32)$$

We compare these fractions with the experimental $S(E_p, E_z)$ and $W(E_p, E_z)$ annihilation parameters, obtained by Doppler broadening of annihilation radiation measurements (see

Chapter 3), in order to test the validity of the parameters used to solve the system of differential equations. The fractions obtained from the model are related to the experimental annihilation parameters as follows

$$S(E_p, E_z) = F_{IF}(E_p, E_z)S_{IF}(E_p, E_z) + F_{Ps}(E_p, E_z)S_{Ps}(E_p, E_z) + F_b(E_p, E_z)S_b(E_p, E_z) \quad (2.33)$$

$$W(E_p, E_z) = F_{IF}(E_p, E_z)W_{IF}(E_p, E_z) + F_{Ps}(E_p, E_z)W_{Ps}(E_p, E_z) + F_b(E_p, E_z)W_b(E_p, E_z) \quad (2.34)$$

$$F_{IF}(E_p, E_z) + F_{Ps}(E_p, E_z) + F_b(E_p, E_z) = 1, \quad (2.35)$$

where the subscripts *IF*, *b*, and *Ps* indicate to which annihilation process the *S* and *W* parameters are related.

Chapter 3

Experimental

In order to perform hydrogen studies on SOI materials a number of practical aspects must be considered. They are mainly related to the omnipresence of hydrogen, adsorbed virtually at any metal surface in vacuum systems or contributing via chemical reactions with chemicals employed during sample processing. In particular, the high contribution of hydrogen to the background in vacuum systems has detrimental effects on mass sensitive measurements of hydrogen, e.g. thermal desorption (TDS) measurements. In order to overcome this problem we systematically treated the samples in deuterium, either by ion implantation or high temperature annealing, as shown in this chapter. This allows us to separate the contributions coming from the background or from the sample during TDS measurements. However, we found that background hydrogen still plays a role via isotope exchange with deuterium released from the samples generating HD molecules. The necessity of keeping the hydrogen background as low and as controllable as possible led us to build a new TDS system with a load-lock device that allows one to move samples into the annealing crucible without exposing the vacuum system to air. Other technical aspects of the TDS technique will be also discussed in this chapter.

The treatments indicated above introduce a significant number of defects in the samples. Many of these defects can be detected by positron beam techniques. In particular, those associated with open-volume or negative centres are easily recognised due to the high positron affinity to such defects. In addition to the description of TDS, an introduction on positron beam techniques is given in this chapter.

3.1. Sample treatment

3.1.1. Cleaning, metallisation and etching

SOI samples such as those described in Chapter 1, were employed for most of the experiments described in this thesis. A number of standard preparation steps were carried out under clean room conditions at the Delft Institute of Micro-Electronics and Submicron technology (DIMES). Next, the different treatments applied to samples described in this thesis are summarised:

- The Si surface was cleaned in fuming HNO_3 .
- Native oxide on Si was removed in 2% HF prior to positron measurements to avoid the undesired influence of this extra oxide layer on the sample surface. This etching treatment was performed at room temperature for a few minutes, sufficient to get the hydrophobic state characteristic of clean Si surfaces.
- The Si top layer was removed in a 6 molar KOH solution at 70°C in order to implant deuterium ions directly into the bare SiO_2 layer, to anneal in deuterium without a capping top Si layer or to improve the depth resolution of positron measurements.
- Occasionally, thick SiO_2 layers had to be removed. For that, etching in 40% HF was performed.
- Metal gates were deposited by evaporation in vacuum (10^{-4} Pa). In general, the metal layer was deposited on a SiO_2 bare layer in order to create a MOS capacitor. The deposition took place through a mask to delineate the shape of the gate and avoid deposition of metal close to the sample edges, which can lead to leakage currents. For standard capacitance-voltage measurements, the gate area was about 1 mm^2 . However, for hole injection experiments on thick oxides (Chapter 4) and positron studies (Chapters 6, 7 and 8) the gate area was close to 1 cm^2 . Commonly, Al and Au were employed. The gate thickness was about 15 nm to allow positron measurements without a significant loss of positrons in the metal gate and to keep the gate semi-transparent for VUV radiation.
- After certain treatments the metal gates were removed. Al gates were removed in ortho-phosphoric acid and Au in aqua regia.

3.1.2. Ion implantation

Ion implantation is a common process in semiconductor processing. In particular, hydrogen is used in the SmartCut method to fabricate SOI samples, see Chapter 1. In this case, hydrogen atoms are implanted into a Si layer through a thermally grown oxide. We simulated this process by performing D^+ implantation in our samples. In addition, ion implantation is an appropriate way to deposit a known dose of atoms in a certain region of the sample. In turn, these atoms can produce damage by atom displacement.

As indicated above, the use of deuterium was intended to improve the TDS measurements. This permits discrimination between background gas and gas desorbed from the sample, see Section 3.2.1 for a discussion of TDS experiments.

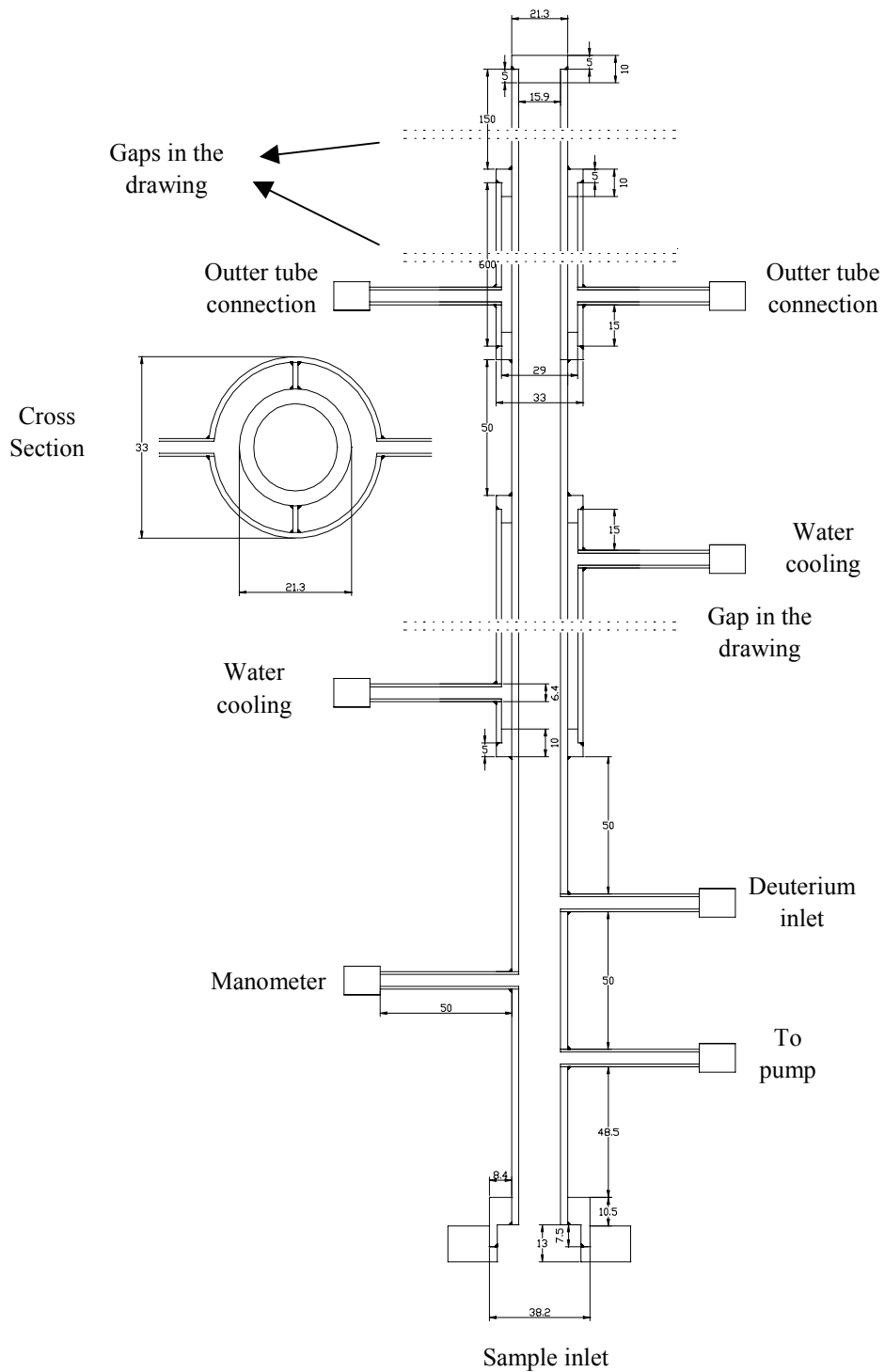


Fig. 3.1. Drawing of the annealing oven employed to perform annealing of samples in deuterium. For safety reasons, a double-wall tube is employed that permits to continuous evacuation of the outer tube during operation.

A number of SOI samples presented in this thesis were implanted with D^+ or He^+ ions with energies from 10 to 30 keV. In some cases implantation took place through the top Si layer and sometimes after removal of the top Si layer, directly into the oxide layer. Two different implanters were used at the Interfaculty Reactor Institute (IRI): a Danfysik 911 with a maximum accelerator voltage of 30 kV and a Varian 350 D with a maximum operation voltage of 140 kV.

In addition, we also employed a low-energy ion gun mounted in our TDS setup which allows in-situ deuterium implantation, see Chapter 2 in [Eleveld 1996]. By means of this system we performed D^+ implantation at an accelerator voltage of 3 kV into bare SiO_2 samples, followed by TDS cycles. In this way we avoid exposing the samples to air after every D^+ implantation step.

3.1.3. Sample annealing

Annealing in the presence of hydrogen is common in semiconductor processing, e.g. forming gas annealing to passivate electrically active interface defects. The interaction of hydrogen with the samples can be studied by annealing the samples in high-purity deuterium gas. The use of deuterium is necessary to perform TDS measurements.

We built an annealing oven to perform these treatments. A schematic drawing is shown in Fig. 3.1. The oven consists of a double-walled steel tube. An external cylindrical heating furnace can be placed around the steel tube in order to heat it up. The sudden removal of the furnace when the tube is hot assures fast cooling down. This process follows an exponential decay law with a time constant of about 10 min. Thus, the cooling rate at temperatures higher than 800 K is larger than 0.5 K/s. At 1000 K, it is as high as 1.5 K/s.

Samples are annealed inside the 15 mm diameter inner tube, but in order to avoid direct contact of the samples with the walls, the samples are introduced in a long quartz sample holder. Deuterium annealing experiments can be performed at pressures varying from 10^{-5} Pa to 1 MPa and temperatures as high as 1300 K. An important issue is related to safety, because deuterium is highly flammable at high temperatures when brought in contact with oxygen. The double-wall tube was designed to prevent the escape of hot deuterium into the atmosphere. The outer tube is connected to an evacuation system with a safety controller that admits a large flow of nitrogen in case of a sudden increase in pressure. In this way, a non-flammable mixture of nitrogen and deuterium can be released into the atmosphere minimising the risk of an accident. In addition, it is important to note that deuterium is able to permeate through steel at temperatures in the operation range. The gas that permeates the inner tube is slowly evacuated, keeping the pressure in the outer tube constant at a value of about 5 kPa, which assures a good thermal conductivity.

3.2. Desorption spectrometry

3.2.1. Thermal desorption spectrometry

Thermal helium desorption spectrometry, see e.g. [Fedorov 2000] has classically been employed to investigate the presence of open volume in materials. Helium, implanted at low energy into the material under investigation, is used as a probe particle. Helium implantation at low energy avoids the creation of damage in the sample. On the other hand, it leads to helium decoration of existing defects. The low solubility of helium in most materials permits one to obtain a high sensitivity for open volume. In particular, the use of helium is of interest because simulation experiments can easily be performed on the nucleation of helium-vacancy clusters originated from (n,α) reactions in reactor structural materials subjected to neutron irradiation.

Thermal helium desorption spectrometry is performed under ultra high vacuum (UHV) conditions. The low-energy helium-implanted sample is annealed with a constant heating rate, usually in the range from 1 to 10 K/s. Simultaneously, the partial pressure (P) of helium in the vacuum system is measured by means of an appropriate mass analyser. From the variation of the partial pressure (dP/dt), the actual flow of molecules thermally desorbed from the sample can be obtained, as discussed below.

The desorption rate obtained in this way can usually be modelled by means of first-order kinetics, since helium in general fulfils the following requirements: (a) the diffusion rate of helium inside the sample is fast compared with the dissociation rate from defects; (b) helium desorption is not hindered by the surface; (c) the release of helium from traps occurs with the production of one single helium atom per dissociation reaction; (d) helium is not re-trapped during the process.

The interpretation of the desorption spectra by means of this model provides useful information on the different types of traps. For each type of trap, the helium activation energy for de-trapping and the total number of helium atoms trapped can be obtained.

In this work, hydrogen studies were performed on SOI samples. The main objective was to characterise hydrogen-related defects in buried oxides (BOX) belonging to samples treated as described in Section 3.1. The physical parameters that can be derived from TDS are the number of defects and the activation energy of every type of defect. These parameters are very valuable for the study of hydrogen interactions with BOX.

Specific aspects of hydrogen studies with the aid TDS

The use of thermal desorption spectrometry (TDS) techniques for hydrogen release is very attractive for the study of defects as well as for the study of hydrogen bonding configurations in a particular sample. However, its application is not as straightforward as in the case of helium. Previous studies have been reported on hydrogen desorption from metals [Eleveld et al. 1992, Eleveld et al. 1994]. However, certain technical aspects of the technique, not extensively considered in previous work, will be described here. These aspects are mainly related to the role of background hydrogen, the interaction of hydrogen with deuterium and the proper way of calibrating the desorption signal. An extra difficulty arises when annealing

non-metallic samples because the determination of the sample temperature is not as simple as in the case of metals. The application of TDS to hydrogen desorption from SiO_2 , as described in this work, can be extrapolated to other materials, making the technique potentially attractive for defect characterisation in many materials.

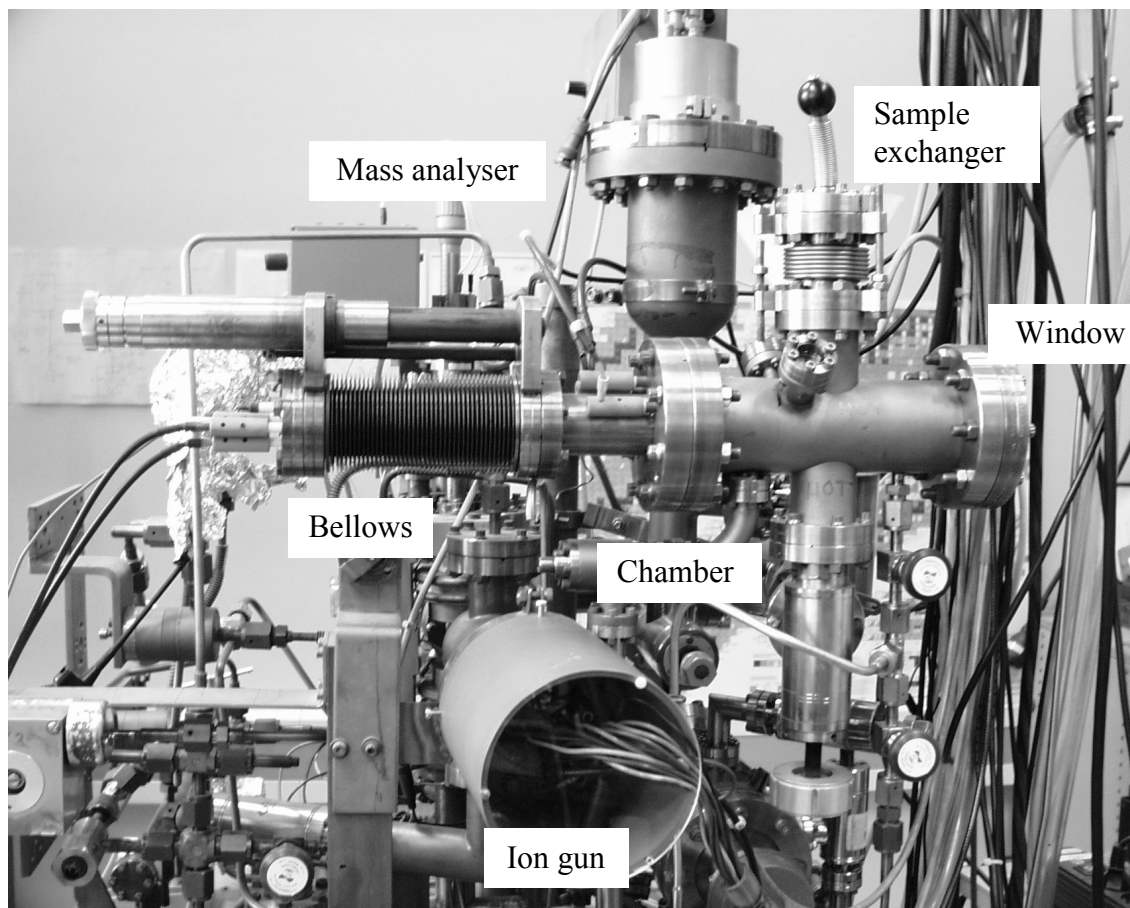


Fig. 3.2. Thermal desorption apparatus. The most important elements of the system are shown: the annealing chamber, the bellows that holds the crucible, the sample exchanger, the window and the mass analyser.

In contrast to thermal helium desorption spectrometry, the study of hydrogen presents a number of difficulties that should be overcome:

1. The presence of hydrogen is unavoidable in vacuum systems even under UHV conditions. Hydrogen is adsorbed at internal surfaces constituting an important contribution to the residual pressure of any vacuum system. The supply of power (by any means) in order to anneal samples in vacuum leads to hydrogen release from adsorption sites giving very large background contributions. In addition, hydrogen permeation easily takes place through hot steel from air. This problem is partially overcome by treating the samples with deuterium, see Section 3.1. This permits one to discriminate in TDS measurements

between the background contribution, mainly due to hydrogen (H), and the sample contribution, mainly due to deuterium (D).

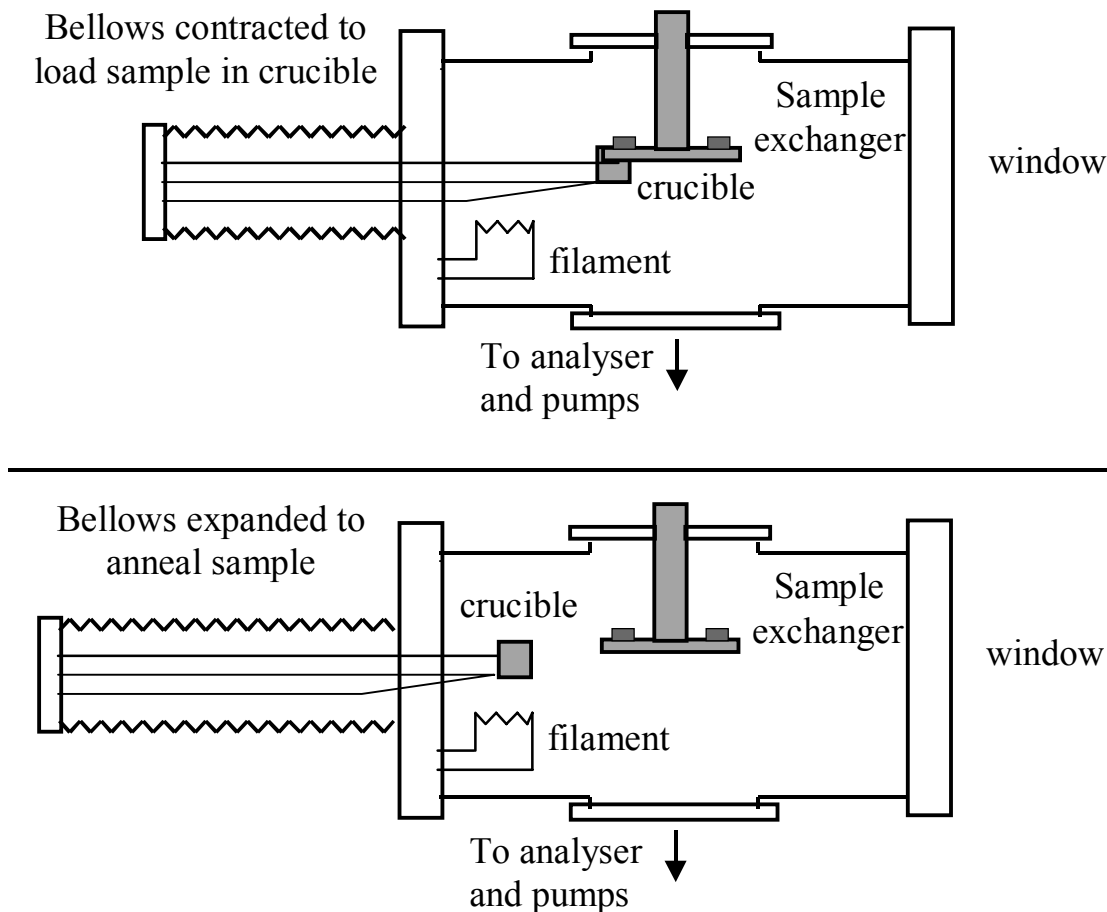


Fig. 3.3. Schematic representation of the TDS setup. The figure shows a detail of the sample exchanger disk on which samples are placed and the crucible, which can be moved by means of the bellows to which it is fixed. The top panel shows the crucible in the loading position to mount samples from the disk. The bottom panel shows the crucible in the annealing position to perform TDS measurements.

2. Despite the use of deuterium the control of the background pressure is an important issue, because the omnipresence of hydrogen in vacuum makes possible the formation of HD molecules. These molecules enter in competition with the D_2 molecules of interest. In particular, the formation of HD is important at the sample surface, in hot regions of the vacuum system (such as filaments) and under high residual pressure (mainly due to H_2 and water).
3. The formation of HD molecules, in turn, affects the quantification of the deuterium desorption rate from the sample. In addition, the adsorption of the released species at internal surfaces of the vacuum system also plays an important role in the quantification of the exact amount of released gas.

4. The modelling of the desorption kinetics is also different from that used when helium desorption measurements are performed (see Section 2.2).

Experimental setup: sample exchanger

In general, the annealing of samples during TDS experiments is performed in closed crucibles, which are loaded in air and then placed in the vacuum chamber. During the exposure of the crucible to air, a considerable amount of gas is adsorbed at the surface and later released during the TDS experiments, contributing undesirably to the background pressure. Previously, it was pointed out that background hydrogen plays a disturbing role during TDS measurements because it can react with deuterium forming HD molecules, therefore affecting the proper signal quantification. We found it of the utmost importance to keep the hydrogen background level as low as possible.

We designed a new system based on a sample exchanger that allows the mounting of samples into and the unloading from the annealing crucible without exposing the system to air. A picture of the TDS system is shown in Fig. 3.2. The most relevant elements are indicated: (i) the chamber in which samples are annealed, (ii) the sample exchanger from where samples are loaded into the annealing crucible, (iii) the bellows attached to the crucible and employed to move the crucible from the annealing position to the loading position, (iv) a window used to control the mounting and annealing operations and (v) the quadrupole mass analyser employed to measure the partial pressure of the different gases of interest during the thermal desorption experiments. In Fig. 3.3 a schematic representation of the system is given. The different elements in the TDS chamber are indicated. The figure contains two panels. The top one shows the crucible close to the sample exchanger in the loading position. The bottom panel shows the crucible close to the filament in the annealing position, ready to perform TDS experiments.

The sample exchanger consists of an aluminium disk, on which up to four samples can be stored, see Fig. 3.4. Thanks to a rotatory tool, the samples can be pushed from the disk to the crucible and back from the crucible to the disk. This configuration allows annealing of the molybdenum crucible at a high temperature before mounting any sample. This strongly reduces the undesired gas that is desorbed from the crucible surface during TDS measurements, enhancing the signal to background ratio. In order to measure the temperature, a platinum thermocouple is welded to the crucible. In addition, a rotary lid covers the sample during the TDS measurements to avoid losses by radiation, thereby making the sample temperature more uniform and helping to reduce the background pressure.

Fig. 3.5 shows the HD and D₂ signals obtained when heating the crucible at 6 K/s. The crucible was empty during the experiment and was annealed at a temperature higher than 1600 K prior to this experiment. The signals shown in the figure can be considered background signals. Thanks to the sample exchanger, the background signal is minimised. In the case of D₂, no background contribution is observed. In addition, the background contribution becomes very reproducible as a consequence of the pre-annealing of the crucible. The existence of a reduced background results in a minimal interaction between hydrogen and deuterium released from the sample. The fact that the background signal is predictable is very desirable for a proper correction of the TDS spectra.

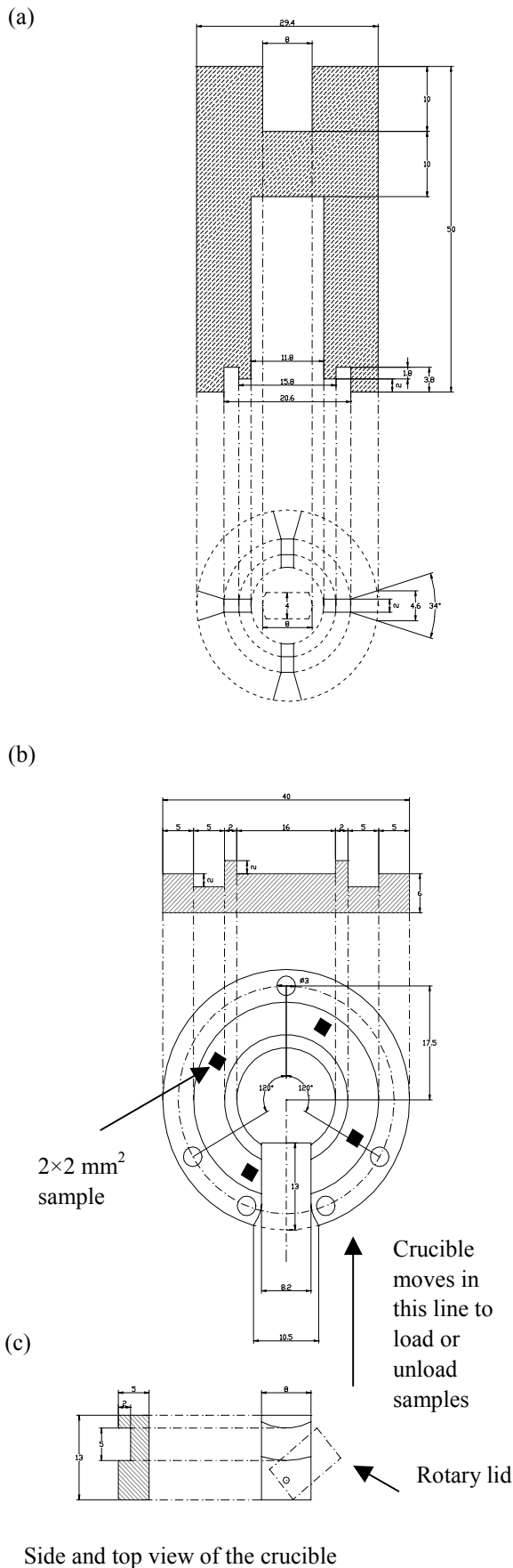


Fig. 3.4. Drawing of the sample exchanger. (a) Cross-section and top view of the rotary device employed to move samples on the disk. This allows loading (unloading) them into (from) the crucible. (b) Cross-section and top view of the disk employed to store the samples. The squares represent samples at full scale. They are placed in a channel existing in the disk. By means of the device shown in (a) they are moved around on the disk. (c) Side and top view of the Mo crucible employed to anneal the samples in vacuum. The crucible is moved from the filament position to the disk with the aid of a bellows. It has a channel that fits in the disk channel and a rotary lid to improve the annealing conditions. The rotary lid is opened by the same device employed to move the samples and is closed when the crucible is moved back to the filament position by the action of the bellows.

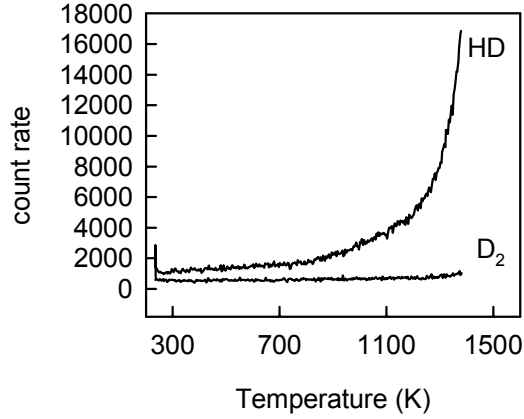


Fig. 3.5. HD and D₂ background signals collected by TDS measurements with an empty crucible.

Gas detection

During TDS measurements, the partial pressure of selected gases is recorded. At time t the partial pressure, $P_m(t)$, of a certain gas (e.g. D₂) is proportional to the number of molecules of that gas, $N_m(t)$, in the system, where m represents the molecular mass of the gas, i.e. 2 for H₂, 3 for HD and 4 for D₂. Using as an approximation the ideal gas law, we can write

$$N_m(t) = \frac{VP_m(t)}{k_B T_C}, \quad (3.1)$$

where k_B is Boltzmann's constant, V the volume of the desorption chamber and T_C the temperature of the chamber. Usually, TDS measurements are performed by increasing the temperature, T , of the sample linearly with time. Taking β as the heating rate and T_0 as the initial temperature, one can write

$$T = T_0 + \beta t. \quad (3.2)$$

The D₂ release rate, $L_4(t)$, from a sample can be expressed as

$$L_4(t) = \frac{dN_4(t)}{dt} + \frac{N_4(t)}{\tau_R} + \kappa_E \frac{N_2(t)}{V} \frac{N_4(t)}{V} + \kappa_T \frac{N_4(t)}{V}. \quad (3.3)$$

The first term represents the variation of the number of D₂ molecules in the system. The second term accounts for the finite time necessary to transport D₂ molecules through the vacuum system. τ_R represents the averaged residence time of D₂ in the desorption chamber and is related to the effective pumping speed S by $\tau_R = V/S$. The third term accounts for the isotope exchange taking place as a result of the reaction



The rate constant of isotope exchange Reaction (3.4) is the constant κ_E , used in (3.3). Finally, the fourth term in (3.3) accounts for the D_2 trapping at internal surfaces in the desorption system. The coefficient κ_T is the trapping rate constant.

One can define an effective residence time, τ_{eff} , in the following way

$$\frac{1}{\tau_{eff}} = \frac{1}{\tau_R} + \frac{\kappa_E N_2(t)}{V^2} + \frac{\kappa_T}{V}. \quad (3.5)$$

Combining (3.5) and (3.3), we can write for the D_2 release rate

$$L_4(t) = \frac{dN_4(t)}{dt} + \frac{N_4(t)}{\tau_{eff}}. \quad (3.6)$$

The constant τ_{eff} depends on the temperature because the rate coefficients λ_T and κ_E strongly depend on the temperature of the surface at which D_2 trapping occurs or over which the isotope exchange, via Reaction (3.4), takes place. Note that most of the surface in the desorption system remains at a constant temperature during the annealing of the sample. Only in the crucible and in the region close to the filament the temperature changes significantly. In addition, the H_2 pressure in the system, or equivalently N_2 , changes significantly during the annealing, affecting τ_{eff} . All these effects will cause τ_{eff} to decrease at high temperature.

Signal calibration

The D_2 signal, $C_4(t)$, measured by the mass spectrometer at time t , in counts per second, should be transformed into a physical quantity by a calibration procedure. The signal $C_4(t)$ is proportional to the number of D_2 molecules in the desorption system. Therefore, we can write

$$N_4(t) = KC_4(t), \quad (3.7)$$

where K is a proportionality constant. For calibration purposes, we admit a pulse of D_2 containing a known amount of gas, N_{cal} , into the system. Usually, this is done by expanding the content of a small calibration volume, typically 1 cm^3 containing about 10^{12} molecules, into the system. The number of HD and D_2 molecules in the desorption system, $N_3(t)$ and $N_4(t)$, respectively can be recorded, as a function of time. Fig. 3.6 shows the D_2 and HD signals obtained from typical calibration experiments. In this case the admitted pulse of D_2 contained 1.6×10^{12} molecules. Assuming that the D_2 pulse is a delta function centred at time t_0 , the response function $N(t)$ can be estimated by solving (3.6). This assumption is always valid for a sufficiently large t , when the flow of gas from the calibration volume is actually zero. The solution of this equation gives

$$N_4(t) = N_0 \exp\left(-\frac{t-t_0}{\tau_{eff}}\right) \text{ for } t > t_0, \quad (3.8)$$

where N_0 is a constant. Combining (3.7) and (3.8), we obtain

$$C_4(t) = \frac{N_0}{K} \exp\left(-\frac{t-t_0}{\tau_{eff}}\right) \text{ for } t > t_0. \quad (3.9)$$

We can determine τ_{eff} by fitting the signal obtained from calibration experiments to an exponential function as shown in (3.8). In the example shown in Fig. 3.6, a value of 2.5 s is formed from τ_{eff} . Once τ_{eff} is known, the actual flow can be estimated for all t . Combining (3.6) and (3.7),

$$L_4(t) = K \left(\frac{dC_4(t)}{dt} + \frac{C_4(t)}{\tau_{eff}} \right). \quad (3.10)$$

The derivative within the brackets can be calculated numerically providing the flow of D_2 as a function of time. The integration of the flow over time must give the total number of molecules, N_{cal} , admitted into the system for calibration. In this way, we can determine the proportionality constant, K ,

$$K = \frac{N_{cal}}{\int_0^{\infty} dt L_4(t)} = \frac{N_{cal}}{\int_0^{\infty} dt \left(\frac{dC_4(t)}{dt} + \frac{C_4(t)}{\tau_{eff}} \right)}. \quad (3.11)$$

The proportionality constant K for the calibration example shown in Fig. 3.6 equals 7×10^6 D_2 s counts⁻¹. This value has an error of about 30%, due mainly to the inaccuracy in the determination of the number of D_2 molecules in the calibration volume. The number of molecules in the calibration volume is difficult to measure accurately because this measurement requires a few expansions of D_2 into different volumes. In addition, the D_2 gas stored at a known pressure in a large vessel for calibration purposes interacts with background H_2 giving HD. It may also be lost by internal leaks as shown in Fig. 3.7. Therefore, it is important to perform calibration experiments soon after filling the calibration vessel and to discard measurements performed long after refilling the calibration vessel.

The HD signal shown in Fig. 3.6, was recorded during D_2 calibration experiments. It is interesting to note that the HD signal decays slower. In principle, this is against expectations because HD being lighter than D_2 it would be expected that the HD decay would be faster. However, the isotope exchange mechanism proposed above is in agreement with this expectation. It is likely that a certain amount of HD is released from the calibration vessel when the D_2 calibration experiment is performed. In addition, a significant amount of D_2 is

converted into HD by isotopic exchange, broadening the HD decay signal. An exact quantification of the number of HD molecules in the system and the determination of its origin is very complicated and not necessary for the purpose of this work.

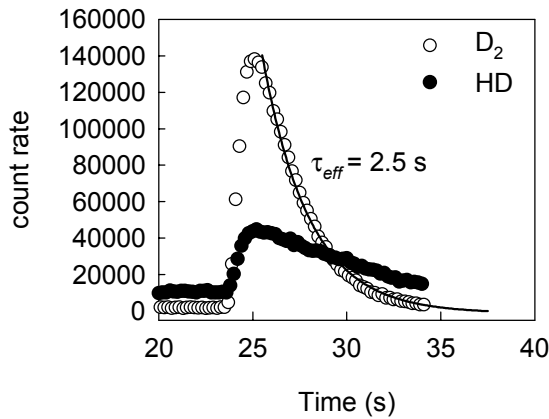


Fig. 3.6. HD and D₂ signals recorded as a function of time when a pulse of gas containing 1.6×10^{12} D₂ molecules is admitted into the system.

In conclusion, once the parameters τ_{eff} and K are established by calibration, the D₂ release rate coming from a sample during a ramp annealing can be calculated by means of (3.10).

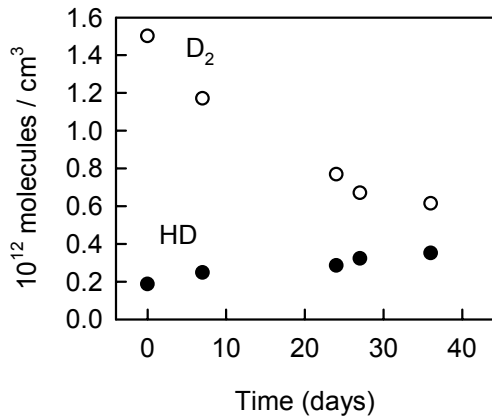


Fig. 3.7. Changes observed in the concentration of D₂ and HD stored in the calibration vessel as a function of the number of days that the gas remained in the vessel.

Dynamic approximation

It is common practice under dynamic conditions, i.e. a sufficiently small τ_{eff} , to simplify equation (3.6) in the following way

$$L_4(t) \approx \frac{N_4(t)}{\tau_{eff}}. \tag{3.12}$$

This simplification often gives reliable results in the case of hydrogen isotopes because the residence time for hydrogen is very short. In addition, the trapping and isotopic exchange

taking place with hydrogen isotopes leads to an even more reduced effective residence time. Finally, as discussed above, the effective residence time is reduced even further at high temperatures.

Using (3.12) and (3.7) we can write

$$N_{cal} = \int_0^{\infty} dt L_4(t) = \int_0^{\infty} dt \frac{N_4(t)}{\tau_{eff}} = \int_0^{\infty} dt K \frac{C_4(t)}{\tau_{eff}} = Q \int_0^{\infty} dt C_4(t), \quad (3.13)$$

where Q is the calibration factor defined as

$$Q = \frac{K}{\tau_{eff}} = \frac{N_{cal}}{\int_0^{\infty} dt C_4(t)}. \quad (3.14)$$

The calibration factor Q estimated from Fig. 3.6 turns out to be 3×10^6 D₂ counts⁻¹ within 30%. Introducing into (3.14) the parameters K and τ_{eff} calculated above, we obtain for Q the same value within the experimental error. Once Q is known, the D₂ release rate from a sample during ramp annealing can be calculated from (3.7), (3.12) and (3.14) according to

$$L_4(t) = QC_4(t). \quad (3.15)$$

Signal calibration by D₂ flow

The estimation of Q by calibration with pulses introduces errors of around 30% as discussed above. An alternative method is to admit a variable flow of D₂ to the system. In this situation, a stationary regime is reached. The flow of D₂ passing through the desorption system can be estimated by

$$q = uSP, \quad (3.16)$$

where S is the pumping speed, P the total pressure in the system and u a constant that accounts for the proper units. Fig. 3.8 shows a calibration experiment by flows performed right after the standard calibration by means of pulses shown in Fig. 3.6, assuming a pumping speed of $S=200$ l/s. The error bars come from the uncertainty in the pumping speed. As expected, the flow of D₂ through the sample is proportional to the signal recorded by the mass analyser. The points obtained can be fitted by linear regression. In this way Q is obtained, resulting in a value of $(2.0 \pm 0.1) \times 10^6$ D₂ counts⁻¹. This value is in agreement with the values calculated above and its accuracy is much better than in the case of pulse calibration.

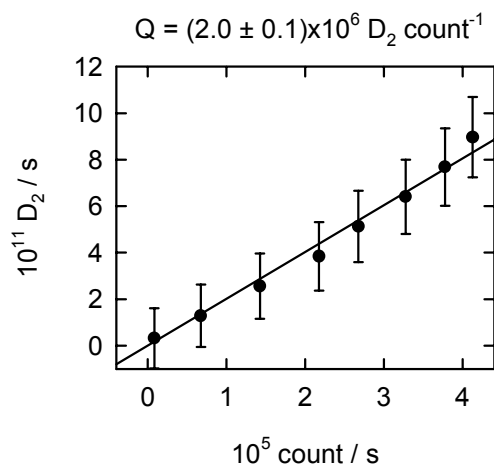


Fig. 3.8. Estimation of the calibration parameter Q by admitting a constant D_2 flows into the desorption system.

Effect of temperature on the desorption signal

Fig. 3.9 shows an example of Q measured by admitting pulses of 1.5×10^{12} D_2 molecules at different temperatures while increasing the temperature of the crucible linearly with time. Q decreases with increasing temperature indicating that the total number of detected molecules decreases with increasing temperature. Therefore, a non-constant calibration factor Q should be used to quantify the number of desorbed D_2 molecules, unlike in the case of He calibration.

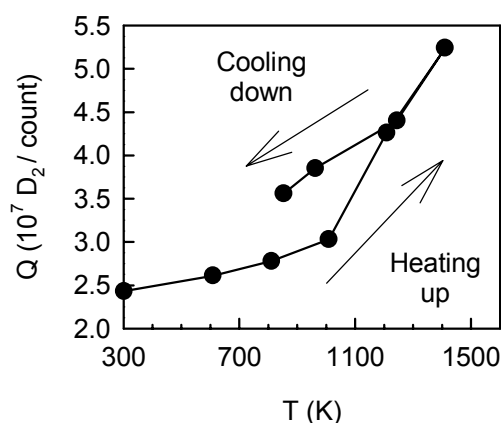


Fig. 3.9. Calibration factor Q measured by admitting a pulse of 1.5×10^{12} D_2 molecules at the indicated temperature while increasing the temperature of the crucible linearly with time. Pulses were admitted both during heating at 4 K/s and during cooling as can be observed in the plot.

The calibration factor strongly depends on the total pressure in the system. The fact that in Fig. 3.9 the trajectory corresponding to Q obtained during heating does not correspond to that obtained during cooling agrees with the pressure dependency. This is in line with the proposed mechanism of isotopic exchange, which increases with increasing pressure. In addition, we observed (not shown) that the effective residence time decreases with increasing temperature, as expected, which is also in agreement with the isotope exchange mechanism.

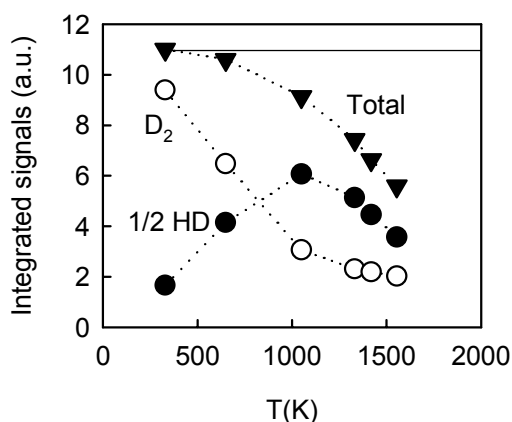


Fig. 3.10. Total number of molecules collected during calibration by pulses at different temperatures while the temperature of the crucible increases linearly with time. The scale is in arbitrary units. The open circles correspond to the total number of D₂ molecules, the solid circles to the total number of HD molecules divided by 2. The triangles represent the sum of the other two symbols. The dashed lines are guides to the eye. The solid line represents the total number of molecules introduced in the system by the calibration pulse.

Results of other calibration experiments by means of D₂ pulses, performed while heating the crucible, are shown in Fig. 3.10. The HD and D₂ signals were recorded simultaneously in this case. The total number of counts obtained by integration of the HD or D₂ signals (solid and open circles, respectively) represents the total number of molecules of every species detected in every calibration cycle. Since one D₂ molecule contributes as much as two HD molecules, the detected HD contribution is divided by 2 (solid circles). In this way, both contributions may be compared. In addition, the triangles represent the total number of molecules detected during every calibration cycle. It is interesting to note that the total number of detected molecules decreases as a function of temperature. This clearly indicates that trapping occurs. Otherwise, this value would remain constant and equal to N_{cal} , the number of molecules introduced by every calibration pulse, indicated by the solid line. The D₂ contribution decreases with increasing annealing temperature. On the other hand, the HD contribution increases until the temperature reaches around 1000 K and then drops fast. Below 1000 K, it is evident that an important isotope exchange takes place, while above 1000 K, trapping effects become very important as inferred from the simultaneous drop of both contributions.

The same effect is expected to occur when measuring the D₂ release rate from a sample. Therefore, the most appropriate way of quantifying the total number of released molecules is to use a temperature dependent Q factor, which increases with temperature, as shown above.

Note that in real TDS experiments a significant fraction of the released molecules are HD molecules, which are formed inside or at the surface of the sample. Therefore, this effect should also be considered by adding up the contribution of HD divided by a factor 2.

Temperature calibration

An important issue is to determine the difference between the crucible temperature and the real sample temperature. This difference can be considerable in non-metallic samples due to their poor thermal conductivity. We found an extreme case when performing thermal desorption measurements on Si-based samples in a Pt crucible. The Pt crucible is adequate in view of the low background caused by it. However, Si and Pt strongly interact at high

temperature forming undesired chemical compounds. To prevent direct contact between Si and Pt, alumina supports were placed in the Pt crucible. In this case, the sample temperature suffered delays with respect of the crucible temperature as large as 200 K.

In order to estimate the temperature delay between the Mo crucible, used in the chamber of the sample exchanger, and the sample, we employed low energy-Ar-sputtered Si samples. These samples show a strong Ar desorption peak at around 1000 K. The exact value depends on the heating rate. This desorption peak was attributed to Si recrystallisation and modelled accordingly. Fig. 3.11 shows the crucible temperature when the Ar desorption spectrum reached its maximum. For comparison the expected peak positions as a function of the heating rate (solid circles) are also shown in the figure. The error bars represent the variance of our measurements. The figure allows one to estimate the sample temperature. It is evident that at low heating rate the sample temperature is very close to that of the crucible while at 6 K/s a serious discrepancy begins to occur. This indicates that with large heating rates the sample can not follow the crucible temperature. In order to get the most accurate temperature signal, the heating rate should be kept as low as possible. However, it is important to realise that at too low heating rates the desorption signal is too low. In the case of a low signal new inaccuracies arise due to the strong influence of the background. In this thesis, TDS measurements were generally performed at heating rates lower than 6 K/s and higher than 0.5 K/s.

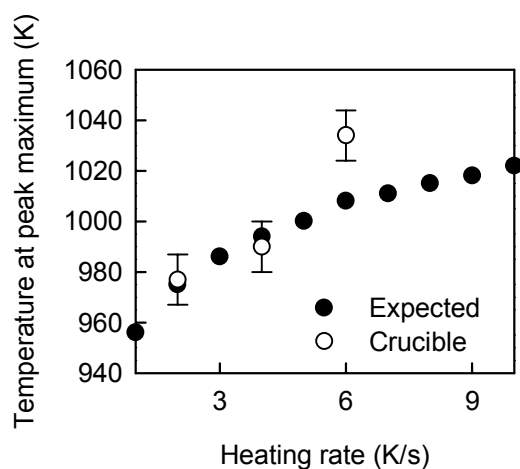


Fig. 3.11. Thermal desorption experiments of low energy Ar-sputtered Si. The open circles represent the crucible temperature at which the Ar desorption peak showed a maximum. They are plotted as a function of the annealing rate. For comparison, the expected temperature corresponding to the Ar desorption maxima is included by solid circles.

3.2.2. Radiation-induced desorption spectrometry

In order to study the release of hydrogen (isotopes) as a consequence of hole and electron injection into SiO₂, a VUV Kr source was coupled to the TDS apparatus. MOS capacitors were fabricated as described in Section 3.1. The thin metal layers evaporated onto the oxides are semi-transparent for the 10 eV VUV photons originating from the Kr source. This assures that a significant fraction of electron-hole pairs is generated by the VUV photons in the first 10 nm of the oxide. By selecting the appropriate voltage on the gate either electrons or holes can be drifted through the oxide. In this way, the application of a positive bias to the gate while illuminating the sample with VUV light causes injection of holes into the oxide.

Similarly, the application of a negative bias to the gate induces electron injection into the oxide. The injection experiments were performed in a vacuum better than 10^{-5} Pa.

As described in Chapter 4, the interaction of holes with Si-H groups in the sample leads to the release of hydrogen, see also Chapter 2. Once again, hydrogen from the background plays an important role in the determination of the desorption spectra. The VUV illumination of internal surfaces in the desorption apparatus leads to the immediate generation of hydrogen. In order to minimise the effect of hydrogen from the background, the MOS capacitors were subjected to post-metallisation annealing in deuterium. When this treatment leads to the incorporation of a large amount of deuterium into the sample by isotope exchange, the HD and D₂ signals can be employed to monitor the effect of hole or electron injection in the release. This will be successfully demonstrated in Chapter 4.

3.3. Positron beam analysis

The main advantage of using monoenergetic positron beams to carry out positron studies is that depth selective information on the sample under study can be acquired. This permits one to obtain defect depth profiles of the subsurface region with good resolution up to depths of a few microns. The physical phenomena taking place in positron beam experiments are summarised briefly below.

Positrons are implanted into the sample with typical energies from 0 to 100 keV, depending on the experimental setup. Once the positrons have entered the sample, they lose their energy by different scattering processes. By means of this slowing-down process, positrons reach thermal energies in less than 10 ps. Next, the thermalised positrons diffuse through the material. Due to the high electronic density of matter, in a relatively short time (from about 100 ps to a few ns) the positron meets an electron and annihilates producing, in most cases, 2 γ -rays. If the annihilation occurs when the e^+e^- pair is at rest, the γ -rays are emitted collinearly but in opposite directions with an energy of $511 \text{ keV} = m_0c^2$ each, where m_0 is the electron rest mass and c the speed of light. If the momentum of the positron-electron pair is $\mathbf{p} \neq 0$, relative to the laboratory frame, the energy of the γ -rays deviates from 511 keV, due to the Doppler effect. The energy deviation appears as a broadening of the 511 keV peak, which is detected by Doppler broadening of annihilation radiation (DBAR) measurements. The energy shift is given by

$$\Delta E = \frac{cp_l}{2}, \quad (3.17)$$

where p_l is the longitudinal component of \mathbf{p} , as illustrated in Fig. 3.12.

Since positrons participating in the annihilation process are usually thermalised or quasi-thermalised, the annihilation gives information about the momentum of the electron involved. Positron annihilation can take place (i) with an electron from the bulk of the material or (ii) after trapping in a defect with an electron from the trap region. The latter occurs due to the large positron affinity to some defects, in particular open volume or

vacancy-like defects where the positive nuclei are absent. (iii) Finally, positron annihilation can occur after the formation of a hydrogen-like bound state between one positron and one electron. This state is called positronium (Ps).

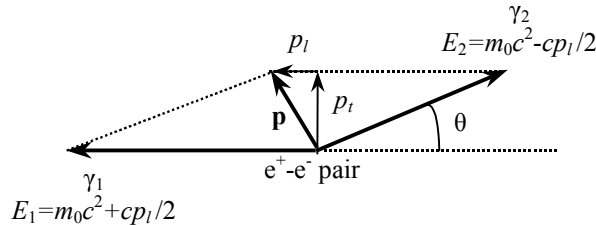


Fig. 3.12. Schematic representation of the momentum conservation in the two-photon annihilation process. The momentum of the positron-electron pair is denoted by \mathbf{p} , p_l and p_t being its longitudinal and transversal components, respectively. The deviation from exact collinearity is denoted by the angle θ .

Ps occurs in two ground states. In the singlet state, called para-positronium (p-Ps), the electron and positron spins are anti-parallel. It mainly decays by emission of two 511-keV photons, due to its near zero intrinsic momentum and has a lifetime of 125 ps. In the triplet state, called ortho-positronium (o-Ps), the electron and positron spins are parallel. It decays in three photons with energies from 0 to 511 keV and has a lifetime of 142 ns. Usually in solids, the o-Ps lifetime is reduced to at most a few ns as a result of the so-called *pick-off* process. In this process a positron in an o-Ps state annihilates with an electron from the material that has anti-parallel spin. This is possible due to the large electron concentration in solids. The pick-off process leads to the emission of two γ -photons, as in the two-photon annihilation process described above. In the absence of external fields, the formation of o-Ps is three times more probable than the formation of p-Ps, due to spin statistics.

The distance between a positron and an electron in a Ps state is twice the classical radius of hydrogen. Due to the quantum mechanical character of Ps, its formation is only possible when enough space is present in the material to accommodate it. For example in Si, Ps is only formed when voids larger than 0.35 nm in radius exist (see Chapter 7 in [Hakvoort 1993]). In addition, the principle of energy conservation demands that the formation of Ps is only possible with non-firmly bound electrons, as explained next. This is particularly important in semiconductors and insulators, which have a low electron concentration in the conduction band.

The formation of Ps in vacuum leads to an energy gain of 6.8 eV, i.e. the Ps binding energy, E_B . Notice, though, that the Ps binding energy in the bulk of a material is usually smaller than 6.8 eV. In addition, when Ps is formed in a solid, the energy spent to take a positron and an electron out of their bands should be considered. In this way, the energy gain G in the formation of Ps with electrons from the conduction band in a semiconductor or insulator, e.g. Si or SiO₂, is given by [Nagashima et al. 1998]

$$G = E_B - \phi_+ - \chi, \quad (3.18)$$

where E_B equals 6.8 eV if Ps is formed at the surface or a smaller value otherwise; ϕ_+ is the positron work function and χ is the electron affinity, i.e. the energy necessary to bring an electron from the bottom of the conduction band to the vacuum level.

Similarly, the energy gain when Ps is formed with an electron of the valence band is given by

$$G = E_B - \phi_+ - \chi - E_G , \quad (3.19)$$

where E_G is the band gap of the semiconductor or insulator material. From (3.19), we can determine the maximum value of E_G at which Ps formation with electrons from the valence band is energetically favourable:

$$E_G < E_B - \phi_+ - \chi . \quad (3.20)$$

Since $E_G = 8-9$ eV for SiO_2 , it is evident from (3.20), that Ps will not be formed with electrons from the valence band but only with electrons from the conduction band. This process is strongly limited by the low concentration of electrons in the conduction band. However, during the slowing down of implanted positrons, a sufficient number of electrons are promoted to the conduction band contributing to the Ps formation. This is the basis of the spur model [Mogensen 1974], which will be employed in Chapter 7 to explain Ps-limited positron transport in SiO_2 under electrical bias.

It should be mentioned that Ps plays a main role in positron studies of SiO_2 , as shown in this thesis. The fraction of annihilations coming from Ps states can be as large as 90% [Uedono et al. 1994]. In addition, this fraction varies depending on sample structure (Chapter 6) or by the application of external electric fields (Chapter 7). This makes the interpretation of positron results totally dependent on the Ps behaviour.

3.3.1. Doppler broadening of annihilation radiation

Doppler broadening of annihilation radiation (DBAR) measurements [van Veen et al. 2000] were performed using the variable energy positron beam (VEP) [van Veen 1990] of the Positron Centre at the Delft University of Technology. The diameter of the beam is about 8 mm and the intensity at the target of the order of $10^5 \text{ e}^+ \text{ s}^{-1}$. The photon detection in the VEP apparatus is performed with the aid of an intrinsic germanium detector with 1.2 keV resolution at 511 keV photon energy.

The Doppler broadening of the annihilation spectra is generally characterised by the S (shape) parameter, defined as the ratio between the intensity of the central part of the annihilation peak in the energy spectrum and the total peak (Fig. 3.13). This parameter reflects the positron annihilation with valence electrons (low momentum). In general, a high value of S , relative to that of bulk annihilation, indicates positron annihilation in open volume defects. Very high S values are related to the self-annihilation of para-positronium (p-Ps), due to its near zero intrinsic momentum. On the other hand, o-Ps annihilation via pick-off gives a similar contribution to DBAR measurements as that obtained from free-positron annihilation in the solid. A second useful parameter for the analysis is the W (wing) parameter, which reflects the positron annihilation with high momentum electrons (core electrons). Fig. 3.13 schematically shows the definition of both parameters and the energy windows ΔE_S and ΔE_W

set to define the integration areas. Both parameters can be combined in S - W maps with a third variable, e.g. the positron implantation energy, the applied electric field, the temperature or the mechanical stress, as a running parameter. These maps are useful to trace positron annihilation at different states present in the samples. In general, the measured $S(X)$ and $W(X)$, where X is the running parameter, are a linear combination of the S_i and W_i values of the different annihilation states involved, weighted by the fraction of positrons trapped in each state $F_i(X)$. Thus, one can express the measured parameters in the following way:

$$S = \sum_i F_i(X) S_i(X), \quad (3.21)$$

$$W = \sum_i F_i(X) W_i(X), \quad (3.22)$$

$$1 = \sum_i F_i(X). \quad (3.23)$$

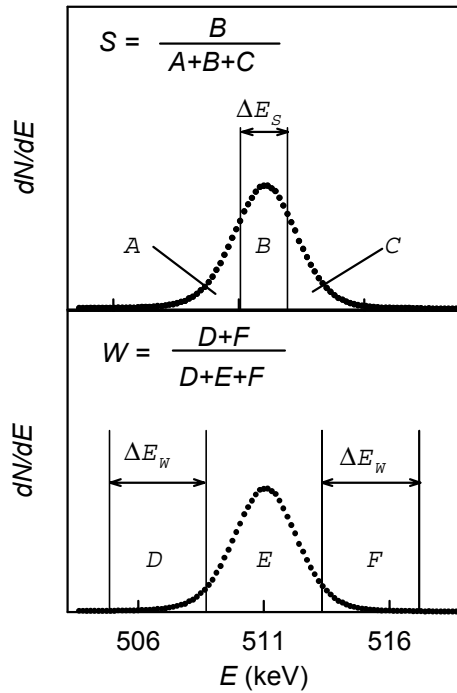


Fig. 3.13. Schematic definition of the shape (S) and wing (W) parameters from the 511 keV annihilation photo-peak. The S parameter is defined as the area B (limited by the energy window ΔE_S) divided by the total area $A + B + C$. The W parameter is defined as the area of the wings D and F (limited by the energy windows ΔE_W) divided by the total area.

The analysis of the data is done with the aid of the VEPFIT program [van Veen et al. 1990]. This program provides an algorithm that simulates the implantation of the positrons and solves the diffusion equation, taking into account the trapping and annihilation of the positrons in the material. The samples are considered as a stack of layers characterised by their thickness (d_i), S_i and W_i parameters and the positron effective diffusion length (L_i). The S_i and W_i parameters are characteristic of the type of defects present in every layer, while L_i can be used to estimate the number of those defects present in a pre-determined layer (i) using the following expression, (see e.g. Chapter 3 in [Krause-Rehberg et al. 1999]),

$$L_i = \sqrt{\frac{D_i}{\lambda_b + \sum_j \kappa_j}}, \quad (3.24)$$

where D_i is the diffusion coefficient of positrons in the bulk of layer i , λ_b is the bulk annihilation rate that equals the inverse of the positron bulk lifetime (τ_b) and κ_j is the positron trapping rate into every type of defect (j) present. When the trapping process in the defect type j is reaction-limited (RL), the positron trapping rate is given by

$$\kappa_j^{\text{RL}} = v_j n_j, \quad (3.25)$$

where v_j is the positron specific trapping rate for the defect type j and n_j is the concentration of traps of type j . In this case n_j is given as an atomic fraction.

When the trapping in the defect of type j is diffusion-limited (DL), one should write

$$\kappa_j^{\text{DL}} = 4\pi D_i n_j R_j, \quad (3.26)$$

where R_j is the radius of the spherical trap of type j . Please note that in this case, n_j is given in units of concentration (cm^{-3}).

In layered structures, when only one type of defect is present in layer i , the positron trapping rate, κ , of this defect can be estimated by means of (3.24). The effective diffusion length, L_i , can be obtained by fitting the experimental S and W curves with the aid of VEPFIT. Finally, making use of a layer of the same material but free of defects, the diffusion coefficient D_i can be estimated. In any case, the bulk annihilation rate, λ_b , must be obtained from positron lifetime measurements.

An alternative method can be employed when there is no transport of positrons across the layer boundaries, e.g. for small diffusion lengths. This method is based on the relation between trapped fractions, F_j and positron trapping rates, κ_j , at different types of defects, j . Assuming that a certain layer, i , of the sample contains n different types of defects, one can write

$$\frac{\kappa_1}{F_1} = \frac{\kappa_2}{F_2} = \dots = \frac{\kappa_n}{F_n} = \frac{\lambda_b}{1 - \sum_j F_j}. \quad (3.27)$$

As before, the bulk annihilation rate, λ_b , must be estimated by means of lifetime measurements. The fraction of positrons trapped at every layer can be calculated by means of equations (3.21) to (3.23). In this sense, the S - W maps of defects are useful aid to determine cluster points corresponding to 100% trapping at a certain type of defect. Another possibility is to employ other positron techniques, such as lifetime measurements or two-dimensional correlation of annihilation radiation, for this purpose.

Once the positron trapping rate, κ_j , for a certain type of defect is known, the concentration of those defects can be calculated from (3.25) or (3.26). However, it is necessary to know the specific trapping rate, ν_j , for rate-limited trapping or on the diffusion coefficient, D_i , and the radius R_j of the trapping defect for diffusion-limited trapping. Determination of these parameters requires measurements on samples with known concentrations of defects. This will be illustrated in Chapter 6 and Chapter 8.

In the case of MOS structures, the interfaces can be studied by means of the application of electric fields [Clement et al. 1997]. Positrons implanted in the oxide are drifted by the applied electric field. When a positive bias is applied to the gate (with the substrate grounded), positrons move in the direction of the SiO₂-Si interface where they accumulate. Further movement is not possible due to the potential barrier at the interface. Thus, the fraction of positrons annihilating at the interface under positive bias conditions increases drastically when compared to the field-free case, enhancing the interface signal and enabling one to carry out reliable interface studies, see Chapter 7.

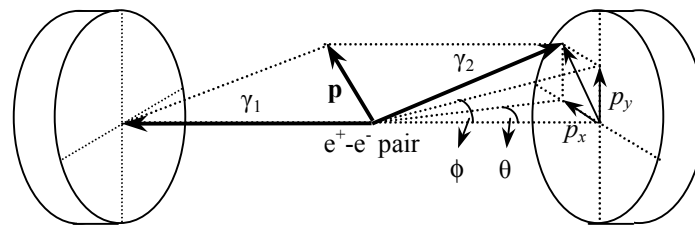


Fig. 3.14. Schematic diagram of a detection system in a typical 2D-ACAR setup. The deviation from collinearity of the two annihilation photons is determined by the angles ϕ and θ , related to the components of the momentum in the directions X and Y, respectively.

3.3.2. Two-dimensional correlation of annihilation radiation

Two-dimensional correlation of annihilation radiation (2D-ACAR) measurements were performed with the unique high-intensity, monoenergetic positron beam of the Positron Centre Delft at the Delft University of Technology. Positrons are produced near the core of a nuclear reactor by pair production induced by hard γ -rays [van Veen et al. 1997, van Veen et al. 2001]. Then, they are magnetically guided to the sample over a distance of about 25 m. The intensity of the beam at the sample is $\sim 10^8$ e⁺/s and its diameter ~ 3 mm.

The annihilation photons are detected by two position-sensitive detectors located opposite to each other. The angle formed by the annihilation photons can be extracted from their impact point in the detectors when measured in coincidence, see Fig. 3.14. The small angles shown in the figure are related to the transversal components, p_x and p_y , of the momentum of the positron-electron pair by

$$\theta \equiv \frac{p_x}{m_0 c}, \quad (3.28)$$

$$\phi \equiv \frac{p_y}{m_0 c}. \quad (3.29)$$

In this way, one can obtain a two-dimensional projection of the three-dimensional electron momentum density in the surroundings of the annihilation sites.

In our system the distance between the detectors can be varied up to 23 m apart, improving the resolution of the system. When the detectors are located at this distance from each other the full width at half maximum (FWHM) of the resolution function along the p_x direction is 1.4 mrad and along the p_y direction 1.2 mrad, i.e. at least a factor 4 better than in DBAR measurements. An extensive description of the 2D-ACAR apparatus is given by [Falub 2002].

Chapter 4

Hydrogen-related hole capture and positive charge build up in buried oxides

This chapter is intended to contribute to the understanding of the positive charge build up upon hole injection in SiO_2 , which is known to be an important degradation process. Our results are in agreement with a recently proposed model of charge generation. We have observed the release of HD molecules upon hole injection in MOS capacitors that received a post-metallisation annealing in 100 kPa D_2 at 680 K. It was observed that the release of every HD molecule is related to the capture of one hole by one $\text{O}_3\equiv\text{Si}-\text{D}$ centre. This centre is converted into the neutral $\text{O}_3\equiv\text{Si}\cdot$ centre accompanied by the liberation of one deuteron D^+ , which, when neutralised, recombines with H giving the observed HD and when trapped, is responsible for the positive charge build up. The release of HD is suppressed when the number of generated $\text{O}_3\equiv\text{Si}\cdot$ centres is high enough to trap all the generated HD. This occurred when only 25% of the initial $\text{O}_3\equiv\text{Si}-\text{D}$ groups had dissociated by hole trapping. The positive charge build up was found to be dependent on the sample treatment indicating the strong influence of external sources of hydrogen in the described processes. The $\text{O}_3\equiv\text{Si}\cdot$ groups generated upon hole injection were found to be located close to the surface, distributed over a layer with a thickness dependent on the strength of the electric field applied during the hole injection, i.e. 220 nm for 1.0 MV/cm and 400 nm for 2.0 MV/cm.

4.1. Introduction

The build up of positive charge in oxides upon irradiation has been classically associated with the trapping of holes by oxygen vacancies leading to paramagnetic E' centres, which were supposed to be positively charged [Lenahan et al. 1984, Witham et al. 1987, Kim et al. 1988]. This model has been questioned [Afanas'ev et al. 2000] due to evident contradictions with a large number of experiments, see e.g. Refs. in [Afanas'ev et al. 2000]. Alternatively, a model based on the interaction between hydrogen and oxides has been proposed [Afanas'ev et al. 2001]. This model can explain a large number of experiments in which the positive charge did not correlate with the E' signal, see Section 2.1.

With this chapter we contribute to the understanding of the phenomena taking place during the irradiation of SiO₂. Several fundamental aspects of the model described in Section 2.1 were studied. First, previous studies used the changes observed in the inversion capacitance of MOS structures with B-doped p-substrate as a proof of the hydrogen release during irradiation [Afanas'ev et al. 2001b]. Alternatively, here, we give direct evidence of hydrogen release by monitoring the HD release rate during hole injection in deuterium annealed samples. For this purpose we used the equipment commonly employed for thermal desorption experiments (TDS) attached to a VUV source that generates electron-hole pairs in the oxide. This is what we call radiation-induced desorption spectrometry (RDS). By means of this method useful quantitative information was obtained on the processes involved. Second, the positive charge generated during the injection was monitored by high frequency capacitance voltage (CV) measurements. The positive charge was correlated with the hydrogen release. Third, the effect of the radiation experiments on the bulk oxide was monitored by Doppler broadening of annihilation radiation (DBAR) measurements using a positron beam. This is a non-destructive technique that permits distinguishing different types of defects and provides depth resolution. In this way, a depth profile of O₃≡Si• defects close to the sample surface was obtained upon irradiation of the samples.

4.2. Experimental

See Chapter 3 for a detailed description of the experimental techniques employed.

4.2.1. Sample preparation

Unibond samples with 3- μ m thick oxides sandwiched between n-Si were employed. The relatively large thickness of the buried oxides (BOX) allows to monitor the irradiation-damage depth profile by (DBAR). MOS structures were created after chemically etching the top layer. 15 nm Al layers were evaporated through a mask on the bare oxides. The area of the capacitors was 0.8 cm². A 100 nm thick Al layer was deposited on the back of the sample to create an ohmic contact.

Some of the MOS samples were annealed in 100 kPa high purity D₂ for 1 h at 680 K. This process is commonly called post metallisation annealing (PMA).

Only some of the results are shown in this work. We remark that the results shown in this chapter were fairly well reproduced for similar samples under similar treatments. Table 4.1 presents the samples used in this study.

Table 4.1. Description of the samples employed in this chapter.

Sample	Size (mm×mm)	PMA in D ₂	Accumulated number of injected holes	TDS	RDS	CV	PBA
1	4.5×4.0	Yes	-	Yes	No	No	No
2	20×20	Yes	1.1×10 ¹⁵ cm ⁻² at 1.0 MV/cm	No	Yes	Yes	No
3	20×20	No	2.5×10 ¹⁵ cm ⁻² at 1.0 MV/cm	No	No	Yes	Yes
4	20×20	No	0.6×10 ¹⁵ cm ⁻² at 2.0 MV/cm	No	No	No	Yes
5	20×20	No	-	No	No	No	Yes

4.2.2. Comments on the large area capacitors

The relatively large capacitor areas have a triple function: (i) to enhance the number of holes injected in the sample and therewith the number of released molecules; (ii) to enable CV measurements that otherwise would be impossible for thick oxides because the capacitance increases inversely to the oxide thickness; (iii) to carry out DBAR, as the beam has a diameter of about 5 mm (see Chapter 3).

However, the large area capacitors have important disadvantages: (i) the appearance of leakage currents may relatively readily occur, especially at high fields; (ii) further treatment of the capacitor, both before and after metalisation easily leads to degradation.

In order to establish comparisons with different sample treatments we tried to anneal different samples in D₂ at temperatures higher than 800 K. Unfortunately we failed because these treatments, unlike PMA, induce degradation, leading to leakage currents, which are hardly avoidable for large area capacitors.

4.3. Results

In order to estimate the amount of D₂ introduced in the oxide by the PMA annealing, we performed TDS measurements on sample 1, which is a 4.5×4.0 mm² piece cut from a MOS sample that received standard PMA in D₂ (see above). The Al gate was removed prior to the TDS experiments. The PMA treatment leads to the exchange of H in Si–H groups by D. This is possible thanks to the metal gate that promotes the generation of highly reactive atomic D during the annealing. We do not expect additional creation of Si–D groups during the PMA process. The creation of these Si–D defects would only be possible by disruption of regular oxide bonds, which is highly improbable, especially at the low temperature of the PMA process. Samples without metal gate annealed in D₂ ambient at 680 K did not show a

significant incorporation of deuterium due to the low reactivity of molecular D_2 at this low temperature. We assume, in principle, full H–D exchange, below we give more evidence of this. Fig. 4.1 shows the results of this experiment. The release rate of HD and D_2 is plotted as a function of the temperature during a ramp annealing at 4 K/s. We assume that two HD molecules contribute as much as one D_2 molecule. One single peak appears centred around 900 K as previously observed for low temperature annealings [Rivera et al. 2001], see Chapter 5. This indicates that deuterium is mainly trapped forming Si–D groups. The amount of deuterium in the sample was found (by integration of the peak) to be about 1.6×10^{14} D/cm².

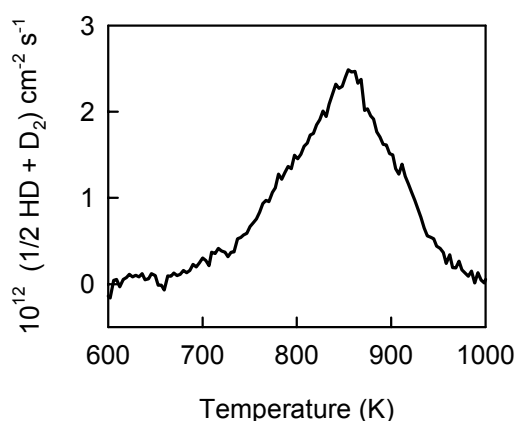


Fig. 4.1. TDS spectrum obtained for sample 1, annealed in 100 kPa D_2 at 680 K for 1 h. The HD and D_2 signals were recorded while increasing the sample temperature at a rate of 4 K/s. The HD signal is divided by 2 because two HD molecules contribute as much as one D_2 molecule.

Sample 2 was irradiated as shown in Fig. 4.2. Note that the horizontal axis represents time during the experiments but the time gap between subsequent experiments is totally arbitrary. Typically, subsequent experiments were performed with a pause of a few minutes. In some cases CV measurements were performed during the pause. Initially, (**experiment 1**) the sample was illuminated by VUV with gate and substrate at 0 V. It is evident that both the H_2 and HD release signals increase with respect to the vacuum level (zero). The increase can not be ascribed to hole trapping in the oxide because there is no electric field across the oxide. The increase is due to gas release from different surfaces in the vacuum system as a consequence of the VUV illumination. Thus, the increase in the signal can be considered as a raise in the background level due to the VUV light (VUV background). These levels are denoted by horizontal lines in Fig. 4.2. During all these experiments the D_2 signal was also recorded, but due to the lack of sensitivity no significant changes were observed. Therefore, D_2 data are not shown. **Experiment 2** was performed illuminating the sample while applying an electric field of +1.0 MV/cm. Both H_2 and HD release rates increase with respect to the identified VUV background levels. In addition, we observe that both H_2 and HD signals decay during the time of the experiment (30 s corresponding to a fluence of 0.4×10^{13} holes cm⁻²) but following a rather different mechanism. The huge increase in the H_2 signal can not be related to hole capture, because the number of H_2 molecules released per cm² is two orders of magnitude larger than the injected hole dose. **Experiment 3** corresponds to hole injection at 1.0 MV/cm for 130 s (accumulated dose 1.9×10^{13} holes cm⁻²). During the injection the sensitivity of the TDS system was optimised; therefore, the recorded data were not useful and are not shown. **Experiment 4** shows again an increase in both H_2 and HD signals

accompanied by a decay during the time of irradiation at 1.0 MV/cm (76 s, accumulated dose 2.8×10^{13} holes cm^{-2}). It is important to note that while the HD signal follows a continuous exponential decay with respect to the previous experiments, the H_2 signal does not. The latter signal seems now larger than in experiment 2, indicating that different sources contribute to this signal, i.e. background pressure, adsorbed atoms, and gas on the metal layer. This makes the behaviour of this signal rather unpredictable. **Experiment 5** consisted of another exposure for 90 s at 1.0 MV/cm (accumulated dose 3.9×10^{13} holes cm^{-2}). Again both signals increase as an effect of the irradiation and show a decay during the time of the experiment. Finally, **experiment 6** was performed with gate and substrate at 0 V. The HD signal does not change with respect to the previously found VUV background level (horizontal line) while the H_2 signal is lower than that level. Apparently, the VUV background level during illumination changes in the case of H_2 , showing once again its unpredictable behaviour.

We should mention that the photocurrent remained rather constant at a value of $(1.2 \pm 0.2) \times 10^{11}$ holes $\text{s}^{-1} \text{cm}^{-2}$ for all the experiments presented in which low doses were injected. The sample was subjected to further hole injection treatments at 1.0 MV/cm (not shown). These experiments showed that further hole injection leads to a raise in the HD signal up to the level reached when the previous experiment was stopped. This continuity of the decaying spectra was not observed for the H_2 signal. The photo-current measured during the hole injection experiments increased at doses higher than a few times 10^{14} holes cm^{-2} . In line with these observations, we should mention that charge-free samples were injected with electrons at low doses showing an increase in the HD signal to values similar to the VUV background level shown in Fig. 4.2.

In a conclusion, we observed that the HD release rate increases significantly above VUV background levels only in the case of simultaneous application of VUV illumination and positive electric field, i.e. hole injection. The HD spectra decay during the period of time that hole injection is applied. The decay is continuous from one injection experiment to the next. The H_2 signal behaves unpredictably and without continuity between one experiment and the next.

Following the model mentioned in the introduction and described in Section 2.1, we can link the desorption of HD during hole injection experiments to hole trapping. We can assume for low hole doses that the D^+ ions generated upon hole capture by Si–D groups, following Reaction (2.1), are drifted swiftly to the interface. Once at the interface, they quickly neutralise, following Reaction (2.2) and form HD molecules with H atoms by means of Reaction (2.3). Note that H atoms are abundant as inferred from the H_2 spectra of Fig. 4.2. Under these assumptions the rate limiting process for HD formation is the hole capture by Si–D groups. Then the kinetics of HD formation should be the same as the kinetics of hole capture. We modelled the HD release rate by first order kinetics [Buchanan et al. 1991]. The HD release rate can be simply fitted by an exponential decay with only one free parameter, the hole capture cross section (σ), in the case of constant photocurrent. This condition is fulfilled at low injected hole doses corresponding to the injection experiments 2, 3, 4 and 5 (shown in Fig. 4.2). In Fig. 4.3, the fitting of the experimental data to the first order model is shown. The data are plotted as a function of the injected hole dose skipping the pauses between consecutive experiments. The resulting value of σ is found to be $(3.7 \pm 0.5) \times 10^{-14}$

cm^2 . The uncertainty is due to small fluctuations in the photo-current, $(1.2 \pm 0.2) \times 10^{11}$ holes $\text{s}^{-1} \text{cm}^{-2}$. This value is in perfect agreement with the expected value for hole trapping in SiO_2 . The data corresponding to H_2 can not correspond to hole capture as explained above. In any case it can not be fitted in the same way because the H_2 release curves corresponding to consecutive experiments are not continuous. Even within every experiment the data did not fit the first order kinetics model.

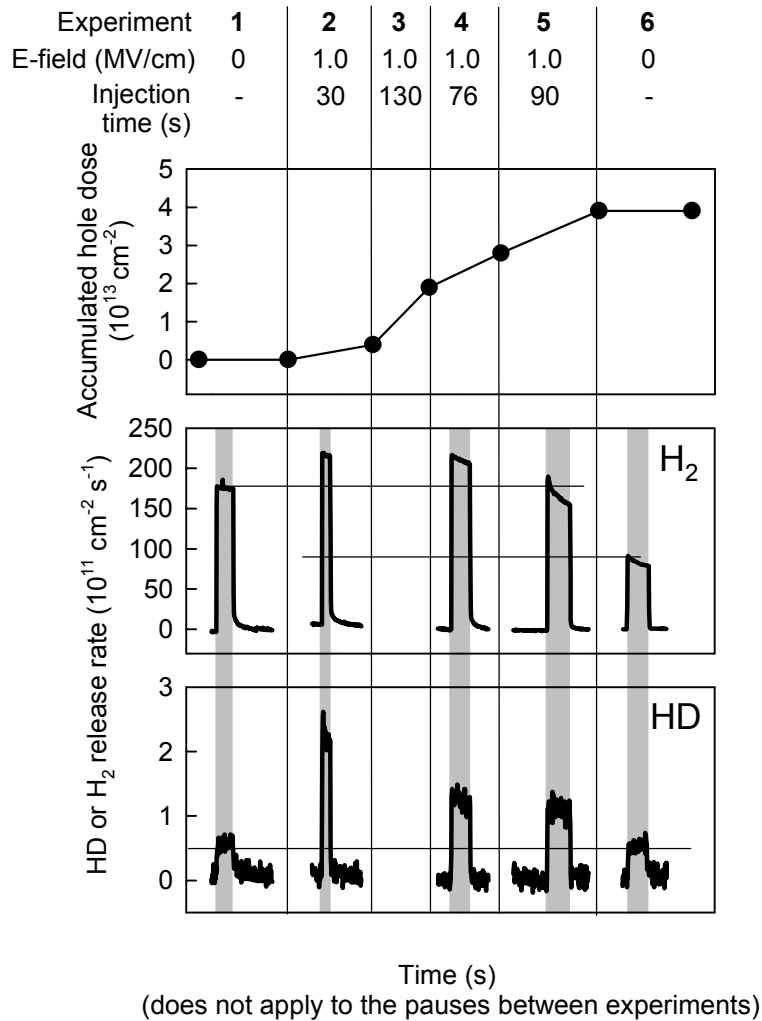


Fig. 4.2. Irradiation experiments performed on sample 2, which received a PMA treatment. The shaded areas indicate the periods in which the VUV source was on. The conditions of the experiments are indicated at the top. The bottom panels show the H_2 and HD release rate as a function of time for every experiment. The top panel indicates the hole dose accumulated after every experiment. Note that the gaps between consecutive experiments are arbitrarily large.

Another aspect of the model is the accumulation of positive charge upon hole capture. In order to correlate the hydrogen release during hole injection with the positive charge generation we performed CV measurements on samples 2 (with PMA) and 3 (no PMA) after

the injection of certain doses of holes. Fig. 4.4 shows the density of positive charge as a function of the injected hole dose. The sample that was subjected to the PMA process showed a much slower build up of positive charge than the sample without PMA. The importance of the sample processing is clearly evidenced at this point. In addition, the total HD released is presented (solid curve) as a function of the injected hole dose. This curve was obtained by extrapolating the curve resulting from the fitting (Fig. 4.3) and integrating it. At low injected doses, the kinetics of HD formation and that of charge build up are quite similar. (In fact, with the selected scales of Fig. 4.4, both overlap, looking like a fit). This suggests that the formation of positive charge strongly depends on the presence of hydrogen species. However, at higher doses the release of HD appears suppressed whereas the positive charge build up is not stopped.

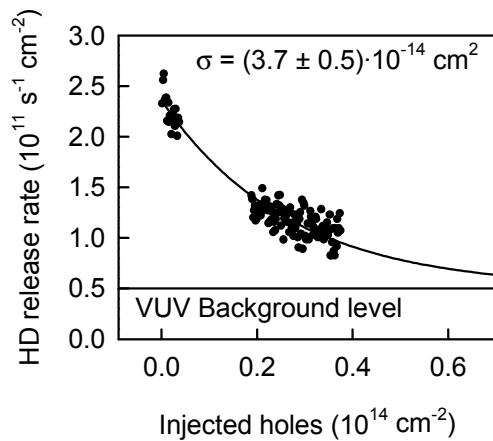


Fig. 4.3. First order kinetics fit of the HD release rate, which was assumed to follow the same kinetics as the hole capture (see text). The only free parameter is the hole capture cross section, found to be $\sigma = (3.7 \pm 0.5) \times 10^{-14} \text{ cm}^2$.

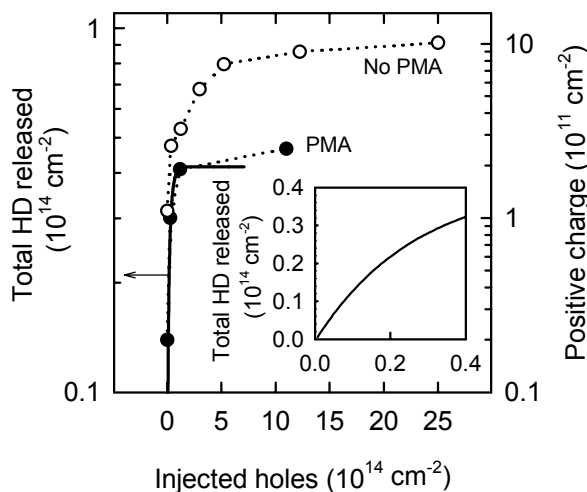


Fig. 4.4. Comparison between the total number of HD molecules released (solid line associated to left axis) and the accumulation of positive charge (dots associated to right axis) as a function of the injected hole dose. The solid symbols correspond to sample 2, which received a PMA treatment, while the open symbols correspond to sample 3, which did not receive a PMA treatment. The dotted lines are guides to the eye. The insert shows the HD molecules released at low injected hole doses.

Samples 3, 4 and 5 were used for positron studies. Holes were injected into sample 3 at 1.0 MV/cm up to a dose of $2.5 \times 10^{15} \text{ cm}^{-2}$, sample 4 was injected at 2.0 MV/cm up to a dose of $6 \times 10^{14} \text{ cm}^{-2}$ and sample 5 was not injected in order to use it as a reference sample. By means of positron studies we can obtain a defect depth profile of the studied samples. Fig. 4.5 shows

the S and W annihilation parameters as a function of positron energy. For convenience the S and W parameters are normalised to the c-Si bulk values ($S_{c-Si} = 0.578$, $W_{c-Si} = 0.032$). The positron energy can be transformed into positron mean implantation depth giving depth information. The vertical line shown in Fig. 4.5 was obtained in this way and represents the boundary between the Al gate and the oxide layer. The 15 nm Al gate is easy to identify by its high S value and low W value. At positron energies higher than about 5 keV, most of the positrons are implanted and annihilated in the SiO_2 layer, giving the typical S - W values for annihilation in SiO_2 (as seen in the curves belonging to sample 5). On the other hand, the samples that were injected with holes exhibit a lower S value in the region close to the gate. This indicates that defects remained after hole injection and positrons were effectively trapped at these defects.

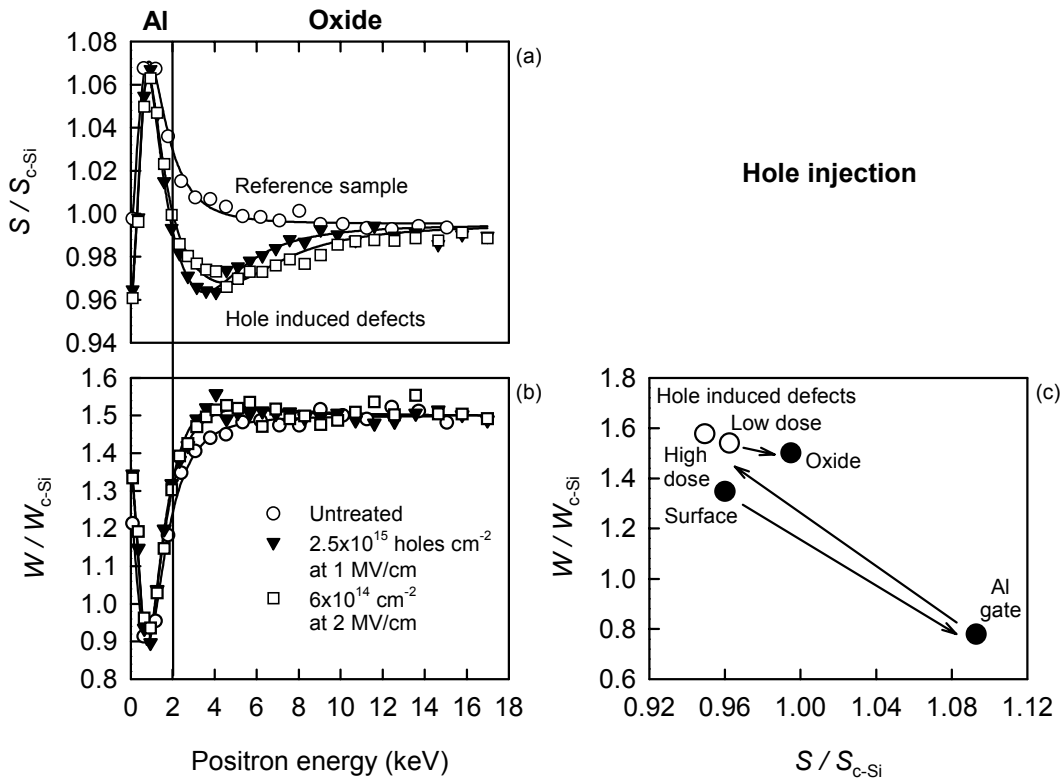


Fig. 4.5. DBAR experiments on MOS samples that did not receive a PMA treatment and were subjected to hole injection as indicated in the legend. (a) and (b) S and W parameters normalised to the c-Si bulk values and plotted as a function of the incoming positron energy. The vertical line represents the boundary between the Al gate and the oxide layer. The solid lines are the fits obtained by VEPFIT. (c) S - W map of defects. The different layers involved (surface, Al gate, oxide layer and hole-induced defects) are represented by pairs of coordinates in the map. It is easy to distinguish the difference between the defect states created by a high or low dose of holes (open symbols).

The process can be explained as follows. In untreated SiO_2 a large amount of positronium (Ps) is usually found [Rivera et al. 2001b], see Section 6.2. Positronium is

formed due to the attractive coulombic interaction among the incoming positrons and electrons excited during the thermalisation of the positrons. Ps formation is possible because there is enough space in the open amorphous SiO₂ to accommodate the atom-like Ps. The presence of Ps leads to a relatively high S value due to the self-annihilation of the near-zero momentum para-Ps. Positrons trapped at certain defect locations overlap with electrons belonging to the defects, with which they annihilate. The formation of Ps with these electrons is not favourable because their binding energy is larger than the binding energy of Ps. Thus, the absence of Ps leads to a drop in the S value, see Section 3.3.

Briefly, we can say that the defects generated by the injection of holes lead to a drop in the S parameter with respect to the bulk value. In this way, by means of the S parameter we obtain a defect depth profile. It is known that the defects generated by hole injection are E' centres in a neutral state [Afanas'ev et al. 2000]. We assume that positrons are sensitive to E' centres. However, we can not assure that all the defects detected by DBAR correspond to paramagnetic E' centres because it is possible that positrons are trapped at similar defects regardless of their paramagnetic character. We can call them E'-like centres.

We fitted the experimental curves by means of VEPFIT using a model of two layers for the reference sample, i.e. a 15 nm thick Al layer and a 3 μ m thick oxide layer. In the case of the samples subjected to hole injection, an extra layer is introduced to account for the defects introduced by the injection of holes. A characteristic S - W pair of coordinates and the positron diffusion length are obtained from the fit for every layer. In addition, we can estimate the thickness of the defect layer. VEPFIT assumes that the layers are homogeneous. This is certainly not the case but, anyway, with this approximation we can get useful results about the defect depth profile. The positron results obtained from the fit for the defect layers generated by hole injection are summarised in Table 4.2. It appears that the defect layer obtained for hole injection at 2.0 MV/cm is broader than that obtained when the injection was carried out at 1.0 MV/cm. On the other hand, the S value drops to lower values with increasing hole dose. We applied a PMA process to sample 3 after the positron measurements just shown followed by new positron measurements on this sample. We observed a complete recovery of the S - W parameters (data not shown) after PMA despite the low annealing temperature, indicating that the defects induced by hole injection are again passivated by deuterium.

Table 4.2. Summary of the DBAR results obtained for the hole-induced defective layer of samples 3 and 4. L is the positron diffusion length in the defective layer and d is the thickness of the layer.

Sample	Treatment	S	W	L (nm)	d (nm)
3	2.5×10^{15} holes cm ⁻² at 1 MV/cm	0.949	1.577	20	220
4	0.6×10^{15} holes cm ⁻² at 2 MV/cm	0.963	1.540	20	400

Fig. 4.5c shows the S - W map of defects; the arrows indicate the direction of increasing positron energy. By means of this map the different annihilation sites can be easily identified and compared. In this case the surface, Al layer, defect layer and oxide layer are described by

a characteristic S - W point in the plot. The effect of the hole injection is clearly visible and more pronounced at higher injection dose.

In the S - W map of Fig. 4.6 we compare the results obtained by hole injection with those obtained in Chapter 8 in [Clement 1998] for electron injection in thermal oxides. We can observe that the trend is clearly different. At high electron doses S drops and W increases, both drastically. The high W value is related to annihilation with core electrons. The only source of such core electrons in these samples is related to the presence of oxygen atoms at the positron trapping site. This indicates that the defects created by electron injection are related to these atoms. Thus, we assume that the microscopic structure of such defects is related to Si-O• groups. These defects can be generated by the interaction of electrons with Si-OH groups that are known to have a small cross section for electron capture. Many of these defects are negatively charged and form a very attractive coulombic trap for positrons. On the other hand, the defects associated with hole injection do not show a big change in the W parameter, which follows the picture of positron trapping at Si• groups generated by the hole capture in existing Si-H groups. In addition, the fact that positrons are trapped at these defects strongly excludes the possibility that they are positively charged as previously suggested [Lenahan et al. 1984]. Contrarily, upon hole trapping the positively charged species is the liberated H⁺ or D⁺ ion, as proposed in the model of charge build up [Afanas'ev et al. 2001]. In short, by means of positrons we are able to distinguish both electron and hole traps in SiO₂ and to give some details about essential properties of such traps like charge state or microscopic nature.

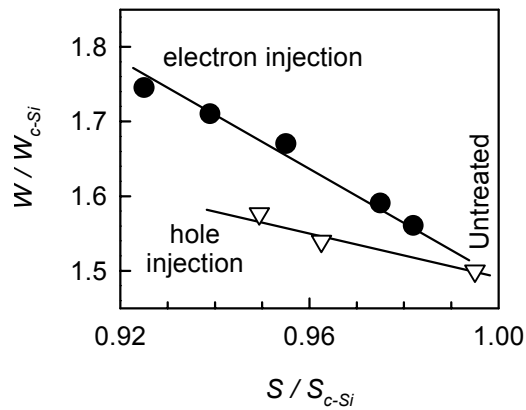


Fig. 4.6. S - W plot showing the effect of hole (open symbols) and electron (solid symbols) injection into MOS capacitors. Hole injection experiments performed on samples 3 and 4 by illuminating the samples with VUV light (photon energy 10 eV) are shown. The hole injected doses were 2.5 and $0.6 \times 10^{15} \text{ cm}^{-2}$ at 1 and 2 MV/cm respectively corresponding to the first and second open symbols from left. The rightmost open symbol corresponds to a non-injected MOS sample with 3 μm Unibond oxide. The solid symbols correspond to one sample with a 1 μm wet oxide grown at 1050°C on n-Si and exposed to low energy electrons ($< 10 \text{ eV}$) in order to charge it negatively (from Chapter 8 in [Clement 1998]). The solid circles (from right to left) correspond to accumulated negative charge densities of 0, 0.5, 1.0, 3.5 and $6.0 \times 10^{12} \text{ cm}^{-2}$. The lines are guides to the eye.

4.4. Discussion

4.1.1. Evidence of hole-induced hydrogen release

We present the experiments shown in Fig. 4.2 as a new evidence of hydrogen release upon hole capture by Si–H groups in SiO₂, in agreement with the model proposed in [Afanas'ev et al. 2001]. In fact, the hole cross section obtained from Fig. 4.3 agrees perfectly with the well known hole capture cross sections in SiO₂ indicating that the observed HD release is due to hole injection. Following we give more experimental information showing that HD is generated upon hole capture in Si–D groups.

The use of deuterium allowed us to distinguish the desorption signal produced by hole injection from unavoidable other contributions to the desorption spectra. These contributions can be related to different layers of the sample, i.e. Al, Si substrate and interfaces. One could argue that deuterium trapped for example in the Al layer during the PMA process was liberated during the VUV illumination. However, we observe that the increase in HD release rate is very huge only when the gate is at positive voltage during the VUV illumination. This corroborates the idea of HD release related to the injection of holes in the oxide. Furthermore, the cross section for H-release from Al is very small (in the range of 10⁻¹⁶ cm²) [Afanas'ev et al. 2001b]. This means that at the low injection doses used in the experiments presented in Fig. 4.2 and Fig. 4.3, the observed HD release can not be related to the Al layer.

According to the TDS results (Fig. 4.1), nearly all the existing Si–H traps were exchanged by Si–D traps during the PMA process (see Section 4.3). An independent confirmation of this observation is obtained from that the ratio between the number of injected holes and the number of released HD molecules which is about 1 for low injected doses (see insert in Fig. 4.4). Therefore, at low doses, all the injected holes must be trapped at Si–D groups. A significant participation of Si–H groups in the hole capture process would imply a different ratio due to the employment of a fraction of the holes to produce H⁺ to the detriment of D⁺ production. The D⁺ species liberated by the hole trapping process described by Reaction (2.1) are neutralised at the Si/SiO₂ interface following Reaction (2.2), and recombine with H⁰ giving HD by Reaction (2.3). The formation of D₂, i.e. the recombination of two atoms originally released by holes, is not observed. In addition it is excluded by the ratio of the number of holes to the number of HD molecules, which is 1 hole per molecule, while to create one D₂ it would have to be 2 holes per molecule.

In conclusion, we observed that the entire initially detected release signal is in the form of HD, where the D atom comes from a Si–D hole trap and the H atom comes from the background, probably, introduced in the oxide by the VUV illumination.

4.4.2. Relation between hole capture and charge build up

The kinetics of charge build up seems similar to that of HD release for low injected hole doses (Fig. 4.4). When the number of hole generated defects (Si•) becomes larger the trapping of the hole-generated species, (D⁰ and HD) or the background species (H⁰ and H₂) becomes important, see Reactions (2.4) and (2.5). Due to this, Si–H groups are created which can enter the proton generation cycle. Therefore, due to retrapping, the hydrogen release is stopped and

the positive charge density continues increasing, as shown in Fig. 4.4 for sample 2. In addition, external sources of hydrogen can supply extra hydrogen that enhances the positive charge build up. Sample 3 did not receive a PMA treatment after depositing the Al gate. The amount of positive charge generated in this case is much larger than in the case of sample 2, which received PMA. This is in agreement with previous results [Afanas'ev et al. 2001] and evidences the large influence of the treatments and surroundings on the generation of positive charge in the samples and the important role of hydrogen in these processes. Many of the generated positive centres are unstable, which means that at some point a balance is reached between the number of generated charged centres and that of the centres being neutralised [Drujif et al. 1995].

From the hole injection experiments obtained for sample 2 at low hole dose, we can estimate the number of holes that should be captured by Si-D groups to produce one D^+ related positive charge centre. This number amounts to about 300 holes per positive centre. This value is probably rather constant because the rate limiting process is the production of protons (H^+ or D^+). However, it can differ for different samples depending on aspects as sample treatment, stress, bonding distribution or interface configuration.

4.4.3. Relation between hole capture and generation of Si• defects

The release of HD observed for sample 1 during hole injection was stopped when only about 4×10^{13} HD cm^{-2} had released (Fig. 4.4). This means that the process stopped when only 25% of the initial amount (1.6×10^{14} cm^{-2}) had released. The release suppression occurs when the number of hydrogen traps (Si•) is sufficiently high to trap all the generated atomic or molecular hydrogen. We can give an upper limit to the number of de-passivated defects, n , i.e. Si• groups, likely paramagnetic E' centres. This value corresponds to the total number of HD molecules released, 4×10^{13} HD cm^{-2} . Typically, the number of E' centres after hole injection is much lower than this value. This suggests that not all the Si• groups are paramagnetic, or more likely, that many of these groups were passivated by external hydrogen that entered the charge build up cycle.

The positron experiments supply more useful information to this picture. Sample 3 was injected at 1.0 MV/cm with holes up to a dose of 2.5×10^{15} holes cm^{-2} and sample 4 at 2.0 MV/cm up to a dose of 6×10^{14} cm^{-2} . PMA was not applied to these samples. The thickness of the layers with the hole generated defects depends on the electric field applied to the sample (Table 4.2). A first look suggests that the hole capture cross section drops with increasing electric field. However, this can not explain by itself why the thickness of the defect layers is much smaller than the estimated thickness (d) of SiO_2 that can effectively trap all the injected holes at low doses. d can be calculated assuming a hole trapping cross section $\sigma = 3.7 \times 10^{-14}$ cm^2 and a density of Si-H groups (hole traps) of 1.6×10^{14} cm^{-2} . Then the volume density of hole traps, assuming that they are homogeneously distributed, is given by $\rho = 1.6 \times 10^{14}$ $\text{cm}^{-2} / 3 \times 10^{-4}$ $\text{cm} = 5.3 \times 10^{17}$ cm^{-3} , where the denominator is the thickness of the oxide layer. The probability of total hole trapping imposes $1 = \sigma \cdot \rho \cdot d$; from which $d = 507$ nm.

However, based on the DBAR measurements, we believe that the damage profile does not extend beyond 220 nm for 1.0 MV/cm hole injection and beyond 400 nm for 2.0 MV/cm.

This is due to atomic and molecular hydrogen retrapping at the hole generated defects. A competition is established between depassivation by hole injection and passivation by H or H₂. The first process is more probable near the Al gate, while the second process is more probable near the Si/SiO₂ interface. The electric field enhances the probability of capturing holes further from the surface. This in turn contributes to a thicker defect layer, regardless of the hole dose injected, as shown in Fig. 4.5 for sample 4, compared with sample 3. According to our results the Si• groups resulting from the hole injection experiments are distributed close to the surface. Previous results obtained for the distribution of E' centres generated by irradiation should be carefully re-examined. For example, in [Lenahan et al. 1984] the E' concentration was found by means of etch back experiments to be located very close to the Si/SiO₂ interface. These results are not comparable to ours, because the oxides studied were very thin (120 nm) and were irradiated with γ rays at +20 V.

The defect layers of samples 3 and 4 contain a mixture of Si–H and Si• defects. This is evidenced by the difference in the *S*-*W* parameters for the defect layer. In sample 4 a low dose of holes is accommodated along a thick layer (400 nm thick), whereas sample 3 received a high dose of holes accommodated in a much thinner layer (220 nm). One expects that the density of Si• defects (those detected by positron analysis) is lower in the defect layer of sample 4 compared to the density of defects in the defect layer of sample 3. The lower *S* value obtained for the defect layer of sample 3 compared to the *S* value for the defect layer of sample 4 is in agreement with the expectations. By means of these measurements we can give an upper value for the density (*n*) of Si• in the defect layer of sample 3 after hole injection. For this purpose, we assume that all the defects in this layer are depassivated (Si•). A simple calculation then leads to $n = \rho \times 220 \text{ nm}$, where 220 nm is the thickness of the defect layer, giving $n = 1.2 \times 10^{13} \text{ cm}^{-2}$. This value is more realistic than the value obtained above without considering the positron results. Anyway, we should remark that the assumption of full depassivation is rather improbable.

4.5. Conclusions

In this chapter we have presented a number of new experiments in order to estimate the validity of the hydrogen model for irradiation induced charge build up in SiO₂ [Afanas'ev et al. 2000, Afanas'ev et al. 2001]. All our results are in agreement with this model. Direct information has been obtained on the hydrogen release upon hole capture and the depth distribution of generated Si• centres (E' or E'-like centres).

According to our results, molecular hydrogen is released from SiO₂ when holes are injected. The source of hydrogen is the Si–H group that acts as a hole trap producing H⁺ upon hole capture. The H⁺ species are drifted to the interface, where they are trapped generating a positive charge centre or neutralised with electrons from the substrate, producing molecular hydrogen after recombination with another H atom. The substitution of all the $1.6 \times 10^{14} \text{ Si–H cm}^{-2}$ groups by Si–D groups permits one to follow the hole induced hydrogen release. At low hole dose, the injection of every hole is accompanied by the release of one HD molecule. The rate limiting process for the generation of HD is the hole capture by Si–D groups, whose cross

section was found to be $\sigma = (3.7 \pm 0.5) \times 10^{-14} \text{ cm}^2$ in agreement with reported values for the hole capture cross section. The charge build up shows the same kinetics as the hole trapping process. We found that about 300 holes are trapped per every positive charge centre created.

The formation of molecular HD is in competition with the retrapping of atomic or molecular hydrogen species by the $\text{Si}\cdot$ centres generated by hole capture. When the number of these centres is sufficiently high, HD release is no longer observed, but the positive charge build up continues due to the capture of holes by the newly generated Si-H or Si-D centres. In addition, an external supply of hydrogen, i.e. hydrogen accumulated in different layers of the sample, enters the cycle when trapped at radiation-induced $\text{Si}\cdot$ centres. This leads to a very high positive charge density without a corresponding high $\text{Si}\cdot$ (E') centre density.

The Si-H depassivation by hole trapping is more likely in the region close to the gate while the $\text{Si}\cdot$ passivation by hydrogen trapping is more probable close to the Si/SiO_2 interface. The result is a few hundred nm thick layer of $\text{Si}\cdot$ centres close to the gate, probably corresponding to the EPR-active E' centres. The thickness of the defect layer mainly depends on the applied electric field during the hole injection. The fact that positrons are trapped at the $\text{Si}\cdot$ groups excludes that these are positively charged.

Finally, we would like to mention some implications of this work. Despite the beneficial role of hydrogen as a passivating agent of P_b centres [Stesmans 2000], its concentration should be kept as low as possible, not only in the oxide but in any layer from which hydrogen could be injected in the oxide during operation. Even more important, oxides with a low number of hole traps (Si-H groups) are less sensitive to radiation induced degradation. This point should be especially considered when dealing with buried oxides, which usually contain a large concentration of these defects. The reduction of any kind of hydrogen contents will strongly reduce the degradation of devices, especially when operating in hostile environments.

Chapter 5

Hydrogen uptake and release in buried oxides

Because of technological relevance a vast number of publications has been published on Si/SiO₂ interface studies. In comparison, the number of studies devoted to the bulk SiO₂ layer is considerably less. However, many important device degradation processes take place in the SiO₂ layer. In particular, hydrogen-related defects play an important role when the samples are exposed to ionising radiation, as shown, for example, in Chapter 4.

SIMOX is known to contain a large concentration of hydrogen in its BOX layer. This makes SIMOX samples appropriate for TDS studies. We have studied SIMOX buried oxide samples implanted either with D⁺ (10¹⁴-10¹⁵ cm⁻²) or annealed in D₂ (300-500 kPa at 1073 K). Thermal Desorption Spectrometry (TDS) performed on these samples after removal of the top Si layer shows two important desorption peaks related to the release of deuterium from Si-D and Si-OD defects. The first peak is dominant in implanted samples and the second one in deuterium-annealed samples. In TDS experiments on samples with a top layer the deuterium release is limited by three processes: diffusion in SiO₂, D₂-cracking at the Si/SiO₂ interface and permeation through the top Si layer. In these samples the D₂ signal is related to release through lateral surfaces, whereas the HD signal is produced by release through the top Si layer.

5.1. Introduction

Hydrogen in SiO₂ plays a role in a number of degradation processes: trap creation [DiMaria et al. 1995, Afanas'ev et al. 1995], donor generation at the Si/SiO₂ interface [de Nijs et al. 1994] and depassivation of dangling bonds [Stesmans 2000b]. In addition, it may also cause leakage currents [Afanas'ev et al. 1999]. The presence of hydrogen in the SiO₂ layer is of great importance since under certain circumstances hydrogen can become free and enter some of the mentioned degradation processes.

In a number of hydrogen-SiO₂ studies it is of advantage to use deuterium rather than hydrogen. In general differences in thermodynamic behaviour of the two isotopes are small, although not always negligible.

It is known that deuterium in SiO₂ is retained in SiD and Si-OD groups, the latter being the more stable [Revesz 1979]. The interactions of deuterium with SiO₂ were studied by [Myers et al. 1990] with nuclear reaction analysis (NRA). These authors associated activation energies of 2.8 and 3.2 eV with Si-D and Si-OD defects, respectively.

In SIMOX buried oxides the hydrogen uptake during annealing in hydrogen is surprisingly high [Myers et al. 1993] compared to thermal oxides. In previous studies [Zimmerman et al. 1998] it was shown that deuterium is mostly trapped in the SiO₂ rather than in the Si layer and it was suggested that when annealing in hydrogen at high temperature strained bonds can be broken by hydrogen interaction, resulting in stable OH centres.

In the present investigation we use Thermal Desorption Spectroscopy (TDS) in combination with annealing in deuterium gas and ion implantation to study SIMOX samples. This approach provides quantitative information on the hydrogen trapping sites and permits one to establish the transport paths and mechanisms of the released deuterium.

5.2. Experimental

As extensively discussed in Chapter 3, TDS allowed quantifying the rate of gas release produced by thermally activated desorption of deuterium from trapping sites when the temperature increase is linear with time (typical heating rate 1-6 K/s). HD and D₂ were monitored simultaneously. Single implant SIMOX wafers from IBIS manufacturer with a 190 nm top Si layer and a 360 nm buried oxide (BOX) layer were used in this study. Details on sample treatment and desorption experiments are given in Table 5.1.

The top Si layer of samples 1 and 2 was removed in KOH prior to further treatment. Sample 1 was then annealed in high purity deuterium under a pressure of 500 kPa and a temperature of 1073 K for 2.5 h. Subsequently, it was cooled down in the same deuterium pressure. Sample 2 was implanted *in situ* in the TDS setup with deuterium ions. The implantation energy was 1.5 keV. The doses are indicated in Table 5.1. A TDS measurement was performed after every implantation step. The sample was also implanted with 5.6×10^{14} cm⁻² D⁺ ions while kept at 500, 600 or 700 K.

Sample 3 was annealed in D₂ and subsequently measured by means of TDS with a top Si layer.

Table 5.1. Description of the samples employed in this chapter, the treatments applied and the TDS experiments performed. Please, note that the presence or absence of a top layer prior to a certain treatment or experiment is indicated.

Sample	Treatment			TDS experiments	
	Size (mm ²)	Top layer	Description	Top layer	Remarks
1	5×10	No	-Annealing: 500 kPa D ₂ , 2.5 h at 1073 K, cool down in D ₂	No	Cut into 2×2 mm ² pieces from implanted sample + TDS
2	5×10	No	-Implantation: 1.5 keV D ⁺ , doses 3.2, 5.6, 10.0×10 ¹⁴ cm ⁻² . -Implantation: 1.5 keV D ⁺ , dose 5.6×10 ¹⁴ D ⁺ cm ⁻² also performed while keeping the sample at 500, 600 and 700 K	No	Same 5×10 mm ² sample for implantation + TDS
3	5×10	Yes	-Exposure: 300 kPa D ₂ , 2.5 h at 1073 K, cooled down in D ₂	Yes	Cut into 2×2 mm ² pieces from annealed sample + TDS

5.3. TDS results on samples with top Si layer removed

5.3.1. Annealing in deuterium gas

The results of TDS experiments on sample 1 are shown in Fig. 5.1. Different peaks (labelled P1-P4) were observed. A first order desorption model was applied to fit the data. Peaks P2 and P3 could not be resolved independently and are considered as one single peak. Attempt frequencies (ν) were allowed to vary between 10¹²-10¹³ s⁻¹. From this we obtained the activation energies $E_a=1.8$ eV for peak P1, $E_a=2.3-2.5$ eV for P2-P3 and $E_a=3.4$ eV for P4.

In agreement with [Myers et al. 1990] (see Section 5.1), peak P4 can be attributed to the dissociation of Si-OD and peak P2-P3 to the dissociation of different Si-D bonds. No clear assignment can be made for Peak P1. It is probably related to weakly bound deuterium.

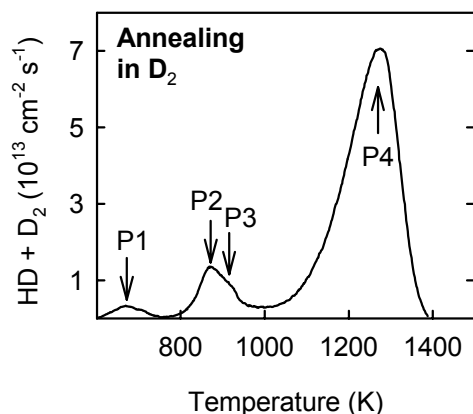


Fig. 5.1. TDS desorption spectra from SIMOX sample 1 annealed in D₂ gas without top layer,

Peaks P2 and P3 correspond to similar defects with similar dissociation energies and are most likely related to deuterium trapping at different Si• dangling bond configurations. These can be different E' type defects or P_b configurations. Stresses at the interfaces may lead to a spread in the dissociation and passivation energies for P_b defects [Stesmans 2000b]. A similar effect in the stressed buried oxide [Revesz et al. 1997] may lead to a spread in the dissociation energy of P2-P3. It is worth noting that a more complicated release model is needed to describe peak P2, which is the only peak that deviates from first order behaviour in some cases.

5.3.2. Ion implantation

TDS results obtained for samples implanted with deuterium ions are shown in Fig. 5.2a and Fig. 5.2b. The first graph panel (a) corresponds to implantations at room temperature, panel (b) to implantations at the indicated temperatures. Unlike the case of sample 1 (Fig. 5.1) the dominant peak corresponding to room temperature implantation of sample 2 (Fig. 5.2a) is P2-P3. The contribution of peak P4 is negligible. P4 only appears dominant when deuterium implantation is performed at a significantly higher temperature (Fig. 5.2b). On the basis of the discussion in Section 5.3.1, one might conclude that deuterium implantation leads only to the creation of Si-D groups, since these groups were ascribed to peak P2-P3. However, this interpretation is not plausible because both Si-O and Si• traps are created as well by ion implantation and they are expected to be effective traps for deuterium. In fact, experimental evidence obtained by infra-red studies has demonstrated in different SiO₂ structures that OD (or OH) groups are formed after implantation, see e.g. [Arnold et al. 1982].

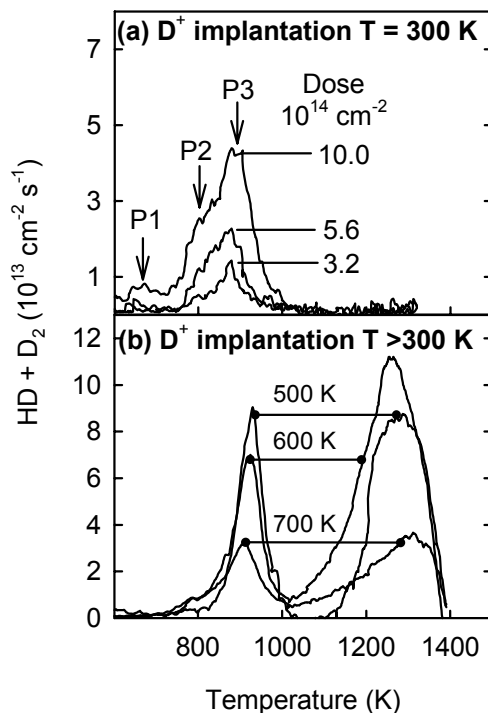


Fig. 5.2. (a) TDS desorption spectra from sample 2, a bare SIMOX sample subjected to implantation series at indicated doses, (b) same sample implanted at the indicated temperature with 5.6×10^{14} D⁺ cm⁻².

Since the doses introduced in the sample by ion implantation equal the amount of deuterium released in every TDS cycle, one might conclude that OD groups dissociate at the same time as Si-D groups. However, it was concluded above that OD groups are more stable than Si-D [Myers et al. 1990, Revesz 1979]. Therefore, there must be a process facilitating the release of deuterium from stable OD groups. This process is the production of atomic deuterium in the sample during the dissociation of the Si-D groups. In turn, the produced atomic deuterium can interact with OD groups liberating deuterium.

The implantation at high temperature leads to a desorbed quantity significantly larger than the implanted dose. This is due to the uptake of deuterium from the background during ion implantation at elevated temperature. For comparison, the samples were exposed to deuterium gas at the temperature and pressure employed during the same time (results not shown). These experiments showed that a certain amount of deuterium became trapped in the sample and that was released via peaks P2-P3 and P4. However, the amount was by far much smaller than the amount of deuterium introduced by ion implantation, $5.6 \times 10^{14} \text{ D}^+ \text{ cm}^{-2}$.

The quantity desorbed from the sample after implantation of $5.6 \times 10^{14} \text{ D}^+ \text{ cm}^{-2}$ at elevated temperature is inversely proportional to the implantation temperature. The appearance of peak P4 indicates the dissociation of OD groups and suggests that atomic deuterium is not produced during the dissociation of Si-D groups in high concentrations. This is probably due to the reduction of cracking sites by the high temperature employed during the ion implantation experiments.

5.3.3. Discussion

Deuterium is trapped forming Si-D and Si-OD groups, the latter being more stable. The following reactions could be considered to govern the deuterium release



However, they can not explain the TDS measurements for samples implanted with deuterium at room temperature because these measurements do not show the release peak P4, which would be associated with (5.2). In addition, ab initio calculations [Vitiello et al. 2000] indicate that these reactions can only occur at very high temperatures. Instead, we consider the interaction of dissolved molecular hydrogen (H_2 , HD or D_2) with Si-D and Si-OD. In this way the release of deuterium from Si-D groups giving $\text{O}_3\equiv\text{Si}\cdot$, follows the reaction sequence



where ΔH indicates the activation energy of the reaction. The activation energy of Reaction (5.4) is in principle not known (indicated by X). Note that in (5.3) D_2 is assumed to be the

dissolved molecular species. The molecular species could also be any other molecular species, i.e. H₂ or HD.

Similarly, the following equations can be written for the case of Si-OD dissociation giving Si-O• groups



The global reactions can be written from (5.3)-(5.5) and (5.6)-(5.8) for both types of defects (Si• and Si-O•), as



respectively, where the activation energy of Reaction (5.9), $H_{Si-D} = 2.3-2.5 \text{ eV}$ and the activation energy of Reaction (5.10), $H_{O-D} = 3.4 \text{ eV}$ are the experimental values obtained in TDS experiments under the assumption of first order kinetics. The validity of this assumption relies on the fact that the concentration of dissolved species (mainly H₂) is more or less constant, which implies that the kinetics is governed by the concentration of Si-D and Si-OD groups. Making use of these values, the factors X and Y in Reactions (5.4) and (5.7), respectively, can be calculated. One obtains $X = 4.4-4.6 \text{ eV}$ and $Y = 5.5 \text{ eV}$. These values are in fair agreement with ab-initio calculations [Vitiello et al. 2000], who reported 4.42 eV and 5.25 eV for Reactions (5.4) and (5.7), respectively.

Fig. 5.3 shows a diagram of the total energy of deuterium in the SiO₂ system. It schematically shows the difference between the barriers to the release of atomic deuterium from Si-D or Si-OD groups (4.6 and 5.5 eV respectively) and the barriers to the release of molecular deuterium (2.5 and 3.4 eV). It appears that the release of molecular species is much more favourable than the direct dissociation of the Si-D and Si-OD groups giving atomic deuterium.

The molecular hydrogen (H₂, HD or D₂) obtained from Reactions (5.9) and (5.10) can escape from the sample, to be detected by TDS. It can also help to liberate bound deuterium by means of Reactions (5.9) and (5.10), or interact with the Si• and Si-O• defects generated leading to a passivation effect by means of the following passivation reactions



In the case of ion implantation, the number of dangling bonds (Si• and O•) is very significant. They act as D₂ cracking centres according to Reactions (5.11) and (5.12). Reaction (5.11) is very important when the concentration D₂ becomes significant. This occurs during the dissociation of the Si-D groups at around 900 K. The D₂ molecules released will then

undergo an important retrapping process by means of (5.11), producing atomic D which is very reactive. This species is able to dissociate OD bonds at this temperature by means of the inverse of (5.12). This explains why TDS measurements on deuterium-implanted samples do not show the high temperature peak P4.

During the implantation at elevated temperature, a significant number of dangling bonds become passivated by deuterium. This explains why the accumulated dose is significantly higher than the implanted dose. This effect strongly reduces the number of remaining dangling bonds, which disables Reactions (5.11) and (5.12). As a consequence, the concentration of atomic D is not high enough to suppress peak P4. On the other hand, the accumulated dose decreases with increasing implantation temperature. This can only be explained by accepting that the number of generated displaced atoms that survive recombination is larger at lower temperature.

A sample originally containing Si-H and Si-OH groups and annealed in D_2 will exchange the hydrogen present in these groups by deuterium, by means of the set of Reactions (5.3)-(5.12). This scheme is basically a hydrogen isotope exchange that occurs at elevated temperature or when a significant number of cracking centres is present [Shelby 1980, Shelby et al. 1979].

In all these processes foreign hydrogen, coming from other layers or from the background, plays an important role because it takes part in these reactions. This is similar to the role of foreign hydrogen observed in Chapter 4 during hole injection. In fact, it was observed that a significant fraction of the released deuterium occurs in the form of HD.

Prolonged annealing in deuterium gas leads to the appearance of OD groups at high temperature, when (5.9) is in equilibrium leading to the generation of $Si\cdot$ groups that take part in (5.11) producing atomic D. In the case of SIMOX, the number of such OD groups produced by annealing was found to be much larger than the initial concentration of intrinsic OH groups [Myers et al. 1993, Zimmerman et al. 1998]. It has been proposed that stressed Si-O-Si bonds are ruptured by interaction with deuterium generating $Si-O\cdot$ centres [Revesz et al. 1997], which interact with the abundant D_2 species producing the OD groups.

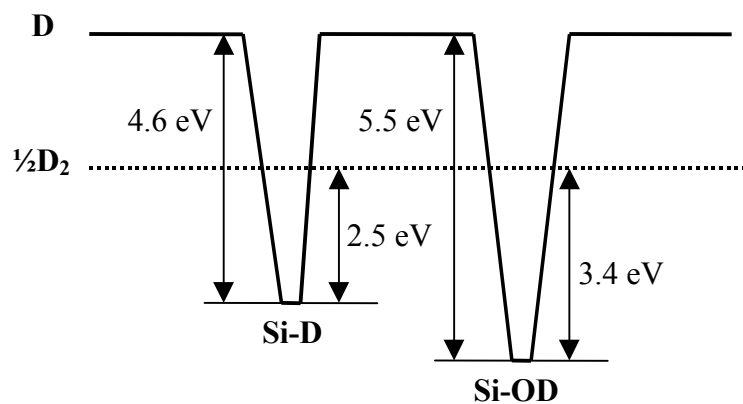


Fig. 5.3. Diagram of the total energy of a deuterium atom in interaction with SiO_2 . Two trapping sites Si-D and Si-OD are shown. $\frac{1}{2} D_2$ denotes D bound to in the molecule D_2 .

5.4. The effect of the top Si layer

Two release paths are possible: (i) through the lateral BOX surfaces and (ii) through the top Si layer. (i) is similar to the release in samples with the top layer removed but is much slower due to the long average distance to the lateral BOX surfaces (of the order of mm). The release through lateral surfaces during TDS experiments is a diffusion-limited process. (ii) is only possible if D_2 molecules dissociate at the top-Si/SiO₂ interface (D_2 cracking) before entering the top Si layer. After permeating through the top Si layer they will recombine at the Si surface before escaping into vacuum. Recombination at the surface is an easy process whereas cracking at the Si/SiO₂ interface is limited by the number of accessible cracking sites, mostly P_b centres [Stesmans 2000]. Therefore, the release through the surface is an interface and permeation-limited process. The barrier effect caused by the top layer is expected to introduce a considerable delay in the desorption peaks. Using data on the D_2 cracking rate at the interface [Stesmans 2000], permeation through the top Si layer [Myers et al. 1993] and diffusion in SiO₂ [Griscom 1985], we conclude that release path (i) is faster than (ii) at low temperature. (i) and (ii) become comparable at temperatures higher than 1300 K.

By means of TDS experiments on samples with a top Si layer we can monitor both release paths. D atoms travelling through the top Si layer will finally be released into vacuum when they form mostly HD molecules with H atoms, which are abundant at the Si surface due to the hydrogen background of the vacuum system. On the other hand, deuterium travels through the oxide mainly in the molecular state. When such a molecule reaches the lateral surface of the oxide it can simply escape to vacuum as D_2 without any further interaction. Thus, the HD signal is predominantly related to gas released through the top Si layer, whereas the D_2 signal is related to release via the lateral BOX surfaces.

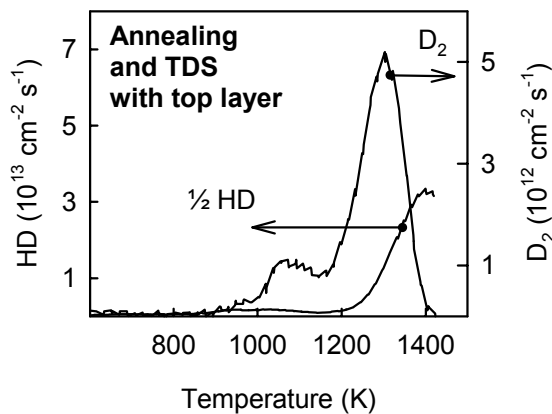


Fig. 5.4. TDS from sample 3, exposed to D_2 and subjected to TDS with top layer

Fig. 5.4 shows the HD and D_2 desorption curves for sample 3. This sample can be compared with sample 1, which was treated in a similar way but without top layer. According to the expectations the HD peak observed at high temperature and corresponding to P4 is shifted, indicating that release through Si is only important at temperatures higher than 1300 K. In addition, a small peak is observed in the D_2 spectrum around 1100 K, which corresponds to peak P2-P3 observed in Fig. 5.1 at 900 K. This delay is due to the large

average distance for diffusion to the lateral BOX surface (in the order of mm). Finally HD and D₂ peaks appear shifted with respect to each other, indicating that both HD and D₂ spectra are related to different release mechanisms. This is only observed for TDS on samples with a top layer.

5.5. Conclusions

TDS can be used to characterise the release of deuterium from SIMOX samples annealed in deuterium gas or implanted with deuterium ions. The most stable defects are Si-D bonds and Si-OD bonds with dissociation energies of 2.3 to 2.5 eV and 3.4 eV, respectively.

The mechanisms of uptake and release are related to the concentration of deuterium in the oxide. In this sense, a high concentration of atomic deuterium is obtained when a sufficient number of cracking centres is present in the sample, i.e. after ion implantation experiments. This high concentration results in the dissociation of trapped deuterium via the formation of molecular species. In this case all the trapped deuterium dissociates at the temperature of peak P2-P3.

TDS experiments on samples with a top layer show that the desorption of deuterium from the buried oxide can no longer be described by a first order model because it is limited by diffusion along the oxide, D₂-cracking at the Si/SiO₂ interface and permeation through the top Si layer. Release through the top Si layer is associated with the HD signal; release via the lateral BOX surfaces with the D₂ signal. This phenomenon can be used to distinguish diffusion and permeation processes through the oxide and the silicon top layer, which makes the method of considerable practical use.

Chapter 6

Defect generation and annealing

Positron techniques are based on the tendency of positrons to be trapped at certain defects. In particular, open volume and negatively charged defects act as very effective positron traps. Once trapped, positrons annihilate with surrounding electrons yielding specific signatures of the chemical environment. Treatments commonly used in the semiconductor industry lead to the generation of defects which can be properly monitored by positron techniques. Common treatments are annealing in a hydrogen-containing ambient, ion implantation and exposure to ionising radiation. Annealing is often employed, e.g. for post-metallisation treatments, diffusion of impurities or activation of dopants. Ion implantation is the basis of Unibond samples created by the SmartCut method. In this method, hydrogen ions are implanted through an oxide layer to reach the underlying c-Si layer. Finally, ionising radiation is employed in photolithography and is usually present during dry plasma etching. An immediate effect of radiation exposure is the generation of charge carriers in the samples. In addition, devices operating in hostile environments such as those found in satellites in space are continuously exposed to ionising radiation.

The first section of this chapter is dedicated to the study of the crystalline top silicon layer of SOI structures. By means of positron techniques we shall show that the top silicon layer of SIMOX, in contrast to Unibond materials, contains a significant number of oxygen-related defects. The second section treats the generation and annealing of defects in SiO₂ by annealing in deuterium gas, electron-hole injection and ion implantation. The defects associated with the different treatments will be discussed.

6.1. The top silicon layer of SOI structures

Oxygen is considered to be one of the most important impurities in silicon. Its presence may affect the performance of integrated circuits. It is well known for its beneficial role as a sink for metallic impurities when it appears in non-active regions. On the other hand, clusters of point defects associated with oxygen precipitates, present in electronically active regions, may change the electrical properties of the circuits. Furthermore, the presence of oxygen during thermal treatments can induce effects such as the growth or retrogrowth of stacking faults, the generation of thermal donors or the creation of oxygen precipitates (see e.g. Chapter 3 in [Barbottin et al. 1991]).

In transistors fabricated from SOI (silicon on insulator) materials the silicon top layer acts as the electrically active region. When this layer is very thin, it becomes completely depleted during the transistor operation. Hence, the concentration of impurities in this layer should be well controlled during the manufacturing of integrated circuits to obtain the required electrical characteristics. In the separation by implantation with oxygen (SIMOX) structures a buried oxide (BOX) layer is synthesised by the implantation of oxygen ions into a silicon substrate at elevated temperature, followed by an annealing at high temperature (~ 1570 K) in an inert atmosphere containing $\sim 1\%$ oxygen (see Chapter 1). The fabrication of Unibond SOI samples requires prolonged annealing at high temperature (Section 3.1). Under these extreme conditions a very good control of the point defects and contaminants like oxygen becomes crucial to fulfil the strict requirements of the device manufacturers. For instance, it has been suggested [Ericsson et al. 1997] that the concentration of atomic oxygen present in the SIMOX top layer acts as an important rate limiting mechanism for the BOX growth and defect annealing during the fabrication of low-dose SIMOX.

Our aim is to perform positron studies to characterise the electrically active region of SOI samples. The use of positron beams to analyse SOI structures has shown to be very valuable for the study of point defects, especially vacancy-like defects. Doppler broadening of annihilation radiation (DBAR) measurements have given direct evidence of the existence of oxygen-related defects in the SIMOX top layer in such a low concentration that they escaped detection by TEM [Fujinami 1996].

In order to follow the behaviour of these defects in SIMOX samples, annealing experiments were carried out in vacuum, a deuterium gas ambient or an inert gas ambient (argon). Some of the samples were exposed to deuterium plasma at room temperature. The evolution of these defects during the thermal treatments and their interaction with deuterium will be discussed. We shall also show the remarkable result that Unibond samples do not contain these oxygen-related defects.

6.1.1. Sample description

Two Unibond samples are used with specifications as follows: The first sample consisted of a $1.2\ \mu\text{m}$ Float Zone (FZ) Si top layer on a $1.0\text{-}\mu\text{m}$ thick BOX layer. The second sample consisted of a $1.2\text{-}\mu\text{m}$ thick Czochralski (Cz) Si top layer on a $3.0\text{-}\mu\text{m}$ thick BOX layer.

The SIMOX samples used in our experiments come from commercial IBIS wafers, single implant in p-substrate. The top silicon layer had a thickness of 190 nm and the BOX

360 nm. All samples were analysed by Doppler broadening of annihilation radiation (DBAR) measurements. Prior to the positron analysis, the samples received a chemical etch in diluted HF (1%) in order to remove the native oxide film formed on top of the SIMOX structure by exposure to air. Some of the samples were analysed by means of SIMS in order to determine the amount of deuterium in the top layer after the deuterium exposure experiments. The different sets of samples were given the following treatments:

1. Exposure to pure deuterium or argon inside a steel tube furnace for 150 min. Pressures were varied from 75 to 1000 kPa and temperatures from 870 to 1070 K. It should be noted that the argon ambient contained about 1% H₂.
2. Exposure to a deuterium plasma produced by a constricted plasma source [Anders et al. 1998].
3. Vacuum anneal (about 10⁻⁴ Pa) of sets 1, 2 and reference samples at different temperatures. These treatments were carried out in situ in the positron beam apparatus.

6.1.2. Results and discussion

The top Si layer of Unibond samples

First of all, the results of Unibond samples are described. The positron energy is related to the mean implantation depth of positrons (see Section 3.3). This provides a depth sensitive analysis of the samples by plotting the S and W annihilation parameters as a function of the positron implantation energy, as shown in Fig. 6.1. By convenience these parameters are normalised to the bulk crystalline Si ones ($S_{c-Si} = 0.578$ and $W_{c-Si} = 0.032$). The vertical line represents the boundary between the top Si layer and the BOX. We can distinguish the first two layers of the Unibond samples: the top Si and the BOX layer. For the sample containing the 1 μm -thick BOX, the Si substrate can also be distinguished at high positron energy. The native oxide was not removed from the surface of the samples; for this reason the S surface value is low and the W surface value high compared to the Si substrate. In the top Si layer the normalised S and W parameters approach unity, the value expected for c-Si. However, the S parameter of the Cz-Si top layer is slightly lower than 1. Values of S lower than 1 were observed for Cz-Si samples [Dannefaer et al. 1986] and indicate the presence of oxygen-related defects that supply high momentum electrons causing the low S values (see Section 3.3). In our case the reduction of S is not as pronounced as that presented in [Dannefaer et al. 1986] indicating that in any case the concentration of oxygen-related defects is rather low. In contrast, the results of positron analysis of the SIMOX samples show drastic changes in the top layer associated with the presence of oxygen.

Oxygen-related defects in the top Si layer of SIMOX; passivation effect by hydrogen

Fig. 6.2 shows the annihilation parameters S and W versus the positron energy for SIMOX samples after receiving different treatments: (a) SIMOX sample as-received, (b) SIMOX sample exposed to deuterium plasma, (c) SIMOX samples annealed in D₂ or in Ar (with ~1% H₂) under different conditions (870 to 1070 K, 75 to 1000 kPa). The S and W parameters of

the samples are confined to the band formed by the curves with the error bars (c). The vertical lines represent the boundaries between adjacent layers. In the case of SIMOX as-received, both the interfaces between the top layer and the BOX and the interface between the BOX layer and the substrate, can be clearly observed by the change in the S and W parameters. The S and W values for the top Si layer and the bulk Si layer differ considerably. S and W have the typical values for pure Si in the third layer, the Si substrate. In the top layer the S value is much lower (about 8%) than in the substrate and the W value is much higher (about 50%). This simple observation suggests that the annihilations in the top layer take place with electrons carrying a higher momentum than the electrons annihilating in the bulk Si. This means that there are impurities in the top layer located close to the trapping sites for positrons that supply high momentum electrons. Since oxygen is the most prevalent impurity during the fabrication of SIMOX, it seems logical to assume that the high momentum electrons are associated with oxygen. This leads to the explanation that many of the positrons implanted in the top Si layer are trapped in oxygen-related sites where they can annihilate with high momentum electrons. Previous positron and infrared studies [Fujinami 1996, Dannefaer et al. 1990, Lee et al. 1976, Ikari 1995, Kawasuso et al. 1995] support this explanation.

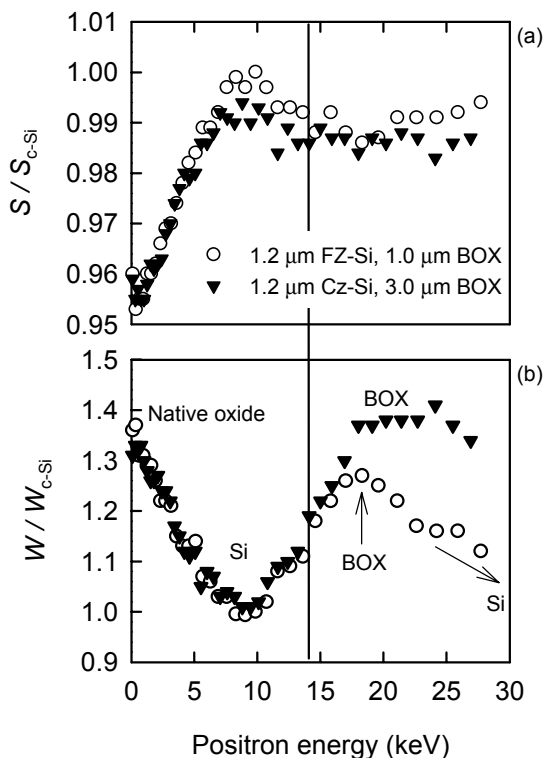


Fig. 6.1. S and W positron annihilation parameters versus positron energy (depth) for the Unibond samples indicated in the legend. The vertical line represents the boundary between the top Si layer and the BOX. The different annihilation states, surface, top Si, BOX and Si substrate, can be distinguished (the latter only for the sample with a thin BOX).

The S - E and W - E curves (Fig. 6.2), where E represents the positron implantation energy, have been fitted with the aid of VEPFIT [van Veen et al. 1990], see also Section 3.3. For the fit, a layered structure was considered. Three layers, two interfaces and the surface were used as possible positron annihilation regions. The fitting program determines the S - W values and the effective diffusion length for positrons $L_{+,eff}$ for each layer and each interface.

The different contributions can more easily be identified in the S - W plots of Fig. 6.3. Fig. 6.3a shows S - W parameters for SIMOX as received. The points obtained for increasing positron energy (depth) start at the surface state and run toward the region of oxygen-related defects in silicon, bend over to a point attributed to the BOX and finally end at the value of bulk Si. The effect of the interfaces is not as clear as the contribution by the different layers. The curvature in between the layers, suggests the existence of trapping at the interfaces (the interface S - W coordinates are located close to the surface coordinates, see Chapter 7).

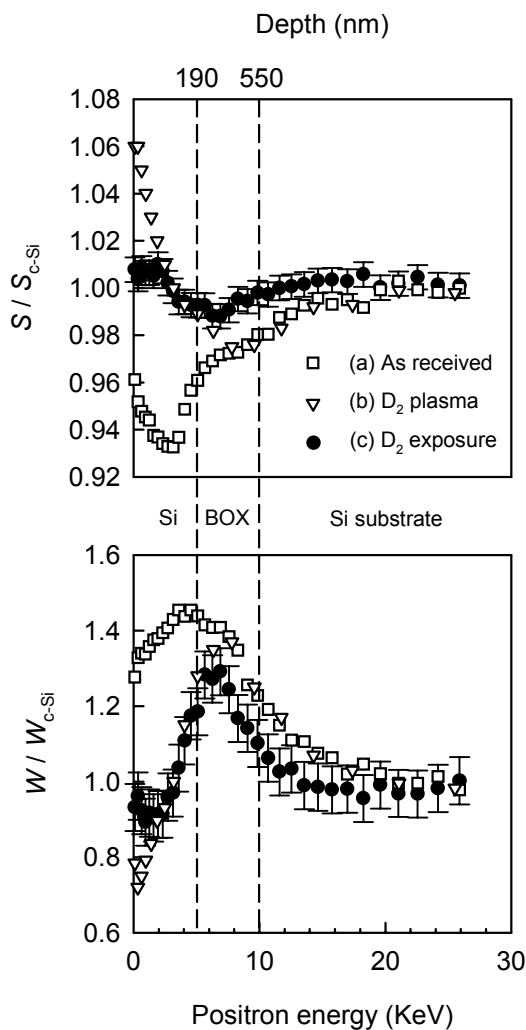


Fig. 6.2. S and W positron annihilation parameters for SIMOX versus the positron energy (depth). The vertical lines are a guide to distinguish the 3 layers of SIMOX. (a) corresponds to SIMOX as received, (b) to SIMOX exposed to deuterium plasma. The band delimited by the error bars (c) corresponds to a number of samples exposed in the furnace to D_2 or Ar under different conditions.

Some samples were annealed for 150 min at temperatures from 870 to 1070 K in argon or deuterium ambients in the tube furnace (Fig. 6.2). The top layer and the Si substrate show similar annihilation parameters after the annealing treatments. The S - W map (Fig. 6.3c) shows the curve starting at the surface S and W coordinates. From that point it reaches directly the Si coordinates (positrons annihilating in the top layer). Then, it runs towards the BOX coordinates and finally returns to the Si point (positrons annihilating in the substrate). It is evident that a long-term annealing in the furnace tube induces an important change in the annihilation parameters of the top layer.

In addition we have studied the effect of introducing deuterium in the samples at low temperature. In order to introduce deuterium species in the samples at room temperature, we have exposed some samples to a deuterium plasma [Anders et al. 1998]. Since the plasma source generates different species (not only charged ones) it is difficult to estimate exactly the amount of deuterium introduced into the samples. The effect of the exposure can be seen in Fig. 6.2. The annihilation parameters change drastically at the surface. We can attribute these changes to damage created by the plasma in the near surface region. The S - W map on Fig. 6.3b shows clearly how the S - W cluster point for the top layer changes by effect of the exposure to the plasma. After the exposure the S - W coordinates for the top layer have values close to those for bulk Si, as it was found for the high temperature deuterium treatments of Fig. 6.3c.

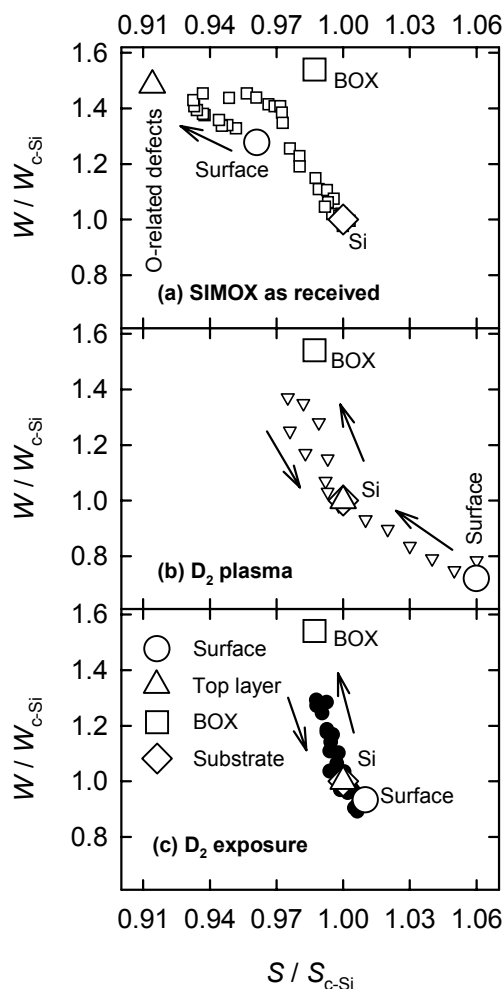


Fig. 6.3. S - W plots with the positron energy as the running parameter for (a) SIMOX as received, (b) SIMOX exposed to deuterium plasma, (c) SIMOX exposed to 5 bar D_2 for 150 min at 1070 K. Fitted values are indicated for every layer.

It is evident that the introduction of deuterium causes a very significant modification of the defects in the top layer. The result suggests that deuterium is able to passivate the oxygen-related defects suppressing the annihilation of positrons with high momentum electrons. Deuterium acts as a passivating agent when the samples are annealed in a deuterium ambient or exposed to deuterium plasma. In the case of exposure to Ar, the passivating agent is the

estimated 1% H₂ contribution to the background gas. This indicates that a low concentration of hydrogen species is sufficient to get the passivation effect. We discard the possibility that the oxygen-related defects dissociate during the annealing treatments because these defects survived much higher temperatures during the fabrication process (Section 3.1). Previously, it was reported by [Kawasuso et al. 1995] that oxygen-related defects that survive high temperature annealing are multi-vacancy- multi-oxygen complexes (V_xO_y, where x, y > 2). SIMS measurements on a sample exposed to 300 kPa D₂ at 1070 K for 150 min showed that the concentration of deuterium in the top layer was below the sensitivity limit, about 10¹⁷ D cm⁻³. This imposes an upper limit for the concentration of oxygen-related defects in the top Si layer and supports the idea that a small amount of hydrogen is sufficient for full passivation. Probably only one D atom is necessary per oxygen-related defect to reach passivation. This would lead us to an upper limit of 10¹⁷ cm⁻³ defect concentration.

The concentration of defects can be further quantified by means of the effective diffusion length for the top Si layer of an untreated sample, $L_{+,eff} = 50$ nm, obtained by VEPFIT fits. The calculations require some assumptions about the specific trapping rate for positrons in the defects present in every layer (Section 3.3). Taking into account the upper limit for the concentration of defects in the top layer just estimated, the specific trapping rate for positrons must be higher than 10¹⁶ s⁻¹. According to previous work [Hautojärvi et al. 1995] this high value for the specific positron trapping rate at one defect indicates that the defect is negatively charged. Therefore, we must assume that a significant fraction of the oxygen-related defects is negatively charged.

Effect of thermal annealing on the oxygen-related defects

Fig. 6.4 shows the effect of isochronal vacuum annealing steps of 15 min (a) on a non-treated sample and (b) on a sample annealed in deuterium in the tube furnace. The post-exposure vacuum annealing was performed in the positron beam apparatus under a pressure lower than 1×10⁻⁴ Pa. The annihilation spectra were recorded at room temperature after each step. The squares in Fig. 6.4 represent the top layer coordinates in the *S-W* map. They are labelled with numbers that identify the temperature at which the sample was annealed before the positron annihilation experiment.

In Fig. 6.4 it is observed that the cluster points for the top layer are lying on a line, connecting the coordinates found for the oxygen-related defects in the as-received samples and the bulk Si coordinates. This indicates that the annihilations in the top Si layer come from two states: either from positrons trapped at oxygen-related defects or from free positrons in the top Si layer. These annihilation states correspond to the endpoints of the dotted lines in Fig. 6.4. The fraction of positrons trapped at the oxygen-related defects depends on the thermal treatment.

After the annealing step of the reference sample at 670 K in vacuum, see Fig. 6.4a, the coordinates for the top layer reach a value close to those for c-Si. Further annealing moves these coordinates towards the coordinates for the top layer in an as-received sample. Beyond 870 K the trend is reversed and the coordinates move towards the cluster point corresponding to bulk Si. The sample exposed to deuterium (Fig. 6.4b) shows a similar behaviour. Post-exposure annealing up to 870 K leads to a movement in the coordinates of the top Si layer

toward the cluster point found for the untreated sample. Further annealing causes the process to reverse, reaching the bulk Si cluster point at 1170 K. Upon repetition of the cycle shown in Fig. 6.4b the same cycling results were obtained. Thus, there is no release of hydrogen, else the second cycle should have given different results.

The complex behaviour shown in Fig. 6.4 does not follow a simple passivation-depassivation scheme. The negatively charged oxygen-related defects associated with the low S value in the top layer are not expected to conserve their charge state after the thermal annealing steps. A change in the negative charge state leads to a considerable decrease in the positron trapping cross-section for the defects. This means that the fraction of positrons trapped (and annihilated) in these defects reduces considerably when the defects are neutral and becomes even negligible for positively charged defects. We can speculatively relate the observed effects to the activation and deactivation of oxygen donors at different temperatures [Pearton et al. 1986]. In any case, we should keep in mind that hydrogen could also play an important role in the change in charge state of oxygen-related defects as supported by first-principles calculations in [Rashkeev et al. 2001].

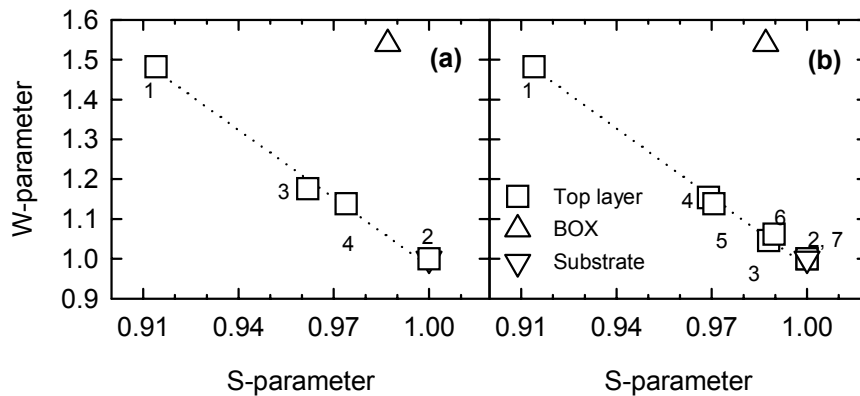


Fig. 6.4. S - W plots for isochronal annealing experiments in vacuum (10^{-4} Pa) for periods of 15 min. (a) For a SIMOX sample as received. The labelled coordinates represent (1) the top layer of the sample as-received, (2) after 670 K, (3) after 870 K and (4) after 1070 K. (b) For a SIMOX sample in the furnace for 150 min at 1070 K and 300 kPa D_2 . The labelled coordinates represent (1) the top layer of a sample as received, (2) after the exposure to deuterium in the furnace, (3) after 670 K, (4) after 870 K, (5) after 970 K, (6) after 1070 K and (7) after 1170 K.

6.1.3. Conclusions

Positron measurements have been shown to be a valuable technique for monitoring oxygen-related defects in the top Si layer of SIMOX. The defects escape detection by TEM. According to the fitting results, the defects found in the top layer are in a negatively charged state; for this reason they are very effective traps for positrons.

The exposure to deuterium or argon (containing hydrogen) leads to positron annihilation parameters in the top layer nearly equal to those of pure silicon. A similar effect was observed by exposure to deuterium plasma. A small amount of hydrogen gas was found to be sufficient

to perform the passivation process. The background gas of our tube furnace appears to contain enough hydrogen to complete the passivation. SIMS measurements on samples exposed to deuterium confirm the presence of a low concentration of deuterium in the top layer ($<10^{17}$ cm⁻³).

From annealing experiments in vacuum, it was observed that the oxygen-related defects do not diffuse out and do not release trapped hydrogen, but are modified in such a way that the positron trapping at these defects is reduced. It is suggested that these changes represent variations in the charge state of the defects induced at different temperatures by the thermal treatments.

6.2. Defect generation and annealing in SiO₂

In this section, we show how we can extract interesting information on defects in a variety of SiO₂ structures by means of positron studies. Chapter 4 was devoted to the effects created by hole injection and the interaction with hydrogen. In particular, it was shown that, despite traditional belief [Lenahan et al. 1984], the Si dangling bonds (probably E' centres) generated upon hole injection act as positron traps. Another, more effective, positron trap is observed after electron injection, see Chapter 8 in [Clement 1998]. It is related to a negatively charged defect associated with an oxygen atom. In addition, positronium (Ps) plays a major role in positron studies of amorphous SiO₂. It is formed in large amounts in SiO₂ [Uedono et al. 1994, Dannefaer et al. 1993]. Small changes in the Ps fraction will lead to important differences in the measurement results.

Different types of samples were subjected to electron-hole injection, deuterium and helium ion implantation and thermal annealing in vacuum and in deuterium under different conditions of pressure and temperature. These treatments allow the study of SiO₂ structures containing different defects and provide a comprehensive picture containing valuable fundamental information on the defects.

6.2.1. Sample description

We employed fused quartz, Unibond and SIMOX samples. In order to introduce different types of defects at different concentrations, the samples received different treatments as summarised in Table 6.1. As an aid to the reader, labels were assigned to sample types and treatments in such a way that every sample is identified by a combination of such labels.

- Fused quartz samples (type Q) were implanted with 30 keV D⁺ ions (treatment D30) reaching doses of (a) 2×10^{14} , (b) 1×10^{15} and (c) 1×10^{16} cm⁻². Sample Q-D30-b underwent post-implantation vacuum annealing steps of 15 min at 570, 840 and 1090 K. Other Q samples were implanted with 30 keV ⁴He⁺ ions (treatment He30) attaining doses of (a) 3×10^{14} and (b) 1×10^{15} cm⁻². Sample Q-He30-a was subjected to post-implantation vacuum annealing steps of 15 min at 470, 670, 820 and 970 K.
- SIMOX samples (type S) with a 190 nm-thick top n-Si layer on a 360 nm buried oxide (BOX) on p-Si substrate were implanted with 20 keV D⁺ ions (treatment D20) attaining doses of (a) 2×10^{14} , (b) 2×10^{15} and (c) 2×10^{16} cm⁻². SIMS was performed on sample S-

D20-b in order to determine the deuterium profile after implantation. Other S samples were implanted with 30 keV D^+ ions (treatment D30) at doses of 1×10^{14} , 2×10^{15} and $1 \times 10^{16} \text{ cm}^{-2}$. After removing the top Si layer, sample S-D30-b underwent post-implantation vacuum annealing steps of 15 min at 470, 670, 820 and 970 K.

- Unibond samples with 1 μm thick BOX layers were employed to fabricate MOS capacitors (type Ua). After removing the top Si layer in KOH, a 15 nm thick Al gate was deposited on the bare BOX layer. 30 keV He^+ ion implantation through the gate (treatment He30) was performed at a dose of $1 \times 10^{16} \text{ cm}^{-2}$. Subsequently, sample Ua-He30 went through isochronal vacuum annealing steps of 15 min at 470, 570, 670 and 770 K.
- Unibond samples with 3 μm thick BOX layers were employed to fabricate MOS capacitors (type Ub). After removing the top Si layer in KOH, a VUV semi-transparent, 15 nm thick Al gate was deposited on the bare BOX layer. The sample was illuminated with VUV light (10 eV). Holes were injected in the oxide by applying positive gate voltages on the gate leading to oxide fields of 1 MV/cm and 2 MV/cm (treatments H1 and H2, respectively). The highest injected hole doses were $2.5 \times 10^{15} \text{ holes cm}^{-2}$, for treatment H1 and $0.6 \times 10^{15} \text{ holes cm}^{-2}$ for treatment H2.
- For comparison we include experiments performed in our research unit (see Chapter 8 in [Clement 1998]) on MOS capacitors fabricated with wet thermal oxides with 1 μm thick oxide layers grown on n-Si substrates (type T). These samples were subjected to low-energy electron injection (treatment E) leading to accumulated negative charge densities of 0.5, 1.0, 3.5 and $6.0 \times 10^{12} \text{ electrons cm}^{-2}$.

All the samples mentioned above were studied by Doppler broadening of annihilation radiation (DBAR) measurements with a positron beam. The DBAR setup allowed performing the vacuum ($<10^{-4} \text{ Pa}$) annealing treatments mentioned above in situ, avoiding sample exposure to air between annealing steps. In order to estimate the Ps fraction, we performed positron lifetime measurements on fused quartz samples (type Q) and two-dimensional correlation of annihilation radiation (2D-ACAR) with a monoenergetic positron beam on SIMOX (type S) and Unibond (types Ua and Ub) samples. Some of the MOS samples were characterised by capacitance-voltage (CV) measurements in order to determine the accumulated charge density. A detailed description of the experimental techniques is given in Chapter 3.

In addition, we compare our experiments with those performed by others on different SiO_2 samples to estimate the amount of Ps (Section 6.2.2) or to study SiO_2 after receiving an electron injection treatment (Section 6.2.3).

6.2.2. Positron analysis SiO_2 : the role of positronium

A large fraction of annihilations ($>50\%$) of low energy implanted positrons in SiO_2 originate from positronium (Ps) states. Positronium can be formed in SiO_2 because the network structure is relatively open with enough space for Ps. However, Ps formation is energetically not possible with electrons from the valence band, only with electrons from the conduction

band excited during the slowing-down of the incoming positron. This is the basis of the spur model [Mogensen 1974], the most favoured model for explaining the presence of Ps in SiO₂.

Table 6.1. Description of the samples employed in Section 6.2 and their treatments. Note that the first column describes sample types, not particular samples. Therefore, the treatments indicated in the other columns correspond to individual samples.

Sample type	Treatment	Sample labels	
Q: Fused quartz	0: Untreated	Q-0	
	D30: 30 keV D ⁺ implantation	Doses: (a) 2×10^{14} , (b) 1×10^{15} , (c) 1×10^{16} cm ⁻² Sample (b) underwent isothermal vacuum annealing steps for 15 min at 570, 840 and 1090 K	Q-D30-a—c
	He30: 30 keV He ⁺ implantation	Doses: (a) 3×10^{14} , (b) 1×10^{15} cm ⁻² Sample (a) underwent isothermal vacuum steps for 15 min at 470, 670, 820 and 970 K	Q-He30-a—b
S: SIMOX (190 nm top n-Si on 360 nm BOX on p-Si)	0: Untreated	S-0	
	D20: 20 keV D ⁺ implantation	Doses: (a) 2×10^{14} , (b) 2×10^{15} , (c) 2×10^{16} cm ⁻²	S-D20-a—c
	D30: 30 keV D ⁺ implantation	Doses: (a) 1×10^{14} , (b) 2×10^{15} , (c) 1×10^{16} cm ⁻² Sample (b) underwent isothermal vacuum steps for 15 min at 470, 670, 820 and 970 K	S-D30-a—c
Ua: MOS sample with a 1.0 μm Unibond BOX (1.2 μm top FZ-Si etched, 15 nm Al deposited on BOX grown on n-FZ-Si)	0: Untreated	Ua-0	
	He30: 30 keV He ⁺ implantation after depositing Al gate on BOX	Dose 1×10^{16} cm ⁻² Followed by isothermal vacuum steps for 15 min at 470, 670, 820 and 970 K	Ua-He30
Ub: MOS sample with a 3.0 μm Unibond BOX (1.2 μm top Cz-Si etched, 15 nm Al deposited on BOX grown on n-Cz-Si)	0: Untreated	Ub-0	
	H1: Hole injection in MOS at 1 MV/cm	Dose 2.5×10^{15} cm ⁻²	Ub-H1
	H2: Hole injection in MOS at 2 MV/cm	Dose 0.6×10^{15} cm ⁻²	Ub-H2
T: Wet thermal oxide (1.0 μm oxide grown on n-Si) [Clement 1998]	0: Untreated	T-0	
	E: Low energy electron injection	Accumulated negative charge densities: (a) 0.5, (b) 1.0, (c) 3.5, (d) 6.0×10^{12} cm ⁻²	T-E-a—d

Table 6.2. S , W and Ps fraction for several oxides. Values for oxides 4-10 were taken from the literature. The S and W values, normalised to the bulk c-Si values, are given with an approximate error of 1%. The techniques employed to estimate the Ps fractions are indicated by superscripts (see footnotes). POA in oxide 9 stands for post-oxidation annealing. APCVD in oxide 10 stands for atmospheric-pressure chemical vapour deposition using tetraethylorthosilicate (TEOS) and O_3 .

	Oxide type	S/S_{c-Si}	W/W_{c-Si}	Ps (%)
1	Fused quartz	0.993	1.48	76 ± 3^L
2	SIMOX BOX	0.987	1.54	64 ± 8^{AB}
3	Unibond BOX	0.995	1.50	72 ± 8^{AB}
4	Fused quartz [Dannefaer et al. 1993]	-	-	$\sim 80^L$
5	Fused quartz [Hasegawa et al. 2000]	-	-	$\sim 72^A$
6	Suprasil F300 [Hasegawa et al. 2000]	-	-	$\sim 80^L$
7	Wet thermal oxide (1 μ m thick) grown at 1050°C on n-Si (Chapter 8 in [Clement 1998])	0.982	1.56	-
8	Wet thermal oxide grown at 1000°C on n-Si [Uedono et al. 1994b]	0.990	-	$\sim 81^{LB}$
9	Dry thermal oxide grown at 1000°C on p-Si + 30 min POA in N_2 [Clement 1998]	0.992	1.48	-
10	APCVD oxide in TEOS / O_3 atmosphere [Uedono et al. 1994b]:			
	TEOS / O_3 5.6% at 370°C giving an oxide 312 nm thick	0.946	-	$\sim 39^{LB}$
	TEOS / O_3 5.6% at 400°C giving an oxide 322 nm thick	0.958	-	$\sim 40^{LB}$
	TEOS / O_3 5.6% at 430°C giving an oxide 288 nm thick	0.957	-	$\sim 51^{LB}$
	TEOS / O_3 0.56% at 400°C giving an oxide 305 nm thick	0.938	-	$\sim 33^{LB}$

^L) Lifetime

^{LB}) Lifetime with a pulsed monoenergetic beam

^A) 2D-ACAR

^{AB}) 2D-ACAR performed with a monoenergetic positron beam

The Ps fraction strongly depends on the number of available electrons in the surroundings of the thermalised positron. In this way, Ps formation can be suppressed by the application of sufficiently high electric fields which efficiently separate electrons and positrons. In Chapter 7, the spur model will be employed to account for effects on Ps formation and transport of positrons in electrically biased SiO_2 .

Many studies have shown that the Ps fraction formed in SiO_2 structures is very significant. Table 6.2 shows some earlier results published in addition to our own measurements on fused quartz (obtained with the positron lifetime technique), SIMOX and Unibond oxides (obtained with the aid of 2D-ACAR using a monoenergetic positron beam). For oxides deposited using the atmospheric-pressure chemical vapour deposition method (APCVD) [Uedono et al. 1994b] the Ps fraction was found to be between 33 and 51%. In the case of fused quartz, thermally grown oxides and buried oxides (SIMOX and Unibond samples), the Ps fraction was found to be larger than 64%.

Since the measured S and W parameters are the weighted sums of the contributions of the S and W parameters of every annihilation state involved, one can write

$$S = F_b S_b + F_{Ps} S_{Ps} = F_b S_b + \frac{3}{4} F_{Ps} S_{o-Ps} + \frac{1}{4} F_{Ps} S_{p-Ps} \quad (6.1)$$

$$W = F_b W_b + F_{Ps} W_{Ps} = F_b W_b + \frac{3}{4} F_{Ps} W_{o-Ps} + \frac{1}{4} F_{Ps} W_{p-Ps} \quad (6.2)$$

where S_b and W_b are the annihilation parameters of bulk SiO₂ assuming that no Ps is formed, while F_b represents the fraction of positrons annihilating in the bulk. S_{Ps} and W_{Ps} are the annihilation parameters of Ps states in SiO₂. These parameters are composed of two contributions, ortho-positronium (o-Ps) and para-positronium (p-Ps), see Section 3.3. In the former state, electron and positron spins are parallel whereas in the latter state they are antiparallel. According to spin statistics the o-Ps to p-Ps formation ratio is 3:1. Assuming that spin conversion does not occur prior to annihilation, we can use this ratio to split the Ps term into the o-Ps and p-Ps contributions, as indicated in (6.1) and (6.2). Finally, F_{Ps} represents the fraction of positrons annihilating at Ps states.

The annihilation of o-Ps in the samples considered here usually takes place via pick-off with surrounding electrons, therefore the o-Ps annihilation parameters are similar to those of bulk material. On the other hand, p-Ps is subjected to self-annihilation giving a sharp contribution to the 511 keV peak due to its near-zero intrinsic momentum (see Section 3.3). This means that the S and W annihilation parameters of p-Ps are very different compared to those of the bulk material. Since the fraction of Ps, F_{Ps} , is very significant, as mentioned above, the last term of equations (6.1) and (6.2) becomes very important. Evidently, this has a strong influence on the measured S and W parameters. In Fig. 6.5a, the Ps fraction measured by different techniques for a variety of SiO₂ samples is compared with the S parameter of these samples. The results correspond to oxide types 1, 2, 3 and 8 (open circles) and 10 (solid circles) listed in Table 6.2. As expected, there is a strong dependency of the S parameter on the Ps fraction formed in the samples.

Assuming that positrons annihilate in bulk SiO₂ or in Ps states, it is of interest to estimate the S - W cluster point of SiO₂ as a function of the Ps fraction. For this purpose, a 3 μm Unibond oxide (type Ub-0 in Table 6.1) was measured after removing the top Si layer. The 511 keV peak obtained at a positron energy of 14 keV was employed because it corresponds to a mean implantation depth near the centre of the oxide layer and causes 100% of the annihilations to take place in the oxide. The peak was decomposed [Alba García et al. 2001] into three gaussians corresponding to the following contributions: 1) annihilations with core electrons (broad gaussian), 2) annihilations with valence electrons (narrow gaussian) and 3) annihilations from p-Ps states (sharp gaussian). In order to reduce the number of fitting parameters for the decomposition, we made use of accurate data obtained from the high resolution 2D-ACAR measurements on sample Ub-0 at 14 keV. These measurements indicate that the p-Ps contribution amounts to (18 ± 2) %. This value was fixed when decomposing the DBAR peak. Assuming a p-Ps to o-Ps ratio of 1 to 3, we obtained for the total Ps fraction a value of 72% (see Table 6.2). The full width at half maximum (FWHM) of the sharp p-Ps

contribution was found to be (1.51 ± 0.04) keV for DBAR measurements, in perfect agreement with the results of 2D-ACAR measurements when the resolution of the DBAR method was taken into account. The parameters obtained by the decomposition of the DBAR peak for the other contributions are given in Table 6.3. In order to estimate how the 511 keV annihilation peak changes with the Ps fraction formed in the sample, we kept the FWHM of the p-Ps component constant while we varied the fraction of p-Ps that it is formed (by varying the area of the third component). We assume that the annihilations with core electrons are not affected by the Ps formation process. Therefore, the parameters for the first component are kept fixed. On the other hand, we let the contribution of the second component free, while keeping its FWHM fixed. The sum of the gaussian areas was unity. In this way, we constructed the expected annihilation peaks for the following Ps fractions: 0, 20, 40, 60, 80 and 100%. With the constructed peak for every Ps fraction we calculated the S and W parameters according to their definition (see Section 3.3).

The results are shown in Fig. 6.5a where the open diamonds indicate the Ps fraction as a function of the S parameter calculated from the constructed peaks. It is interesting to note that the expected S values obtained in this way are in fair agreement with the experimental data also shown in Fig. 6.5a. The comparison of the W parameter with the Ps fraction is more difficult due to the larger scattering found in the determination of W , which originates from poorer statistics than in the case of the S determination. In addition, very few studies are published which include data for the W parameter. This makes comparisons with the literature rather difficult. However, we systematically make use of the W parameter. The open diamonds of Fig. 6.5b represent the S - W cluster points corresponding to the annihilation peaks constructed for different Ps fractions. Therefore, the Ps fraction is the running parameter of the S - W plot. By means of this plot, we can predict the Ps fraction formed in different SiO₂ samples when the S - W cluster point of the material is on the straight line connecting the open diamonds. If the cluster point is not on this straight line, it is an evidence that positrons annihilate at states different from bulk SiO₂. This is a valuable method to estimate Ps fractions in DBAR measurements, which do not provide direct accurate access to this important parameter.

We attribute the variation in the Ps fraction in different SiO₂ samples to differences in the electron concentration around just thermalised positrons. This is due to the presence of OH groups that interact with electrons in the following way (see e.g. pages 538 and 657 of [Nicollian et al. 1982])



According to (6.3), the concentration of electrons available to form Ps decreases with increasing OH concentration. In agreement with this, (see also [Uedono et al. 1994b]), an inverse relation is found between the Ps formation probability and the concentration of OH defects.

We should mention that some discrepancies appear in the determination of the S and W parameters in different experimental setups due to the different resolution of the gamma detectors. However, the experimental S and W parameters normalised to the c-Si characteristic

parameters (used throughout the present work) are reproducible in the majority of the experimental setups. This allows us to compare experimental results obtained by others, as just shown above.

Table 6.3. Parameters used to decompose the 511 keV peak obtained from DBAR experiments when implanting positrons at 14 keV in a 3 μm thick Unibond oxide. The intensity of the sharp gaussian was taken from the p-Ps fraction obtained by 2D-ACAR experiments.

Gaussian	Fraction (%)	FWHM (keV)
Sharp: p-Ps (fixed)	18	1.51 ± 0.04
Narrow: valence electrons	77 ± 2	2.70 ± 0.03
Broad: core electrons	5 ± 5	6 ± 3

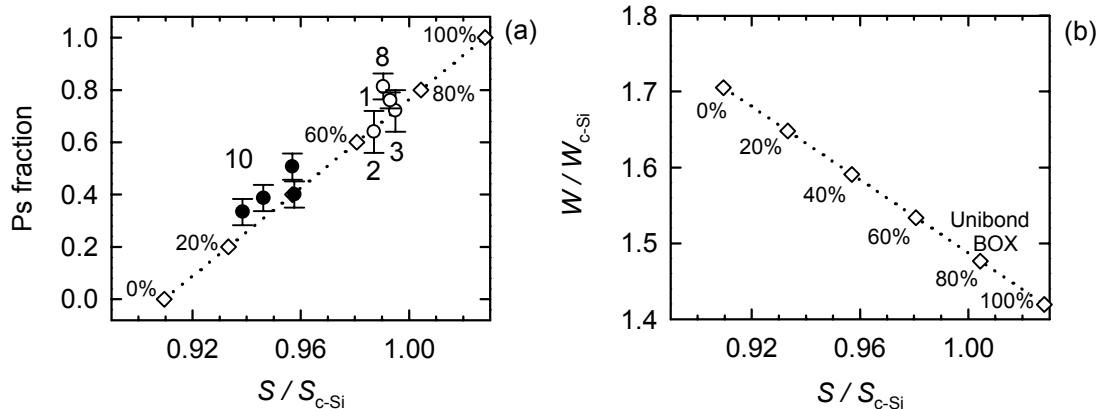


Fig. 6.5. (a) Ps fraction as a function of the S parameter normalised to c-Si for the samples described in Table 6.2. (b) Expected S - W cluster points of the Unibond sample Ub-0 when the Ps fraction formed in the oxide changes as indicated.

6.2.3. Hole and electron injection in SiO_2

Positron studies of samples that have been subjected to low energy hole or electron injection treatments are of importance because these injections create well-defined defects. Electrons injected into SiO_2 interact with Si-OH groups and, following (6.3) give a negatively charged defect (Si-O^-). The latter defects are not neutralised during the injection when the energy of the employed electrons is smaller than the SiO_2 band gap, since hole generation is then not possible. In the case of hole injection (see the comprehensive discussion in Chapter 4) the most important effect is the interaction of holes with Si-H groups giving a Si dangling bond ($\text{Si}\cdot$) following the reaction

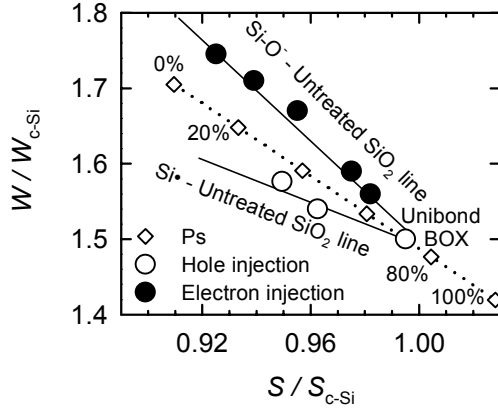


Fig. 6.6. S - W plot showing the effect of hole injection (open circles) and electron (solid circles) injection into MOS samples described in Table 6.1. The open circles from left to right correspond to samples Ub-H1, Ub-H2 and Ub-0, respectively. The solid circles correspond to from right to left samples T-0 and T-E-a-d, respectively. The open diamonds correspond to the expected S - W cluster points of sample Ub-0 for the indicated Ps fractions. The lines are to guide to the eye.

In Fig. 6.6 we recall the results shown in Fig. 4.6 for hole injection in samples Ub-H1 and Ub-H2 and electron injection in sample T-E, see Table 6.1. We compare these results with the estimated S - W cluster points for a Unibond oxide with different Ps fractions, as shown in Section 6.2.2. The hole injection experiments (open circles) were performed on a 3- μm thick Unibond oxide while the electron injection experiments (solid circles) were carried out on a 1- μm thick wet thermal oxide (see Chapter 8 in [Clement 1998]). In both cases the characteristic cluster points lie on straight lines different from the one formed by the open diamonds (with the Ps fraction as the running parameter). This indicates the presence of different positron annihilation states upon electron or hole injection. We assign these annihilation states to the different products of electron and hole injection reactions, i.e. Si-O^- and $\text{Si}\cdot$ defects, respectively, given by Reactions (6.3) and (6.4).

The high W value obtained for the electron-injected oxide indicates that annihilations take place with high momentum electrons which can only be supplied by oxygen atoms, in agreement with positron annihilation at Si-O^- defects. On the other hand, the characteristic cluster points obtained for hole-injected oxides indicate that the defects generated by the injection act as positron traps. The W parameter for hole-injected oxides is smaller than in the case of electron injection and smaller than in the case of bulk annihilations in a sample in which a small Ps fraction is formed. We conclude that the overlap of positrons trapped in hole-generated defects with high momentum electrons is reduced in comparison with the previous cases: bulk SiO_2 and electron-generated defects. This agrees with annihilation at $\text{Si}\cdot$ defects.

In principle, it is difficult to say whether trapped positrons are able to form Ps or not. However, the low S (high W) values corresponding to the generated defect states (extrapolation of the straight lines shown in Fig. 6.6) suggest that Ps is not formed in these traps. This can be understood as follows: once a positron is trapped, it is screened from the surrounding free electrons. These electrons can not enter the trap and the formation of Ps with bound electrons of the trap is energetically not favourable. Experimentally, it was observed, see e.g. [Hasegawa et al. 2000], that the Ps formation in irradiated oxides decreases with increasing dose. Since the defects generated during the irradiation process are similar to those

presented in this section, the observed reduction in the Ps formation is in agreement with the low probability of Ps formation with trapped positrons.

In order to further characterise the detected defects, their specific trapping rates are estimated next. These parameters are of great importance because once they are known the defect concentration can be extracted from DBAR measurements. Recalling equations presented in Section 3.3 and treating Ps as a positron trap (Section 6.2.2 and Chapter 7), we can write for defect-free SiO₂

$$\frac{\kappa_{Ps}}{F_{Ps}} = \frac{\lambda_b}{F_b}, \quad (6.5)$$

where κ_{Ps} is the Ps formation rate, λ_b is the bulk annihilation rate and F_{Ps} and F_b are the fractions annihilating as Ps or in the bulk as free positrons, respectively. λ_b is the inverse of the positron bulk lifetime, which equals $\tau_b = 290$ ps [Dannefaer et al. 1993]. F_{Ps} equals 0.72 in the case of Unibond samples, see Table 6.2, while $F_b = 1 - F_{Ps} = 0.28$. Thus, we obtain for κ_{Ps} a value of 8.8×10^9 s⁻¹. This value will also be employed for the thermal oxide employed for electron injection experiments, since the exact value for the Ps fraction is not known. In any case, Table 6.2 shows that in general the Ps fractions do not differ much from Unibond oxides to thermal oxides.

When there are defects in the oxide able to trap positrons, (6.5) should be written as follows

$$\frac{\kappa_{Ps}}{F_{Ps}} = \frac{\lambda_b}{F_b} = \frac{\kappa_d}{F_d}, \quad (6.6)$$

where κ_d is the trapping rate at the defects and F_d the fraction of positrons trapped at such defects. (6.6) can be rewritten as

$$\begin{aligned} F_{Ps}\kappa_d &= F_d\kappa_{Ps} \\ F_b\kappa_d &= F_d\lambda_b \end{aligned} \quad (6.7)$$

Adding up both equations, we obtain

$$(F_{Ps} + F_b)\kappa_d = F_d(\kappa_{Ps} + \lambda_b). \quad (6.8)$$

Making use of $1 = F_d + F_{Ps} + F_b$, one obtains an expression for κ_d

$$\kappa_d = \frac{F_d}{(F_{Ps} + F_b)}(\kappa_{Ps} + \lambda_b) = \frac{F_d}{(1 - F_d)}(\kappa_{Ps} + \lambda_b) = \frac{F_d}{(1 - F_d)}\kappa_{ox}. \quad (6.9)$$

An effective bulk annihilation rate for the oxide, $\kappa_{ox} = \kappa_{Ps} + \lambda_b = 1.2 \times 10^{10} \text{ s}^{-1}$, which includes the effect of Ps formation, was employed in (6.9). The specific trapping rate, v_d , corresponding to the involved defect type can be obtained from κ_d , in the following way

$$\kappa_d = v_d n_d, \quad (6.10)$$

where the defect concentration, n_d , must be estimated by other techniques. In the particular case of electron injection, the defect concentration is given by the negative charge density obtained from CV measurements, assuming that the charge density is homogeneous throughout the oxide. In the case of hole injection the estimate made in Section 4.1.3 will be employed.

The only parameter required to know the defect trapping rate, κ_d , is F_d . It can be obtained from DBAR measurements once the defect characteristic S and W parameters are known, using the following equations

$$S = F_b S_b + F_{Ps} S_{Ps} + F_d S_d = F_{ox} S_{ox} + F_d S_d \quad (6.11)$$

$$W = F_b W_b + F_{Ps} W_{Ps} + F_d S_d = F_{ox} W_{ox} + F_d S_d. \quad (6.12)$$

The oxide contribution, including the Ps fraction, to the experimental S and W parameters is taken into account by $F_{ox} = 1 - F_d$. The characteristic S and W parameters corresponding to annihilations in the oxide or in the defects are indicated by the subscripts ox and d , respectively. S_{ox} and W_{ox} contain both the contribution of Ps in the oxide and the contribution of positrons freely annihilating in the oxide. These parameters are known, however the determination of S_d and W_d requires special care.

In the case of electron injection, the oxide cluster point was obtained from the experiments on the sample prior to electron injection, see Fig. 6.7a. Note that this point is different from the characteristic Unibond oxide point. On the other hand, the defect cluster point was estimated on the basis of the ion implantation experiments shown in the next sections. It is assumed that since both electron injection and ion implantation lead to positron trapping at oxygen-related defects, the saturation point is similar.

F_d can be obtained from both (6.11) and (6.12). In Fig. 6.7a, the average F_d is indicated. By means of (6.9), κ_d was obtained. The specific trapping rate v_d was then calculated from the slope of the line representing κ_d vs. defect concentrations, see Fig. 6.7b. The resulting specific trapping rate for the Si–O⁻ defects generated by electron injection was $v_d = 6.7 \times 10^{-7} \text{ cm}^3/\text{s}$. This value could be overestimated because of the inaccuracy in the determination of the S_d and W_d parameters. However, its high value is a clear indication of negatively charged defects, as assumed above.

In the case of hole injection, the S_d and W_d parameters could be accurately estimated from DBAR experiments under negative gate voltage, as shown in Section 7.1.8. The application to this voltage drifts positrons to the region where the hole-generated defects were created, enhancing the positron transport to these defects to near 100%. The S_d and W_d parameters corresponding to Si• defects generated by hole injection correspond approximately

to the leftmost solid circle in Fig. 6.6, which was found for sample Ub-H1, injected with 2.5×10^{15} holes cm^{-2} . Therefore, trapping after this injection dose is 100%. On the other hand, the trapped fraction in the defect region of sample Ub-H2 can be obtained from (6.11) and (6.12). Around 67% of the positrons annihilating in the defect layer are trapped at defects. This corresponds to a positron trapping rate $\kappa_d = 2.9 \times 10^{10} \text{ s}^{-1}$, obtained from (6.9). The upper limit for the Si^\bullet concentration after hole injection was estimated in Chapter 4. This limit is $5.3 \times 10^{17} \text{ cm}^{-3}$. Thus, by means of (6.10) the specific trapping rate, v_d , for Si^\bullet defects generated by hole injection is estimated at $v_d = 5.6 \times 10^{-8} \text{ cm}^3/\text{s}$. This value is about one order of magnitude smaller than that found for $\text{Si}-\text{O}^-$ defects, clearly indicating that the trapping at $\text{Si}-\text{O}^-$ is much more efficient due to their negatively charged state. However, the trapping at Si^\bullet defects is large enough to discard their association with positive charge.

In summary, it has been shown that the defects generated by hole injection and by low energy electron injection can be distinguished by means of DBAR. The first type is ascribed to Si dangling bonds and the second one to negatively charged oxygen defects, in agreement with expectations.

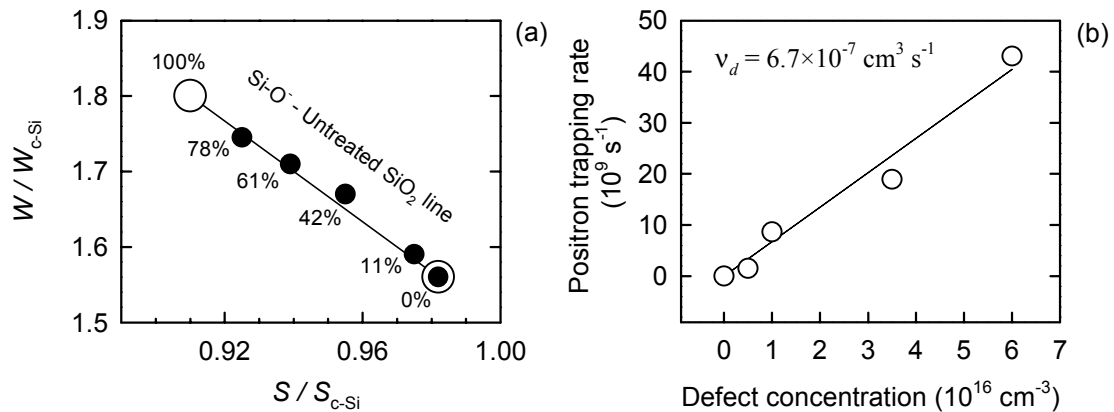


Fig. 6.7. (a) S - W plot showing in detail the electron injection experiments. The open symbols correspond to 0 and 100% positron trapping at the electron-generated defects. The positron fraction trapped after every injection is indicated. (b) positron trapping rate at the electron generated defects as a function of the negative charge density.

6.2.4. Deuterium and helium implantation in SiO_2 structures

Several positron studies showed the effect of neutron, high energy electron, X-ray, γ -ray and ion irradiation on amorphous SiO_2 [Hasegawa et al. 2000, Uedono et al. 1994c, Zhu et al. 1998, Dannefaer et al. 1993, Fujinami et al. 1993, Asoka-Kumar et al. 1995]. These treatments, contrary to the case of low energy electron or hole injection presented in Section 6.2.3, lead to the displacement of atoms and the rupture of different types of bonds. As a consequence, the resulting defect structure is more complex than in the previous case. It was found that Ps is reduced after irradiation due to the trapping of positrons at generated defects. It was proposed [Hasegawa et al. 2000] that the trapping sites are non-bridging oxygen hole centres (NBOHC) and interstitial oxygen atoms. In this section we supply new data to support

the crucial role of Ps and identify the different defects introduced in SiO_2 by different methods.

Ion implanted-fused quartz

Samples belonging to type Q in Table 6.1 were implanted with D^+ and $^4\text{He}^+$ ions. Fig. 6.8 shows results corresponding to fused quartz samples implanted with 30 keV D^+ (Q-D30). The S and W annihilation parameters are given as a function of the positron mean implantation depth. For comparison, the results of TRIM calculations [Biersack et al. 1980] of 30 keV D^+ in SiO_2 are given in Fig. 6.8c. Both the profile of displaced atoms (left axis) and the profile of implanted D (right axis) are plotted.

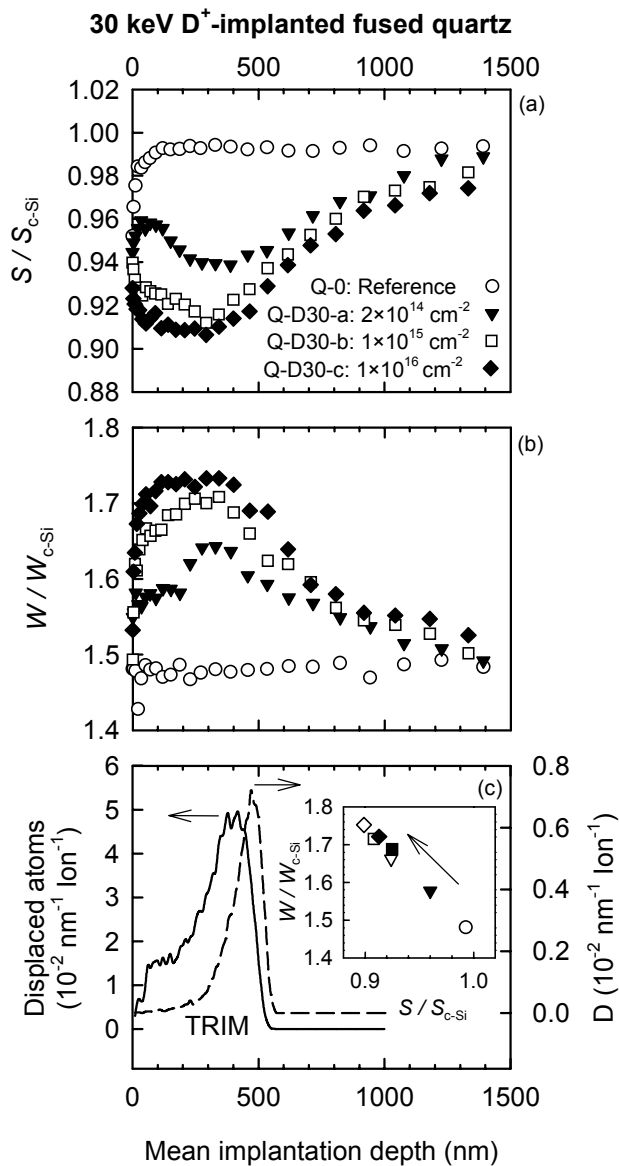


Fig. 6.8. DBAR results for fused quartz samples (Q-D30-a—c in Table 6.1) implanted with 30 keV D^+ ions at the indicated doses. (a) and (b) the S and W parameters, respectively, normalised to the c-Si values as a function of the positron mean implantation depth. (c) the results of TRIM calculations in SiO_2 implanted with 30 keV D^+ ions. Both the profile of displaced atoms and the profile of D atoms are plotted. The insert shows the S - W cluster points corresponding to a region within 200 nm from the surface (solid symbols) and to a damaged region between 200 nm and 600 nm from the surface (open symbols).

We should keep in mind that TRIM calculations assume that the implantation occurs at 0 K. Under real conditions of room temperature implantation, some of the displaced atoms can return to the original position and restore the chemical bonds. Anyway, we observe that the profile of displaced atoms given by TRIM agrees well with the depth profile given by the S and W parameters in Fig. 6.8a-b. Especially, the spectra corresponding to a dose of $2 \times 10^{14} \text{ D}^+ \text{ cm}^{-2}$ (Q-D30-a) are very similar to the displaced atom profile given by TRIM. A shoulder appears in the TRIM curves in the region close to the surface (below $\sim 200 \text{ nm}$), together with a pronounced peak at around 400 nm . These features correspond to a plateau in both S and W close to the surface followed by a peak in the case of the W parameter and a valley in the case of the S parameter. Experiments performed by implantation of other ions lead to qualitatively similar observations [Fujinami et al. 1993].

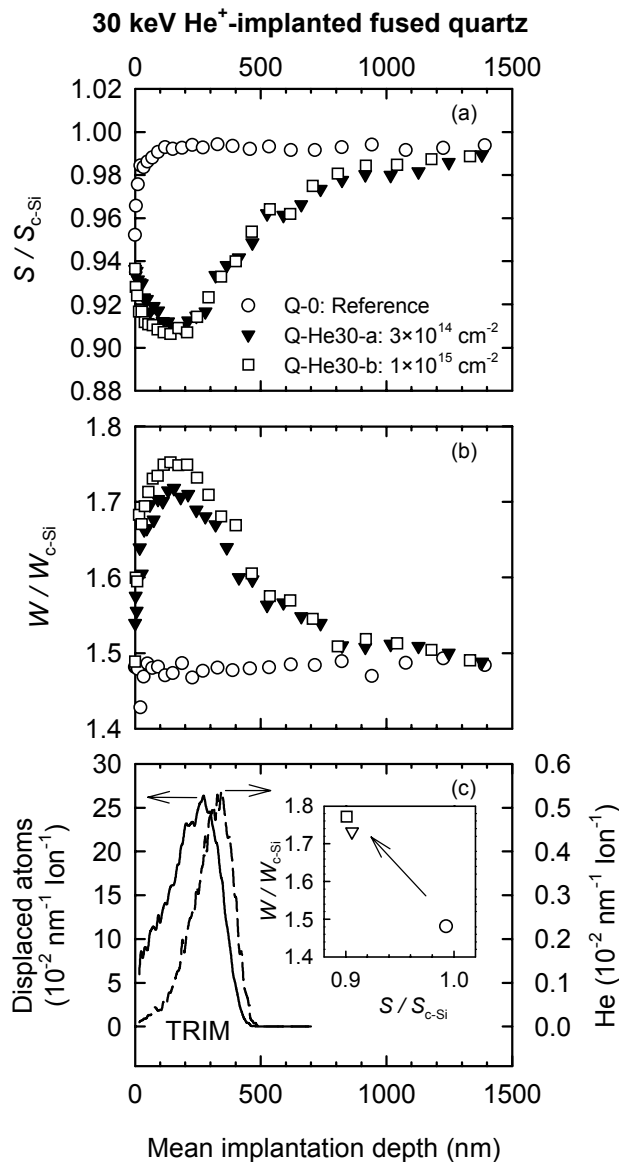


Fig. 6.9. DBAR results for fused quartz samples (Q-He30-a—c in Table 6.1) implanted with 30 keV He⁺ ions at the indicated doses. (a) and (b) the S and W parameters, respectively, normalised to the c-Si values as a function of the positron mean implantation depth. (c) the results of TRIM calculations in SiO₂ implanted with 30 keV He⁺ ions. Both the profile of displaced atoms and the profile of D atoms are plotted. The insert shows the S - W cluster points corresponding to the damaged region within 400 nm from the surface.

The region where the most significant fraction of the D ions was implanted corresponds to the peak in the D profile given by TRIM. Positrons do not show significant changes in this region with respect to the unimplanted sample (Q0). However, the peak in the W plot appears slightly shifted to the left with respect to the peak in the TRIM plot. Owing to the high mobility of both atomic and molecular hydrogen species at room temperature [Griscom 1985, Fink et al. 1995], the implanted D can reach the damaged region occupying a significant fraction of the positron traps. This effect is not considered in the TRIM calculations and explains the small discrepancy in the positions of the peaks obtained by TRIM and DBAR.

The curves corresponding to the D^+ implanted samples shown in Fig. 6.8a-b were fitted by means of VEPFIT [van Veen et al. 1990]. A model of three defect layers, corresponding to the near-surface low defect concentration region, the high defect concentration region and the bulk, was used for the fitting. The resulting S - W coordinates of the first two defect layers are shown in the insert of Fig. 6.8c. The solid symbols correspond to the first layer while the open symbols correspond to the high defect concentration layer. Increasing the implantation dose causes cluster points to move away from the cluster point corresponding to the unimplanted sample (Q0). However, at implantation doses higher than $1 \times 10^{15} D^+ cm^{-2}$ a saturation effect appears in the high defect concentration layer. Further increase in the implanted dose does not lead to a significant shift of the cluster point position. It is evident from Fig. 6.8a-b that at high implanted doses, the annihilation parameters of the near-surface layer approach those corresponding to the high defect concentration layer. This occurs despite the much higher concentration of damage accumulated in the latter layer and is in line with the saturation effect just mentioned.

The results of $^4He^+$ implantation are shown in Fig. 6.9. Since the projectile ion, He^+ , has a larger mass than D^+ , the profiles of displaced atoms and the ion range show their maxima closer to the surface for He^+ implantation than for D^+ implantation. In addition, the damage created per incoming ion is much larger for He^+ implantation than for D^+ implantation, as shown in Fig. 6.9c. The displaced atom profile for He^+ implantation can be described by means of one single peak. This profile is monitored by a drop in the S parameter (increase in the W parameter) in the damage region. On the other hand, we observe that a relatively low dose of implanted He^+ ions ($3 \times 10^{14} cm^{-2}$, sample Q-He30-a) causes a saturation effect, as clearly observed in the S - W plot inserted in Fig. 6.9c.

Ion-implanted SIMOX

SIMOX samples (type S), similar to those employed in Section 6.1, were implanted with D^+ ions as indicated in Table 6.1. The results of D^+ implantation at 20 and 30 keV are shown in Fig. 6.10 and Fig. 6.11, respectively. The effect of D^+ implantation is clearly detected by DBAR. In the top Si layer, the initially low S parameter (see Section 6.1) increases drastically after D^+ implantation for both 20 and 30 keV implantation. The opposite behaviour is found for the W parameter. This effect is well-known in implanted bulk crystalline Si [van Veen et al. 1996] and is related to the creation of vacancy-like defects as a consequence of the displacement of network atoms. The S and W parameters show opposite behaviour in the

BOX layer. The S parameter decreases (W increases) due to the ion implantation, as in the case of implanted fused quartz.

The majority of the implanted ions was stopped in the BOX layer as shown by means of TRIM calculations. In order to establish the depth profile of deuterium in the samples, the SIMOX sample implanted with 20 keV D^+ to a dose of $2 \times 10^{15} \text{ cm}^{-2}$ was studied by means of SIMS. The resulting deuterium profile is shown in Fig. 6.10c. Note that the D-profile obtained by SIMS is significantly broader than the calculated D-profile by TRIM. This is due to the mobility of deuterium at room temperature [Griscom 1985, Fink et al. 1995]. Furthermore, it is found that the deuterium profile obtained by SIMS overlaps the expected damage profile obtained by TRIM. This suggests that a significant fraction of the implantation-generated defects is passivated by the implanted deuterium. This is in agreement with the implantation of deuterium in fused quartz, for which a small difference was found between the TRIM profile of displaced atoms and both the S and W spectra, due to significant passivation of the positron trapping defects (see above).

The positron results shown in Fig. 6.10 and Fig. 6.11 were fitted with the aid of VEPFIT. A model consisting of three layers, a top Si layer, a BOX layer and the Si substrate, was assumed for the fit. The resulting S - W cluster points corresponding to the top Si layer and the BOX layer of the 20 and 30 keV implanted samples are plotted in Fig. 6.12. The effect of ion implantation can be followed by means of these S - W plots. The unimplanted sample shows the typical values for oxygen-related defects in the top Si layer of SIMOX as discussed in Section 6.1. The S - W coordinates corresponding to the top layer moves towards higher S (lower W) values with increasing implanted deuterium dose. At high implanted doses the S - W coordinates saturates at values close to (1.04, 0.80), typical for divacancies in c-Si [van Veen et al. 1996]. These defects are probably deuterium-free, since the D-profile calculated by TRIM for both 20 and 30 keV, shows a peak much deeper in the BOX layer. On the other hand, the S - W coordinates corresponding to the unimplanted BOX moves towards lower S (higher W) values showing a saturation effect at high implanted doses. The saturation point is at about (0.90, 1.80), the same within the experimental error (1%) as that found for D^+ - and He^+ -implanted fused quartz (Fig. 6.8 and Fig. 6.9, respectively).

Discussion of the ion implantation experiments

The data presented indicate that the effect of ion implantation in different SiO_2 structures can be clearly monitored by DBAR. A drastic change in the S and W annihilation parameters occurs already for low ion-implantation doses. The profile of displaced atoms corresponds to the S and W vs. E curves indicating that the positron trapping sites are related to ion-generated damage.

The S parameter appears related to the damage introduced by ion implantation and not to the specific ion used as a projectile. A clear saturation effect in the S parameter was observed beyond about 50×10^{19} displaced atoms cm^{-3} . Since the displacements per atom produced by He implantation are quite large, the saturation effect is very pronounced in samples implanted with He atoms.

As will be shown in Chapter 7, positrons are unable to drift under the application of external electric fields when the damage level is high. This indicates that positrons are

efficiently trapped at the generated defects. The S - W cluster points corresponding to the ion implantation-generated defects move on a line with the implantation dose as a running parameter. Two annihilation states are involved. Their characteristic cluster points are the endpoints of the line. These annihilation states correspond to annihilation from positrons trapped at the generated defects and positron annihilation in SiO_2 (including the effect of Ps, see Section 6.2.2).

The microscopic environment of the trapped positron seems similar to that of bulk SiO_2 because the S - W cluster point of the positron traps is similar to that expected for SiO_2 with a reduced Ps fraction (see Section 6.2.2). This agrees qualitatively with the picture that suggests NBOHC defects as positron traps [Hasegawa et al. 2000]. The dangling bond associated with the oxygen atom is expected to be attractive to positrons. A positron captured by this defect experiences a SiO_2 environment.

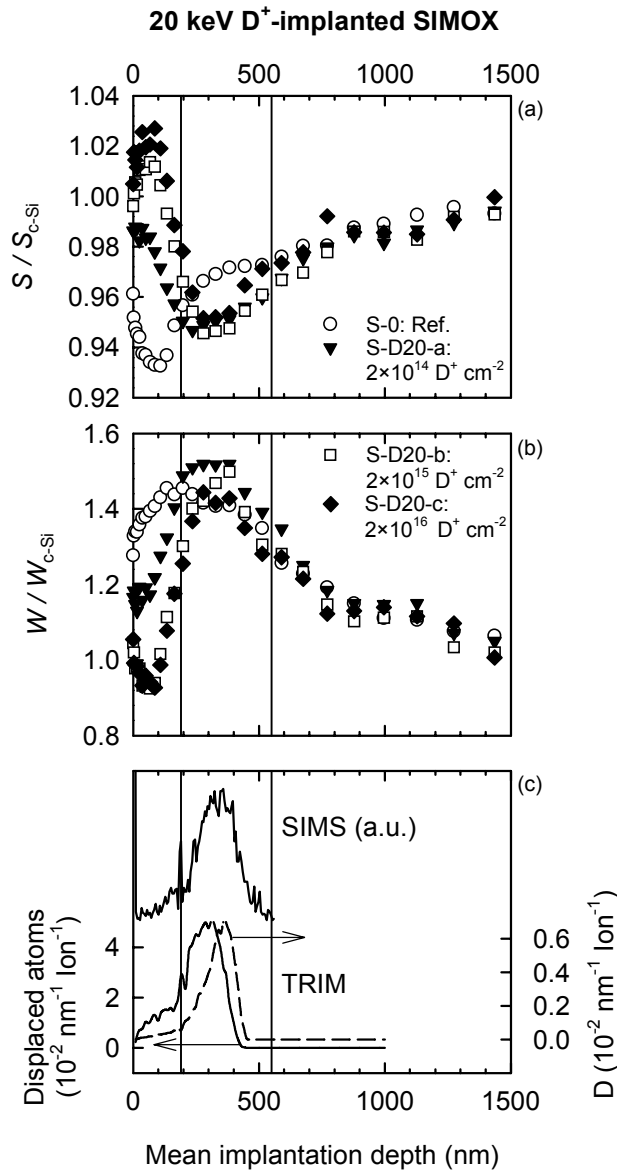


Fig. 6.10. DBAR results for SIMOX samples with a 190 nm top Si layer and a 360 nm BOX layer (S-D20-a—c in Table 6.1) implanted with 20 keV D^+ ions at the doses indicated in the legend. (a) and (b) the S and W parameters, respectively, normalised to the c-Si values as a function of the positron mean implantation depth. (c) the results of SIMS experiments and of TRIM calculations in SiO_2 implanted with 20 keV D^+ ions. Both the profile of displaced atoms and the profile of D atoms obtained by the TRIM calculations are plotted. The vertical lines in the figures represent the boundaries between the top Si layer and the BOX layer and between the BOX layer and the Si substrate.

Positron results obtained for samples implanted with different doses of He and D can not be compared directly. First, we should make an estimate of the damage generated during the implantation process. By means of TRIM we can calculate the expected number of displaced atoms generated by an incoming He⁺ or D⁺ ion with a certain energy. In this way, Fig. 6.13 shows a plot of the *S* parameter obtained for the different layers of the D⁺- and He⁺-implanted samples as a function of the total number of displaced atoms, as calculated with TRIM. Remarkably, the values of the *S* parameter follow the same trend, independently of the type of implantation: He or D. Clearly, the *S* parameter is strongly dependent on the concentration of displaced atoms. It shows the already mentioned saturation effect above a concentration of displaced atoms of about $50 \times 10^{19} \text{ cm}^{-3}$. This saturation effect begins to occur when most of the positrons are trapped, which implies that a further increase in the number of defects does not affect the fraction of trapped positrons.

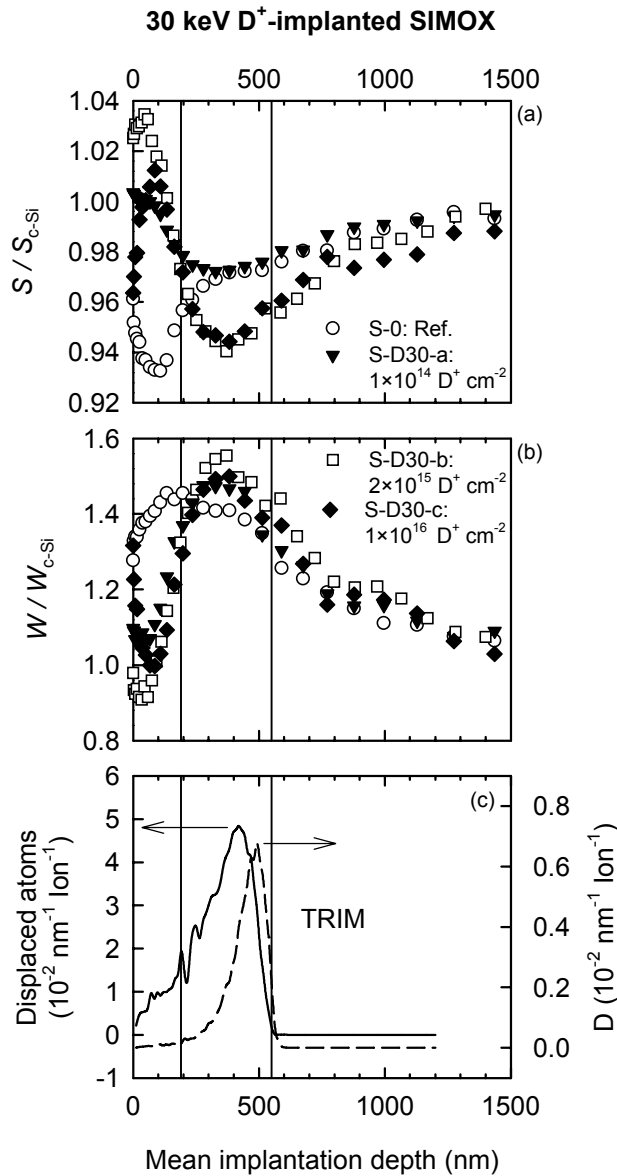


Fig. 6.11. DBAR results for SIMOX samples with a 190 nm top Si layer and a 360 nm BOX layer (S-D30-a—c in Table 6.1) implanted with 30 keV D⁺ ions at the doses indicated in the legend. (a) and (b) the *S* and *W* parameters, respectively, normalised to the c-Si values as a function of the positron mean implantation depth. (c) the results of TRIM calculations in SiO₂ implanted with 30 keV D⁺ ions. Both the profile of displaced atoms and the profile of D atoms are plotted. The vertical lines in the figures represent the boundaries between the top Si layer and the BOX layer and between the BOX layer and the Si substrate.

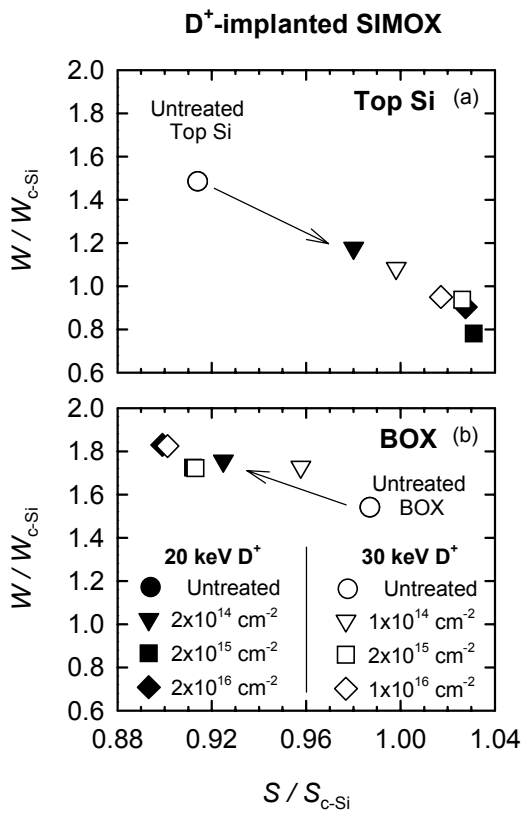


Fig. 6.12. *S-W* plots corresponding (a) to the top Si layer and (b) to the BOX layer of SIMOX samples (S-D20-a—c and S-D30-a—c in Table 6.1) implanted with 20 keV D⁺ (solid symbols) and 30 keV D⁺ (open symbols). The running parameter is in both cases the implanted dose and the arrows indicate the direction of increasing implanted dose.

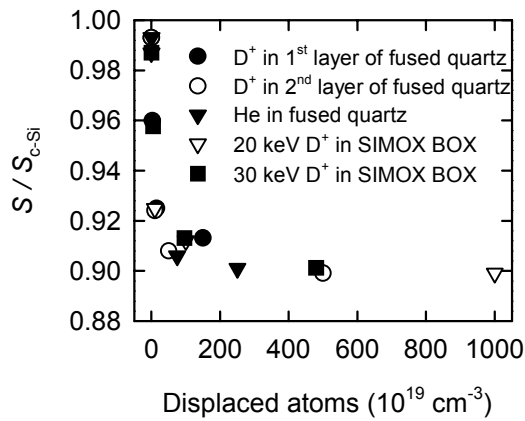


Fig. 6.13. *S* parameter normalised to the c-Si value as a function of the displaced atom density obtained from TRIM for fused quartz implanted at different doses with 30 keV D⁺ and He⁺ and for the SIMOX samples implanted with 20 and 30 keV D⁺ (Fig. 6.8 to Fig. 6.11). The *S* parameter is given with an error of 1%.

It should be noted that the total concentration of displaced atoms given by TRIM is not related to any particular defect type. In particular, the concentration of NBOHC centres, proposed as positron traps, can not be extracted from TRIM. At room temperature the number of generated defects is much lower (one or two orders of magnitude) than that calculated by TRIM, owing to recombination of some of the atoms displaced by the ion implantation. In addition, some of the generated NBOHC centres will be occupied by deuterium. This means that positrons will not detect them. Finally, we should note that the concentrations of defects

surviving recombination can depend on the implanted species and saturate rather than remaining linear at high implanted doses, as shown in some cases [Miyamaru et al. 1996].

Due to the difficulties in estimating the defect concentration, it is impossible to determine accurately the specific trapping rate, ν_d , of those defects. A very rough estimate assuming that only 5% of the displaced atoms constitute positron traps leads to a value for $\nu_d \sim 3 \times 10^{-9} \text{ cm}^3/\text{s}$. This value is much smaller than those obtained for defects generated by electron or hole injection (see Section 6.2.3). Therefore, the defects generated by charge carriers are more efficient positron traps than those generated by ion implantation.

6.2.5. Annealing of defects

Annealing of ion-implantation generated defects in fused quartz

The fused quartz sample (Q-D30-b) implanted with 30 keV D^+ to a dose of $1 \times 10^{15} \text{ cm}^{-2}$ (presented in Fig. 6.8) was subjected to vacuum annealing treatments of 15 min at the temperatures indicated in Fig. 6.14. The implantation led to two defect regions characterised by low S (high W) parameters, as explained in Section 6.2.4. The subsequent annealing steps caused an increase in the S (decrease in W) parameters restoring the characteristic values of the untreated sample. The defect profiles represented by the S and W parameters in Fig. 6.14 indicate that the restoration of the defect layers occurs faster in the near-surface region than in the deeper layer which originally contained a higher concentration of defects. The S - W points corresponding to the various layers, as obtained from VEPFIT, are shown in Fig. 6.14c. It can be observed that the annealing steps result in a shift in the S - W points towards higher S (lower W) values. This shift is more pronounced in the layer close to the surface, represented by the solid symbols. Interestingly, while the S - W points corresponding to the second layer approach the untreated oxide point, those belonging to the near-surface layer move towards S values higher (W values lower) than those of the untreated oxide.

Similarly, the fused quartz sample (Q-He30-a) implanted with 30 keV He^+ to a dose of $3 \times 10^{14} \text{ cm}^{-2}$ (presented in Fig. 6.9) was subjected to vacuum annealing treatments of 15 min at the temperatures indicated in Fig. 6.15. As in the previous case, the annealing steps gradually restore the S - W values corresponding to untreated fused quartz. The S - W plot indicates that the near-surface is restored faster than the deep-lying high defect concentration layer, as in the previous case. However, the effect is not as pronounced as in the case of deuterium implantation.

Annealing of ion implantation-generated defects in the BOX layer of SIMOX

The SIMOX sample (S-D30-b) implanted with 30 keV D^+ to a dose of $2 \times 10^{15} \text{ cm}^{-2}$ (presented in Fig. 6.11) underwent, after removal of the top Si layer in KOH, vacuum annealing treatments of 15 min at the temperatures indicated in Fig. 6.16. The removal of the top Si layer improves the depth resolution of the DBAR measurements.

The annealing experiments restore the annihilation parameters to the values corresponding to the untreated oxide. Clearly, an important effect is observed at the interface between BOX and substrate. The experiments were fitted by means of VEPFIT with a model

consisting of two layers: BOX and substrate, contrary to the fused quartz case, for which a three-layer model was used. We recall that the D^+ implantation in the SIMOX sample took place through the top Si layer. Fig. 6.11c showed the TRIM calculations corresponding to this implantation. The major part of the damage generated by the implantation can be represented by a peak, which is entirely located in the BOX layer. This peak is similar to that obtained by TRIM calculations of D^+ implantation in fused quartz (Fig. 6.8c) corresponding to the second layer, used in the VEPFIT model to represent the major part of the generated damage. However, since the top Si layer of SIMOX was removed before the annealing and DBAR experiments, the damage peak in the SIMOX sample became effectively positioned close to the surface, similarly as the first damage peak found for the implanted fused quartz samples. The thermal recovery of the S and W values occurs in a similar way as in the first layer of the fused quartz sample, indicating an important surface effect. After the annealing step at the highest temperatures (820 K and 970 K) the S - W point corresponding to the BOX layer (Fig. 6.16c) moves towards the high S -low W region.

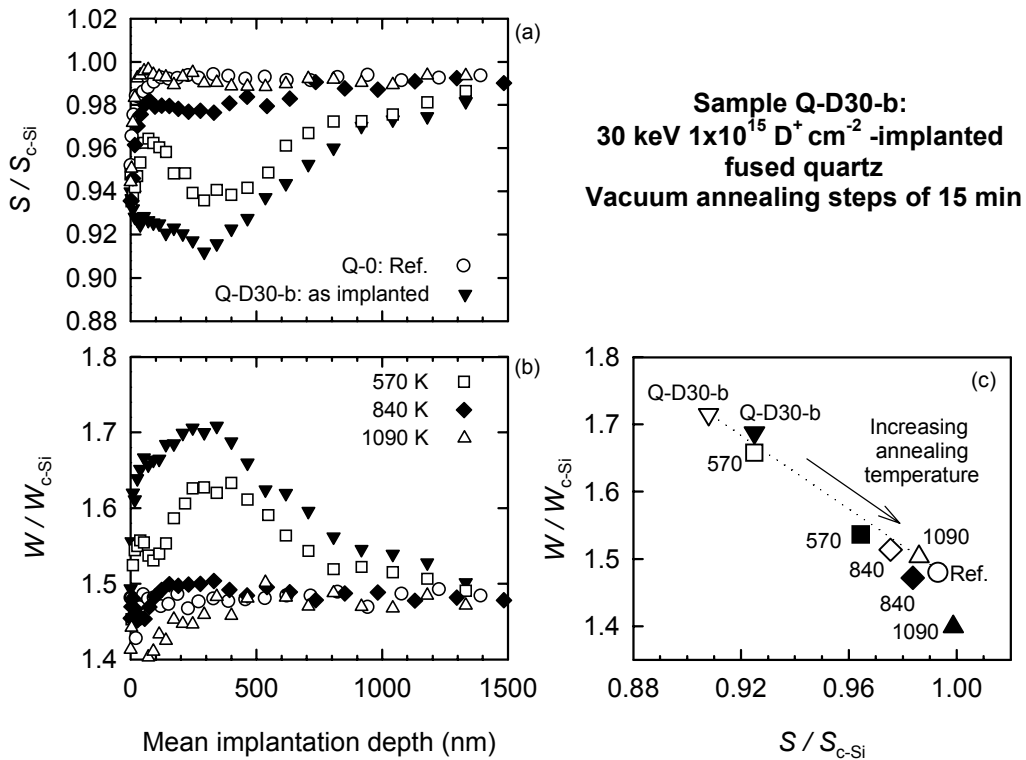


Fig. 6.14. DBAR results for a fused quartz sample (Q-D30-b in Table 6.1) implanted with 30 keV, $1 \times 10^{15} cm^{-2} D^+$ ions. The sample underwent post-implantation vacuum annealing steps of 15 min at the temperatures indicated in the legend. (a) and (b) the S and W parameters respectively normalised to the c-Si values as a function of the positron mean implantation depth. (c) the S - W cluster points corresponding to a region within 200 nm from the surface (solid symbols) and to a damaged region between 200 nm and 600 nm from the surface (open symbols). The numbers indicate the annealing temperature in K. The running parameter is the annealing temperature. The arrow indicates the direction of increasing annealing temperature, while the dotted line only serves to guide the eye.

Annealing of ion-implantation generated defects in the oxide of a MOS sample

The MOS capacitor Ua-He30 (Table 6.1) was implanted with 30 keV He^+ ions to a dose of $1 \times 10^{16} \text{ cm}^{-2}$. Subsequently, it underwent vacuum annealing treatments of 15 min at the temperatures indicated in Fig. 6.17. As in the previous cases, the annealing steps resulting in the gradual recovery of the S - W cluster point characteristic of the untreated oxide. The Al top layer appears to play an important role in the annealing experiments. The recovery of the S - W cluster point occurs more slowly in this case than in previous ones. The maximum temperature reached was 770 K in view of the limit imposed by the melting point of Al. At this temperature, the damage recovery was far from complete.

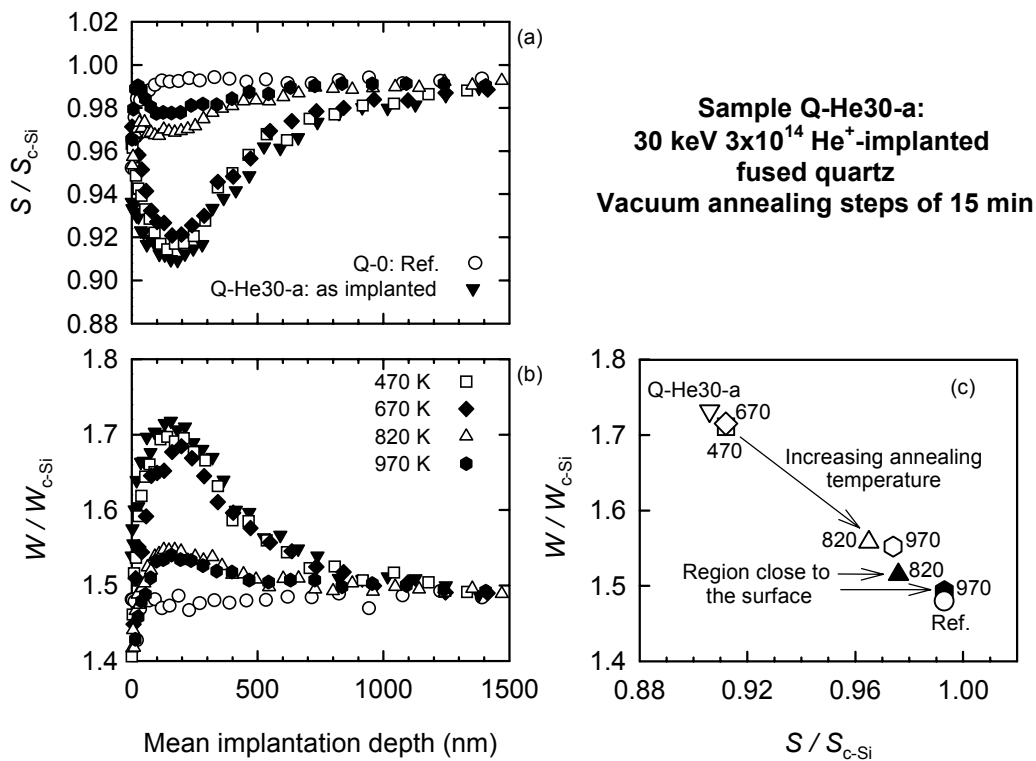


Fig. 6.15. DBAR results for a fused quartz sample (Q-He30-a in Table 6.1) implanted with 30 keV, $3 \times 10^{14} \text{ cm}^{-2} \text{ He}^+$ ions. The sample was subjected to post-implantation vacuum annealing steps of 15 min at the temperatures indicated in the legend. (a) and (b) show the S and W parameters, respectively, normalised to the c-Si values as a function of the positron mean implantation depth. (c) the S - W cluster points corresponding to the damaged region within 400 nm from the surface. Above the annealing step at 820 K another defect layer within 80 nm from the surface is considered (solid symbols). The numbers indicate the annealing temperature in K. The arrow indicates the direction of increasing temperature.

Other experiments

Firstly, untreated SIMOX samples were annealed in D_2 gas. These experiments led to the incorporation of a large amount of deuterium into the BOX layer, as shown in Chapter 5, and to the accumulation of positive charge in the oxide [Vanheusden et al. 1994]. When these treatments were performed on samples with a top Si layer, a significant concentration of mobile D^+ ions was also found [Vanheusden et al. 1997]. Despite these important effects, the

S - W coordinates of the BOX layer did not show any change. This indicates that no positron traps were formed by the D_2 annealing experiments. On the other hand, the interface appeared affected by these experiments.

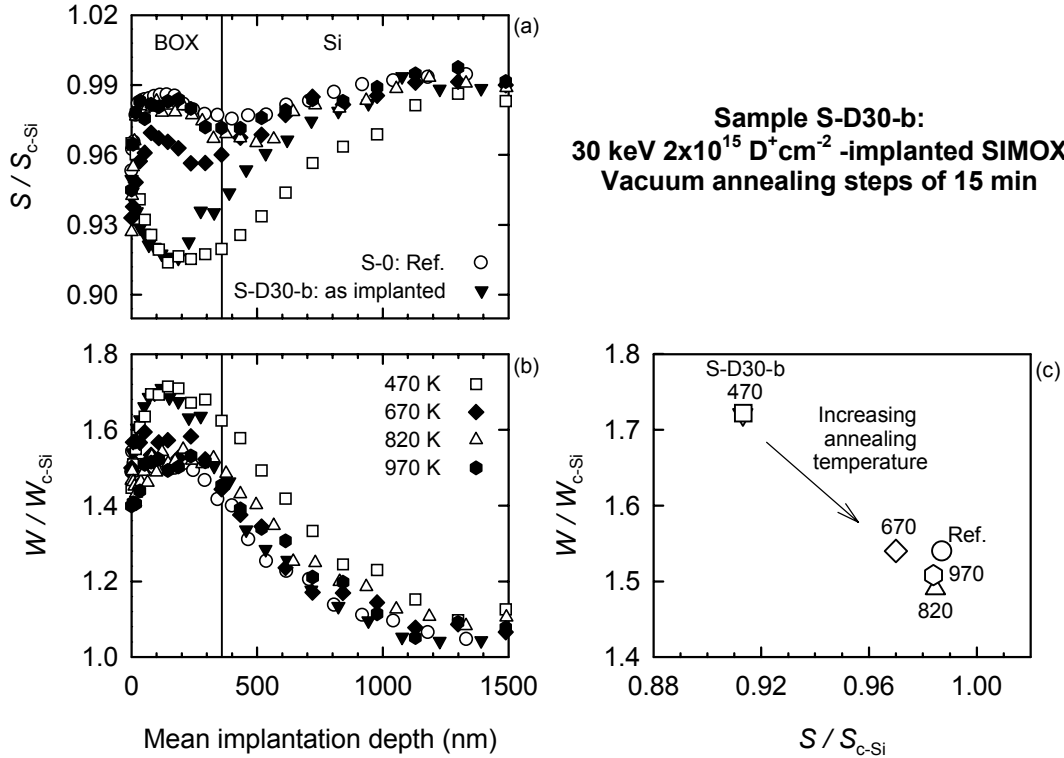


Fig. 6.16. DBAR results for a SIMOX sample with a 190 nm top Si layer and a 360 nm BOX layer (S-D30-b in Table 6.1) implanted with 30 keV , $2 \times 10^{15} \text{ cm}^{-2} \text{ D}^+$ ions. After removing the top Si layer the sample went through post-implantation vacuum annealing steps of 15 min at the temperatures indicated in the legend. (a) and (b) show the S and W parameters respectively normalised to the c-Si values as a function of the positron mean implantation depth. The vertical line represents the boundary between the BOX layer and the Si substrate. (c) the S - W cluster points corresponding to the BOX layer. The numbers indicate the annealing temperature in K. The arrow indicates the direction of increasing temperature.

Secondly, annealing in D_2 at temperatures higher than 500 K of samples containing defects introduced by any of the means shown above, was very effective to reduce the concentration of such defects, indicating that these defects are effectively passivated by deuterium.

Discussion of the annealing experiments

It was mentioned that the oxide annihilation parameters of samples containing defects readily recover to the characteristic values of untreated oxide when annealed in D_2 . Although not as efficient, vacuum annealing of samples containing defects also led to recovery of the original S - W values. On the other hand, we could not detect any significant effect in oxides without

defects annealed in D_2 . This suggests that interstitial deuterium does not interact with the oxide in such a way that positron trapping sites, i.e. dangling bonds, are generated. In addition, it indicates that D_2 acts as a very efficient passivating agent for defects in SiO_2 .

In uncovered samples, the annealing steps led to characteristic S - W values in the region close to the surface. The S values appeared to be higher than those of the untreated SiO_2 while the W values appeared to be lower after annealing steps at high temperature. The trend was to approach values characteristic of Si rather than SiO_2 . A possible explanation for this phenomenon is the interaction of interstitial oxygen with implanted deuterium leading to the formation of water molecules that in turn can (i) interact with defects or (ii) escape through the surface [Shelby 1994]. (ii) is only possible in the near-surface region, otherwise (i) is expected to dominate. The net effect is the loss of oxygen in the near-surface region, thereby leading to a structure similar to amorphous Si (see Chapter 8).

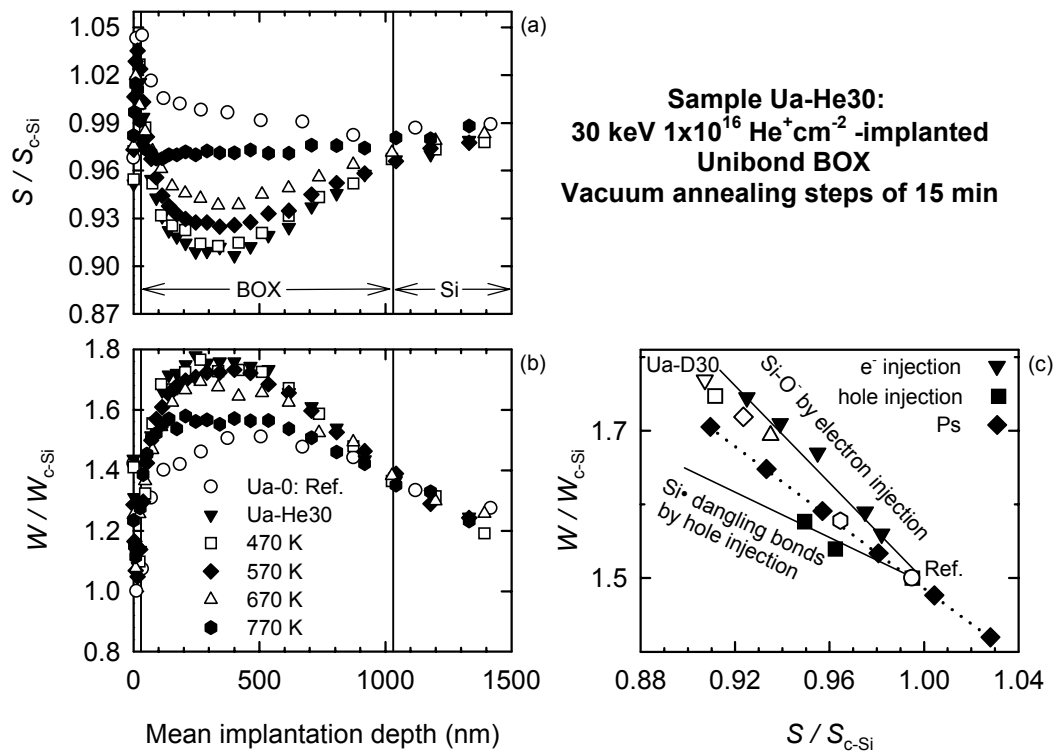


Fig. 6.17. DBAR results for a MOS sample with a 1 μm Unibond oxide (Ua-He30 in Table 6.1) implanted with 30 keV, $1 \times 10^{16} \text{ cm}^{-2}$ He^+ ions. The sample was subjected to post-implantation vacuum annealing steps of 15 min at the temperatures indicated in the legend. (a) and (b) show the S and W parameters, respectively, normalised to the c-Si values as a function of the positron mean implantation depth. The vertical lines represent the boundaries between the Al gate and the BOX layer and between the BOX layer and the Si substrate. (c) the S - W cluster points (open symbols) corresponding to the BOX layer. For comparison, the S - W cluster points, presented in Fig. 6.5, corresponding to electron injection, hole injection and different Ps fractions in the oxide are shown (solid symbols).

6.2.6. Conclusions

Different types of SiO_2 samples were studied after applying certain treatments that introduced defects in the oxides. By means of positron analysis, we were able to identify a number of defects in the samples.

It was shown that the S and W annihilation parameters are linearly dependent on the Ps fraction formed in the oxides. This means that in the absence of positron trapping sites, the S and W coordinates of a SiO_2 layer give a direct estimate of the Ps fraction. The S - W plot can be employed to obtain the Ps fraction once a proper calibration is carried out. For this purpose, a number of experimental results on different oxides were employed. In addition, the Ps line in the S - W plot was obtained from reconstructed 511 keV annihilation peaks containing the desired Ps fraction. The line obtained in this way fairly fits the experimental results and has a considerable practical interest for DBAR studies.

The Ps fraction in SiO_2 was found to be very high, usually around 70%. The presence of OH groups plays an important role in the Ps formation, likely because these defects are electron traps.

Hole injection introduces defects that act as effective positron traps. This proves that these defects are not positively charged, as previously had been suggested. The defects correspond to Si dangling bonds generated upon hole capture at Si-H defects. On the other hand, electron injection leads to the generation of negatively charged defects associated with oxygen atoms. These defects are very efficient positron traps due to their charge state.

The exact estimation of the specific trapping rates associated with hole- and electron-generated defects is complicated. However, some estimates were obtained. They indicate that electron-generated defects are negatively charge constituting very attractive positron trapping centres. Hole-generated defects have a significantly lower specific trapping rate, however, they still constitute effective positron traps.

Ion implantation in the different oxides leads to the generation of a large number of defects as a consequence of displacement of network atoms. The projectile employed seems not to play a major role. Positrons are trapped at oxygen-related defects rather than at silicon-related defects. Annealing experiments show that the positron traps disappear, indicating that they are passivated even by residual hydrogen in the case of vacuum experiments. Passivation of defects in the near-surface region is easier than passivation of defects in deeper regions.

Chapter 7

Positron transport in MOS systems: application to interface studies

The study of interfaces in MOS systems is of considerable interest. In particular, the SiO₂/Si interface is of great importance because many of the problems related to device degradation have their origin at this interface. By means of electrical techniques, the electrical activity of the interface is inferred and accurate estimates on charge accumulation and interface states are obtained. Positron studies at the interface are in general difficult due to the small fraction of positrons that annihilates in this region. In order to increase this fraction, positrons implanted in the oxide of a MOS structure can be drifted to the interface by means of an external electric field. In order to apply this method successfully, one should first understand the basis of positron transport in MOS systems.

As in Chapter 6, the positronium formation process must be taken into account in a proper description of positron transport experiments. Ps is the principal annihilation state in SiO₂. It accounts for about 70% of the annihilations. The probability of Ps formation is a function of the applied electric field because the field plays a role in charge separation, reducing the probability of positron-electron encounters. Therefore, when electric fields are applied, the Ps fraction decreases whereas the fraction transported to and annihilated at interface states increases. These questions will be considered in this chapter in order to describe the experiments performed with electric fields.

First, the fundamentals of positron transport are discussed and then the technique using electric fields will be applied to the study of interfaces in MOS systems.

7.1. Positron transport in SiO₂

MOS samples were employed [Clement et al. 1997] in order to study the SiO₂/Si interface. When external electric fields are applied, positrons implanted in the oxide layer are drifted towards the interface, enhancing the fraction of positrons annihilating at the interface and therefore, the interface signal. The experiments suggested a large positron mobility. This is in contrast with previously reported values of positron mobility [Kong et al. 1991]. An attempt was made in a recent paper to unify the controversial results [Petkov et al. 2002]. Measurements of the annihilation centroid shift performed by Doppler broadening of annihilation radiation (DBAR) experiments on a bulk silica sample [Kobayashi et al. 2001] produced inaccurate results.

The data reported in the literature suggest that positron mobility strongly depends on sample characteristics, e.g. the fabrication process or history. In addition to this, it is important to note that the studies mentioned above did not consider the role of Ps in their results. In this chapter, it will be shown that the Ps formation process can not be excluded from the discussion. Results will be explained on the basis of Ps formation and suppression as a function of the applied electric field.

7.1.1. Experimental

Silicon-On-Insulator (SOI), Unibond samples, like those presented in Chapter 6 with labels “Ua” and “Ub”, were employed to fabricate MOS capacitors. The buried oxide (BOX) of the SOI samples was used as the MOS oxide. Thus, first, the Si top layer was etched in KOH. Then, ~15 nm Al or Au layers were deposited by evaporation onto the bare oxide to act as the gate electrode, see Section 3.1. Table 7.1 gives a description of the different types of MOS capacitors employed. Note that in general more than one sample of every type was employed for experiments.

The samples were studied by positron beam techniques: Doppler broadening of annihilation radiation (DBAR) and two-dimensional correlation of annihilation radiation (2D-ACAR), see Section 3.3. Many of the experiments were performed under the application of external electric fields. This was always performed in the following way: the gate voltage was 0 V, while the voltage applied to the substrate was set to the appropriate level in order to apply the desired electric field to the oxide layer. The sign definition is as follows: a positive electric field means that the electric field drifts positrons away from the gate layer while a negative electric field means that the electric field drifts positrons to the gate layer. Of course, electrons will be drifted in opposite directions due to their negative charge. This sign definition means that in order to apply positive fields to the MOS oxide, negative voltages were applied to the substrate while keeping 0 V on the gate.

In situ high-voltage capacitance-voltage (CV) measurements were regularly performed during the positron experiments in order to estimate the accumulation of charge in the samples because of positron irradiation. No charge accumulation was introduced by DBAR measurements. However, the high intensity positron beam employed for 2D-ACAR experiments introduced positive charge densities higher than $6 \times 10^{11} \text{ cm}^{-2}$ when operating at high oxide fields ($\geq 1 \text{ MV/cm}$) for a few days, resulting in sample degradation.

Table 7.1. Description of the samples employed for positron transport experiments. The labels introduced in Chapter 6 to denote the samples are indicated in brackets.

Sample type	Gate	Oxide	Si substrate
1 Unibond (Ub)	~15 nm Al or Au	3 μm thick	2.3 Ωcm n-Si(100)
2 Unibond (Ua)	~15 nm Al or Au	1 μm thick	2.3 Ωcm n-Si(100)

7.1.2. Observation of positron transport in SiO_2

MOS capacitors of type 1 in Table 7.1 with Al and Au gates were employed for DBAR measurements. Fig. 7.1 shows the results of these measurements. At low energy the influence of the Al or Au gate layer is noticed. The Al layer is associated with a high S value while the Au layer carries a low S value. On the other hand, the W value associated with the Al gate is low while that for the Au gate is high. At higher energies, the characteristic S and W values of SiO_2 are reached. Experiments on the Au-gated capacitor were performed at energies higher than 20 keV, corresponding to mean positron implantation depths beyond 2200 nm, as estimated when assuming a Makhovian implantation profile [Valkealahti et al. 1983, Valkealahti et al. 1984]. An indication of the Si substrate is given by the W parameter, which drops at high positron energy, approaching the characteristic value of Si.

The different annihilation states involved are indicated by open circles in Fig. 7.1c. The running parameter in this plot is the positron energy. The arrows indicate the direction of increasing positron energy. The Si and BOX cluster points are well known and they were comprehensively discussed in Chapter 6. In order to get the Al and Au characteristic cluster points, thick layers were deposited in order to make all implanted positrons annihilate in these layers. The trajectory of the S - W plot in the Au-gated MOS sample starts at the surface annihilation state. It moves to the Au layer with increasing positron energy to reach the SiO_2 at about 5 keV. Due to the high density of Au, a large fraction of positrons is stopped in this layer, giving its typical annihilation signal. At high energy, as indicated above, the Si layer is detected, as shown by the turn of the S - W trajectory towards the Si characteristic cluster point. In the case of the Al-gated sample, the S - W trajectory starts at the surface state, moving towards the Al cluster point. However, due to the low density of Al, not all positrons implanted at low energy are stopped in the Al layer. This is illustrated by the direction of the S - W trajectory, which does not move directly towards the Al cluster point. A significant fraction annihilates at the Al/ SiO_2 interface. This cluster point will be discussed below, but for clarity it is already shown in the plot. By means of these experiments, no information can be extracted about the SiO_2 /Si interface or the Au/ SiO_2 interface, while the Al/ SiO_2 signal is not clear due to the contribution of neighbouring layers.

The application of electric fields results in positron transport towards the interfaces, which enhances the interface annihilation signal. Experiments were performed on similar samples as those presented in Fig. 7.1, in order to study the positron transport and the interfaces.

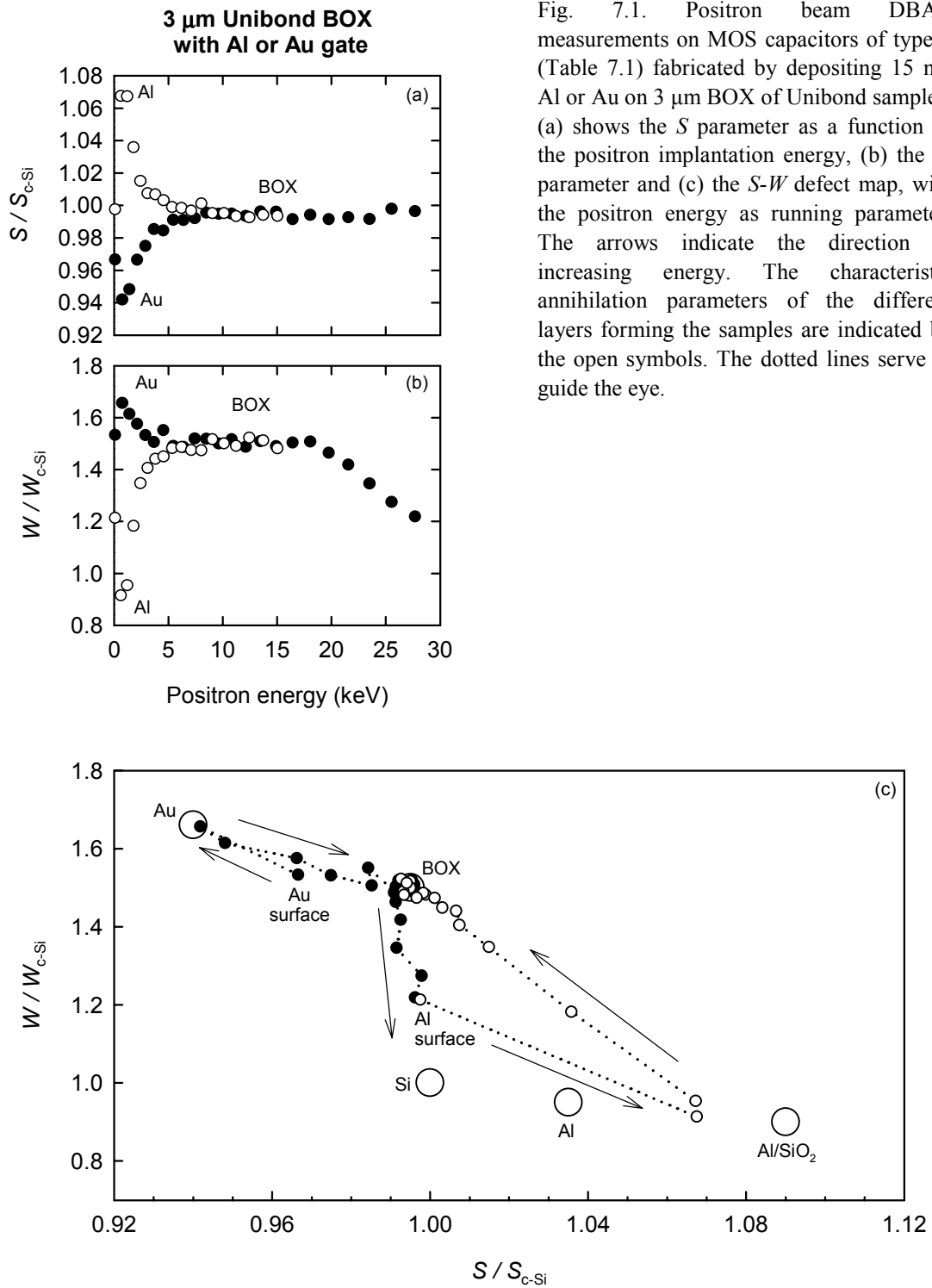


Fig. 7.1. Positron beam DBAR measurements on MOS capacitors of type 1 (Table 7.1) fabricated by depositing 15 nm Al or Au on 3 μm BOX of Unibond samples. (a) shows the S parameter as a function of the positron implantation energy, (b) the W parameter and (c) the S - W defect map, with the positron energy as running parameter. The arrows indicate the direction of increasing energy. The characteristic annihilation parameters of the different layers forming the samples are indicated by the open symbols. The dotted lines serve to guide the eye.

Conclusive evidence of positron transport in the oxide layer is given in Fig. 7.2. Positron beam 2D-ACAR measurements were performed on the Au-gated MOS capacitor

with a 3 μm BOX layer (type 1 in Table 7.1), already presented in Fig. 7.1. The positron energy was fixed at 14 keV during the 2D-ACAR measurements. This implies a positron mean implantation depth of about 1300 nm and assures that 100% of the positrons are stopped in the BOX layer. In all the measurements the Si substrate was oriented in such a way that the p_x and p_y axes are parallel to the directions [010] and [100], respectively. The isotropic components were removed from the 2D-ACAR momentum distributions. In the absence of an electric field, no anisotropy was found in the momentum distribution as expected for amorphous samples, see Fig. 7.2a. In Fig. 7.2b the spectrum obtained at 1.2 MV/cm is shown. Anisotropy features significantly exceeding background are visible. For comparison, the anisotropy of the momentum distribution measured with fast positrons for Si(100) is presented in Fig. 7.2c. The same type of anisotropy is observed for this sample as for the MOS capacitor at 1.2 MV/cm. Anisotropic peaks at $(\pm 3, \pm 3) \times 10^{-3} m_0 c$ appear. This anisotropy can only be produced when positrons overlap with electrons in a periodic structure like the Si substrate. This proves that positrons were drifted by the electric field to the interface where a fraction of them annihilated with electrons from the underlying Si substrate. The fraction of positrons annihilating with Si electrons is as low as 8%, as estimated from the momentum distribution.

Similarly, one can observe positron transport when a negative bias is applied. Fig. 7.3 shows DBAR measurements on Al- and Au-gated MOS capacitors with the thinner oxides (1 μm), i.e. type 2 in Table 7.1. At 6 keV positron implantation energy, the mean implantation depth is about 330 nm. Nearly 100% of the positrons is stopped in the BOX layer. At high negative electric field most of the positrons are drifted back to the gate. The results show a clear dependency on the gate material employed. Al-gated MOS capacitors show a high S (low W) value at negative fields, associated with annihilations at the Al/SiO₂ interface.

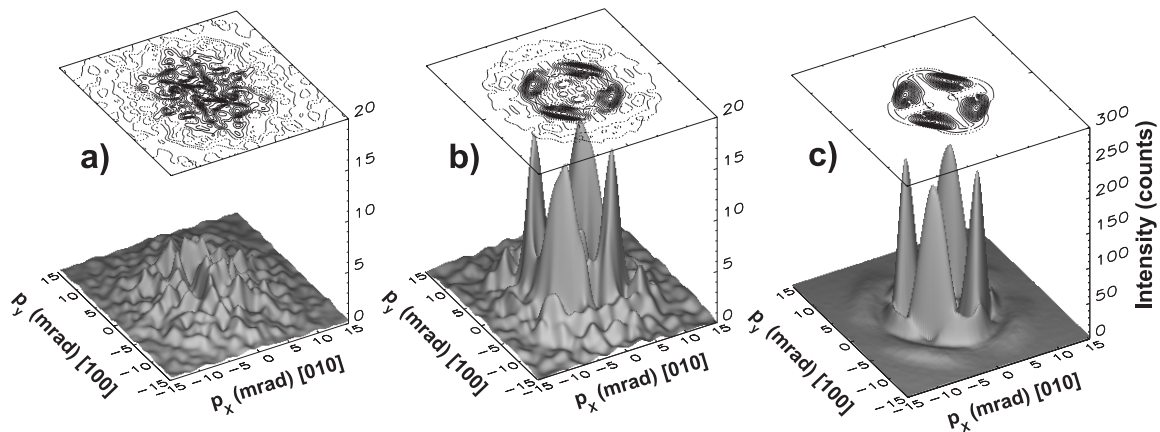


Fig. 7.2. Anisotropy of the 14 keV 2D-ACAR momentum distributions obtained (a) without the application of an external field and (b) with a positive electric field of 1.2 MV/cm across the oxide. For comparison, the anisotropy of the 2D-ACAR momentum distribution obtained with fast positrons for a bulk Si(100) sample is presented in (c).

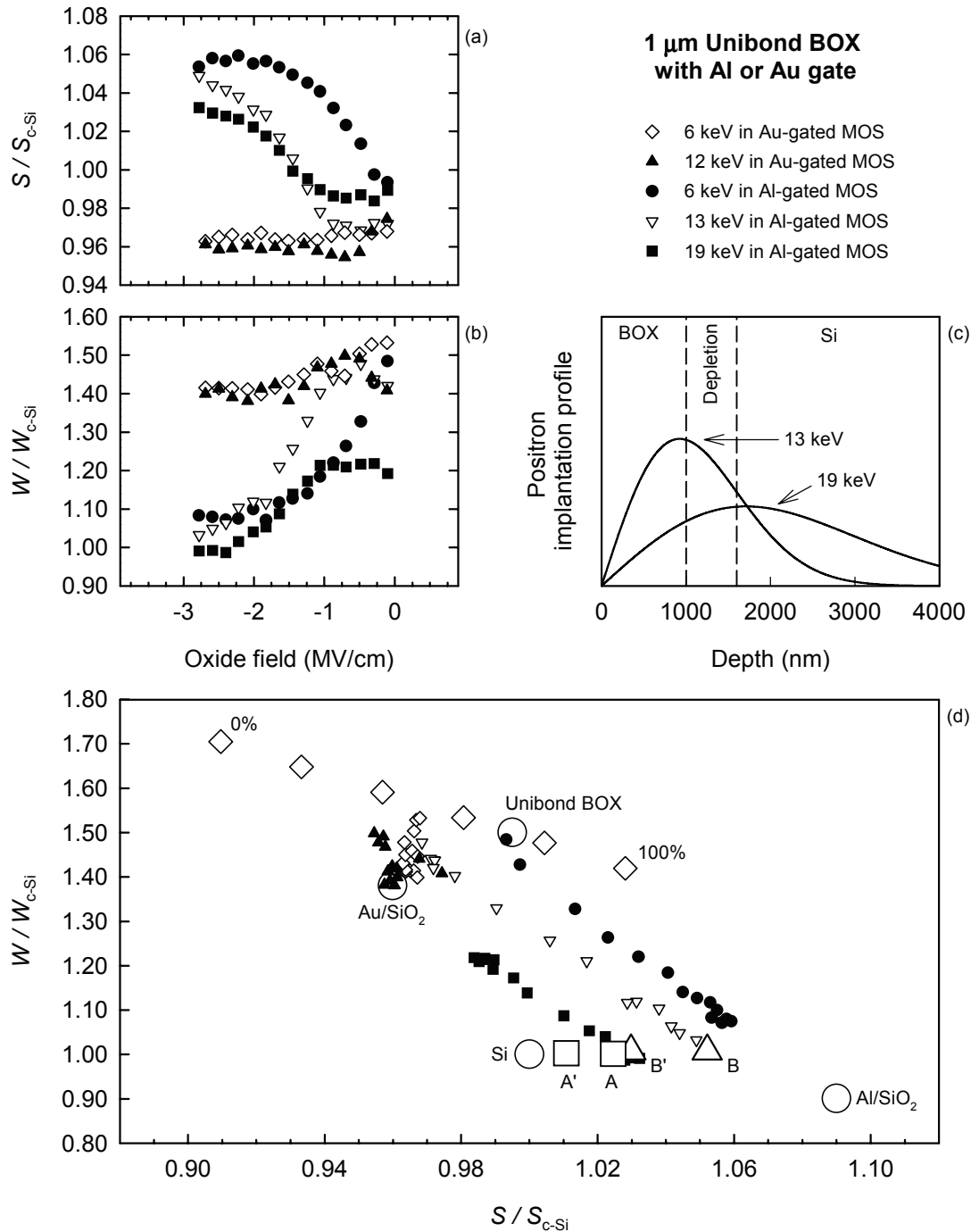


Fig. 7.3. DBAR measurements on MOS capacitors fabricated by depositing 15 nm Al or Au on 1 μm BOX of Unibond samples (type 2 in Table 7.1). (a) shows the S parameter as a function of the oxide field, (b) the W parameter. (c) shows the Makhovian positron implantation profiles at the indicated positron energies. (d) shows the S - W map of defects, with the oxide field as a running parameter. The different annihilation states are indicated by means of open circles, while the diamonds represent the estimated S - W coordinates corresponding to annihilation in the BOX layer when the fraction annihilated as Ps changes as indicated (see Section 6.2). The squares labelled “A” and “B” represent the annihilation points at -3 MV/cm, corresponding to implantation energies of 19 and 13 keV, respectively. They were calculated from the estimated fractions of positrons annihilating in Ps states, in the BOX, in Si and at the Al/SiO₂ interface, according to the text.

On the other hand, Au-gated MOS capacitors show a low S (high W) value associated with the Au/SiO₂ interface. This is another clear evidence of electric-field assisted positron transport in the BOX layer, as first demonstrated by [Clement et al. 1997] is similar experiments. At higher implantation energies, the Si substrate plays a role because a significant fraction of positrons is implanted in the substrate, see Fig. 7.3c. The positron mean implantation depth corresponding to 12, 13 and 19 keV is about 1020, 1160 and 2140 nm, respectively. It will be demonstrated that positrons drifted in the inversion layer of the n-type Si substrate are also drifted back towards the gate, due to the electric field present in the inversion layer (Section 7.1.6).

7.1.3. Determination of the Al/SiO₂ cluster point

In order to obtain quantitative information, it is important to know accurately the cluster points corresponding to the gate/oxide interfaces. However, this is not easy by conventional measurements, as shown in Fig. 7.1. Instead, the Al/SiO₂ interface coordinates can be precisely estimated by means of DBAR measurements as a function of positron implantation energy while applying negative electric fields [Clement et al. 1997]. This is possible because at low energy, the implantation profile is narrow, i.e. most of the positrons are implanted in the SiO₂ layer very close to the Al/SiO₂ interface. For example, at 2 keV the mean implantation depth is ~60 nm and more than 94% of the positrons are implanted in SiO₂ with a significant fraction from the remaining 6% annihilating at the Al/SiO₂ interface. Therefore, most of the positrons implanted at low energy under negative electric field will be drifted to the Al/SiO₂ interface and annihilate there.

Fig. 7.4 shows the result of an experiment on an Al-gated MOS capacitor with 1 μm-thick oxide (type 2 in Table 7.1). The application of electric fields to the MOS sample drastically changes the S and W plots. A positive field results in a significant drop in the S parameter with a minimum at around 6 keV, while a negative field causes a significant increase in the S curve. Opposite effects are observed for W . The S - W plot helps to understand these effects. The application of positive electric fields drifts positrons to the SiO₂/Si interface, significantly enhancing the fraction of positrons annihilated at the interface at the expense of BOX annihilations. This is shown by the direction of the S - W trajectory under positive bias, clearly deviating from the BOX direction and revealing the SiO₂/Si interface cluster point (complete discussion in Section 7.2.2). This is in agreement with results by [Clement et al. 1997].

The mean implantation depth of positrons at 1 keV is about 15 nm. This means that positrons implanted at this energy annihilate in the Al layer or at the interface, giving a signal which is a combination of both states. In Fig. 7.4c, the point corresponding to implantation at about 1 keV is indicated by the label “Al+Al/SiO₂”. Since it is a combination of the Al and Al/SiO₂ states, it must be on the line connecting the Al and the Al/SiO₂, indicated by the dashed line. An increase in the positron energy results in an increased number of positrons implanted in the SiO₂ layer. A fraction of them will annihilate in the SiO₂ layer. However, the application of the electric field causes reduction of the Ps formation. In this case, positrons annihilating in the BOX will give an annihilation signal that differs from that of BOX without

fields, as shown in Section 6.2. The S parameter will drop while the W parameter will increase with decreasing Ps fraction. The characteristic S - W coordinates of the BOX layer for different Ps fractions is indicated by the line of diamonds. It can be observed that the experimental points move along the dashed line when the positron implantation energy increases. The endpoints of this line correspond to annihilations in the BOX layer with a Ps fraction reduced to zero and to annihilations at the Al/SiO₂ interface, respectively. From the diamond line, it can be concluded that the application of an electric field of -0.6 MV/cm causes a reduction of the Ps fraction in the BOX to about 30%. In addition, the Al/SiO₂ interface can be found as the intersection of the two dashed lines, in perfect agreement with experiments performed by [Clement et al. 1997] at higher fields on thermal oxides that were not subjected to post-metallisation annealing, as in our case. As confirmation, we extracted the Al/SiO₂ interface cluster point from the experimental curves presented in Fig. 7.1, making use of the fitting routine VEPFIT [van Veen et al. 1990]. The values found in this way are in agreement with experiments at negative fields.

7.1.4. Positronium reduction under the application of electric fields

Fig. 7.5 shows the decomposition into two components of the 2D-ACAR cross sections in the p_x direction obtained from the momentum distributions presented in Fig. 7.2a and Fig. 7.2b. The narrow component corresponds to p-Ps self-annihilation and the broad component to SiO₂ bulk annihilations. Both components were considered to be gaussian functions. The full width at half maximum (FWHM) corresponding to the p-Ps component was about 3.8×10^{-3} m₀c, while the FWHM of the bulk SiO₂ component was about 10.0×10^{-3} m₀c. Note that these components are convoluted with the resolution function of our 2D-ACAR system which has a FWHM of 1.4×10^{-3} m₀c. The p-Ps fraction was estimated from the contribution of the narrow component. Assuming that the p-Ps to o-Ps ratio is 1 to 3, we estimated the total Ps fraction. The Ps fraction determined in this way is presented in Table 7.2 for sample type 1. The fraction of positrons that forms Ps in SiO₂ is very large (see also Section 6.2), dominating the positron annihilation process. In addition, it decreases with increasing electric field intensity, as shown in the table. It should be noted that the Ps fraction measured by 2D-ACAR at 1.2 MV/cm might include a significant fraction of Ps formed at the SiO₂/Si interface, as will be discussed in the following.

Clear evidence of Ps reduction under the application of an electric field is presented in Fig. 7.6, where DBAR results are shown. The measurements were performed on Al-gated MOS capacitors with a 3 μm thick oxide (sample type 1 in Table 7.1). The curves shown were measured at positron energies of 5, 8, 11 and 17 keV, corresponding to mean implantation depths of ~250, 530, 890 and 1790 nm, respectively. The S parameter decreases at moderate fields and increases when the absolute value of the applied field is high, approaching the value found above for the Al/SiO₂ interface. The decrease at moderate fields leads to the appearance of a valley in the S plot (Fig. 7.6a). This valley becomes more pronounced when the positron implantation depth increases. On the other hand, the opposite effect occurs in the W parameter. It increases at moderate field, showing a maximum in the W plot (Fig. 7.6b). This peak is more pronounced at high positron implantation energies.

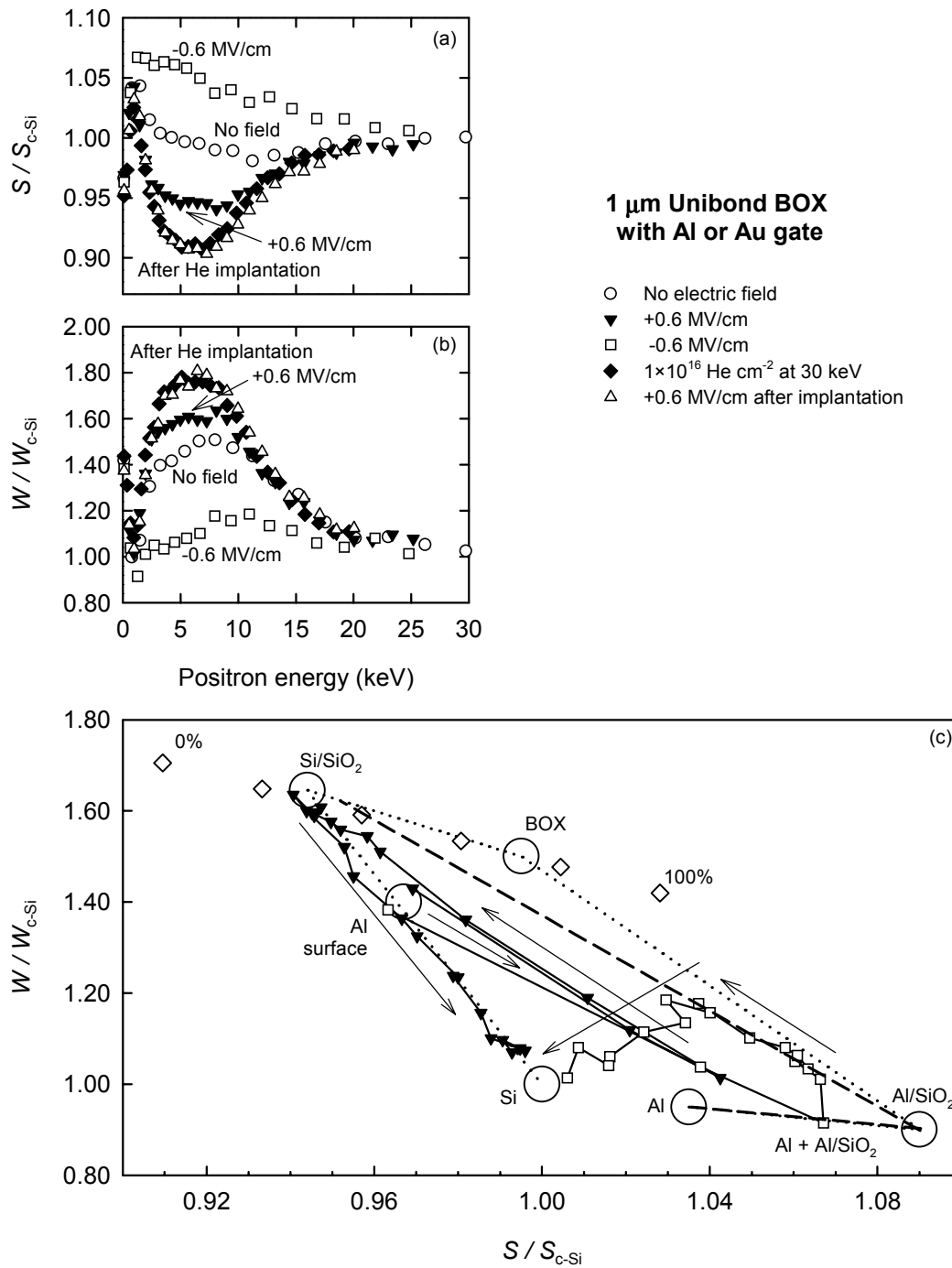


Fig. 7.4. DBAR measurements performed with and without external electric field on an Al-gated MOS capacitor of type 2. The sample was re-measured with and without electric field after implanting He ions into the BOX, as indicated by the legend. (a) shows the S parameter as a function of the positron implantation energy, (b) the W parameter and (c) the S - W map of defects, with the positron energy as a running parameter. The cluster points are indicated by open circles. The diamonds represent the estimated S - W coordinates corresponding to the BOX layer for the indicated Ps fractions (see Section 6.2). The dotted lines connecting the cluster points and the solid lines connecting experimental points are guides to the eye, whereas the arrows indicate the direction of increasing positron energy. The dashed lines join the Al and Al/SiO₂ points and the Al/SiO₂ point and the characteristic BOX cluster point when the Ps fraction is reduced by the electric field to $\sim 30\%$ (see the text).

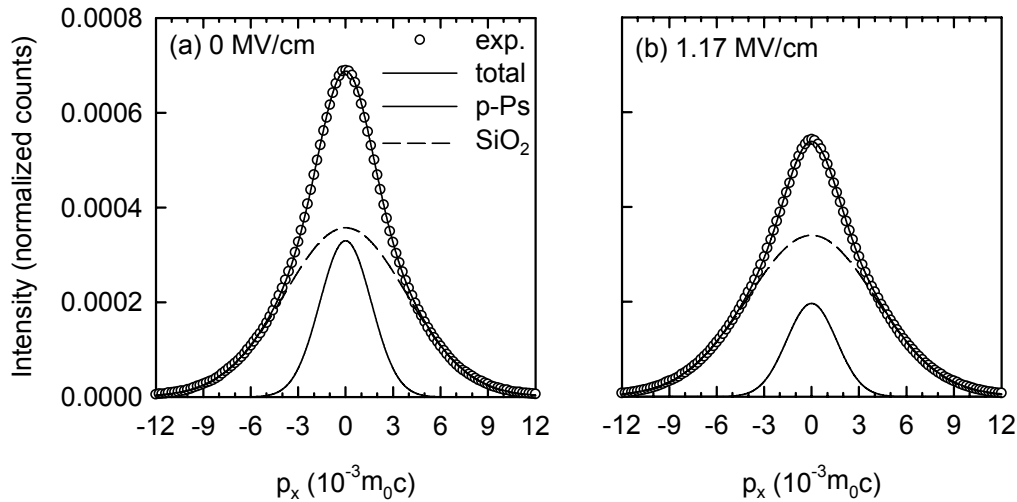


Fig. 7.5. Decomposition into two components (p-Ps and SiO₂) of the 2D-ACAR cross-section in the p_x direction for a MOS capacitor with a 3 μm oxide. (a) in the absence of an electric field, (b) under 1.2 MV/cm.

Table 7.2. Ps fraction calculated from 2D-ACAR measurements on samples presented in this chapter. Note that the total Ps fraction is assumed to be 4 times larger than the p-Ps fraction.

Sample type	Oxide	E (MV/cm)	pPs fraction (%)	Total Ps fraction (%)
1 Unibond (Ub)	3 μm thick	0	18 ± 2	72 ± 8
		1.2	12 ± 4	48 ± 8

The S - W curves corresponding to positron implantation energies of 5 and 17 keV are shown by means of solid curves in Fig. 7.6c. As in previous figures, the diamond symbols represent the S - W cluster point corresponding to annihilations in the Unibond oxide layer when the Ps fraction changes as indicated by the labels (see Section 6.2). At moderately negative fields, the S - W trajectory moves along the line of Ps reduction, following the imaginary line joining the diamond symbols, as indicated by the arrow. At larger negative fields, the S - W trajectory clearly deviates from this line and approaches the cluster point corresponding to Al/SiO₂. The probability of reaching this point increases when positrons are implanted at the lowest energy, because they need to travel a shorter distance. In the S - W plot the cluster points corresponding to the different annihilation states are clearly identified. They are labelled as “0%”, “100%” and Al/SiO₂, corresponding to the annihilations in the following states: the BOX layer when no Ps is formed, Ps in the BOX layer and the Al/SiO₂ interface, respectively.

The observed trend clearly indicates that the Ps fraction decreases with increasing electric field intensity, leading to an S - W trajectory that moves from the typical BOX cluster

point towards the cluster point associated with annihilations in the BOX when 0% Ps is formed and turning towards the Al/SiO₂ interface at high fields (in absolute value).

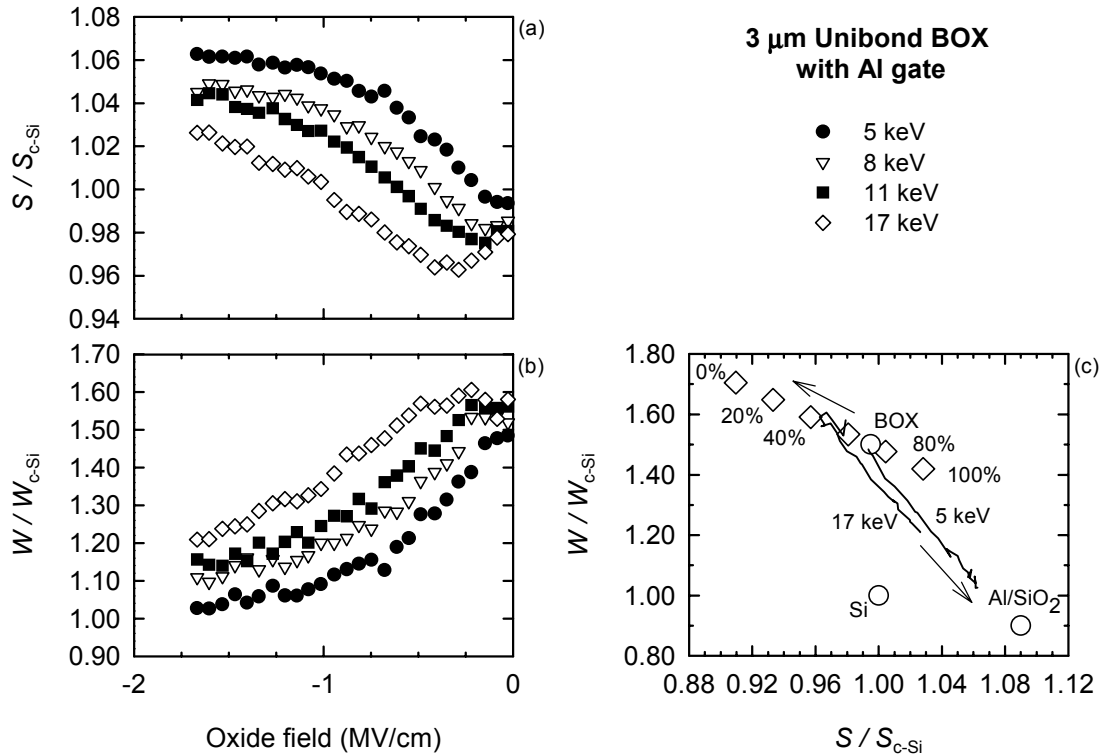


Fig. 7.6. Positron beam DBAR measurements on MOS capacitors fabricated by depositing 15 nm Al on 3 μ m BOX of Unibond samples. (a) shows the S parameter as a function of the oxide field, (b) the W parameter and (c) the $S-W$ defect map, with the oxide field strength as running parameter. For reasons of clarity, the experimental curves corresponding to experiments performed at 5 and 17 keV positron energy, are represented by thick solid lines. The different annihilation states are indicated by means of open circles. The diamonds represent the estimated $S-W$ coordinates corresponding to annihilation in the BOX layer for varying Ps fraction, as indicated (see also Section 6.2).

7.1.5. Modelling the combined effect of positron transport and Ps reduction

Once the cluster points are known the annihilation fractions at every state can be calculated from the experimental data. This will be shown for the experiments presented in Fig. 7.6. Since only three states are involved, the system of the three following equations has an analytical solution for F_i : $S = \sum F_i S_i$, $W = \sum F_i W_i$ and $1 = \sum F_i$, where S and W represent the experimental parameters, F_i the fraction of positrons annihilating at every layer and S_i-W_i the characteristic annihilation parameters of every state i involved, see Section 3.3. The symbols in Fig. 7.7 represent the resulting fractions of positrons as a function of the electric field.

When the experimental $S-W$ points presented in Fig. 7.6 are on the Ps line, represented by diamonds, only two states were assumed to contribute: annihilations from Ps states in the BOX (labelled “100%”) and positron annihilation in the BOX (“0%”). The fraction of

positrons reaching the Al/SiO₂ interface was assumed to be zero. Notice that this is a drastic approximation that results in an overestimation of the positron fraction annihilated in the bulk at low electric fields. The Ps fraction at 5 keV was found to differ from the Ps fraction at other energies. It was fitted by a decaying exponential function, as indicated in Fig. 7.7. The Ps fractions obtained at other energies were fitted simultaneously (see also Section 7.1.7).

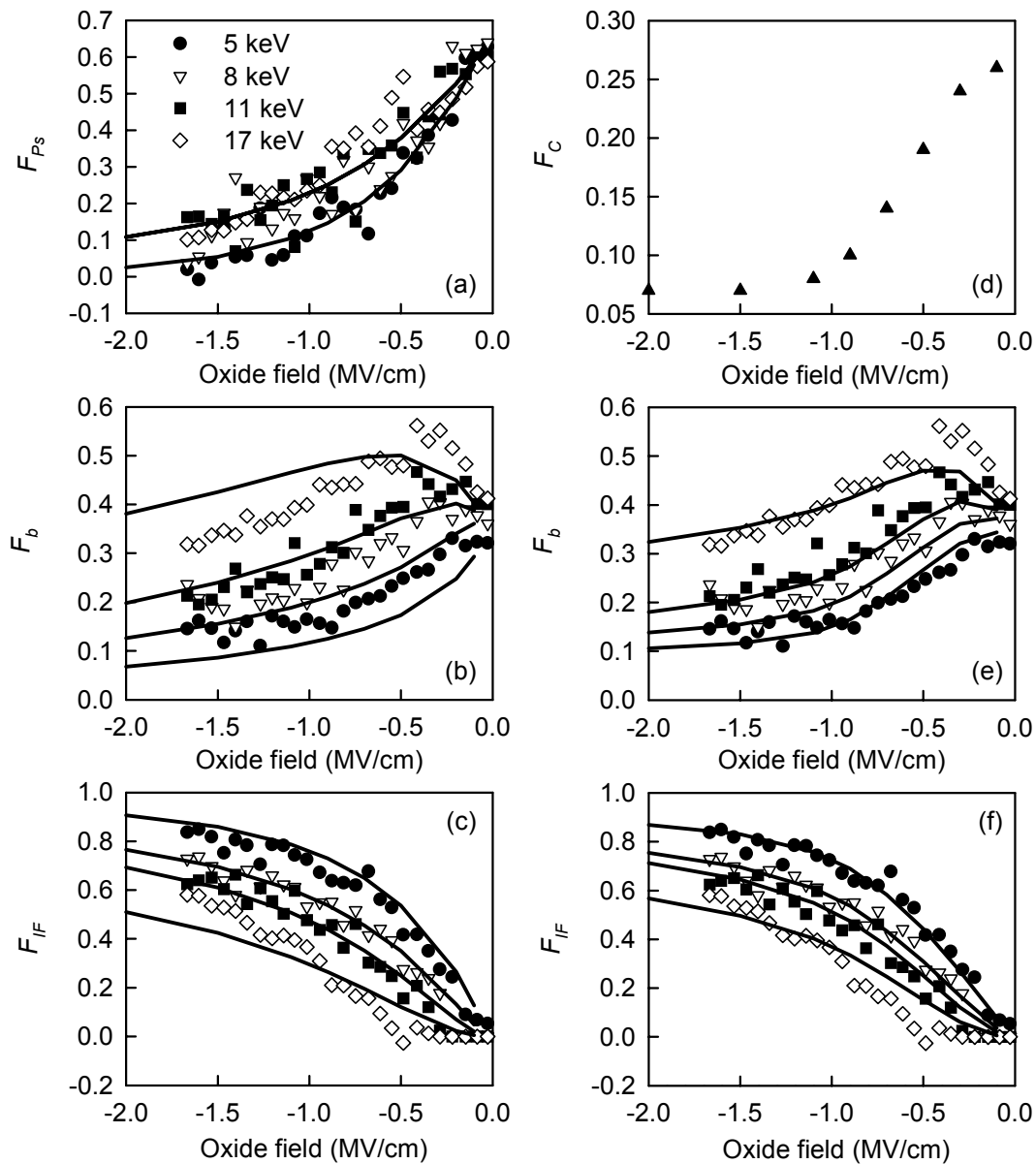


Fig. 7.7. Fractions of positrons as a function of the electric field that annihilate as Ps, in the bulk and at the interface for an Al-gated MOS capacitor of type 1. The F_{Ps} curves were fitted by means of decaying exponential functions. All curves obtained at energies higher than 5 keV were fitted together, while the 5 keV curve was fitted independently. The F_b and F_{IF} fractions were modelled as indicated in the text. For panels (b) and (c), a constant positron diffusion length of 21 nm was assumed, while in panels (e) and (f), a field-dependent fraction of positrons F_C was assumed to be confined during the Ps formation process (see text). F_C is plotted in (d).

The experiments can be understood in terms of the positron branching ratios resulting from the different processes that take place. This is schematically shown in Fig. 7.8 and Fig. 7.9 for samples of type 1. It is assumed that these samples do not contain significant concentrations of positron trapping sites. In the absence of an electric field, the implantation of positrons at energies between 11 and 15 keV leads to results in about 100% of the positrons thermalised in the BOX layer, see Fig. 7.8. As discussed in Section 6.2, Ps is readily formed resulting in 72% of the positrons being in Ps states (both p-Ps and o-Ps). After certain characteristic time elapses, positrons in p-Ps, o-Ps or free in the bulk annihilate. In total, 100% of the annihilations take place in the oxide layer. When an electric field is present the positron branching ratios change significantly, see Fig. 7.9. Implantation at 11 keV leads to 100% of the positrons being thermalised in the oxide layer, as in the previous case. However, the effect of the electric field leads to a much smaller Ps formation. At 1.2 MV/cm, only about 20% of the positrons will form Ps. The remaining 80% is in principle free to travel along the oxide and is drifted towards the Al/SiO₂ interface by the applied electric field, as indicated in Fig. 7.9. It is observed in Fig. 7.7 that at 11 keV and 1.2 MV/cm about 55% of the positrons reach the interface. As will be discussed in Section 7.2.3, once positrons reach the interface Ps may be formed due to the availability of electrons. In total, 55% of the implanted positrons annihilate at interface states while 45% annihilate in the oxide layer both at Ps states or free in the oxide.

In order to model the results we used the formalism described in Section 2.3. It was assumed that the fraction of positrons forming Ps, F_{Ps} , is not drifted by the applied electric field since the mobility of Ps is much lower than that of free positrons. The fraction of remaining positrons, $F_0 = 1 - F_{Ps}$, was assumed to obey the stationary drift-diffusion equation [van Veen et al.1990]. The solution of the diffusion equation, assuming that the mobility and the diffusion constant are linked by the Einstein relation, only depends on the positron effective diffusion length for a given implantation energy and a given electric field. The positron diffusion length is defined as

$$L_{eff} = \sqrt{\frac{D_p}{\kappa_t + \lambda_b}} \quad (7.1)$$

where D_p represents the diffusion constant for positrons, κ_t the positron trapping rate and λ_b the bulk annihilation rate (see Section 3.3).

The solid lines in the plots on the left side of Fig. 7.7 for F_b and F_{IF} correspond to the solution of the diffusion equation for the fraction of positrons F_0 transported by the electric field. A positron diffusion length $L_{eff} = 21$ nm was found to give the best fit to the experimental fractions. The model yields a fair approximation of the experimental fractions. However, it is unable to predict the calculated fractions simultaneously for all positron implantation energies. Evidently, there is some aspect not included in the model.

The assumption that the number of positrons available for transport by the electric field was $F_0 = 1 - F_{Ps}$, might be not true. As explained in Section 3.2, Ps is formed by interaction with electrons promoted to the conduction band during the slowing-down of the incoming

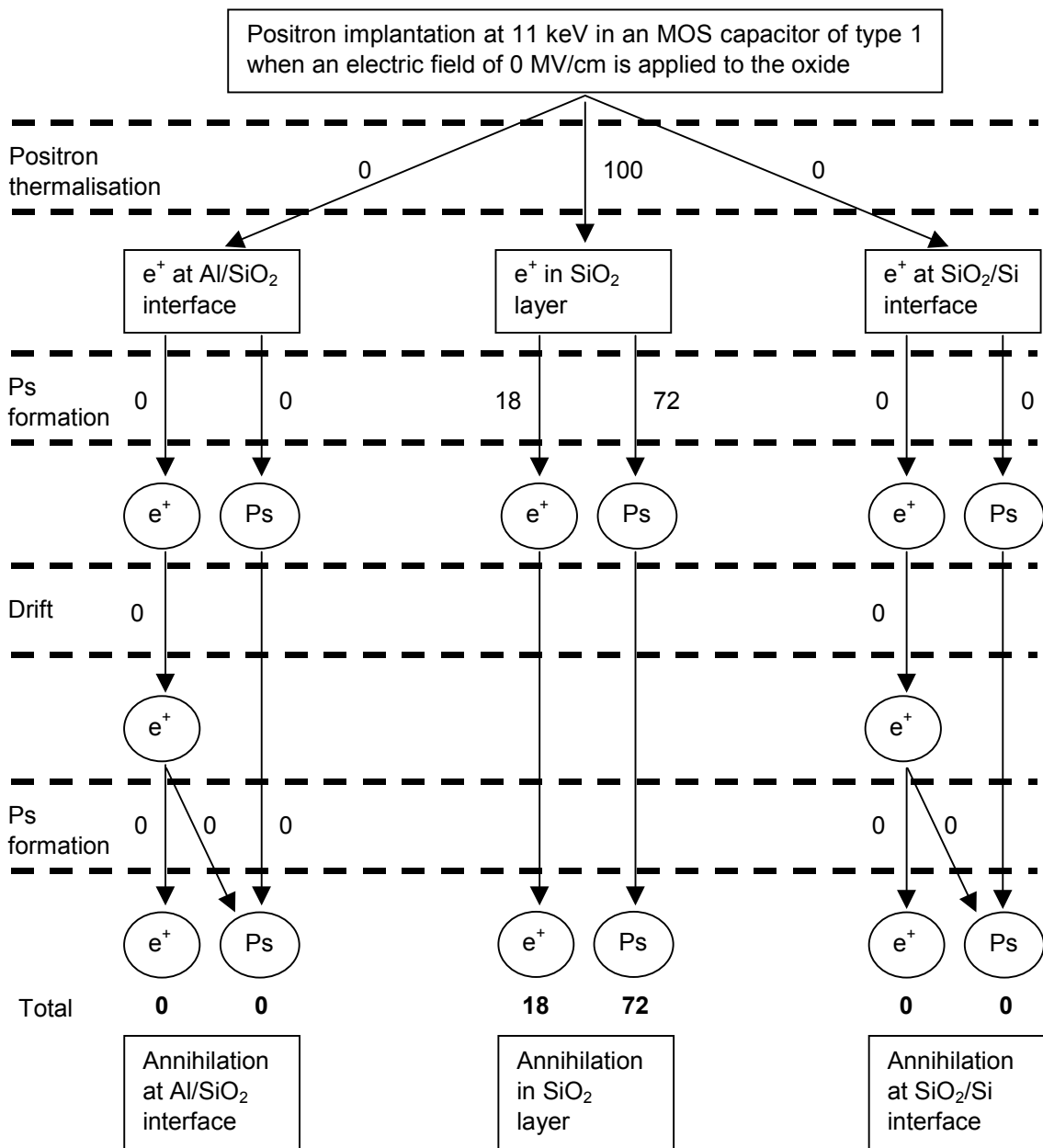


Fig. 7.8. Positron branching ratio diagram corresponding to a sample of type 1 when no electric field is applied to the oxide. The numbers indicate the percentage of the implanted number of positrons annihilating from a specific state in each process.

positron. These electrons form a spur around the stopped positron. A significant number of positrons can be confined during the Ps formation stage in this spur, reducing the initial number of positrons available for transport. This confinement effect is related to screening of the applied electric field by the cloud of electrons, which move in opposite direction from positrons, [Stepanov et al 2002]. In addition, a large concentration of holes is present in the

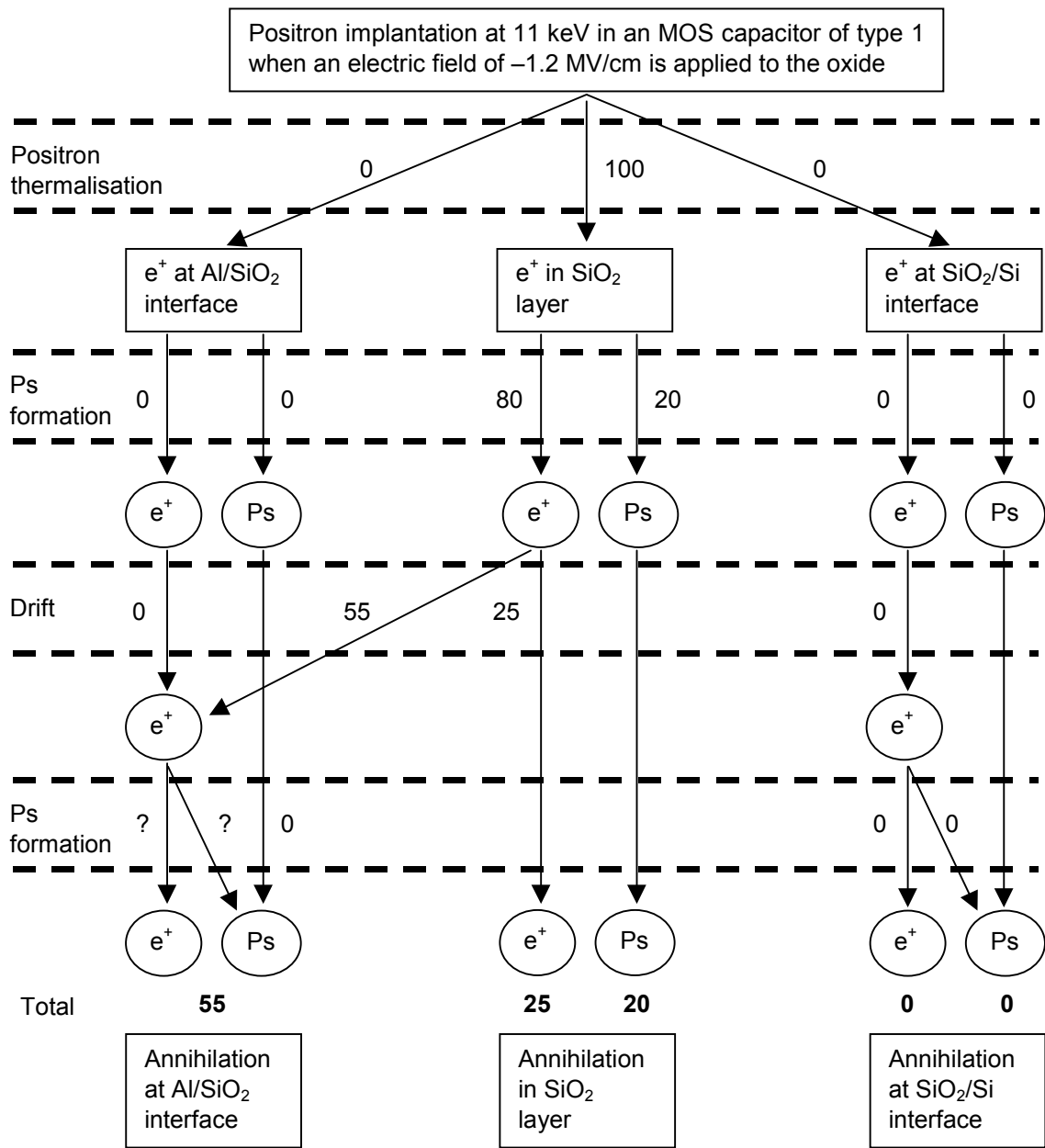


Fig. 7.9. Positron branching ratio diagram corresponding to a sample of type 1 when an electric field of -1.2 MV/cm is applied to the oxide. The numbers indicate the percentage of the implanted number of positrons annihilating from a specific state in each process.

spur. The mean free path of positrons in this region can be significantly reduced, resulting in a reduced mobility.

This confinement effect implies that the initial fraction of positrons available for transport is reduced to

$$F_0 = 1 - F_{Ps} - F_C \tag{7.2}$$

where F_C represents the fraction of positrons confined during the Ps formation process. The results, obtained when F_0 is taken equal to the initial number of positrons that can be drifted by the electric field, are shown by solid lines in Fig. 7.7e and f. The diffusion length L_{eff} was found to be 28 nm. The values employed for F_C in order to model the data are presented in the top right panel of Fig. 7.7. The confinement effect reduces with increasing electric field intensity, in agreement with the assumption of confinement in the spur. Clearly, this correction makes fitting possible for all positron implantation energies. However, at low electric fields there are still disagreements with the experimental fractions. Possibly, the reason is that the assumption of 0% positrons reaching the interface at low field is too drastic, which results in an overestimate of F_b .

From the diffusion length estimated by the model, 28 nm, the positron diffusion coefficient can be calculated. Assuming that positrons that do not form Ps are free to move and assuming that no positron traps are present in the sample, we can write from (7.1)

$$L_{eff}^2 = \frac{D_p}{\lambda_b} = D_p \tau_b \quad (7.3)$$

where τ_b is the positron lifetime in SiO₂. Using results from [Dannefaer et al. 1993], $\tau_b = 290$ ps. Thus, a positron diffusion coefficient in SiO₂ of $D_p = 0.03$ cm²/s is obtained. Assuming that the Einstein relation is valid, the positron mobility then equals $\mu_p = 1.2$ cm²/(Vs).

We considered that the strength of the electric field in the BOX layer is in absolute value the same, irrespectively of the bias polarity applied to the gate. It is true that a certain voltage drop takes place in the depletion region formed in the underlying Si substrate when it is in depletion or inversion. This occurs at a negative gate voltage for n-Si and a positive gate voltage for p-type Si. However, this drop is smaller than 1 V, which is totally negligible when calculating the electric field intensity in thick oxides. Please, note that in [Petkov et al. 2002] the authors overestimated the drop in the depletion layer, inducing them to conclude that the electric field strength depends on the polarity. Even in the case of deep depletion the voltage drop in the depletion layer is not so important as to account for significant differences in oxide fields when dealing with thick oxides. In addition, positron measurements are performed over long periods of time at room temperature in which an inversion layer can easily be formed by thermal generation of minority carriers, eventually avoiding the deep depletion situation.

7.1.6. Positron implantation in the depletion layer of the Si substrate

The application of a negative bias to the gate of a MOS capacitor with an n-Si substrate, will result in the formation of a depletion layer in the substrate. Once the Si substrate is in inversion due to a sufficiently large negative bias, the width of this layer will not change and will depend mainly on the doping level of the substrate. Positrons implanted in this layer will be affected by the electric field. Owing to the large positron mobility in Si, ~ 100 cm²/(Vs) [Simpson et al. 1989], they will be drifted towards the SiO₂/Si interface and injected into the BOX layer.

Making use of the model proposed, we will explain the DBAR measurements obtained for Al-gated MOS capacitors with 1 μm -thick oxide (type 2 in Table 7.1) shown earlier in Fig. 7.3. In Fig. 7.3d, two points labelled “A” and “B” are indicated. They represent the annihilation signal at -3 MV/cm for the samples implanted at 19 and 13 keV, respectively. They contain the contribution of the following states: Al/SiO₂ interface, Ps in the BOX, free annihilations in the BOX and Si substrate.

At this value of the negative electric field, the maximum fraction of positrons that will form Ps is about 7% according to the results shown in Fig. 7.7. The fraction of positrons implanted in the oxide is 44% and 16% for positron energies of 13 and 19 keV, respectively, as obtained by integration of the Makhovian profiles shown in Fig. 7.3c. Thus, the Ps fraction in the oxide is $0.44 \times 0.07 \sim 3\%$ and $0.16 \times 0.07 \sim 1\%$, for 13 and 19 keV positron implantation energy, respectively.

In addition, we can estimate the fraction of positrons implanted in the depletion layer formed at negative voltage in the n-Si substrate. Since the thickness of this layer is about 600 nm, estimated on the basis of the conductivity of the n-Si substrate, the fraction of positrons stopped in this layer is expected to be 33 and 20% for positron energies of 13 and 19 keV, respectively. These positrons can not form Ps after injection into the BOX due to the lack of available electrons in the oxide (see Section 3.3). The fraction of positrons annihilating deeper in the Si substrate, beyond the depletion region, is 23% and 64% for 13 and 19 keV positron energy, respectively.

A fraction of the positrons drifted from the Si depletion layer towards the gate will annihilate in bulk SiO₂. This fraction was estimated for positrons implanted into SiO₂ and it was found to depend on the implantation energy. However, these fractions were calculated for positrons implanted exclusively in SiO₂, on 3 μm -thick oxides. We consider that the results obtained for energies lower than 11 keV, which implies a mean implantation depth of ~ 890 nm, can be employed for samples with a 1 μm -thick oxide, because positrons implanted in the depletion layer will swiftly be injected back into the oxide and those implanted in the substrate will not contribute to transport processes. According to the model, at -3 MV/cm this fraction is $\sim 10\%$. Therefore, at 13 keV, $(0.44 + 0.33) \times 0.1 \sim 8\%$ of the positrons will annihilate in the BOX and at 19 keV $(0.16 + 0.20) \times 0.1 \sim 4\%$.

Summarising, the fractions calculated at 13 keV were 4, 8 and 23%, corresponding to annihilations from Ps in the BOX, free positrons in the BOX and in the Si substrate. The remaining 65% will annihilate at the Al/SiO₂ interface. At 19 keV, the fraction of annihilations from Ps in the BOX, free positrons in the BOX and free positrons in the Si substrate were 1, 4 and 64%, respectively, resulting in 31% of the annihilations at the Al/SiO₂ interface.

Once these fractions are known, the annihilation S and W values corresponding to positron implantation energies of 13 and 19 keV and a field strength of -3 MV/cm can be calculated, as indicated by labels B and A, respectively, in Fig. 7.3c. It is evident that these points agree with the experimental S - W trajectories.

This demonstrates that most of the positrons implanted in the depletion layer are effectively transported to the Al/SiO₂ interface. For comparison, the points B' and A', corresponding to 13 and 19 keV, respectively, are indicated. These points were calculated in

the same way as B and A but assuming that positrons implanted in the Si depletion layer are not injected into the BOX. The discrepancy with the experimental results is evident.

In addition, we observed that samples containing a p-Si substrate did not show the same results (not shown). Experiments performed at -3 MV/cm while implanting high energy positrons into the Si substrate, clearly showed that about 100% of the positrons annihilate in the Si substrate. No contribution from the gate could be inferred from these experiments. This is in agreement with the fact that the p-Si substrate of MOS capacitors subjected to a negative gate voltage are in accumulation and therefore, no electric field appears in the Si substrate because no depletion layer is formed.

No trapping was detected at the SiO₂/Si as previously suggested [Leung et al. 1993]. Despite the possible existence of traps at the SiO₂/Si interface, it is very unlikely that positrons injected from the Si substrate into SiO₂ become trapped in such traps, because owing to the potential barrier present at the interface, positrons must first lose their energy gained by the injection. Since the energy loss only occurs by phonon scattering, the energy loss rate is rather small, 7×10^{12} eV/s as estimated in [Petkov et al. 2002]. Assuming an energy gain of 1 eV by the positron injection into SiO₂, this means that it would take 0.1 ps to thermalise an injected positron. During this time the positron is able to travel a few nm, definitively escaping from the interface region when an external electric field is applied to the oxide. However, we do not completely discard the possibility of trapping at the SiO₂/Si interface under a negative bias, but only in the case of a very low electric field strength

7.1.7. Modelling the positronium reduction in the presence of an electric field

The Ps fraction determined for the MOS capacitors with 3 μm -thick BOX (type 1 in Table 7.1) strongly depends on the applied electric field, as shown in Fig. 7.7. In Section 7.1.5 the Ps fraction as a function of the electric field was approximated empirically by an exponentially decaying function. In this section it will be described in a more realistic way.

In order to quantify the Ps formation process a simplified model was employed, as described in detail in Chapter 2. In short, we have performed the following steps to describe the Ps formation problem:

- We simulated by means of Monte Carlo calculations [Pimblot et al. 2000] the positron implantation process in order to obtain the average distribution of electrons and holes around any implanted positron.
- These distributions were employed as an input to solve the system of time-dependent three-dimensional drift diffusion equations corresponding to electrons, holes and positrons for each value of the applied electric field. We included a Ps formation term to account for the probability of Ps formation.

Monte-Carlo. We performed Monte-Carlo simulations of positrons implanted in SiO₂ at different energies and calculated the distribution of electrons and holes around the hole centroid as described in Section 2.3. In addition, we calculated the probability of finding the positron at a certain distance from the centroid. We assumed that these distributions are three-

dimensional gaussians. Their standard deviations are: 7 nm for electrons and holes and 9 nm for the positron. The intensity of the gaussian corresponding to the electron or hole distribution was found to be $1 \times 10^{19} \text{ cm}^{-3}$. Please, note that Monte-Carlo calculations only simulate the positron slowing down to 25 eV. Therefore, we must find proper values for electron and positron thermalisation lengths.

The Monte-Carlo calculations predict an energy-independent distribution of holes, electrons and positrons. This explains why the Ps fraction appears to be independent of the positron implantation energy (Fig. 7.7) at implantation energies higher than 5 keV. Ps is formed with electrons generated by ionisation during the positron slowing-down process, see Section 3.3. The probability of Ps formation depends mainly on the last ionisation events and this is independent of the initial implantation energy beyond a certain energy threshold. In contrast, at 5 keV, F_{Ps} is lower than for the other energies. This is probably due to the significantly lower number of generated electrons leading to a smaller electron concentration around the stopped positron.

Drift-diffusion model: We employed the distributions obtained by Monte-Carlo as the initial concentrations to solve the three-dimensional drift diffusion system of equations for electrons, holes and positrons. We used known values for the electron-hole recombination coefficient and the electron drift velocity and considered that the Ps formation coefficient was similar to that for electron-hole recombination because both types of interactions are purely coulombic and dominated by electron behaviour.

The Ps fraction obtained from this model is shown by the solid line in Fig. 7.10. The results appear in good agreement with the experimental fractions obtained for positron implantation energies higher than 5 keV.

The values considered for the electron and positron thermalisation lengths were 8 and 2 nm, respectively. These values are difficult to estimate experimentally. Calculations are also complicated due to the large inaccuracies in the positron cross-sections at energies lower than 25 eV. However, they appear to lie in the expected range. They can be employed in combination with the gaussian distributions to estimate the electron density around implanted positrons in the early stages of Ps formation.

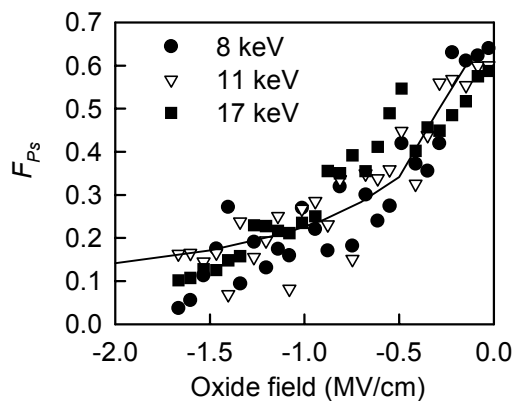


Fig. 7.10. Ps fraction in the BOX (solid line) calculated as a function of the electric field with the aid of the model described in the text. For comparison, the experimental Ps fractions in the BOX layer obtained at different positron energies are given.

Another result of the modelling is that the Ps formation was found to be completed within the first few ps. The formation time was found to vary from 3 ps at 0.1 MV/cm to 0.5 ps at 1.5 MV/cm. This is due to positron-electron separation, which increases with increasing electric field, in agreement with the approach followed in Section 7.1.5. That approach was based on the fact that Ps formation can be separated from positron transport. The Ps formation can be modelled as shown in this section, while positron transport is purely a stationary positron drift-diffusion problem.

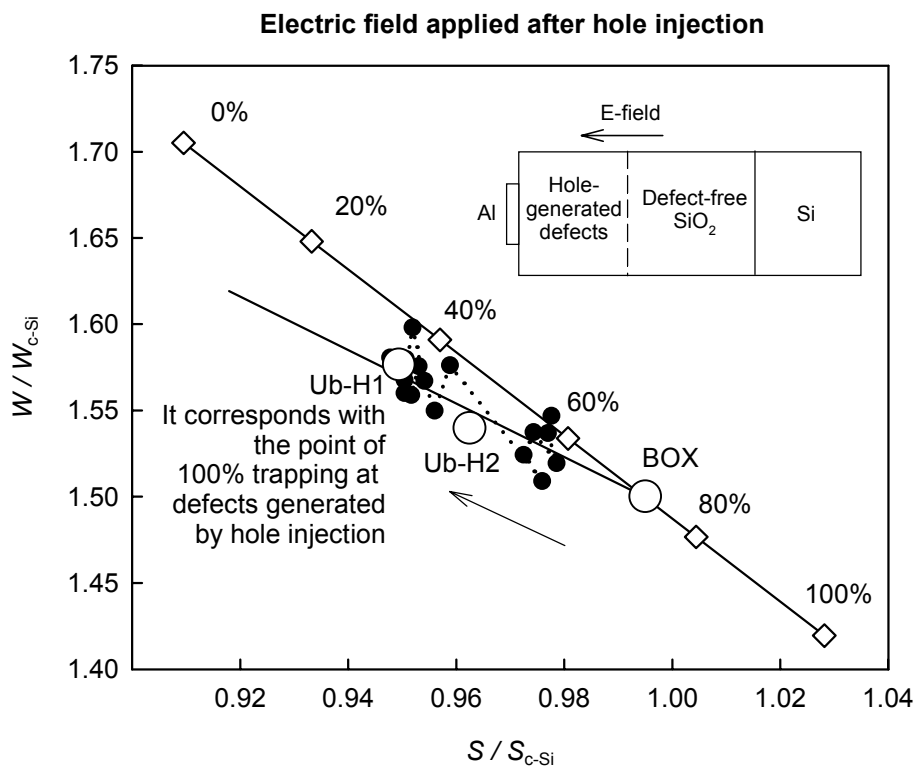


Fig. 7.11. S - W plot obtained at 8 keV positron implantation energy when a negative electric field was applied to sample Ub-H1, presented earlier in Chapter 6. This sample had been injected with holes to a dose of $2.5 \times 10^{15} \text{ cm}^{-2}$. The arrow indicates the direction of increasing electric field strength. The highest applied field was -2 MV/cm . For comparison, the S - W coordinates corresponding to the BOX layer with different Ps fractions are indicated by the diamonds while the open circles represent the S - W coordinates of samples Ub-H1 and Ub-H2, described in Table 6.1.

7.1.8. Suppression of positron transport

When defects are introduced into the sample by He implantation (see Section 6.2), positrons become swiftly trapped and are not drifted anymore by the electric field. The sample of type 2 shown in Fig. 7.4 (Ua-He30 in Chapter 6) was implanted with 30 keV He^+ ions to a dose of $1 \times 10^{16} \text{ cm}^{-2}$. The effect on the S and W parameters can be clearly observed. S drops significantly while W increases. The application of electric fields after implantation does not alter the S and W curves indicating that the defects are efficient positron traps.

The hole-injected sample Ub-H1, presented earlier in Chapter 6, was employed for DBAR studies at different positron energies under the application of negative electric fields. Fig. 7.11 shows the S - W plot corresponding to this type of measurement with a positron implantation energy of 8 keV. At that energy positrons are implanted in the region indicated as “defect-free SiO₂” in the insert. The application of a negative electric field drifts most of the positrons to the region indicated as “hole-generated defects” where they are trapped. This is clearly demonstrated by the fact that positrons do not reach the Al/SiO₂ interface in contrast with experiments shown in Fig. 7.6. Assuming that most of the positrons are trapped at defects generated by hole injection, the S and W parameters obtained in a -2 MV/cm field correspond to the characteristic S and W parameters of these defects.

The annealing of this sample in 100 kPa D₂ gas at 670 K resulted in a recovery of the S and W parameters to values characteristic of the Unibond BOX and enabled the transport of positrons towards the Al/SiO₂ interface. It is interesting to mention that the S - W coordinates corresponding to this interface changed with the annealing (not shown). The S parameter decreased while the W parameter increased with respect to the values of the Al/SiO₂ interface obtained for as-metallised capacitors (section 7.1.3).

7.2. SiO₂/Si interface studies

Due to the large spread in implantation depth at high energy, the depth resolution becomes very poor. This reduces the fraction of positrons implanted near the SiO₂/Si interface, rendering its characterisation very difficult. In contrast, when using thin oxides, low energy implantation with narrow implantation profiles assures that a significant fraction of positrons implanted in the interface region annihilates at interface sites, which facilitates its identification [Leung et al. 1993]. In order to overcome the difficulty for thick oxides, studies can be performed under the application of electric fields that strongly enhance the fraction of positrons reaching the interface. Once the positron transport issues are understood, the positron experiments under electric fields can be successfully interpreted.

7.2.1. Samples and sample treatments

- The same type of MOS capacitors as those employed in Section 7.1, will be employed for this section, see Table 7.1.
- In addition, results on SIMOX samples with a 190 nm-thick Si top layer and a 360 nm-thick BOX on p-Si will be shown. These samples were employed in Chapter 6, with the label “S”. One of the samples, S-D30-b (Table 6.1), was implanted with 30 keV D⁺ ions to a dose of 2×10^{15} cm⁻² and annealed in vacuum after removing the Si top layer for periods of 15 min at 470, 670, 820 and 970 K. The effect of these treatments on the interface will be shown.
- Other SIMOX samples were annealed in D₂ gas at pressures from 0.1 to 1 MPa and temperatures from 870 to 1170 K, similar to those used in Chapter 5.

- A 15 nm-thick Al-gated MOS capacitor with a 360 nm-thick SIMOX oxide was fabricated in the same way as the other MOS capacitors presented in this chapter, see Section 7.1.1.

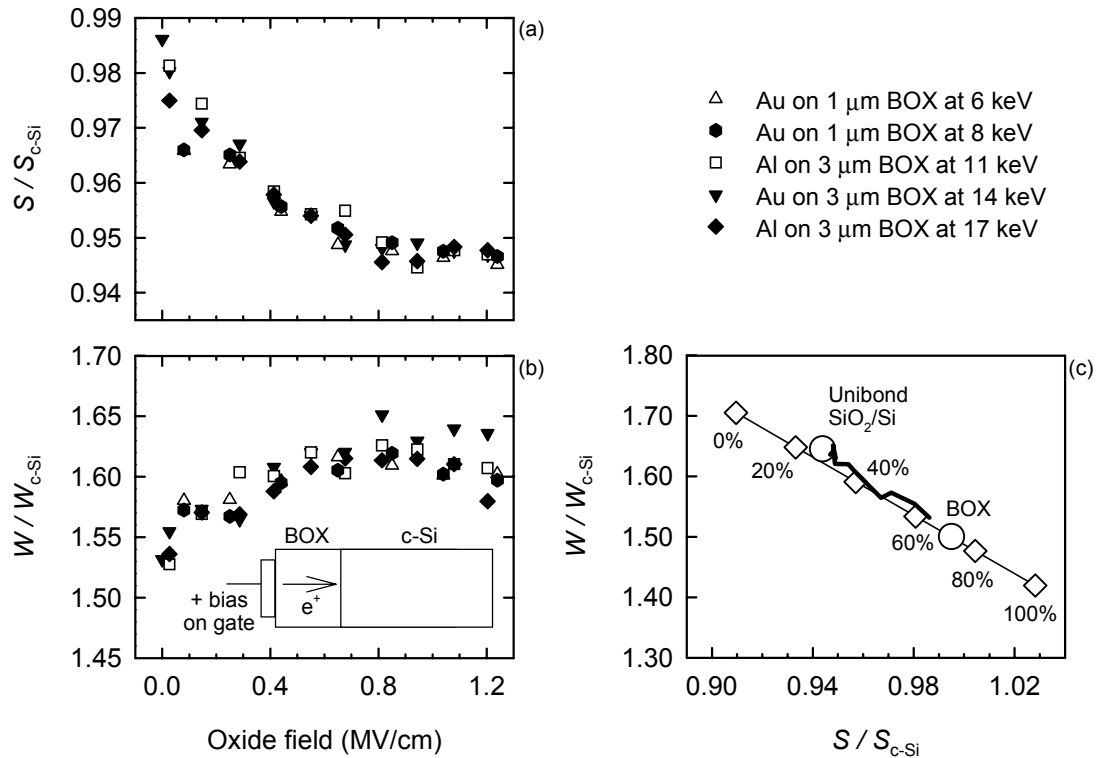


Fig. 7.12. Positron beam DBAR measurements on MOS capacitors fabricated by depositing 15 nm Al or Au on 3 μm BOX of Unibond samples. (a) S parameter as a function of the oxide field, (b) W parameter and (c) S - W defect map, with the oxide field as a running parameter. For reasons of clarity, the experimental curve corresponding to a Au-gated MOS at 14 keV positron energy is represented by the thick solid line. The different annihilation states are indicated by means of open circles, while the diamonds represent the estimated S - W coordinates corresponding to annihilation in the BOX layer when the fraction annihilated as Ps changes as indicated (see Section 6.2). The insert is a schematic description of the MOS capacitor.

7.2.2. Identification of the SiO_2/Si interface

In order to study the annihilation properties of positrons at the interface we employed the technique of electric field driven positron transport to carry positrons to the Si/SiO₂ interface. To that end, a positive electric field was applied to MOS capacitors while positrons were implanted in the oxide at different energies. In this way, information is obtained for different implantation profiles. Two types of MOS capacitors were used. They had Unibond oxides of thicknesses 1 and 3 μm , see Table 7.1.

Fig. 7.12 shows experiments performed when positive electric fields were applied to the MOS capacitors. The positron energy was kept constant at the values indicated in the legend while the electric field across the oxide was varied. All samples showed similar behaviour irrespective of the BOX thickness or the positron implantation energy. The S parameter

decreased with increasing field while W increased. The trajectory in the S - W plot (Fig. 7.12c) follows the Ps line indicated by diamonds, see also Section 6.2. This could indicate that the only effect of the electric field is to reduce the Ps formation. However, it was conclusively shown in Section 7.1.2 that the application of electric fields results in a significant fraction of positrons being transported to and annihilated at the interface. Therefore, the interface cluster point plays a role in addition to the points corresponding to annihilations in bulk oxide (labelled “0%”) and annihilations from Ps states in the oxide (labelled “100%”). However, the determination of the interface cluster point is not straightforward because the experimental trajectory in the S - W plot is collinear with the line connecting the points “0%” and “100%”.

Since the Ps formation is fully symmetric with respect to the bias polarity, we can make use of the Ps fractions obtained as a function of the electric field by the model presented in Section 7.1.7. In addition, making use of the transport model presented in Section 7.1.5, we can estimate the fraction of positrons that travels to the interface when positive electric fields are applied to the oxide, see Fig. 7.13. Note that the mean implantation depth at 8, 11 and 14 keV is about 530, 880 and 1300 nm, respectively. Thus, the distance that positrons need to travel to reach the Al/SiO₂ interface is significantly smaller than the distance to the Si/SiO₂ interface. In agreement with this, the fractions of positrons reaching the Al/SiO₂ interface at positron implantation energies of 8, 11 and 14 keV are larger than the fractions of positrons reaching the SiO₂/Si interface at these energies (compare Fig. 7.7 and Fig. 7.13).

Fig. 7.14 shows the positron branching ratios when the implantation energy is 11 keV and the applied electric field is +1.2 MV/cm. 100% of the positrons are thermalised in the oxide layer. Subsequently, about 20% of the positrons form Ps. The remaining 80% is free to travel through the oxide and is drifted towards the Si/SiO₂ interface by the applied electric field. It is observed in Fig. 7.13 that at 11 keV and 1.2 MV/cm about 40% of the positrons reach the interface. Once positrons reach the interface, Ps may be formed due to the availability of electrons as indicated in Fig. 7.14, see discussion in Section 7.2.3. In total, 40% of the implanted positrons annihilate at interface states, (28% at Ps states) while 60% annihilate in the oxide layer (20% at Ps states).

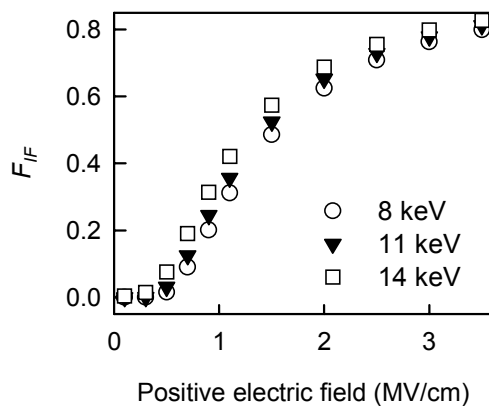


Fig. 7.13. Fractions of positrons that reach the interface, calculated as a function of the applied electric field. Positron implantation energies are indicated. These energies result in about 100% positron stopping in the 3 μm oxide layer.

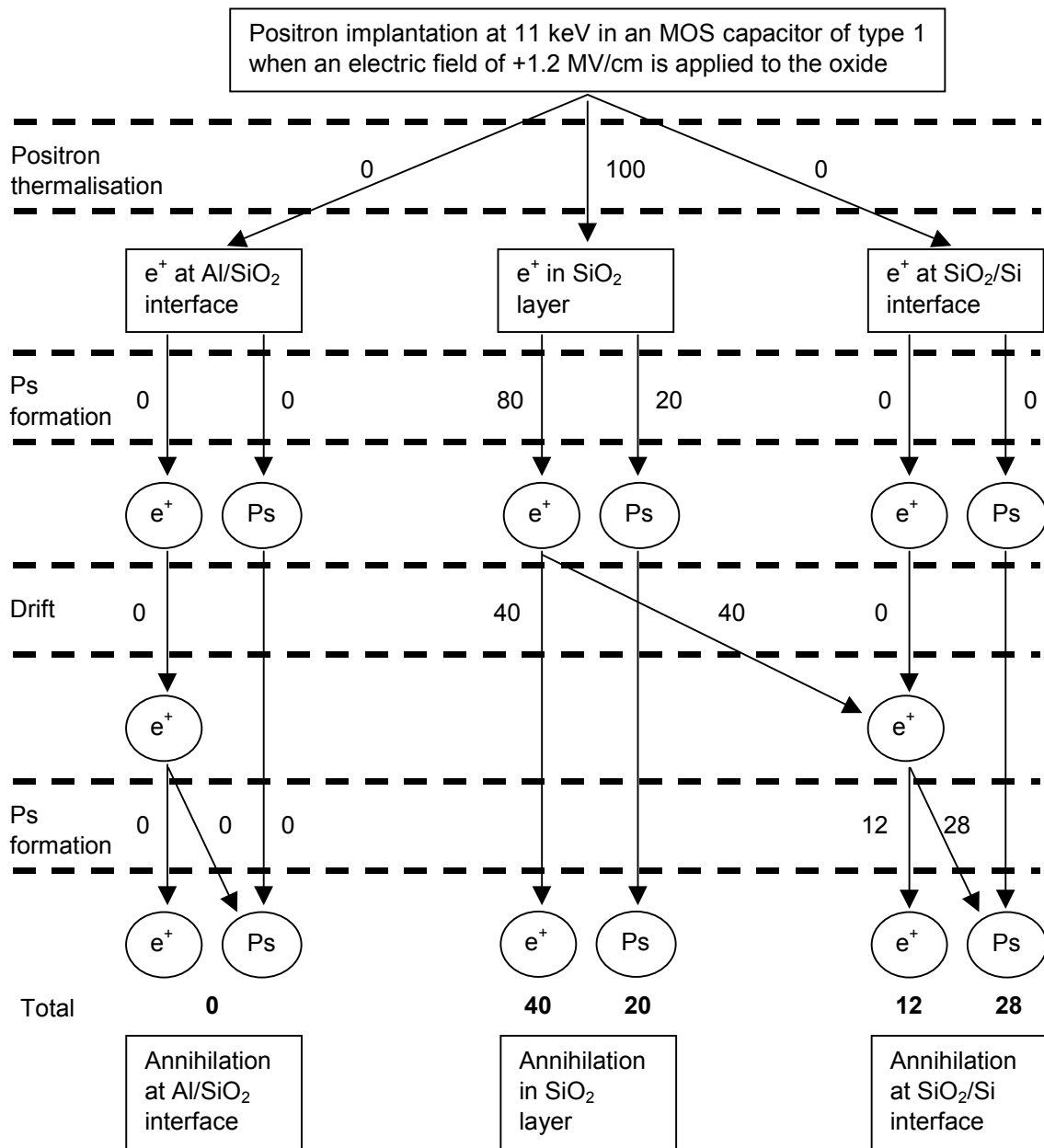


Fig. 7.14. Positron branching ratio diagram corresponding to a sample of type 1 when an electric field of +1.2 MV/cm is applied to the oxide. The numbers indicate the percentage of the implanted number of positrons annihilating from a specific state in each process.

Once the fractions of positrons annihilating from states in the oxide layer, from Ps states in the oxide layer and at the interface have been established the S and W parameters can be reconstructed. The only unknown parameters are the characteristic S and W parameters of the Si/SiO₂ interface. These parameters are obtained as the best fit of the reconstructed curves to the experimental ones. A fair agreement was obtained (not shown) when the SiO₂/Si interface point was chosen as indicated in Fig. 7.12c.

7.2.3. Positronium formation at the interfaces

The Ps fraction at the Si/SiO₂ interface obtained from 2D-ACAR measurements at +1.2 MV/cm is 48% (Table 7.2). On the other hand, by means of DBAR measurements we obtained the Ps fraction formed and annihilated in the oxide layer. This fraction amounts to about 20% at 1.2 MV/cm. We should note that the experimental and calculated Ps fractions shown in Fig. 7.10 correspond to Ps formed in the oxide, whereas by means of 2D-ACAR p-Ps is detected irrespectively of its origin. Therefore, the difference between the Ps fractions estimated by both methods gives the Ps fraction formed at the interface, i.e. 48% - 20% = 28%, as indicated in Fig. 7.14.

This result is not surprising since it is well known that holes in SiO₂ within a few nm of the SiO₂/Si interface are effectively neutralised by tunneling electrons [Benedetto et al. 1985, Schmidt et al. 1992]. In addition, experimental evidence has recently been obtained from Age Momentum Correlation (AMOC) experiments, which suggests that Ps is formed at the interface [Suzuki et al. 2002]. Therefore, we believe that the annihilation signals at interface sites contain a certain contribution of Ps states intrinsic to the interface.

7.2.4. Potential barrier at the SiO₂/Si interface

In the following, we explore the positron drift towards the SiO₂/Si interface in more detail. Fig. 7.15 shows the results of DBAR measurements on Au-gated MOS capacitors with 1 μm oxide (type 2 in Table 7.1). Positrons were implanted at 10 or 12 keV while varying the electric field in the oxide from 0 to about 1.2 MV/cm. In this case a significant fraction of the positrons is implanted in the underlying Si layer. Fig. 7.15c shows the Makhovian implantation profiles for both implantation energies. The trajectories of the *S-W* curves in Fig. 7.15d, with the electric field as a running parameter, follow the arrows. When no electric field is applied, the annihilation signal is a combination of three positron annihilation states: the oxide layer, the SiO₂/Si interface and the underlying Si substrate.

However, when the electric field is about 1 MV/cm the annihilation signal lies on the interface-Si dotted line. This indicates that only two states are involved in the annihilation process, i.e. the interface and the Si substrate. From the *S-W* plot the fraction of positrons annihilating in each layer can be extracted. For that we simply assume that the measured annihilation signal is a linear combination of the two states involved. In this way, we found that when an electric field of about 1 MV/cm is applied to the oxide, around 80% of the positrons implanted at 10 keV annihilate at interface sites, while around 60% of the positrons implanted at 12 keV annihilate at interface sites. Remarkably, these values are very similar to the fractions of positrons implanted in the oxide layer, which were obtained by integration of the Makhovian profiles shown in Fig. 7.15c. This confirms that positrons implanted in the oxide effectively travel to the interface where they find a potential barrier which prevents the injection of positrons into Si.

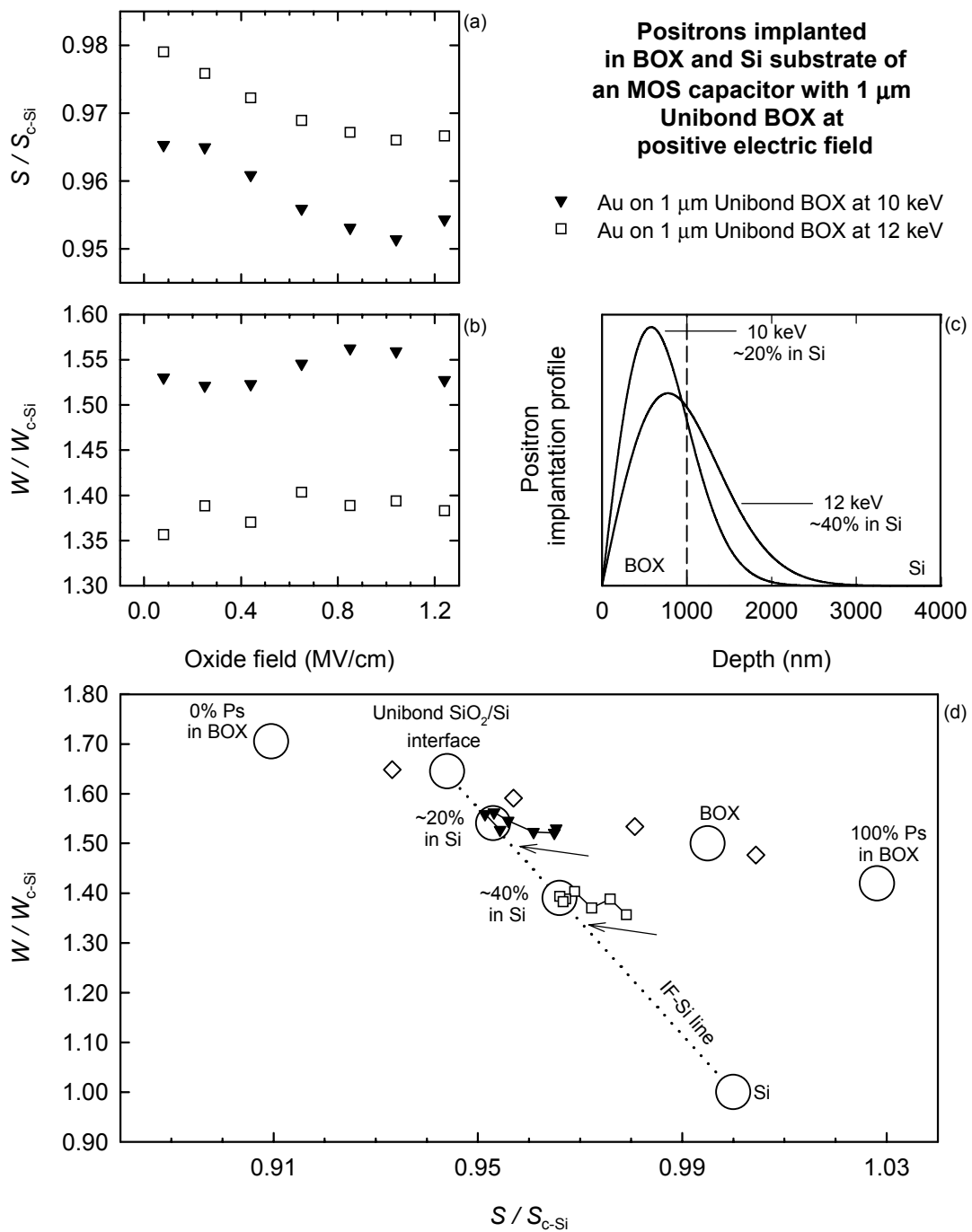


Fig. 7.15. Positron beam DBAR measurements on MOS capacitors fabricated by depositing 15 nm Au on 1 μm BOX of Unibond samples (type 2). (a) S parameter as a function of the oxide field, (b) W parameter. (c) Makhovian profiles corresponding to the positron energies employed during the measurements, i.e. 10 and 12 keV (d) S - W defect map, with the oxide field as a running parameter. The different annihilation states are indicated by means of open circles.

7.2.5. SiO₂/Si interface for different oxides and treatments

An Al-gated MOS capacitor fabricated with SIMOX was studied by DBAR measurements under the application of electric fields. The results are shown in Fig. 7.16 by means of the thick solid line. The arrow indicates the effect of increasing positive bias. A new cluster point associated with the SIMOX SiO₂/Si interface is identified. This point is significantly different from the Unibond SiO₂/Si interface, identified above and shown for comparison.

DBAR measurements on SIMOX samples were also performed as a function of energy in the absence of an electric field after removing the top Si layer, as shown in Chapter 6. The interface point (solid circle) can then be extracted with the aid of VEPFIT [van Veen et al. 1990]. This is possible because the oxide layer is relatively thin (360 nm) and the parameters corresponding to the neighbouring layers are known. The interface points obtained by both methods are in agreement.

Similarly, the interface points (solid circles) were obtained for sample S–D30–b, which was subjected to annealing steps after D⁺ implantation (Chapter 6). These results were presented in Fig. 6.14. No effect was found at the interface after the implantation, but, in contrast, a significant effect was observed in the SiO₂ layer (Fig. 6.14). This is expected because the implantation profile did not reach the interface, as shown in Fig. 6.9.

It is interesting to compare the effects observed at the SIMOX interface after vacuum annealing treatments with DBAR measurements on MOS capacitors fabricated with thermal oxides, presented in Chapter 8 of [Clement 1998]. These measurements were performed under the application of positive electric fields. The treatments applied to the MOS capacitors are indicated in the caption of Fig. 7.16. The SIMOX SiO₂/Si interface point appears very close to point “b”, corresponding to a MOS capacitor subjected to post-oxidation annealing (POA) in N₂. The annealing at 470 K produced a huge change in the interface annihilation parameters. The *S* parameter decreased drastically while *W* increased. This point does not correspond to any of the points reported by [Clement 1998]. Further annealing steps at higher temperatures gradually led to the recovery of the original *S* and *W* values. Interestingly, the annealing step at 670 K resulted in a SIMOX SiO₂/Si interface point in good agreement with point “d”, corresponding to a MOS capacitor subjected to a post-metallisation annealing (PMA) in forming gas (10% H₂ – 90% N₂) at 670 K. Annealing at 820 K produced a SIMOX SiO₂/Si interface point between points “b” and “c”, in the vicinity of the Unibond SiO₂/Si interface. Annealing at 920 K led to an interface point close to that corresponding to the unannealed sample. Finally, annealing of SIMOX samples in D₂ produced an interface point close to “a”, which corresponds to a MOS capacitor that did not receive any POA treatment.

It is known that Si dangling bonds exist at the interface constituting paramagnetic defects which are called P_b centres and can be detected by electron spin resonance (ESR) measurements [Stesmans et al. 1998]. These defects can be passivated with the aid of H atoms, leading to Si–H defects, undetectable by ESR [Brower et al. 1990]. The optimum passivation is obtained by applying PMA treatments at approximately 670 K to the capacitors [Stesmans 2000]. In this situation, the presence of H at interface defects screens the Si substrate. Therefore, positrons overlap with electrons from surrounding oxygen atoms giving

a high W value, see point “d” in Fig. 7.16. On the other hand, an incompletely passivated interface results in positron annihilation at Si dangling bonds. The overlap with oxygen atoms is strongly reduced and the W parameter, consequently, decreases. In addition, as mentioned in Section 7.2.3, Ps can be formed at the interface. It is expected that the Ps fraction will be larger when the interface is incompletely passivated because positrons can approach the interface more closely enhancing the probability of picking up electrons from the substrate to form Ps. The formation of Ps will lead to high S values.

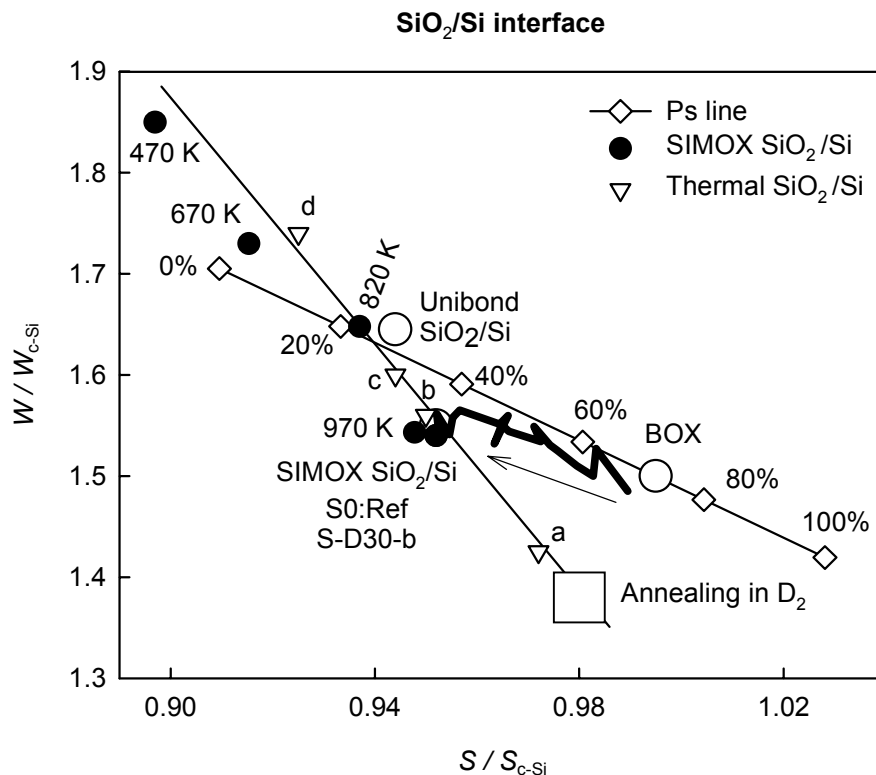


Fig. 7.16. S - W interface coordinates corresponding to the SIMOX sample S-D30-b, (see Chapter 6) as implanted with 30 keV, $2 \times 10^{15} \text{ D}^+ \text{ cm}^{-2}$ and after an annealing period of 15 min at the indicated temperature (solid circles). The big open square represents the area where interface states, presented in SIMOX samples annealed in D_2 from 870 to 1170 K, appear. For comparison, experiments from Chapter 8 of [Clement 1998] (inverted triangles) on MOS capacitors with 15 nm Al on thermal oxides are included. The symbols correspond to: (a) a capacitor with an oxide which did not receive any post-oxidation anneal (POA), (b) a capacitor with an oxide subjected to POA in N_2 , (c) a capacitor with an oxide annealed before metallisation at 670 K in 10% H_2 – 90% N_2 , (d) a capacitor subjected to post-metallisation annealing with an oxide subjected to POA. The diamonds represent the Unibond layer when the Ps fraction changes as indicated (see Section 7.2). The thick solid line refers to experiments on a MOS sample with SIMOX oxide under positive bias. The interfaces found by positive bias experiments on Unibond and SIMOX samples are shown by open circles, while the straight lines serve to guide the eye.

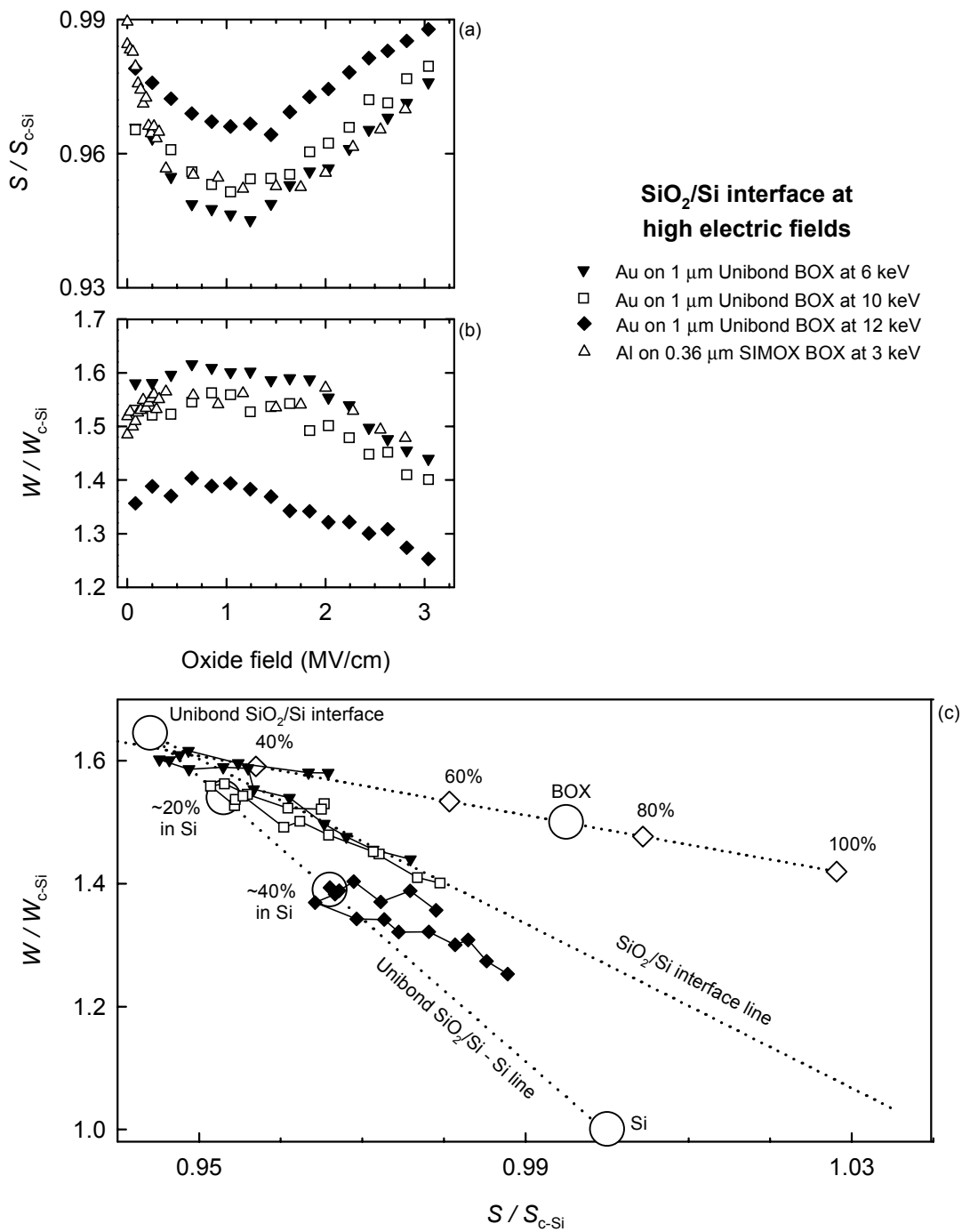


Fig. 7.17. Interface studies under high electric fields for the samples indicated. (a) shows the S value, and (b) the W value as a function of the applied electric field. (c) is the S - W map of defects with the electric field as running parameter. The large open dots indicate cluster points and the diamonds the Ps line.

The interface points detected for SIMOX, Unibond or thermal oxides lie on a line, the endpoints of which are associated with annihilations at a hydrogenated and non-hydrogenated interface, respectively. The annealing steps at 470 and 670 K in vacuum results in low S , high

W values, associated with the hydrogenation of the interface. Probably, a fraction of the hydrogen introduced into the sample by ion implantation was not firmly bound, which allows it to reach the interface passivating Si dangling bonds. After the annealing step at 470 K, part of the hydrogen at the interface might be in the molecular state at interface voids. This would result in a reduction in the Ps fraction at the interface and, therefore, to lower S and higher W values than in the step performed at 670 K. The subsequent steps performed at higher temperatures resulted in the presence of a significant density of Si dangling bonds at the interface, as indicated by the shift in the S - W coordinates towards higher S and lower W values.

Interface studies by means of DBAR measurements of this type are appropriate to obtain a rapid estimate of the interface conditions and can be easily combined with standard capacitance-voltage measurements. In addition, they can also be performed on samples without metallisation, reducing the number of processing steps.

7.2.6. SiO₂/Si interface under very high positive fields; electron injection from the Si substrate

A surprising effect was discovered when experiments with electric fields were applied to study SiO₂/Si interfaces. At both positive and negative high electric fields the S parameter increased drastically while W decreased accordingly, see Fig. 7.17. This effect was not observed when studying other interfaces in the presence of high electric fields, such as Al/SiO₂ or Au/SiO₂, see Fig. 7.3.

In Fig. 7.17, it can be seen that the trend is similar in all the experiments shown. At electric fields higher than 1.5 MV/cm, a strong effect is observed, regardless of the substrate type p or n, the BOX thickness or the positron implantation energy. The S - W plot shows that the interface coordinates move along the interface line introduced in Section 7.2.5. Apparently, saturation is not observed.

The strong dependence on the electric field can be related to the injection of electrons from the substrate by a tunneling effect. This, in turn, results in an increase in the Ps fraction. 2D-ACAR measurements with a positron beam were performed on the MOS capacitor with 3 μm -thick Unibond BOX (sample type 1, also employed for the experiments shown in Fig. 7.2 and Fig. 7.5). The results indicate that at 3 MV/cm, the Ps formation increases (not shown) confirming the proposed explanation. This explains why the S parameter increases so drastically with the applied field. It is also interesting to note that the samples, studied by 2D-ACAR with the high intensity positron beam under the application of a high electric field, degraded after a few hours of measurement. Unfortunately, this prevented the performance of long measurements necessary to collect 2D-ACAR spectra with enough statistics to analyse anisotropic components, as shown in Fig. 7.2.

7.3. Conclusions

By means of positron beam 2D-ACAR and DBAR techniques, it has been shown that positrons, under the application of external electric fields, effectively travel long distances in

SiO₂. A definitive proof is supplied by positron beam 2D-ACAR measurements on Au-gated MOS capacitors with 3 μm oxides: when positrons implanted at 14 keV were transported to the SiO₂/Si interface at 1.2 MV/cm where they annihilated with electrons from the Si substrate, they gave rise to an anisotropic signal similar to that obtained for Si(100). The application of negative electric fields to MOS capacitors with different gate materials also showed that positrons were sensitive to the gate material. This clearly indicated that positrons were drifted to the gate/oxide interface.

A model for positron transport in SiO₂ has been proposed. It describes positron drift on the basis of Ps formation. Due to the low mobility of Ps, positrons forming Ps states are effectively trapped and do not participate in transport processes. The application of electric fields to the sample results in a reduction of Ps formation which simultaneously increases the number of positrons free to move with the electric field. Quantitatively, the model agrees with the experimental data.

Data on Ps reduction as a function of the electric field obtained by analysing the results with the aid of the proposed model, were compared with the Ps fraction measured by means of 2D-ACAR experiments at 1 MV/cm. We concluded that an important fraction of Ps finds its origin at the SiO₂/Si interface. This process is probably related to Ps formation with tunneling electrons coming from the underlying Si substrate.

The electric field technique was applied to perform interface studies with the aid of DBAR measurements. The interface annihilation parameters of the Unibond BOX/Si and SIMOX BOX/Si were identified. They were compared with a number of measurements on thermal oxides and with SIMOX samples subjected to different treatments. The interface signal is very sensitive to the presence of hydrogen. A typical interface line was found in the *S-W* plot. The application of high electric fields leads to a strong dependence of the *S-W* interface parameters on the field. The Ps fraction was found to increase as a consequence of electron injection from the Si substrate.

Chapter 8

Amorphous and heterogeneous hydrogenated silicon deposited on silicon dioxide

Amorphous hydrogenated silicon layers (a-Si:H) deposited by plasma enhanced chemical vapour deposition (PECVD) or hot wire chemical vapour deposition (HWCVD) on SiO₂ were studied by Doppler broadening of annihilation radiation (DBAR) with a positron beam. No significant differences were found between the studied layers. The measurements revealed concentrations of vacancy-like defects at about 0.1 at.% levels. Hydrogenated heterogeneous silicon containing both amorphous and crystalline phases was deposited by hot wire chemical vapour deposition. Two-dimensional correlation of annihilation radiation (2D-ACAR) experiments performed with a monoenergetic positron beam revealed that positronium is formed in these layers, indicating the presence of nanovoids. The spectrum could be decomposed in different contributions related to para-positronium, void surface and bulk annihilations. DBAR measurements showed that the positron effective diffusion length is ~14 nm. The *S* parameter for these layers is ~9% higher than for amorphous silicon layers. Infrared experiments showed the presence of an intense absorption peak at 2100 cm⁻¹ in the case of heterogeneous layers. This peak is attributed to hydrogen atoms at internal void surfaces, amounting to 0.46 at.% of H. Combining the three techniques, the void radius was estimated to be (8±6) nm corresponding to a void concentration in the range (4×10¹⁵ – 4×10¹⁶) cm⁻³, homogeneously distributed along the layer. As a by-product, we concluded that positronium annihilates in the voids prior to thermalisation with an energy of about 0.16 eV. Positrons implanted in the SiO₂ were drifted by externally applied electric fields to the a-Si:H/SiO₂ interface, increasing the fraction of positrons annihilating there. The experiments showed similar a-Si:H/SiO₂ interfaces regardless the deposition method employed. The results indicate that positrons at the interface between the a-Si:H layers and SiO₂ are trapped at open volume defects and probably annihilate with electrons associated with dangling bonds. In addition, the results suggest that electron injection takes place. This process strongly depends on the applied electric field.

8.1. Introduction

Hydrogenated amorphous silicon (a-Si:H) is a technologically relevant material due to its applications in the opto- and micro-electronics industry. In particular, it is commonly used for solar cells and as the active element of film transistors (TFT) employed in low frequency devices such as displays [Chu et al. 1997, Meiling et al. 1997]. The properties of a-Si:H are intimately linked to the presence of hydrogen. In particular, it was found that a-Si:H films exhibiting good electronic properties contained a high concentration of hydrogen (~10 at.%) [Triska et al. 1975]. This beneficial behaviour is related to the passivation of unsaturated bonds by hydrogen as well as to hydrogen-induced mechanical stress reduction. In addition, hydrogen also plays an important role in the degradation of opto-electronic properties by light (Staebler-Wronski effect), [Staebler et al. 1977], because this process is strongly correlated to the depassivation of silicon dangling bonds.

The deposition of a-Si:H films is routinely performed by plasma-enhanced chemical vapour deposition (PECVD) using silane as the source gas. Positively charged ions from a RF plasma as well as neutral chemically active species (radicals) contribute to the film growth in the PECVD technique. When the standard frequency of 13.56 MHz is used we speak about a glow discharge (GD). Alternatively, hot-wire chemical vapour deposition (HWCVD) has appeared as a promising technique [Wiesman et al. 1979, Matsumura 1983, Doyle et al. 1988, Matsumura 1989] that offers high deposition rates and produces films more resistant to degradation. In fact, TFT devices fabricated with the HWCVD technique show a reduced degradation upon illumination as compared to devices fabricated with conventional PECVD films [Mahan et al. 1991, Papadopoulos et al. 1993]. The HWCVD method is based on the dissociation of a molecular gas by the catalytic action of a hot tungsten or tantalum filament. The dissociation of silane into Si and H radicals is very efficient at filament temperatures above 1600°C. Only radicals contribute to the film growth because ionisation of the gas molecules does not occur. HWCVD layers deposited at a high substrate temperature (~510°C) contain a low H concentration (2.2 at. %) and have a heterogeneous structure (het-Si:H), i.e. consists of amorphous and crystalline Si phases. It was found that het-Si:H layers also exhibit higher resistance to degradation than GD layers [Brockhoff et al. 1999].

Positron techniques are very sensitive to the presence of open volume. In particular, the observation of positronium (Ps) by the high resolution two-dimensional correlation of annihilation radiation (2D-ACAR) measurements is a clear indication of void formation. In the case of Si, Ps formation indicates that the void radius is at least 0.35 nm [van Veen et al. 1995]. The detection of voids by other techniques is very difficult and in the case of amorphous structures it becomes impossible even with the aid of sophisticated high-resolution transmission electron microscopy (TEM). In this sense, the combined use of an intense positron beam ($>10^7$ e⁺/s) with a 2D-ACAR setup at the Delft Positron Centre, allowed us to study the presence of voids in Si layers. This study indicate that the technologically relevant het-Si:H layers contain a significant amount of voids. In this chapter we discuss aspects concerning void size and concentration by combining results obtained by positron beam techniques 2D-ACAR and Doppler broadening (DBAR) with those from infra-red absorption

(IR) measurements. For comparison, a-Si:H samples grown by both HWCVD and GD methods are also presented.

Several works can be found in the literature regarding positron annihilation lifetime (PAL) and DBAR studies of amorphous silicon, however, very few publications exist on 2D-ACAR studies of amorphous silicon. In particular thin layers were never studied. One reference [He et al. 1986] reported the presence of voids in thick samples studied by 2D-ACAR measurements with fast positrons. Although, the deposition methods are very different to ours, critical comparisons will be made concerning the size estimation reported by these authors.

The study of the interfaces between the deposited Si layers and the substrate SiO₂ is of great importance due to its implications for the so-called inverted-staggered type thin film transistors. It has been proposed that these interfaces play an important role in the degradation of electronic devices. This suggests that differences at the interface could explain the different degradation behaviour observed in samples deposited by GD or HWCVD methods [Brockhoff et al. 1999, Brockhoff et al. 1998, Meiling et al. 1998]. In order to compare the interface between layers deposited by both methods and the underlying SiO₂ layer, we have carried out DBAR studies under the application of external electric fields (see Chapter 7). This method assures that the fraction of positrons trapped at the interface of interest is sufficiently large to account for most of the annihilations. Results from these experiments will be discussed in this chapter.

8.2. Summary of previous work

A number of studies have been published on samples deposited under similar conditions as those presented in this work. A summary of results obtained by different characterisation techniques is given in this section. The results were obtained by Raman spectroscopy, cross sectional transmission electron microscopy (XTEM), elastic recoil detection (ERD), X-ray diffraction (XRD), Fourier-transform infrared absorption spectroscopy (FTIR), mechanical stress determination by curvature measurements and electrical measurements on thin film transistors (TFT).

A measure of the short-range order in amorphous materials can be given on the basis of the bond-angle distribution determined by Raman experiments. The bond-angle distribution is assumed to be proportional to the width of the (transverse-optic) TO-like band [Beeman et al. 1985]. Raman spectra revealed that the bond-angle distribution of films deposited under the above described HWCVD and GD conditions was among the narrowest reported for device quality a-Si:H [Brockhoff et al. 1999, Brockhoff et al. 1998]. For HWCVD het-Si:H films, an additional feature was found. It contained crystalline phases revealed by a peak in the Raman spectra at around 520 cm⁻¹. Further investigation by cross-sectional TEM showed that the HWCVD het-Si:H films contained cone-shaped crystallites [Brockhoff et al. 1999, Brockhoff et al. 1998, Meiling et al. 1998]. The base of the cones is at the surface and the cone angle is about 20°. These cones extend down to about 10 nm from the het-Si:H/SiO₂ interface. The average density of such cones is 3.4×10⁹ cm⁻². XRD experiments showed that the preferred

orientation of the crystallites is $\langle 220 \rangle$ and that the lattice plane separation is 0.22 nm [Rath et al. 1997].

The H-concentration in the deposited layer was determined by means of ERD [Brockhoff et al. 1999, Brockhoff et al. 1998]. It amounts to 13 at. % for the GD a-Si:H film, 8.0 at. % for the HWCVD a-Si:H film and 2.2 at. % for the HWCVD het-Si:H film. The H-concentration in the het-Si:H layer drops to about 1 at. % upon thermal annealing at 550°C for a few hours.

FTIR showed that H release occurs at temperatures above 500°C [Brockhoff et al. 1999]. Initially H is released from SiH_n (n>1) groups and from SiH on internal surfaces or voids. Prolonged annealing showed H release from SiH bonds in bulk a-Si:H. Hydrogen escapes from HWCVD het-Si:H layers already during deposition. However, the H concentration in het-Si:H is higher than expected regarding the high substrate temperature. It indicates that a high H chemical potential is established during the growth process, which enhances the H incorporation.

The internal stress in all the a-Si:H layers was found to be compressive while in the HWCVD het-Si:H layers the stress was found to be tensile and of the order of 500 MPa [Brockhoff 2001]. Annealing at 550°C for 120 minutes does increase the stress even further by a factor of 1.8.

Electrical measurements on TFT devices [Brockhoff et al. 1999, Meiling et al. 1998] showed that the TFTs fabricated with HWCVD-deposited films are more stable than those fabricated with GD-deposited films. In particular the threshold voltage shift after stress is more pronounced in the latter devices. This effect was tentatively attributed to differences in the interface configurations of HWCVD and GD samples or to differences in H-bonding structures.

8.3. Sample preparation

The samples described in Table 8.1 were prepared by means of a glow discharge (GD) method or by hot-wire chemical vapour deposition (HWCVD):

-Sample 1. GD a-Si:H film deposited at a substrate temperature of 200°C.

-Sample 2. HWCVD a-Si:H layer deposited from 90 sccm undiluted SiH₄, at 2 Pa, at a substrate temperature of 430°C and a Ta filament temperature of 1900°C. The deposition rate was about 1.2 nm/s.

-Sample 3. Het-Si:H film (containing amorphous and crystalline phases) deposited by the HWCVD method from a mixture 7 % SiH₄ in H₂ at 10 Pa while keeping the substrate at 510°C.

Unibond samples with a 3 μm-thick buried oxide were used as substrate. Identical samples were employed in Chapters 4-7. The top Si layer was chemically etched in KOH prior to the deposition of the amorphous (or heterogeneous) Si layers described above. An approximately 15 nm Al layer was evaporated as gate material on the deposited layers. These Al layers form the contacts of a capacitor-like structure necessary to perform DBAR

measurements under the application of external electric fields. In addition, the Al gate is necessary to avoid charging of the samples by the intense positron beam employed for 2D-ACAR experiments. The resulting structures are formed by the Al gate, the deposited Si layer, the buried SiO₂ layer existing in the original SOI sample and the c-Si substrate, respectively. Another set of samples deposited under the same conditions was also studied. No differences could be observed between the positron results obtained from both sets of samples.

Table 8.1. Parameters obtained for the deposited layers by fitting the experimental values obtained from DBAR experiments with the aid of VEPFIT. The S and W parameters are normalised to c-Si bulk values.

	Deposition method	Deposited layer	Thickness (nm)	S	W	L (nm)
1	GD	a-Si:H	180±20	1.033	0.763	19±3
2	HWCVD	a-Si:H	320±20	1.033	0.780	15±3
3	HWCVD	het-Si:H	260±20	1.120	0.645	14±3

8.4. The deposited layers

Positron beam Doppler broadening (DBAR) experiments were performed on samples 1, 2 and 3 in order to study the deposited layers. The S and W annihilation parameters were obtained as a function of the positron implantation energy (between 0 and 20 keV). The experimental values were fitted by means of VEPFIT [van Veen et al. 1990] assuming a simple model consisting of 3 homogeneous layers plus the surface. These 3 layers correspond to (1) the Al gate region (including contributions of both Al and Al/a-Si:H), (2) the deposited Si and (3) the SiO₂ substrate, respectively. The S and W values, the diffusion length and the thickness of the Al and SiO₂ layers were fixed. The other parameters corresponding to the deposited a-Si:H or het-Si:H layers were obtained by fitting. These fitted values are given in Table 8.1. The layer thickness obtained in this way has an accuracy of ~10%.

Fig. 8.1 shows the experimental and fitted DBAR results obtained for samples 1, 2 and 3, respectively. For convenience, the S and W parameters are normalised to the values of the crystalline silicon bulk (S_{Si} and W_{Si}). The S and W curves allows us to distinguish the surface and the different layers composing the sample: (1) Al region (includes contributions of both Al and the Al/a-Si:H interface), (2) a-Si:H or het-Si:H and (3) SiO₂. Notice that not much effort was made to decompose the gate contribution into Al and Al/a-Si:H components because that is outside the scope of this work. The S and W values for the a-Si:H layers are the same within the experimental error, regardless of the deposition method employed (GD or HWCVD). The positron diffusion length and S - W values (Table 8.1) for the a-Si:H layers in samples 1 and 2 are in fair agreement with values reported in the literature [van Veen et al. 1995, Nasu et al. 1987] for a-Si:H samples deposited under similar GD conditions as sample 1. The low values obtained from the fit for the diffusion lengths indicate that positrons are effectively trapped in the a-Si:H layers. Exact identification of the traps is not possible because the amorphous layers contain a large variety of possible positron traps, e.g. dangling bonds, vacancy-like complexes, negative centres, open volume or extrinsic defects such as

foreign impurity atoms. However, we can establish an analogy with crystalline silicon, considering the amorphous structure as a highly defective material rather than a continuous random network [Britton et al. 2000]. Comparing the S and W values for a-Si:H with experiments on c-Si, we consider that these layers contain a large number of vacancy-like defects. Due to the large hydrogen content, these defects are associated to hydrogen. In order to estimate the number of effective positron traps, C_t , we make use of the effective positron diffusion length, L_{eff} , obtained from VEPFIT (Table 8.1). In addition, we assume that the trapping process is reaction-limited with a positron specific trapping rate, ν_t , of $10^{15}/s$ as for divacancies in c-Si [Krause-Rehberg et al. 1999], see Section 3.3.

With these assumptions we can write

$$C_t = \frac{1}{\nu_t \tau_b} \left(\frac{L_{Si}^2}{L_{eff}^2} - 1 \right) \quad (8.1)$$

where L_{Si} is the positron diffusion length in defect-free Si and τ_b the bulk positron lifetime. C_t is found to be in the range of 0.1 at. % for both types of deposited a-Si:H layers. This value is much lower than the concentrations of hydrogen obtained by ERD, which amounted to 13 at. % for GD a-Si:H films and 8.0 at % for HWCVD a-Si:H films. This large hydrogen concentration is expected to passivate effectively Si dangling bonds.

On the other hand, the het-Si:H layer (sample 3) shows a much higher S value (1.120 relative to S_{Si}) while the W parameter is much lower (0.645 relative to S_{Si}) than that obtained for the a-Si:H layers. In Fig. 8.2, cross-sections of 2D-ACAR spectra obtained for sample 3 (with het-Si:H) are shown. The spectra were obtained at positron energies of 1.5, 3.5 and 16.5 keV and they did not show anisotropy in any case. The sharp contributions to the spectra proofs the occurrence of para-positronium (p-Ps) self-annihilation, which in turn indicates that the layer contains voids where the atom-like Ps states accommodate (see above). The Ps self-annihilation and the presence of open volume explains the high S value obtained for het-Si:H in contrast with the results obtained for a-Si:H. The map of defects shown in Fig. 8.1c allows to distinguish the layers present in the samples and clearly shows the difference between annihilation values for a-Si:H and het-Si:H samples.

According to VEPFIT applied to the DBAR results, about 98% of the positrons implanted at 16.5 keV annihilate in the SiO₂ layer. In agreement, we observe in Fig. 8.2 a typical 2D-ACAR SiO₂ spectrum corresponding to the 16.5 keV measurement (see for comparison Section 7.1). A sharp gaussian contribution is seen to contribute to this spectrum with full width at half maximum (FWHM) of $3.8 \times 10^{-3} m_0c$ corresponding to p-Ps self-annihilation and accounts for 18% of the annihilations. At 3.5 keV more than 95% of the positrons annihilate in the het-Si:H layer. The spectrum measured at 3.5 keV positron energy shows a sharp contribution with FWHM = $(2.0 \pm 0.1) \times 10^{-3} m_0c$ ascribed to p-Ps that accounts for ~7% of the annihilations. This p-Ps contribution decreases by ~55% for the spectrum taken at 1.5 keV positron energy. According to the VEPFIT analysis at this energy ~60% of the annihilations takes place in the het-Si:H layer and the rest in the top Al layer. This is a

strong indication that the p-Ps sharp peak comes from the thin het-Si:H layer, proving the presence of nanovoids where Ps is formed.

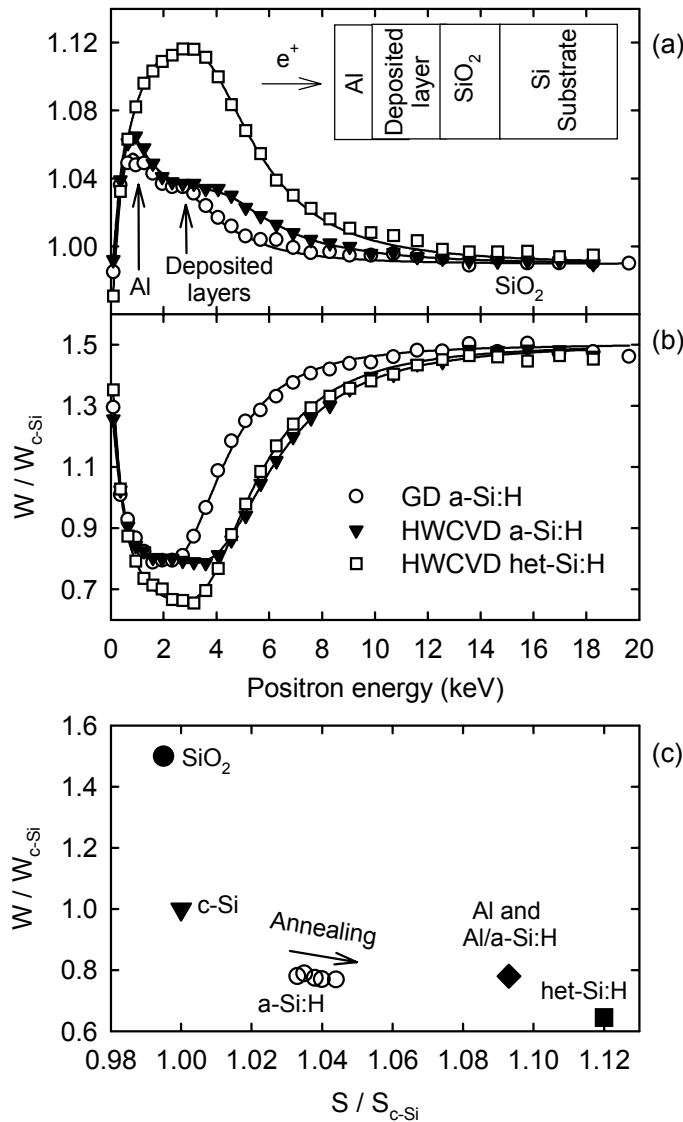


Fig. 8.1. Positron beam Doppler broadening experiments on the samples described in Table 8.1. (a) S parameter as a function of the positron energy. (b) W parameter as a function of the positron energy. (c) S - W plot with the fitted coordinates for every layer. The open symbols correspond to measurements on a HWCVD a-Si:H sample after annealing steps in situ. Therefore the five points shown for the a-Si:H layer correspond to (from left to right) room temperature measurements, measurements after annealing at 450°C for 20 min, 450°C for 60 min, 550°C for 20 min and 550°C for 60 min. The running parameter is the positron energy. In (a) and (b) the solid lines indicate the fit with VEPFIT. The insert shows a schematic representation of the sample.

Results on the decomposition into three components of the spectrum obtained at 3.5 keV are shown in Table 8.2. Besides the first component associated to p-Ps, a second

component is associated to void surface annihilation, including ortho-positronium (o-Ps) annihilation via pick-off and a third component to a-Si:H.

Table 8.2. Contributions to the 2D-ACAR spectrum for the het-Si:H sample at 3.5 keV positron implantation energy. For every component the following parameters are given: the full width at half maximum (FWHM), the fraction of annihilations and the S and W parameters.

	Component	FWHM (mrad)	Fraction (%)	S	W
1	p-Ps	2.0±0.1	7±1	1.586	0.0002
2	Void surface	7.5±0.4	47±16	1.123	0.373
3	Bulk	8.0±0.4 23±10	Rest	1.034	0.773

The projection of the 2D-ACAR spectrum corrected for the difference in resolution between Doppler and ACAR experiments gives a reconstructed Doppler broadening spectrum that can be compared with DBAR measurements performed on sample 3 at 3.5 keV. Both the DBAR measurement and the reconstruction from 2D-ACAR are shown in the insert of Fig. 8.2. The FWHM of the resolution functions was taken as $1.4 \times 10^{-3} m_0c$ for 2D-ACAR experiments and 1.2 keV for DBAR experiments. The similarity between both curves is fair. We also obtained reconstructed DBAR curves associated with the different components obtained by the fitting of the 2D-ACAR cross-sections and plotted them in the insert of Fig. 8.2 (solid lines). We only accepted the decomposition of the 2D-ACAR when it simultaneously fitted both the 2D-ACAR and the DBAR spectra.

The assignment of the first component to p-Ps self-annihilation in voids is evident. However, the other assignments require further justification. The existence of 7% annihilations related to p-Ps indicates that an important fraction of o-Ps exists in the sample. Neglecting spin conversion [He et al. 1986], we would expect that 21% of the annihilations comes from o-Ps pick-off and even in the case of spin conversion the fraction of o-Ps would be significant. The o-Ps pick-off occurs at the void surface. At the same time, free positron annihilation at the void surface giving similar contribution as o-Ps can not be ruled out. Therefore, let us consider that about 21% of the annihilations comes from o-Ps pick-off and 26% from free positrons at void surface. The assignment of the second component to annihilations at the void surface is corroborated by the observed high S and low W parameters, which indicate annihilations with low momentum electrons, as those found in open volumes. The third component is assigned to bulk a-Si:H annihilations. Despite the fact that het-Si:H layer contains crystalline phases, they only account for 6% of the layer volume. The remaining 94% of the volume is formed by amorphous Si, in which positrons will annihilate in a similar way as in purely amorphous layers without voids. It is interesting to note that in Ref. [He et al. 1986] similar components were obtained by PAL measurements for a bulk a-Si:H sample that presented a 2D-ACAR spectrum very similar to that of het-Si:H presented in this chapter.

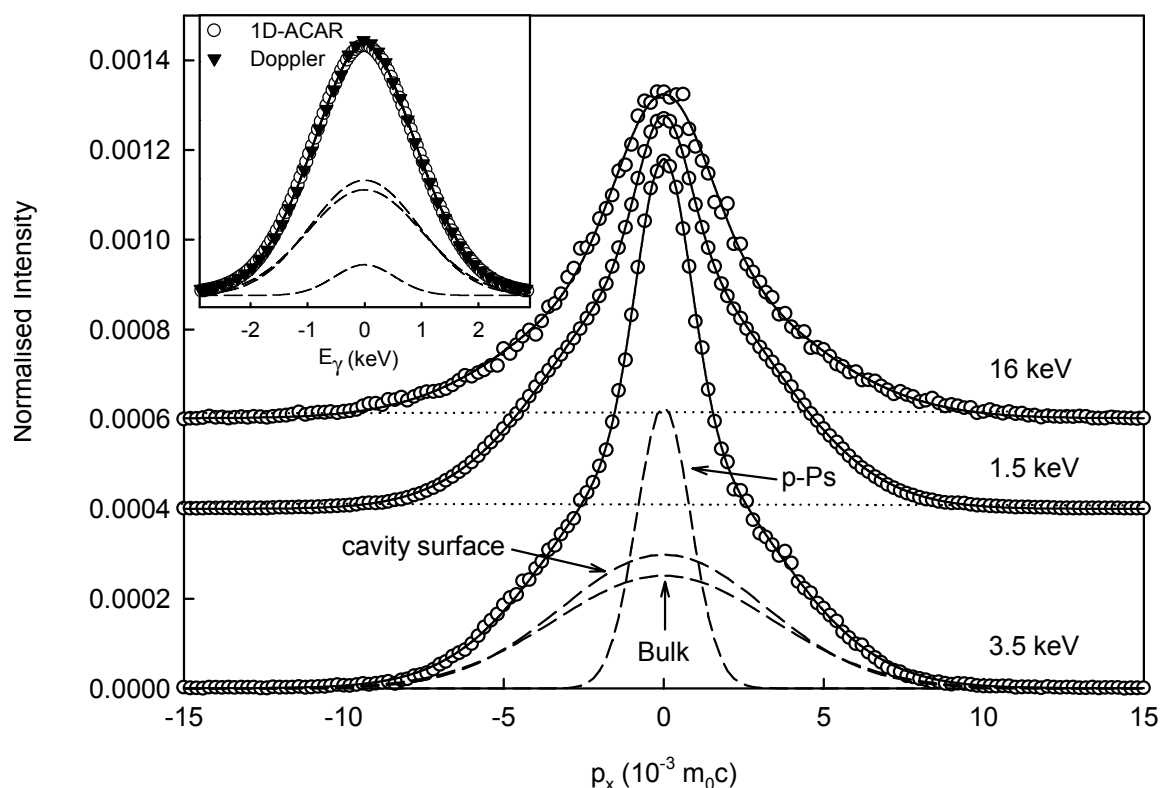


Fig. 8.2. Cross-section of the 2D-ACAR spectra obtained for the het-Si:H sample at 1.5, 3.5 and 16.5 keV. The spectrum obtained at 3.5 keV was decomposed into three components as indicated by dashed lines, corresponding to p-Ps, void surface and bulk annihilations. The solid lines through the points correspond to the fits. The insert shows (open symbols) the projection of the 2D-ACAR at 3.5 keV and the projection of the different components. In addition, the spectrum obtained for the same sample at 3.5 keV positron energy by Doppler broadening measurements is indicated by the solid symbols.

We can calculate the void radius using Jean's model [Jean 1995] under the following assumptions: spherical voids and thermalised Ps. Given a FWHM of $2.0 \times 10^{-3} m_0c$ for the p-Ps component (Table 8.2), we obtain a radius of 0.85 nm, in fair agreement with [He et al. 1986]. However, the assumption of full thermalisation of Ps has been found inappropriate in many cases. In particular for voids of about 10 nm in c-Si, it was found that Ps annihilates prior to thermalisation with energies up to 0.3 eV [Eijt et al. 2001]. Using the FWHM of the 2D-ACAR cross-section, a Ps energy of 0.16 eV is derived, significantly larger than thermal energy. Thus, it is likely that in this case the voids are much larger than expected on basis of Jean's model.

In order to determine the void size properly, we can use additional information provided by IR measurements on het-Si:H films (Fig. 8.3). The absorption peak at 2100 cm^{-1} was attributed to hydrogen at internal void surface [Brockhoff 2001]. Making use of recent IR proportionality constants [Langford et al. 1992], we can estimate the hydrogen content at internal void surfaces to be 0.46 at.%, which corresponds to an averaged hydrogen concentration of at internal void surfaces, C_H , of $2.3 \times 10^{20} \text{ cm}^{-3}$. Assuming full coverage of the

void surface, 10^{15} H/cm² can be accommodated. Thus, the number of H atoms per void is given by $10^{15}A_v$, where A_v is the void surface area. Multiplying by the concentration of voids, C_v , we get C_H as follows

$$C_H = 10^{15} A_v C_v = 4\pi 10^{15} R_v^2 C_v \quad (8.2)$$

Therefore,

$$R_v^2 C_v = \frac{C_H}{4\pi 10^{15}} \quad (8.3)$$

where R_v is the void radius. Thus, by determining C_H from IR measurements, we can determine the product of void radius squared times void concentration, as shown. In order to derive information on the value of $R_v C_v$ from positron beam analysis, we will assume that positron trapping at voids is a diffusion-limited process characterised by the trapping coefficient $\kappa = 4\pi D R_v C_v$, where D is the positron diffusion coefficient in the sample. The fraction of positrons trapped at voids, F_T , is given by the sum of the first two components obtained from the 2D-ACAR spectrum and equals 0.54 (Table 8.2). Since κ is related to the positron annihilation rate in a-Si:H, λ_{a-Si} , by $\lambda_{a-Si} F_T = (1 - F_T)\kappa$, we can write the product $R_v C_v$ as a function of the positron diffusion length in a-Si:H, L_{a-Si} . This value could be estimated from measurements on samples 1 and 2 (Table 8.1). However, we can also write the product $R_v C_v$ as a function of the effective positron diffusion length, L_{eff} , in the het-Si:H, avoiding the use of other experiments. Thus,

$$R_v C_v = \frac{F_T}{1 - F_T} \frac{1}{4\pi L_{a-Si}^2} = \frac{F_T}{4\pi L_{eff}^2} \quad (8.4)$$

Dividing (8.2) by (8.4), we get for the radius R_v a value of (8 ± 6) nm. Once the void radius is known, the void concentration C_v can be estimated, resulting in the range $(4 \times 10^{15} - 4 \times 10^{16})$ cm⁻³. This represents a volume fraction in the range (1-10 %). Similar values have been reported high growth rate films [Han et al. 2002, Baugh et al. 2001].

It is interesting to note that despite the large voids, the Ps fraction remains rather low, about 28%, whereas at clean Si surfaces it is often higher [Chen 1987] or in the underlying SiO₂ layer it reaches 72%. The explanation to this low Ps formation can be related to the presence of hydrogen decorating the void surface and forming Si-H bonds by passivation of dangling bonds, making unfavourable to get an electron from such bonds [Chen 1987]. In fact, Si surfaces exhaustively covered by hydrogen showed a very similar (low) Ps fraction [Chen 1987].

We believe that the voids are distributed randomly in the amorphous phase of the het-Si:H layer. If, otherwise, the voids were localised at the interface between the amorphous materials and the crystallites or inside the crystallites, the layer would not be homogeneous in contradiction with DBAR experiments on het-Si:H layers. In particular, experiments on

samples not covered by Al (not shown), where the depth resolution is rather good, the S and W parameters are constant along the layer, indicating that the defect concentration in the layer is homogeneous.

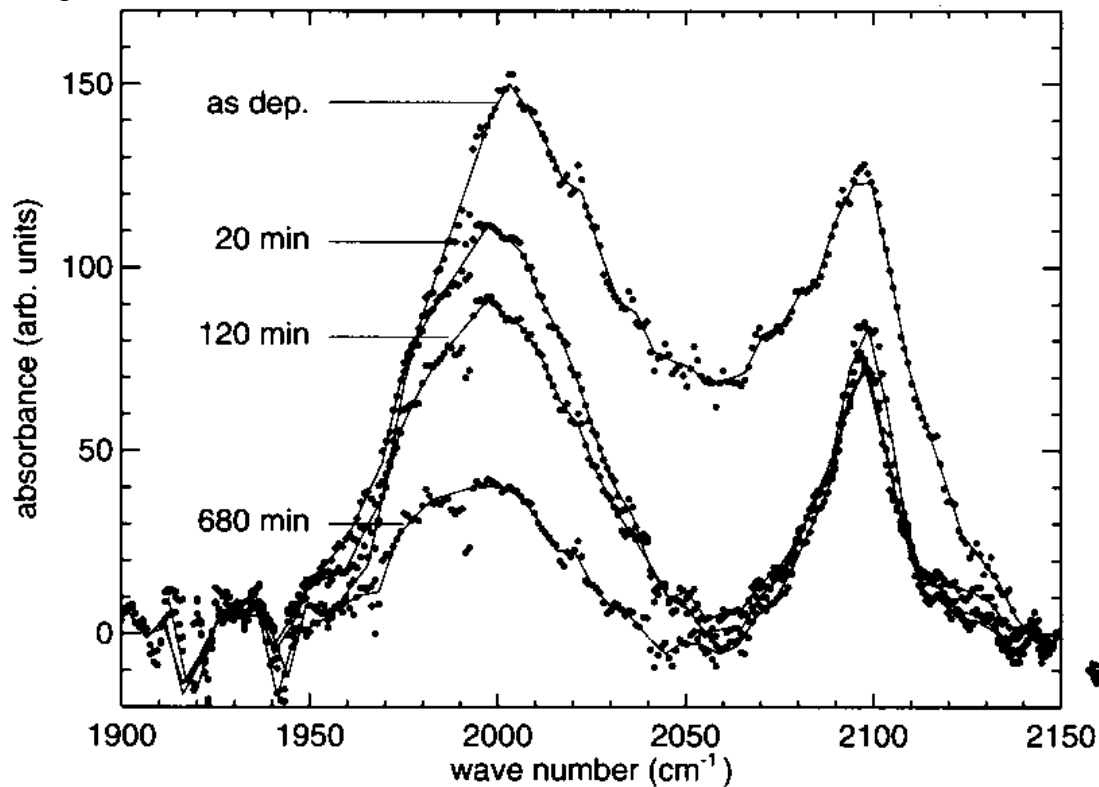


Fig. 8.3. Infra-red absorption spectra of the het-Si:H film before and after annealing at 450°C for 20, 120 and 680 minutes.

The samples deposited by the HWCVD method (samples 2 and 3) were annealed in situ. The results are shown in Fig. 8.1c. The annihilation parameters of the sample with the het-Si:H layer, which contains voids (sample 3), did not change with the annealing steps. This is in agreement with the IR measurements shown in Fig. 8.3 and indicates that the voids were initially empty and their surface did not change significantly with annealing. The high deposition temperature employed to grow the het-Si:H layers is likely responsible for the release of non-bound hydrogen, e.g. molecular H_2 inside the voids. However, the annealing steps had a clear effect on sample 2 (HWCVD a-Si:H). The S parameter increased with every annealing step. This is likely related to nucleation of defects and hydrogen release. The higher S values obtained upon annealing indicate that the vacancy-like defects loose hydrogen during annealing and become more open, though, they remain much smaller than the voids found in het-Si:H layers. This is in agreement with the image of a-Si:H as a defective material.

The observed voids apparently were created due to the deposition conditions, i.e. high substrate temperature (510°C) and low hydrogen flow. At this temperature hydrogen is free to leave the sample as indicated in the previous paragraph. The lack of hydrogen suppresses proper network relaxation during the growth and the appearance of tensile stress, see Section 8.2. This is likely the origin of the detected voids. Post-deposition annealing leads to a drop in

the hydrogen concentration [Brockhoff et al. 1999] and an increase in the tensile stress in the layer. However, no reduction in the number of voids is expected as confirmed by means of the DBAR results. It is interesting to note that depositions at temperature lower than 150°C also led to void formation [van Veen et al. 1995]. A possible explanation can be related again to the generation of stress in the sample as a consequence of the low mobility of the deposited atoms at low temperature leading to the “freezing” of atoms in un-relaxed configurations.

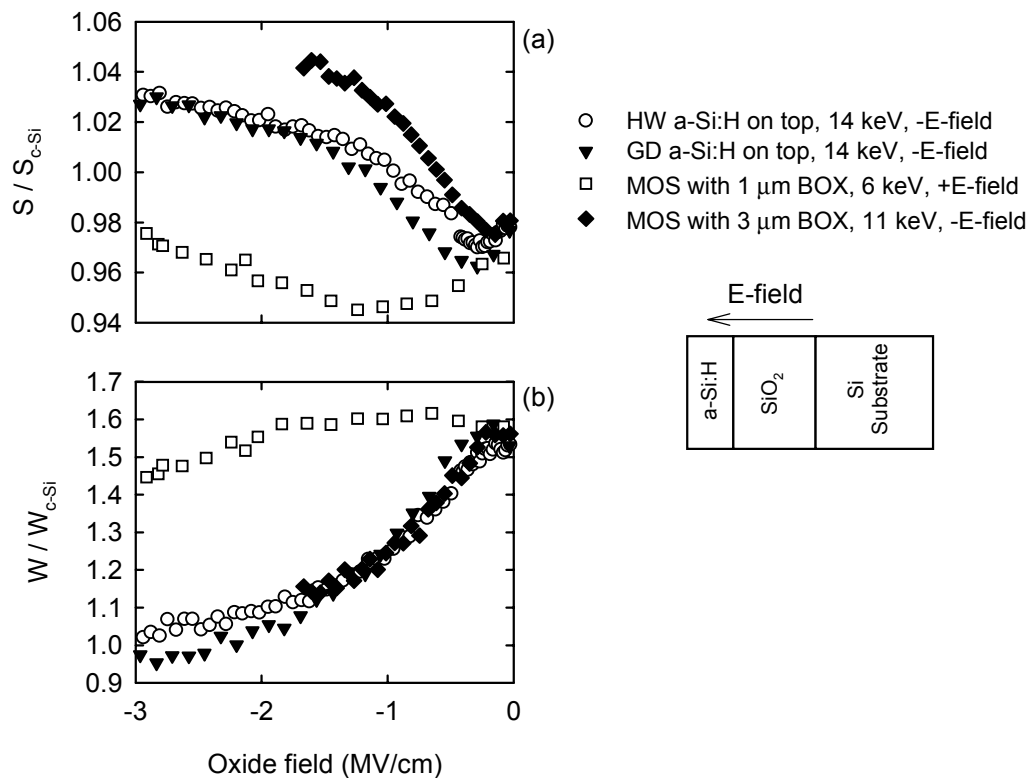


Fig. 8.4. Electric-field experiments on a-Si:H layers deposited by HWCVD and GD methods. For comparison, experiments performed on MOS samples (Chapter 7) are shown. Please, note that the sign of the positive electric field was changed to negative for comparison purposes. (a) S as a function of the applied electric field. (b) W parameter as a function of the applied electric field. The sample structure is schematically represented by the picture on the right.

8.5. The interfaces between the deposited layers and SiO₂

In order to study the interface between the a-Si:H layer deposited by GD or HWCVD and the underlying SiO₂ we performed DBAR measurements while applying electric fields to samples 1 and 2 in Table 8.1. Positrons were implanted at 14 keV this assures that about 100% of the positrons are implanted in the oxide layer. The application of a positive bias to the samples with top a-Si:H (not shown) leads to positron drift towards the SiO₂/c-Si interface. As expected, these experiments are in perfect agreement with those reported in Chapter 7 for

MOS capacitors based on the same type of Unibond samples. On the other hand, the application of negative bias leads to positrons towards the interface of interest, i.e. the a-Si:H/SiO₂ interface. In Fig. 8.4, results are shown for samples 1 (GD a-Si:H) and 2 (HWCVD a-Si:H). For comparison, results of DBAR experiments under positive and negative field on MOS samples with Unibond oxides are included. These results were presented in Chapter 7.

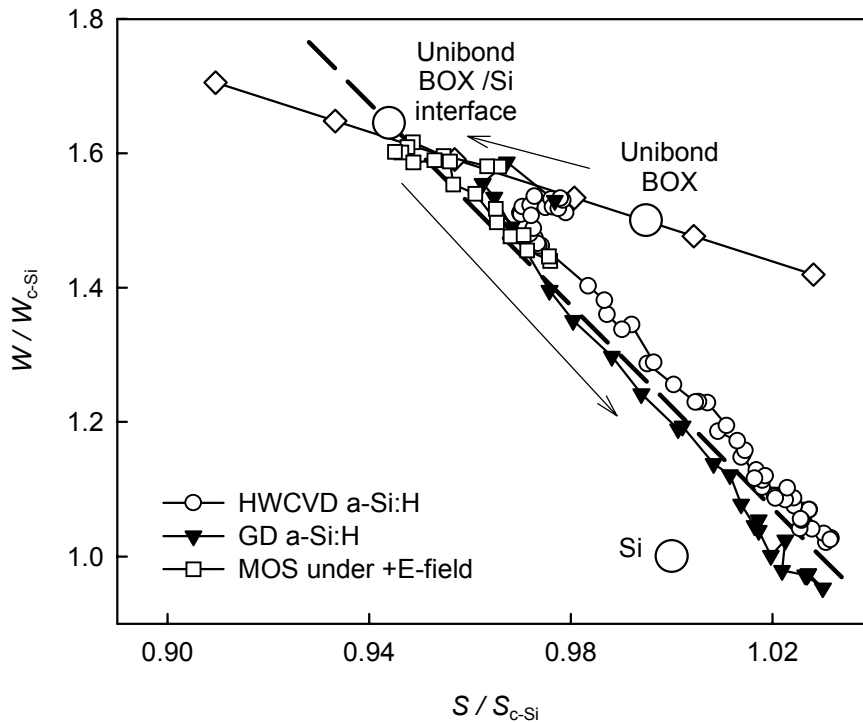


Fig. 8.5. S - W plot with the experimental points (small symbols) and cluster points (open symbols) corresponding to the indicated samples. The running parameter is the electric field. The diamonds correspond to the BOX S - W cluster point with the Ps formation as the running parameter. The dashed line represents the IF line (see Section 7.2).

One can see that the S parameter drops when a moderate negative electric field is applied to the gate, reaching a minimum at about -0.3 MV/cm and increases at higher negative electric fields. W shows opposite behaviour. The results obtained for Al-gated MOS samples show the same effect (solid diamonds). At larger fields the saturation S value characteristic of Al/SiO₂ interface is significantly higher than the highest value observed for the samples with top a-Si:H layers.

The results obtained under positive bias for the MOS sample are completely different. This is a clear indication that the a-Si:H/SiO₂ interface is rather different than the SiO₂/Si interface. At low fields the S parameter of samples 1 and 2 drops as a consequence of the reduction in the Ps formation probability (Section 7.1). The drop is less pronounced for sample 2 (HWCVD sample). This is because the deposited HWCVD a-Si:H is thicker than the GD a-Si:H layer, see Table 8.1. Thus, positrons implanted at 14 keV in sample 2 have to

travel in average a shorter distance to reach the interface. P_s continues decreasing and more positrons are able to travel to the interface contributing with a characteristic very high S -very low W . These values are very different to those obtained for the $\text{SiO}_2/\text{c-Si}$ interface. These results are similar to those obtained for Al-gated MOS samples under negative fields. In contrast, the position of the SiO_2/Si interface leads to a plateau in the S and W parameters, see Fig. 8.5, discussion in Section 7.2.

Electric fields higher than 1.5 MV/cm (in absolute value) led to a significant change in the annihilation parameters. The S value increases while W decreases. This was observed for all the studied SiO_2/Si interfaces, see Section 7.2.6. This effect was attributed to the injection of electrons from the Si layer leading to a larger P_s fraction. This effect is also observed for samples 1 and 2. Due to this effect the S and W values do not reach a saturation value even at large fields. It is therefore difficult to assign a cluster point to these interfaces. In any case, it corresponds to high S -low W parameters. The S - W plot shown in Fig. 8.5 indicates that at high fields the S - W coordinates move following the interface line identified in Chapter 7. They reach the highest S lowest W values measured for any Si/SiO₂ interface. This indicates that the interface between the a-Si:H layers and SiO₂ contain a significant fraction of open volume, which permits the formation of P_s in large amounts (Chapter 7). The results are quite similar for both samples regardless the deposition method employed. Differences were not detected likely due to the high P_s formation probability, which hinders the observation of other effects.

$\text{SiO}_2/\text{c-Si}$ interfaces with values as those found for the a-Si:H/SiO₂ interface would be undoubtedly degraded due to the presence of a large number of unpassivated dangling bonds. However, it is difficult to extrapolate this conclusion to a-Si:H/SiO₂ layers, because the high S -low W values can come in this case from the presence of open volume at the interface.

DBAR measurements under electric fields were also performed on samples 2 and 3 fixing the positron energy at 3 keV. The mean implantation depth of positrons at this energy is about 100 nm, corresponding to approximately the centre of the deposited layers. The fraction of positrons thermalised in the deposited layer amounts to 95 %. No effects were associated to the application of electric fields to the samples under these conditions (results not shown). Therefore, we conclude that no drift is experienced by positrons implanted in the a-Si:H layers. This observation is expected on the basis of the low electric field across the a-Si:H layers (even at high voltages) and the large number of positron traps present in these layers.

8.6. Conclusions

Small vacancy-like defects were found in a-Si:H layers deposited by GD or HWCVD methods. The concentration of these defects is of the order of 0.1 at. %. These defects most likely contain important amounts of hydrogen. No significant differences were found between both types of layers.

Small vacancy-like defects were found in a-Si:H layers deposited by GD or HWCVD methods. The concentration of these defects is in the order of 0.1 at. %. These defects most likely are associated to hydrogen. No significant differences were found between both types

of layers. The HWCVD het-Si:H layer contains a significant concentration of voids, ($4 \times 10^{15} - 4 \times 10^{16}$) cm^{-3} , as revealed for the first time by combined use of positron beam techniques (2D-ACAR, DBAR) and IR measurements. The radius of these voids is (8 ± 6) nm. The fraction of positronium formed in these voids amounts to 28% and annihilates prior thermalisation with an averaged energy of 0.16 eV.

DBAR measurements under the application of bias to the samples were performed in order to study the influence of the deposition method on the a-Si:H/SiO₂ interface. The DBAR technique was unable to detect differences between both types of interfaces. However, we observed that positrons annihilate in open volume associated with the interface. Electrons can be injected in the SiO₂ under the application of a sufficiently high negative electric field, enhancing the Ps formation and thus the *S* parameter. Positrons implanted at the a-Si:H layers were found not to drift under the application of electric fields.

References

- [Afanas'ev et al. 1995] V.V. Afanas'ev, J.M.M. de Nijs, P. Balk, A. Stesmans, J. Appl. Phys. **78** (1995) 6481
- [Afanas'ev et al. 1997] V.V. Afanas'ev, A. Stesmans, A.G. Revesz, H.L. Hughes, J. Appl. Phys. **82** (1997) 2184.
- [Afanas'ev et al. 1999] V.V. Afanas'ev, A. Stesmans, J. Electrochem. Soc. **146** (1999) 3409
- [Afanas'ev et al. 2000] V.V. Afanas'ev, A. Stesmans, J. Phys.: Condens. Matter, **12** (2000) 2285.
- [Afanas'ev et al. 2001] V.V. Afanas'ev, A. Stesmans, Europhys. Lett., **53** (2001) 233.
- [Afanas'ev et al. 2001b] V.V. Afanas'ev, A. Stesmans, Mat. Sci. Semicon. Proc., **4** (2001): 149.
- [Alba García et al. 2001] A. Alba García, L.D.A. Siebbeles, A. Rivera, H. Schut, S.W.H. Eijt, R. Escobar Galindo, A. van Veen, Materials Science Forum, **363-365** (2001) 287.
- [Anders et al. 1998] A. Anders, M. Kühn, Review of Scientific Instruments, **69** (1998) 3.
- [Arnold et al. 1982] G.W. Arnold, B.L. Doyle, Nucl. Instr. Methods **194** (1982) 491.
- [Asoka-Kumar et al. 1995] P. Asoka-Kumar, K.G. Lynn, in: A. Dupasquier, A. P. Mills Jr. (Eds.), Positron Spectroscopy of Solids, AIOS Press, Amsterdam (1995) p. 659 and references therein.
- [Ausman et al. 1975] G.A. Ausman jr., F.B. McLean, Appl. Phys. Lett., **26** (1975) 173.
- [Barbottin et al. 1991] G. Barbottin, A. Vapaille (eds.), Instabilities in silicon devices, vol 1, Elsevier Science Publishers, Amsterdam, 1991.
- [Baugh et al. 2001] J. Baugh, D. Han, A. Kleinhammes, Y. Wu, Appl. Phys. Lett. **78** (2001) 466.
- [Beeman et al. 1985] D. Beeman, R. Tsu, M.F. Thorpe, Phys. Rev. B **32** (1985) 874.
- [Benedetto et al. 1985] J.M. Benedetto, H.E. Boesch, F.B. McLean, J.P. Mize, IEEE Trans. Nucl. Sci. **NS-32** (1985) 3916
- [Benedetto et al. 1986] J.M. Benedetto, H.E. Boesch, jr., IEEE Trans. Nucl. Sci. **NS-33** (1986) 1318.
- [Berger et al. 1964] M.J. Berger, S.M. Seltzer, NASA report SP-3012, Washington, D.C. (1964)
- [Berger et al. 1966] M.J. Berger, S.M. Seltzer, NASA report SP-3036, Washington, D.C. (1966)
- [Biersack et al. 1980] J.F. Biersack, L.G. Haggmark, Nucl. Instrum. Methods, **174** (1980) 257.
- [Britton et al. 2000] D.T. Britton, A. Hempel, D. Knoesen, W. Bauer-Kugelmann, W. Triftshäuser, Nucl. Instr. and Meth. in Phys. Res. B **164-165**, (2000) 1010.
- [Brockhoff et al. 1998] A.M. Brockhoff, E.H.C. Ullersma, H. Meiling, F.H.P.M. Habraken, W.F. van der Weg, App. Phys. Lett. **73** (1998) 3244.
- [Brockhoff et al. 1999] A.M. Brockhoff, H. Meiling, F.H.P.M. Habraken, R.E.I. Schropp, in Proceedings of the fourth symposium on Thin Film Transistor Technologies-1998, edited by Y. Kuo, The Electrochemical Society, Pennington, **98-22** (1999) 288.
- [Brockhoff 2001] A.M. Brockhoff, in: *Hydrogen-related modifications on amorphous silicon and silicon nitride*, (thesis) University of Utrecht (2001).
- [Brower et al. 1990] K.L. Brower, S.M. Myers, Appl. Phys. Lett., **57** (1990) 162.
- [Buchanan et al. 1991] D.A. Buchanan, M.V. Fischetti, D.J. DiMaria, Phys. Rev. B., **43** (1991) 1471.
- [Cheng 1987] D.M. Cheng, Doctoral Thesis, The City University of New York (1987).
- [Chu et al. 1997] V. Chu, J. Jarego, H. Silva, T. Silva, M. Reissner, P. Brogueira, J.P. Conde. Appl. Phys. Lett. **70** (1997) 2714.
- [Clement 1998] M. Clement, in: *Positrons in the MOS system*, (thesis) Delft University of Technology: Delft University Press (1998).
- [Clement et al. 1997] M. Clement, J.M.M. de Nijs, P. Balk, H. Schut, A. van Veen, J. Appl. Phys. **81** (1997) 1943.
- [Curtis et al. 1974] O.L. Curtis jr., J.R. Srouf, K.Y. Chiu, J. Appl. Phys., **45** (1974) 4506.
- [Dannefaer et al. 1986] S. Dannefaer, D. Kerr, J. Appl. Phys., **60** (1986) 1313.
- [Dannefaer et al. 1990] S. Dannefaer, Defect Control in Semiconductors, ed. By K. Sumino, Elsevier Science, Amsterdam, (1990) 1561.
- [Dannefaer et al. 1993] S. Dannefaer, T. Bretagnon, D. Kerr, J. Appl. Phys., **74** (1993) 884.
- [de Nijs et al. 1994] J.M.M. de Nijs, K.G. Druijf, V.V. Afanas'ev, E. van der Drift, P. Balk, Appl. Phys. Lett. **65** (1994) 2428
- [DiMaria et al. 1995] D.J. DiMaria, E. Cartier, J. Appl. Phys. **78** (1995) 3883
- [Doyle et al. 1988] J. Doyle, R. Robertson, G.H. Lin, M.Z. He, A. Gallagher, J. Appl. Phys. **64** (1988) 3215.

- [Druijf et al. 1995] K.G. Druijf, J.M.M. de Nijs, E. van der Drift, E.H.A. Granneman, P. Balk, J. Appl. Phys., **78** (1995) 306.
- [Eijt et al. 2001] S.W.H. Eijt, C.V. Falub, A. van Veen, H. Schut, P.E. Mijnders, M.A. van Huis, Mat. Res. Soc. Symp. Proc. **647** (2001) O14.11.
- [Eleveld 1996] H. Eleveld, in: *Hydrogen and helium in selected fusion reactor materials*, (thesis) Delft University of Technology: Delft University Press, 1996.
- [Eleveld et al. 1992] H. Eleveld, A. van Veen, J. Nucl. Matter., **191-194** (1992) 433.
- [Eleveld et al. 1994] H. Eleveld, A. van Veen, J. Nucl. Matter., **212-215** (1994) 1421.
- [Ericsson et al. 1997] P. Ericsson, S. Bengtsson, Appl. Phys. Lett. **71** (1997) 16.
- [Falub 2002] C.V. Falub, in: *The Delft intense slow positron beam 2D-ACAR facility for analysis of nanocavities and quantum dots*, (thesis) Delft University of Technology: Delft University Press, 2002.
- [Fedorov 2000] A.V. Fedorov, in: *Evolution of point defect clusters during ion irradiation and thermal annealing*, (thesis) Delft University of Technology: Delft University Press (2000).
- [Fedorov et al. 2001] A.V. Fedorov, A. van Veen, H. Schut, Materials Science Forum, **363-365** (2001) 646.
- [Fink et al. 1995] D. Fink, J. Krauser, D. Nagengast, T. Almeida Murphy, J. Erxmeier, L. Palmethofer, D. Bräunig, A. Weidinger, Appl. Phys. A, **61** (1995) 381.
- [Fujinami 1996] M. Fujinami, Phys. Rev. B **53** (1996) 19.
- [Fujinami et al. 1993] M. Fujinami, N.B. Chilton, Appl. Phys. Lett. **62** (1993) 1131.
- [Griscom 1985] D.L. Griscom, J. Appl. Phys. **58** (1985) 2524
- [Hakvoort 1993] R. Hakvoort, M. in: *Applications of positron depth profiling*, (thesis) Delft University of Technology: Delft University Press (1998).
- [Han et al. 2002] D. Han, G. Yue, K. Wang, J. Baugh, Y. Wu, Y. Xu, Q. Xiang, Applied Physics Letters, **80** (2002) 40.
- [Hasegawa et al. 2000] M. Hasegawa, M. Saneyasu, M. Tabata, Z. Tang, Y. Nagai, T. Chiba, Y. Ito, Nucl. Instr. and Meth. in Phys. Res. B, **166-167** (2000) 431.
- [Hautojärvi et al. 1995] P. Hautojärvi, C. Corbel, in: *Positron Spectroscopy of Solids*, ed. by A. Dupasquier and P.A. Mills jr., IOS Press, Amsterdam (1995) 491.
- [He et al. 1986] Y.J. He, M. Hasegawa, R. Lee, S. Berko, D. Adler, A.L. Jung, Physical Review B, **33** (1986) 5924.
- [Holm et al. 1991] B. Holm, K. Bonde Nielsen, B. Bech Nielsen, Phys. Rev. Lett **66** (1991) 2360.
- [Hughes 1973] R.C. Hughes, Phys. Rev. Lett. **30** (1973) 1333.
- [Hughes 1978] R.C. Hughes, Solid State Electronics. **21** (1978) 251.
- [Ikari 1995] A. Ikari, Appl. Surf. Sci., **85** (1995) 253.
- [Jean 1995] Y.C. Jean, in: A. Dupasquier, A. P. Mills Jr. (Eds.), *Positron Spectroscopy of Solids*, AIOS Press, Amsterdam (1995), chapter 5.
- [Kawasuso et al. 1995] A. Kawasuso, M. Hasegawa, M. Suezawa, S. Yamaguchi, K. Sumino, Appl. Surf. Sci. **85** (1995) 280.
- [Kim et al.1988] Y.Y. Kim, P.M. Lenahan, J. Appl. Phys., **64** (1988) 3551.
- [Kobayashi et al. 2001] Y. Kobayashi, C.L. Wang, K. Hirata, N. Kouchi, Materials Science Forum **363-365** (2001) 138
- [Kong et al. 1991] Y. Kong, T.C. Leung, P. Asoka-Kumar, B. Nielsen, K.G. Lynn, J. Appl. Phys. **70** (1991) 2874
- [Krause et al. 1998] S. Krause, M. Anc, P. Roitman, MRS bulletin, **23** (1998) 25.
- [Krause-Rehberg et al. 1999] R. Krause-Rehberg, H.S. Leipner, in: *Positron annihilation in semiconductors*, Springer-Verlag Berlin Heidelberg (1999) chapter 3.
- [Langford et al. 1992] A.A. Langford, M.L. Fleet, B.P. Nelson, W.A. Lanford, N. Maley, Phys. Rev. B **45** (1992) 13367
- [Lee et al. 1976] Y.H. Lee, J.P. Corbet, Phys. Rev. B, **13** (1976) 2653.
- [Lenahan et al.1984] P.M. Lenahan, P.V. Dressendorfer, J., Appl. Phys., **55** (1984) 3495.
- [Leung et al. 1993] T.C. Leung, P. Asoka-Kumar, B. Nielsen, K.G. Lynn, J. Appl. Phys. **73** (1993) 168
- [Lynn et al. 1989] K.G. Lynn, B. Nielsen, D.O. Welch, Can. J. Phys, **67** (1989) 818.
- [Mahan et al. 1991] A.H. Mahan, J. Carapella, B.P. Nelson, R.S. Crandall, I. Balberg, J. Appl. Phys. **69** (1991) 6728.

- [Mäkinen et al. 1990] J. Mäkinen, E. Punkka, A. Vehanen, P. Hautojärvi, J. Keinonen, M. Hautala, E. Rauhala, *J. Appl. Phys.* **67** (1990) 990.
- [Matsumura 1986] H. Matsumura, *Jpn. J. Appl. Phys.* **25** (1986) L949.
- [Matsumura 1989] H. Matsumura, *J. Appl. Phys.* **65** (1989) 4396.
- [Meiling et al. 1997] H. Meiling, R.E.I. Schropp, *Appl. Phys. Lett.* **70** (1997) 2681.
- [Meiling et al. 1998] H. Meiling, A.M. Brockhoff, J.K. Rath, R.E.I. Schropp, in: *Amorphous and Microcrystalline Silicon Technology-1998*, ed. by R. Schropp, H.M. Branz, M. Hack, I. Shimizu, S. Wagner, Materials Research Society, Warrendale, **507** (1998) 31.
- [Mitchell et al. 1990] I.V. Mitchell, P.J. Simpson, P.J. Schultz, M. Vos, U. Akano, C. Wu, in: P.J. Schultz, G.R. Massoumi and P.J. Simpson (Eds.), *Positron Beams for Solids and Surfaces*, AIP Conf. Proc., **218**, AIP, New York, 1990.
- [Mogensen 1974] O.E. Mogensen, *J.Chem. Phys.*, **60** (1974) 998.
- [Miyamaru et al. 1996] H. Miyamaru, T. Tanabe, T. Iida, A. Takahashi, *Nucl. Instr. and Meth. in Phys. Res. B*, **116** (1996) 393.
- [Myers et al. 1990] S.M. Myers, P.M. Richards, *J. Appl. Phys.* **67** (1990) 4064
- [Myers et al. 1993] S.M. Myers, G.A. Brown, A.G. Revesz, H.L. Hughes, *J. Appl. Phys.* **73** (1993) 2196
- [Nagashima et al. 1998] Y. Nagashima, Y. Morinaka, T. Kurihara, Y. Nagai, T. Hyodo, T. Shidara, K. Nakahara, *Phys. Rev. B*, **58** (1998) 12676.
- [Nagashima et al. 2000] ****
- [Nasu et al. 1987] H. Nasu, M. Watanabe, K. Shizuma, T. Imura, Y. Osaka, H. Hasai, *Yogyo-Kyokai-Shi*, **95** (1987) 5.
- [Nelms 1956] A.T. Nelms, *Nat. Bur. Standards, (US) Circ. No. 577* (1956).
- [Nicollian et al. 1971] E.H. Nicollian, C.N. Berglund, P.F. Schmidt, J.M. Andrews, *J. Appl. Phys.* **42** (1971) 5654.
- [Nicollian et al. 1982] E.H. Nicollian, J.R. Brews, *Physics and Technology* (Willey Interscience, New York, 1982).
- [Nieminen et al. 1980] R.M. Nieminen, J. Oliva, *Phys. Rev. B*, **22** (1980) 2226.
- [Pankove et al. 1983] J.I. Pankove, D.E. Carlson, J.E. Berkeyheiser, R.O. Wanze, *Phys. Rev. Lett.* **51** (1983) 2224.
- [Papadopoulos et al. 1993] P. Papadopoulos, A. Scholz, S. Bauer, B. Schröder, H. Öchsner, *J. Non-Cryst. Solids* **164-166** (1993) 87.
- [Pearton et al. 1986] S.J. Pearton, A.M. Chantre, L.C. Kimerling, K.D. Cummings, W.C. Dautremont-Smith, *Mat. Res. Soc. Symp. Proc.* **59** (1986) p. 475.
- [Petkov et al. 2002] M.P. Petkov, K.G. Lynn, A. van Veen, *Physical Review B* **66** (2002) 045322
- [Pimblot et al. 2000] S.M. Pimblot, J.A. LaVerne, A. Alba García, L.D.A. Siebbeles, *J. Phys. Chem. B*, **104** (2000) 9607
- [Rashkeev et al. 2001] S.N. Rashkeev, M. di Ventura, S.T. Pantelides, *Appl. Phys. Lett.*, **78** (2001) 1572.
- [Rath et al. 1997] J.K. Rath, H. Meiling, R.E.I. Schropp, *Jpn. J. Appl. Phys.* **36** (1997) 5436.
- [Revesz 1979] A.G. Revesz, *J. Electrochem. Soc. : Solid state science and technology*, **126** (1979) 122.
- [Revesz et al. 1997] A.G. Revesz, H.L. Hughes, *Microelectronic Engineering* **36** (1997) 343
- [Rivera et al. 2001] A. Rivera, A. van Veen, H. Schut, J.M.M. de Nijs, P. Balk, P.F.A. Alkemande, *Nucl. Instr. and Meth. in Phys. Res. B*, **178** (2001) 287.
- [Rivera et al. 2001b] A. Rivera, I. Montilla, A. Alba García, R. Escobar Galindo, C.V. Falub, A. van Veen, H. Schut, J.M.M. de Nijs, P. Balk, *Materials Science Forum*, **363-365** (2001) 64.
- [Schmidt et al. 1992] M. Schmidt, H. Köster, *Phys. Status Solidi B*, **174** (1992) 53.
- [Shelby 1994] J.E. Shelby, *Journal of non-crystalline solids*, **179** (1994) 138.
- [Simpson et al. 1989] R.I. Simpson, M.G. Stewart, C.D. Beling, M. Charlton, *J. Phys.: Condens. Matter.* **1** (1989) 7251
- [Simpson et al. 1990] P.J. Simpson, P.J. Schultz, T.E. Jackman, G.C. Aers, J.P. Noël, D.C. Houghton, D.D. Perovic, G.C. Weatherly, in: P.J. Schultz, G.R. Massoumi and P.J. Simpson (Eds.), *Positron Beams for Solids and Surfaces*, AIP Conf. Proc., **218**, AIP, New York, 1990.
- [Srouf et al. 1974] J.R. Srouf, O.L. Curtis jr. K.Y. Chiu, *IEEE Trans. Nucl. Sci.*, **NS-21** (1974) 73.

- [Staebler et al. 1977] D.L. Staebler, C.R. Wronski, Appl. Phys. Lett. **31** (1977) 292.
- [Stepanov et al. 2002] S.V. Stepanov, V.M. Byakov, J. Chem. Phys, **116** (2002) 116.
- [Stesmans et al. 1998] A. Stesmans, V.V. Afanas'ev, J. Appl. Phys., **83** (1998) 2449.
- [Stesmans 2000] A. Stesmans, J. Appl. Phys., **88** (2000) 489.
- [Stesmans 2000b] A. Stesmans, Phys. Rev. B **61** (2000) 8393
- [Suzuki et al. 2002] R. Suzuki, T. Ohdaira, A. Uedono, Y. Kobayashi, Appl. Surf. Sci. **194** (2002) 89.
- [Triska et al. 1975] A. Triska, D. Dennison, H. Fritzsche, Bull. Am. Phys. Soc. **20** (1975) 392.
- [Uedono et al. 1994] A. Uedono, L. Wei, S. Tanigawa, R. Suzuki, H. Ohgaki, T. Nikado, T. Kawano, Y. Ohji, J. Appl. Phys. **75** (1994) 3822.
- [Uedono et al. 1994b] A. Uedono, L. Wei, S. Tanigawa, R. Suzuki, H. Ohgaki, T. Nikado, K. Fujino, J. Appl. Phys. **75** (1994) 216.
- [Uedono et al. 1994c] A. Uedono, T. Kawano, S. Tanigawa, H. Itoh, J. Phys: Condens. Matter, **6** (1994) 8669.
- [Valkealahti et al. 1983] S. Valkealahti, R.M. Nieminen, Appl. Phys. A **32** (1983) 95
- [Valkealahti et al. 1984] S. Valkealahti, R.M. Nieminen, Appl. Phys. A, **35** (1984) 51.
- [van Veen 1990] A. Van Veen, Positron beam analysis techniques and gas desorption spectrometry for the characterization of defects in materials. J. Trace and Microprobe Techniques, **8** (1990) 1.
- [van Veen et al. 1990] A. van Veen, H. Schut, J. de Vries, R.A. Hakvoort, M.R. IJpma, in: Proceedings of the Fourth International Workshop on Slow-Positron Beam Techniques for Solids and Surfaces, ed. P.J. Schultz, G.R. Massoumi, P.J. Simpson, AIP, New York 1990, 171.
- [van Veen et al. 1995] A. van Veen, R.A. Hakvoort, H. Schut, P.E. Mijnders, Journal de Physique IV, **5** (1995) C1-37.
- [van Veen et al. 1996] A. van Veen, H. Schut, A. Rivera, A.V. Fedorov, Mat. Res. Soc. Symp. Proc. **396** (1996) 155.
- [van Veen et al. 1997] A. van Veen, F. Labohm, H. Schut, J. de Roode, T. Heijenga, P.E. Mijnders, Appl. Surf. Sci., **116** (1997) 39.
- [van Veen et al. 2000] A. van Veen, H. Schut, P.E. Mijnders, in: P. Coleman (Ed.) *Positron beams and their applications*. World Scientific Publishing, Singapore (2000) 191.
- [van Veen et al. 2001] A. van Veen, H. Schut, J. de Roode, F. Labohm, C.V. Falub, S.W.H. Eijt, P.E. Mijnders, Matter. Sci. Forum, **363-365** (2001) 415.
- [Vanheusden et al. 1994] K. Vanheusden, A. Stesmans, Appl. Phys. Lett. **64** (1994) 2575.
- [Vanheusden et al. 1997] K. Vanheusden, W.L. Warren, R.A.B. Devine, D.M. Fleetwood, J.R. Schwank, M.R. Shaneyfelt, P.S. Winokur, Z.J. Lemnios, Nature **386** (1997) 587.
- [Vitiello et al. 2000] M. Vitiello, N. López, F. Illas, G. Pacchioni, J. Phys. Chem. A, **104** (2000) 4674.
- [Wiesman et al. 1979] H. Wiesmann, A.K. Ghosh, T. McMahon, M. Strongin, J. Appl. Phys. **50** (1979) 3752.
- [Winokur 1989] P.S. Winokur, in: *Ionising radiation effects in MOS devices and circuits*, ed. T.P. Ma and P.V. Dressendorfer, Wiley-Interscience, New York, (1989)
- [Witham et al. 1987] H.S. Witham, P.M. Lenahan, IEEE Trans. Nucl. Sci., **34** (1987) 1147.
- [Zhu et al. 1998] Z. Zhu, Y. Jin, C. Li, Y. Sun, Z. Zhang, Q. Meng, Nucl. Instr. and Meth. in Phys. Res. B, **146** (1998) 455.
- [Zimmerman et al. 1998] L. Zimmerman, A. Rivera, J.M.M. de Nijs, A. van Veen, Mat. Res. Soc. Symp. Proc. **513** (1998) 331

Summary

The booming of microelectronics in recent decades has been made possible by the excellent properties of the Si/SiO₂ interface in oxide on silicon systems. This semiconductor/insulator combination has proven to be of great value for the semiconductor industry. It has made it possible to continuously increase the number of transistors per chip until the physical limit of integration is now almost reached. Silicon-on-insulator (SOI) materials were early on seen as a step in the logical evolution of integrated circuit technology. The basic advantage of the SOI technology is that it keeps the active elements of the integrated circuits electrically insulated from each other, forming Si islands. This prevents undesired effects like parasitic capacitances or cross-talk between devices and improves critical transistor design parameters such as the current gain or the subthreshold characteristics. It turns out that integrated circuits based on SOI materials are very appropriate for applications at high temperature, in hostile environments or in situations in which severe demands are made on power consumption.

Despite these advantages, the development of adequate methods for the fabrication of SOI materials is a relatively recent achievement that in the end has led to the commercial use of SOI-based technology in microelectronics. Nowadays, Unibond is the most successful SOI material. Unibond samples are fabricated by the so-called SmartCut method as described in Chapter 1. SIMOX (separation by implantation of oxygen) is another important SOI material. As the name indicates, a SiO₂ layer is formed underneath a crystalline Si layer by oxygen implantation in a Si substrate and subsequent high temperature annealing.

In contrast with conventional thermal oxidation of Si to form SiO₂ insulating layers, SOI materials are fabricated in rather intrusive ways. This leads to the appearance of new defects in SOI materials, which requires special study. Particularly, the buried oxides of SOI materials are in general more defective than conventional thermal oxides. The interaction with the ubiquitous hydrogen is of importance in view of the large number of degradation effects in which hydrogen is involved. Examples are: trap creation, donor generation at the Si/SiO₂ interface, depassivation of dangling bonds, generation of states in the Si band gap or formation of complexes with shallow dopant impurities. In the case of SOI materials, the occurrence of these effects may be enhanced for various reasons, e.g., the presence of

hydrogen in large amounts as observed for SIMOX, the presence of H₂ cracking sites, the existence of stress in the films or the confined nature of the buried oxide.

This thesis intends to be a contribution to the understanding of the defect mechanisms. SIMOX and Unibond samples were brought into contact with hydrogen (or deuterium) by different methods. The interaction of hydrogen with the samples was studied by a number of techniques, in particular thermal desorption spectrometry (TDS), positron beam analysis (PBA) and capacitance-voltage measurements (CV). The first two techniques are not standard in semiconductor research, and it required a technical effort to adapt them to semiconductor studies. In the thesis it is shown that useful information can be obtained with the combined use of these techniques.

Chapter 1 gives a general overview of the problems mentioned above. In addition, it describes the methods employed to fabricate SOI materials. A description of defects in SiO₂ and the models employed to describe the experimental results are given in Chapter 2. Some important (electro-)chemical reactions involved in defect generation are also discussed. They include the interaction mechanism of holes with Si-H defects in SiO₂ and the release mechanism of chemically bound hydrogen in SiO₂. The first mechanism plays a major role in the generation of positive charge at the SiO₂/Si interface and the appearance of Si dangling bonds in the oxide. The second mechanism emphasises the role of atomic hydrogen in the release of hydrogen and the role of H₂ cracking centres. In addition, a model for positron transport in electrically biased SiO₂ is also presented in Chapter 2. It is assumed that positrons implanted in SiO₂ can readily form positronium (Ps). The remaining positrons may travel, drifted by the electric field. The formation of Ps is described by a time dependent three-dimensional rate-diffusion model. It takes into account the simultaneous interaction of electrons, holes and positrons. The transport of the positrons that do not form Ps is described by the one-dimensional stationary rate-diffusion equation.

The experimental techniques employed in this thesis are described in Chapter 3. Firstly, the sample treatments are introduced. They include cleaning procedures and the different ways employed to bring the samples into contact with hydrogen, i.e. annealing in hydrogen (deuterium) and ion implantation. Secondly, TDS is exhaustively described. In particular, the complications of studying hydrogen desorption in contrast to helium desorption are shown. In addition, it is shown how to study VUV radiation-induced desorption, which allows one to correlate gas release with hole injection in SiO₂ by VUV radiation. This technique is referred to as Radiation-induced Desorption Spectrometry (RDS). Thirdly, the different PBA techniques employed in this thesis are described in detail, i.e. Doppler Broadening of Annihilation Radiation (DBAR) and Two-Dimensional Correlation of Annihilation Radiation (2D-ACAR).

The effects associated with hole injection into SiO₂ are studied in Chapter 4 by the combined use of TDS, RDS, PBA and CV. MOS capacitors were annealed in deuterium gas at 680 K. The concentration of deuterium in the sample was established by TDS measurements. Next, the gas released during hole injection was monitored by RDS, while the profile of defects created in the oxide was monitored by PBA and the accumulation of positive charge by CV. The results are in agreement with the model of hole injection shown in Chapter 2. They prove that hole injection results in the release of hydrogen, the generation of

positive charge at the SiO₂/Si interface and the generation of Si dangling bonds near the Al/SiO₂ interface.

TDS experiments on SIMOX samples implanted with deuterium or annealed in deuterium are presented in Chapter 5. The trapping sites were identified as Si-D and Si-OD groups. It was shown that the presence of Si or O dangling bonds results in a high concentration of atomic hydrogen species in the oxide. This, in turn, leads to the release of bound deuterium via the formation of molecular hydrogen species. It is shown that the Si top layer acts as a barrier for deuterium release since D₂ molecules must first dissociate at the interface in order to travel through the Si top layer or to travel distances in the order of mm to escape via the lateral sides of the sample. TDS allows one to distinguish both release paths.

Ps is formed in large amounts in SiO₂ as shown in Chapter 6. This must be considered when performing PBA experiments on SiO₂. In this chapter a new way of determining the Ps fraction by DBAR measurements is shown. The defects generated by electron or hole injection are discussed. It is shown that hole injection experiments like those shown in Chapter 4 lead to the generation of positron trapping sites, which clearly indicates that they are not positively charged as previously had been suggested. On the other hand, electron injection experiments result in the generation of negatively charged centres, which constitute very attractive positron traps. The treatments employed in Chapter 5 to introduce deuterium into the samples generate defects. Annealing in deuterium does not lead to the generation of positron trapping sites; however, it causes the accumulation of positive charge. On the other hand, ion implantation results in the generation of positron trapping sites associated with the displacement of Si and O atoms and the generation of dangling bonds. The evolution of these defects with thermal annealing is also monitored in Chapter 6 with PBA.

In order to enhance the fraction of positrons annihilated at the SiO₂/Si interfaces, positrons are implanted in the SiO₂ layer and then drifted to the interface by an external electric field. These experiments are described in Chapter 7. However, the simultaneous formation of Ps complicates the interpretation of the results. Therefore, the first part of the chapter is devoted to the study of positron transport in SiO₂. It is assumed that positrons that form Ps are not able to follow the electric field. The positron transport model presented in Chapter 2 is applied here to explain the experimental observations. Once the transport process is understood, positron studies with electric fields are performed. It is demonstrated that Ps is also formed when positrons reach the interface, depending on the interface configuration. For example, a hydrogenated interface results in a smaller Ps fraction than a dehydrogenated one. The use of PBA studies in combination with the application of electric fields proves to be a useful technique for extracting information on interface properties.

Chapter 8 is devoted to other SOI systems. Those that have an amorphous Si layer on top are employed for solar cell applications and the fabrication of thin film transistors. The amorphous Si layers were deposited by glow discharge (GD) or hot wire (HW) techniques. Some of the samples contain embedded crystalline phases. By means of positron beam 2D-ACAR it is demonstrated that these samples also contain large nanovoids which are very difficult to identify by other techniques. DBAR measurements performed under the application of electric fields show that the interface between the deposited amorphous Si and SiO₂ is very similar for samples deposited by either GD or HW techniques. It is shown that

positrons annihilate in open volume defects associated with the interface. In addition, the measurements show that electrons are easily injected from the amorphous layer into SiO₂ where they contribute to an enhanced formation of Ps.

Samenvatting

Het zijn de goede elektrische eigenschappen van de Si/SiO₂ grenslaag, die de explosieve groei van de micro-electronica in de laatste decennia mogelijk gemaakt hebben. Deze halfgeleider/diëlektricumisolator combinatie heeft bewezen excellente eigenschappen te bezitten voor de halfgeleiderindustrie en heeft het aantal transistoren per chip continu doen toenemen waarbij op dit moment bijna de fysische limiet van integratie is bereikt. *Silicon-on-insulator* (SOI) materialen werden in eerste instantie beschouwd als een stap voorwaarts in de logische evolutie van de *integrated circuit* technologie. Het voornaamste voordeel van de SOI technologie is dat het de actieve elementen van de geïntegreerde circuits elektrisch isoleert, waarbij Si-eilanden gevormd worden. Dit voorkomt ongewenste effecten zoals parasitaire capaciteiten of *cross-talk* tussen devices, het verbetert kritische ontwerpparameters voor transistoren zoals de *current gain* en de *subthreshold* karakteristieken. Het blijkt dat geïntegreerde circuits die gebaseerd zijn op SOI materialen heel geschikt zijn om toegepast te worden bij hoge temperatuur, in een vijandige omgeving of wanneer hoge eisen gesteld worden aan het vermogen.

Ondanks deze voordelen is de ontwikkeling van adequate methoden voor het fabriceren van SOI materialen een vrij recente prestatie die uiteindelijk heeft geleid tot het commercieel toepassen van SOI-technologie in micro-elektronica. Tegenwoordig is Unibond het meest succesvolle SOI-materiaal. Unibond-wafers worden gemaakt met de zogenaamde *SmartCut* methode die beschreven wordt in Hoofdstuk 1. SIMOX (*separation by implantation of oxygen*) is een ander belangrijk SOI materiaal. Zoals de naam al aangeeft, wordt een SiO₂ laag gevormd onder een kristallijne Si laag door zuurstofionenimplantatie in een Si substraat dat daarna langdurig verhit wordt op hoge temperatuur.

In tegenstelling tot conventionele thermische oxidatie van Si om isolerende SiO₂ lagen te vormen, worden SOI materialen gefabriceerd op een tamelijk ingrijpende wijze. Dit leidt tot het verschijnen van nieuwe defecten in SOI materialen, hetgeen een specifieke studie vereist. In het bijzonder bevatten de begraven oxydelagen van SOI materialen in het algemeen meer defecten dan conventionele thermisch gegroeide oxiden. De interactie met het alom aanwezige waterstof is van belang vanwege het grote aantal degradatie-effecten waarbij waterstof is betrokken. Voorbeelden daarvan zijn: het creëren van elektronen vangstplaatsen

(traps), donorgeneratie aan de Si/SiO₂ grenslaag, depassivering van ongepaarde elektronen (*dangling bonds*), het genereren van extra elektronen niveaus in de energiekloof (*band gap*) van het silicium of de formatie van defectcomplexen waarbij bepaalde doteringsonzuiverheden betrokken zijn (*shallow dopant impurities*). In het geval van SOI materialen kunnen deze effecten versterkt worden door een aantal factoren die te maken hebben met de defectstructuur, bijvoorbeeld de aanwezigheid van grote hoeveelheden waterstof zoals waargenomen in SIMOX, de aanwezigheid van plekken in het materiaal die H₂ dissociëren (*cracking sites*), het bestaan van mechanische spanningen in de materiaallagen en het feit dat het begraven oxide niet aan een kant vrij is maar omgeven door silicium..

Dit proefschrift ambieert een bijdrage te leveren aan het beter begrip van deze onderwerpen. SIMOX en Unibond monsters werden in contact gebracht met waterstof (of deuterium), gebruik makend van verschillende methoden. De invloed van waterstof op de monsters werd bestudeerd met een aantal technieken, voornamelijk thermische desorptiespectrometrie (TDS), positronbundelanalyse (PBA) en capaciteit-spanning metingen (CV). De eerste twee technieken worden niet vaak toegepast in halfgeleideronderzoek. Een aantal technische inspanningen waren vereist om hen geschikt te maken voor halfgeleiderstudies. In het proefschrift wordt aangetoond dat nuttige informatie kan worden verkregen uit het gecombineerd toepassen van genoemde technieken.

Hoofdstuk 1 geeft een algemeen overzicht van bovengenoemde problemen en verder beschrijft het de methoden die gebruikt worden om SOI materialen te fabriceren. Een beschrijving van de defecten in SiO₂ en de modellen die gebruikt worden om experimentele resultaten te beschrijven worden besproken in Hoofdstuk 2. Enkele belangrijke (elektro-)chemische reacties die van belang zijn voor het optreden van defecten worden besproken. Dit betreft o.a. ook het interactie-mechanisme van gaten met Si-H defecten in SiO₂ en het mechanisme van het vrijkomen van chemisch gebonden waterstof in SiO₂. Het eerste mechanisme speelt een belangrijke rol bij het genereren van positieve lading aan de SiO₂/Si grenslaag en het voorkomen van ongepaarde elektronen in het silicium (*dangling bonds*) in het oxide. Het tweede mechanisme heeft betrekking op de rol van de atomaire vorm van waterstof in het vrijkomen van waterstof en de rol van H₂ dissociatie (*cracking*) centra. Verder wordt in Hoofdstuk 2 ook een model gepresenteerd voor positrontransport in SiO₂ waarover een elektrisch veld is aangelegd. Er wordt aangenomen dat positronen die geïmplanteerd worden in SiO₂ gemakkelijk positronium (Ps) kunnen vormen. De overige positronen kunnen zich verplaatsen waarbij ze gaan drijven onder invloed van het elektrisch veld. De formatie van Ps wordt beschreven door een tijdsafhankelijk, driedimensionaal *rate*-diffusie model waarbij de gelijktijdige interactie van elektronen, gaten en positronen in beschouwing genomen wordt. Het transport van positronen die geen Ps vormen, wordt beschreven door de eendimensionale, stationaire *rate*-diffusie vergelijking.

De experimentele technieken die in dit proefschrift worden gebruikt, worden beschreven in Hoofdstuk 3. Eerst wordt de behandeling van de meetmonsters besproken. Dit betreft ook schoonmaakprocedures en de verscheidene methoden die zijn gebruikt om de monsters in contact te brengen met waterstof, namelijk verhitting in waterstof (of deuterium) en ionenimplantatie. Ten tweede wordt TDS uitgebreid beschreven. In het bijzonder worden de extra complicaties besproken die betrekking hebben op waterstofdesorptie in vergelijking

met heliumdesorptie. Verder wordt getoond hoe VUV-stralingsgeïnduceerde desorptie kan worden bestudeerd, hetgeen het mogelijk maakt om het vrijkomen van gas te correleren met gateninjectie in SiO₂ door VUV bestraling. Deze techniek wordt *Radiation-induced Desorption Spectrometry* (RDS) genoemd. Ten derde worden de verscheidene PBA technieken die gebruikt worden in dit proefschrift tot in detail beschreven, namelijk *Doppler Broadening of Annihilation Radiation* (DBAR) en *Two-Dimensional Angular Correlation of Annihilation Radiation* (2D-ACAR).

De effecten die worden geassocieerd met gateninjectie in SiO₂ worden bestudeerd in Hoofdstuk 4 door het gecombineerd gebruik van TDS, RDS, PBA en CV. MOS capacitors werden verhit in deuteriumgas bij een temperatuur van 680 K. De concentratie van deuterium in het monster werd bepaald met TDS metingen. Verder werd het vrijkomen van gas tijdens de gateninjectie gevolgd met RDS, terwijl met PBA het profiel gevolgd werd van de defecten die in het oxide gecreëerd werden, en tenslotte met CV de accumulatie van positieve lading. De resultaten zijn in overeenstemming met het gateninjectie-model van Hoofdstuk 2. Ze tonen aan dat gateninjectie leidt tot het vrijkomen van waterstof, het genereren van positieve lading aan de SiO₂/Si-grenslaag en de generatie van Si *dangling bonds* dicht bij de Al/SiO₂ grenslaag.

In Hoofdstuk 5 worden de TDS experimenten gepresenteerd die zijn uitgevoerd op SIMOX-monsters die geïmplantieerd zijn met deuterium of verhit zijn in deuterium. De positronenvangstplaatsen zijn geïdentificeerd als Si-D en Si-OD groepen. Er werd aangetoond dat de aanwezigheid van Si of O *dangling bonds* leidt tot een hoge concentratie atomair waterstof in het oxide. Dit leidt weer tot het vrijkomen van gebonden deuterium via de formatie van moleculair waterstof. Er wordt aangetoond dat de Si toplaag dient als een barrière voor het vrijkomen van deuterium omdat D₂ moleculen eerst moeten dissociëren aan de grenslaag om zich vervolgens door de Si toplaag te verplaatsen. Het alternatief is dat waterstofmoleculen afstanden in de orde van millimeters moeten afleggen om te kunnen ontsnappen aan de zijanten van de MOS-structuren. Met TDS kunnen beide ontsnappingsroutes van elkaar onderscheiden worden.

Ps wordt in grote hoeveelheden gevormd in SiO₂, hetgeen wordt aangetoond in Hoofdstuk 6. Dit moet in beschouwing genomen worden wanneer PBA experimenten worden uitgevoerd op SiO₂. In dit hoofdstuk wordt een nieuwe manier gepresenteerd om de Ps fractie te bepalen met behulp van DBAR-metingen. Verder worden de defecten besproken die worden gegenereerd door elektronen- of gateninjectie. Er wordt aangetoond dat gateninjectie-experimenten die beschreven zijn in Hoofdstuk 4 leiden tot de generatie van extra vangstplaatsen voor positronen. Het toont duidelijk aan dat de vangstplaatsen niet positief geladen zijn, zoals voorheen wel is gesuggereerd. Aan de andere kant leiden gateninjectie-experimenten tot de generatie van negatief geladen centra, die zich gedragen als zeer effectieve positronen vangstplaatsen. De behandelingen die worden gebruikt in Hoofdstuk 5 om deuterium in te brengen in de monsters veroorzaken nieuwe defecten. Verhitte in deuterium leidt niet tot de vorming van vangstplaatsen voor positronen, maar leidt wel tot de accumulatie van positieve lading. Ionenimplantatie leidt tot de generatie van vangstplaatsen voor positronen die zijn gerelateerd aan de verplaatsing van Si en O atomen en leidt bovendien tot het genereren van ongepaarde elektronen (*dangling bonds*). De evolutie van

deze defecten tijdens thermische verhitting wordt ook gevolgd met PBA en wordt beschreven in Hoofdstuk 6.

Om het aandeel van de positronen die annihilieren aan de SiO₂/Si grenslagen te vergroten, worden positronen geïmplanteerd in de SiO₂ laag en dan door een extern aangelegd elektrisch veld in het oxyde gedrift naar de grenslaag. Deze experimenten worden besproken in Hoofdstuk 7. De gelijktijdige formatie van Ps maakt de interpretatie van de resultaten echter gecompliceerd. Het eerste deel van het hoofdstuk is daarom gewijd aan het bestuderen van positronentransport in SiO₂. Er wordt daarbij vastgesteld dat positronen wanneer ze Ps vormen niet meer gevoelig zijn voor het elektrische veld en daarom niet onderhevig zijn aan drift. Het positronentransportmodel dat wordt gepresenteerd in Hoofdstuk 2 wordt hier gebruikt om de experimentele waarnemingen te verklaren. Met behulp van dit begrip van de transportprocessen worden positronenstudies met elektrische velden uitgevoerd. Er wordt gedemonstreerd dat er Ps gevormd wordt wanneer positronen de grenslaag bereiken, hetgeen afhankelijk is van de grenslaagconfiguratie. Een grenslaag met veel zuurstof leidt bijvoorbeeld tot een kleinere Ps-fractie dan een grenslaag zonder waterstof. Het gebruik van PBA studies in combinatie met het toepassen van elektrische velden blijkt een nuttige techniek te zijn om informatie te verkrijgen over de eigenschappen van de grenslaag.

Hoofdstuk 8 is gewijd aan andere SOI systemen: deze hebben een amorfe Si toplaag en worden gebruikt voor zonneceltoepassingen en de fabricatie van dunne-film-transistoren. De amorfe Si lagen werden opgedampt met een gloeiontlading (*glow discharge*, GD) of *hot wire* (HW) technieken. Een aantal monsters bevatten ingebedde kristallijne fases. Met behulp van de 2D-ACAR positronenbundel wordt aangetoond dat deze monsters ook een klein aantal holten met nanometerafmetingen bevatten die moeilijk te identificeren zijn met andere technieken. DBAR metingen die worden uitgevoerd wanneer elektrische velden zijn aangelegd, laten zien dat de grenslaag tussen het opgedampte, amorfe, Si en het SiO₂ ongeveer hetzelfde karakter vertoont voor monsters die zijn opgedampt met GD of HW technieken. Er wordt aangetoond dat positronen annihilieren in open volume defecten die zijn gerelateerd aan de grenslaag. Verder laten de metingen zien dat elektronen vanuit de amorfe Si laag makkelijk kunnen worden geïnjecteerd in het SiO₂ waar ze bijdragen tot een toename van de Ps formatie.

Acknowledgements

Undoubtedly, the present thesis would not have been possible without many persons to whom I am sincerely thankful. A good example of this is my supervisor Tom van Veen. Without him this thesis would not exist. He was a continuous support during the years I had the pleasure to work under his supervision. He was always open to suggestions, helpful with brilliant ideas and firm when necessary. A good proof of what I am saying is that I am again working with him in another and even more exciting project. Jan de Nijs was my first supervisor. I am indebted with him for the help he gave me in the beginning when it is more necessary. In addition, despite he left the University he was always ready for meetings to which he always brought many important points to develop or critics to consider. This thesis is based on those meetings. I can not forget Pieter Balk who contributed with his impressive experience to every discussion with the subtlest points, which brought me in many occasions to the important research aspects and kept me out of fruitless labyrinths. Henk Schut was always there. He was always an important help. The discussions with him were very pleasant thanks to his wonderful sense of humour and he always managed to extract the most controversial points after a careful reading of my manuscripts. Thank you Henk. I would like to thank Peter Mijnaerends his tremendous effort reading the whole manuscript. His remarks were extremely important to improve very significantly the thesis. In some cases they sounded like magic to me, because with a few words Pieter converted entire obscure paragraphs in meaningful propositions. It was very nice to work with Anke Brockhoff and Frans Habraken. The discussions with them were always very useful and pleasant. I really learnt very much with them. Thank you both. I am indebted to André Stesmans and Valery Afanas'ev. I must say that I enjoyed with them the most useful scientific discussions that I ever had during my Ph.D. period and actually, this is of great importance for a poor Ph.D. student trying to understand things. Apart of work we had also very amusing conversation about other topics. It was really nice to meet them. The members of the STW user's committee were all a great help for me. It was really nice to meet them every six months and receive suggestions, ideas, critics... from them. Thank you all.

I was lucky to have such a wonderful team at DIMES. Definitely without them I would not have managed to do many experiments, and even better with them I could do it in

just a few minutes, amazing, always much faster than I expected. My thanks go to Tony Zijlstra, Marc Zuidam and Arjan van Zuuk. Also thanks to Emile van der Drift for his total support every time I needed it. Without support at IRI would have also been impossible this thesis. All the staff members were always helpful and it was a pleasure to work with them. Special thanks to Stephan Eijt and Freek Labhom for many interesting discussions and suggestions. Of course I can not forget those persons that make the labs move, thank you Bob Heijenga, Walter Legerstee, Jan de Roode and Kees Westerduin. I must stress my thanks to one person, Sasha Fedorov, definitively he was my guide in the difficult work of a Ph.D. project and not only from the scientific viewpoint but in the lab, with thousands of tricks and ideas that do not appear in any manual. It was wonderful to meet Lars Jorgensen. He introduced me to IRI in 1995 and he accepted me in his house for a few days in 1997. Thank you very much Lars. Let's remember all the beers we had together in Delft, London, Munich or Mainz and let's think where to have the next one, in Grenoble, in Madrid? Olof Dankert was a wonderful companion in my daily walk to the station during the two first years at IRI. We made good use of the time we had available to discuss virtually about anything one can think about. It was nice, thank you Olof. Special thanks to my companions and friends, all the post-docs, Ph.D. students and students that are working hard at IRI. Without you life here would be much harder.

Finalmente, debo agradecer a mi familia todo su apoyo y a Cristina todo su amor y dedicación. Os quiero.

Curriculum Vitae

The author of the present thesis was born on October 1, 1971 in Madrid, Spain where he received his primary and secondary education between 1977 and 1989. In June 1989 he passed the admission exams for the University. In September 1989 he started to study Physics at the Universidad Complutense of Madrid. They were very exciting years in which he performed many activities apart of the academic obligations. He completed two years of French courses and another two years of Russian courses. He played rugby, for some period even simultaneously in two teams and he taught Physics and Mathematics both privately and in an academy to students of high school. The summers were also busy periods. He spent two of them in the United Kingdom to improve his knowledge of English, 1991 and 1993 and in the summer of 1994 he had his first real contact with scientific research. He travelled to Bratislava for a short stay in the Academy of Sciences of Bratislava, Slovakia, funded by an IAESTE scholarship. However, the real immersion in Science occurred in January 1995 when he travelled, funded by an Erasmus scholarship, to the Delft University of Technology in the Netherlands to work in the Defects in Materials groups (at that time part of the Reactor Physics department) at the Interfaculty Reactor Institute (IRI). The research project carried out was titled *Observation of cavity growth in irradiated silicon by means of positron beam analysis*. When he returned to Madrid he spent one year learning about computer programming and completed his studies in Physics, speciality of Physics of Materials in September 1996. In the same month of September he started to work as a programmer for a software company *Profit Gestión Informática*. It was a nice experience that lasted a bit more than one year, until November 1997, when he returned to Science to carry out the research described in this thesis. Since March 2002 he works in a research project at IRI devoted to the study of hydrogen storage materials. One of his dreams is to see in the near future a peaceful revolution in transportation by the introduction of hydrogen-fuelled automobiles.